Geomechanical Study of Underground Hydrogen Storage

Ramesh Kumar, K.

DOI
10.4233/uuid:b3d264ce-e7dc-4e67-b0e1-94f3cc7831ca

Publication date
2023

Document Version
Final published version

Citation (APA)
Ramesh Kumar, K. (2023). *Geomechanical Study of Underground Hydrogen Storage*. [Dissertation (TU Delft), Delft University of Technology]. https://doi.org/10.4233/uuid:b3d264ce-e7dc-4e67-b0e1-94f3cc7831ca

GEOMECHANICAL STUDY OF UNDERGROUND HYDROGEN STORAGE

Proefschrift

ter verkrijging van de graad van doctor
aan de Technische Universiteit Delft,
op gezag van de Rector Magnificus prof. dr. ir. T.H.J.J. van der Hagen,
voorzitter van het College voor Promoties,
in het openbaar te verdedigen op woensdag, 1 November, 2023, om 17:30 uur

door

Kishan RAMESH KUMAR

Master of Science in Mechanical Engineering,
Technische Universiteit Delft, Nederland,
geboren te Bengaluru, India.

Dit proefschrift is goedgekeurd door de promotoren.

Samenstelling promotiecommissie bestaat uit:

Rector Magnificus,	voorzitter
Dr. H. Hajibeygi,	Technische Universiteit Delft, promotor
Prof. dr. ir. J.D. Jansen	Technische Universiteit Delft, promotor
Onafhankelijke leden:	
Prof. dr. I. Berre	University of Bergen
Dr. D. V. Voskov	Technische Universiteit Delft
Dr. A. Barnhoorn	Technische Universiteit Delft
Prof. dr. P. Vardon	Technische Universiteit Delft
Prof. dr. ir. C. Vuik	Technische Universiteit Delft
Prof. dr. S. Geiger	Technische Universiteit Delft, reservelid

This research was carried out within the ADMIRE simulation group at TU Delft sponsored by the NWO, SLB, Shell, Energi simulation, and Chevron.

Keywords: Hydrogen storage, Energy transition, Geomechanics, Numerical simulation, Multiscale methods, Cyclic injection and production

Printed by: GildePrint

Front & Back: Kishan Ramesh Kumar using Firefly

ISBN 978-94-6366-759-3

An electronic version of this dissertation is available at
http://repository.tudelft.nl/.

CONTENTS

List of Figures

List of Tables

SUMMARY

With the rise of renewable energy and the drive to achieve net-zero emissions, energy storage has become a crucial component of the energy sector to address the challenges of intermittency. The vast subsurface environment offers significant storage potential, capable of accommodating terawatt-hour (TWh) capacities. One approach to leverage this storage capacity involves converting renewable energy into hydrogen and storing it underground within salt caverns and depleted porous reservoirs. This stored hydrogen can then be utilized as needed. However, this cyclic injection and production of hydrogen will exert repeated stress on the subsurface, resulting in periodic changes in pressure.

One critical aspect that requires investigation for the safe storage of hydrogen (H2) is the field of geomechanics, which becomes essential in both salt caverns and depleted reservoirs. To gain a better understanding of this, a comprehensive review of the geomechanics involved in underground hydrogen storage was conducted to examine existing knowledge and identify research gaps. To delve deeper into the influence of geomechanics, particularly regarding the inelastic creep deformation of rocks in salt caverns and depleted porous reservoirs, numerical simulations were employed. Given the potential costliness of fine-scale simulations, multiscale simulations were carried out using algebraic multiscale methods. Constitutive models were utilized to analyze deformation patterns in and around the reservoir, assessing their impact on subsidence or uplift.

In order to further comprehend the effects of cyclic loading on rocks, constitutive models were developed based on extensive experimental data obtained from sandstone rocks subjected to long-term stress conditions. These models aided in uncovering the underlying physics of rock behavior when exposed to different stress regimes during prolonged cyclic loading. Subsequently, these models were integrated into finite element method (FEM) simulations to observe their impact on field-scale scenarios, with a synthetic Bergermeer case study serving as an example.

To enhance the computational efficiency of multiscale methods, unsupervised machine learning techniques were applied to optimize the formation of computational grids, utilizing graph theory techniques such as Louvain and random walk algorithms. These optimized grids were then compared with the grids generated from METIS to evaluate the computational performance of pressure solvers in a commercial scale simulator.

SAMENVATTING

Met de opkomst van hernieuwbare energie en de ambitie om netto nul emissies te bereiken, is energieopslag een cruciaal onderdeel geworden van de energiesector om de uitdagingen van intermittentie van hernieuwbare energiebronnen aan te pakken. De uitgestrekte ondergrondse omgeving biedt aanzienlijk opslagpotentieel, dat in staat is terawattuur (TWh) capaciteit te accomoderen. Een benadering om dit opslagvermogen te benutten, omvat het omzetten van hernieuwbare energie in waterstof (H2) en het opslaan ervan ondergronds in zoutkoepels en uitgeputte poreuze reservoirs. Deze opgeslagen waterstof kan dan worden gebruikt wanneer dat nodig is. Echter, deze cyclische injectie en productie van waterstof zal herhaalde spanning op de ondergrond uitoefenen, resulterend in periodieke veranderingen in druk.

Een kritisch aspect dat onderzocht moet worden voor de veilige opslag van waterstof is het vakgebied van de geomechanica, dat essentieel wordt in zowel zoutkoepels als uitgeputte reservoirs. Om hier een beter begrip van te krijgen, werd een uitgebreide review van de geomechanica die betrokken is bij ondergrondse waterstofopslag uitgevoerd om bestaande kennis te onderzoeken en onderzoekshiaten te identificeren. Om dieper in te gaan op de invloed van geomechanica, met name met betrekking tot de onelastische kruipdeformatie van gesteenten in zoutkoepels en uitgeputte poreuze reservoirs, werden numerieke simulaties toegepast. Gezien de potentiële kostbaarheid van fijnschalige simulaties, werden multiscale simulaties uitgevoerd met behulp van algebraïsche multiscale methoden. Constitutieve modellen werden gebruikt om de deformatiepatronen in en rond het reservoir te analyseren en hun impact op verzakking of opheffing te beoordelen.

Om de effecten van cyclische belasting op gesteenten verder te begrijpen, werden constitutieve modellen ontwikkeld op basis van uitgebreide experimentele gegevens verkregen uit zandstenen die aan langdurige spanningscondities werden blootgesteld. Deze modellen hielpen bij het onthullen van de onderliggende fysica van het gedrag van gesteenten wanneer ze werden blootgesteld aan verschillende stressregimes tijdens langdurige cyclische belasting. Vervolgens werden deze modellen geïntegreerd in de eindige-elementenmethode (FEM) -simulaties om hun impact op veldschaalscenario's te observeren, waarbij een synthetische Bergermeer-case study als voorbeeld diende.

Ter verbetering van de rekenkundige efficiëntie van multiscale methoden, werden onbegeleide machine learning-technieken toegepast om de vorming van rekenkundige roosters te optimaliseren, waarbij gebruik werd gemaakt van grafentheorie technieken zoals de Louvain- en random-walk-algoritmen. Deze geoptimaliseerde roosters werden vervolgens vergeleken met de roosters gegenereerd door METIS om de rekenkundige prestaties van drukoplossers in een commerciële schaal-simulator te evalueren.

PREFACE

I arrived in the Netherlands in 2017 to pursue my master's degree in Energy, Flow, and Process Technology, driven by a deep fascination for fluid dynamics. My academic journey took an intriguing turn during my honors project when I had the privilege of collaborating with Professor Kees Vuik in the realm of applied mathematics. In the journey of exploration and building my skillset in mechanical engineering, I pursued an internship and thesis in London and Zurich respectively working on experimental projects.

As I approached the culmination of my master's thesis, a decisive shift occurred within me. I resolved to dedicate myself solely to numerical research, prompting me to reach out to Professor Kees Vuik once more, who then directed me to Dr. Hadi Hajibeygi in the Geosciences department. Although I had completed my master's at TU Delft, I was unfamiliar with Dr. Hajibeygi's work and the Geosciences department. Concurrently, I was also interviewing for PhD positions in the United States, having successfully cleared the TOEFL.

My path led me to engage in four rigorous interviews with Dr. Hadi Hajibeygi, spanning personal, technical, and coding domains. His unwavering passion for science left a profound impression on me. Still, I grappled with the decision to transition from mechanical engineering to geosciences. Conducting background research on Dr. Hajibeygi's work became an essential step in my deliberation. While I had undertaken numerous academic internships across the world during my bachelor's and master's, my aspiration was now to undertake an industrial internship. I eagerly sought projects that embraced industry collaboration, and Dr. Hadi Hajibeygi's assurance that his work was indeed applied and open to industrial engagement led me to follow my instincts and commit to that project.

My journey into my PhD program commenced in December 2019. Within the first week, I embarked on a month-long journey to India, a welcome break from my MSc studies and a chance to reunite with my family. Dr. Hajibeygi graciously allowed me to attend courses remotely and initiated my education in multiscale methods. Upon my return to the Netherlands in January, I faced the challenge of completing two courses while concurrently collaborating with two MSc students on salt cavern research. Within just three months of commencing my PhD, I had acquired 10 credits and was actively engaged with three MSc students—an overwhelming yet immensely enriching experience. Then, the COVID-19 pandemic struck, and the world came to a standstill.

However, the advent of the COVID-19 pandemic reshaped the landscape of my PhD journey. The emotional toll of witnessing global suffering, coupled with concerns for the well-being of my family in India, weighed heavily on me. Adapting to remote work became essential, though I cherished the bond I developed with my flatmates during this period. While the world grappled with the pandemic, I learned to navigate the challenges it presented. The next two years were filled with remote work, online meetings, conferences, and limited activity outside of my home.

Throughout this challenging period, my friends in the Netherlands scattered across different cities, and my family in Germany provided unwavering support. These connections sustained my emotional well-being and bolstered my productivity during my PhD. I also could work from India in the consecutive December holidays for a couple of months. My initial aspiration for industry collaboration was eventually realized through a remote internship with SLB, made possible with Dr. Hajibeygi's support and guidance, ensuring a smooth administrative process. During this phase of PhD, I also picked up some Dutch, managed to travel to 10+ countries, and developed a newfound passion for chess, photography, and maintaining my physical fitness.

Over the past year, I seized opportunities to attend conferences across Europe, fostering strong bonds with my fellow Ph.D. colleagues. In retrospect, my journey has been far from straightforward, marked by twists and turns. When asked about my academic background, I still find myself oscillating between mechanical engineering and geosciences. As I embark on the next phase of my career, I am eager to contribute to making the world a better place.

Warm regards,
Kishan Ramesh Kumar
Delft, October 2023

1

INTRODUCTION TO THE MECHANICS OF ROCKS UNDER CYCLIC LOADING RELEVANT TO UNDERGROUND HYDROGEN STORAGE

Summary: *Hydrogen is a promising energy carrier for a low-carbon future energy system, which can be stored in megaton scale (equivalent to TWh of energy) in subsurface reservoirs. Safe and efficient underground hydrogen storage requires a thorough understanding of the geomechanics of the hosting rock under fluid pressure fluctuations. In this chapter, the mechanics of rocks relevant to cyclic underground energy storage is elaborated. Further, a framework employed to integrate lab-scale data into simulation studies is delineated. To gain a broader understanding of the relevance of geomechanics in Underground Hydrogen Storage (UHS), other aspects such as the impact of bio-geochemical interactions on rock mechanical properties, the mechanical integrity of wellbore, and induced seismicity are discussed. The current knowledge gaps and the need to enhance our understanding of the geomechanical aspects of hydrogen storage are also discussed.*

1.1. MOTIVATION

Renewable energy sources, such as solar and wind, provide sustainable alternatives to traditional fossil fuels [25]. However, increasing their contribution in the energy mix presents significant challenges that must be addressed to achieve net-zero goals. Among

This is from the review publication: Ramesh Kumar et al., 2023, Journal of Energy Storage

these challenges, their reliance on unpredictable weather conditions and the fluctuating seasonal trends, which can differ greatly from demand fluctuations stand out [26]. These challenges highlight the need for large-scale storage and fluctuating systems, capable of storing green energy in the range of terawatt-hours (TWh). One approach is to convert green energy, particularly hydrogen (H_2), into a green molecule and store it in underground reservoirs. Alternatively, compressed air energy storage or aquifer thermal energy storage can be used, depending on the storage capacity required and the type of available green energy [27].

Green H_2 produced from renewable energy using electrolysis [28, 29] is regarded as one of the options for energy storage when there is excess electricity produced. The wide range of applications of H_2 such as fuel for transportation, and feedstock for a variety of industrial processes like the production of steel, along with its nearly zero greenhouse gas emission, make H_2 an attractive solution for the current energy landscape [30–33]. Considering the future demand for H_2, suitable options to store H_2 in the subsurface have to be evaluated. Underground Hydrogen Storage (UHS) involves utilizing underground formations like aquifers, salt caverns, and depleted oil and gas fields in a safe, efficient, and reliable manner [34–36]. Figure 1.1 shows a schematic illustration of UHS in depleted reservoirs and salt caverns.

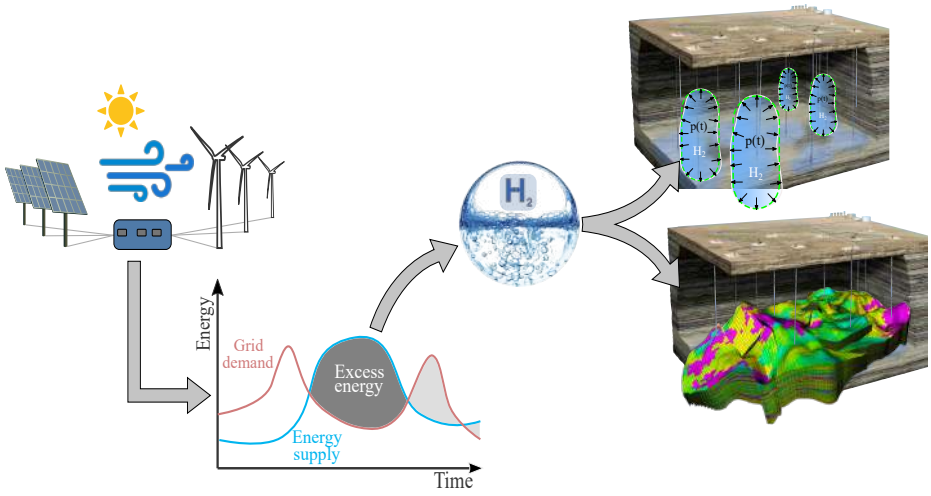

Figure 1.1: An illustration describing UHS in salt caverns and depleted reservoirs using green H_2 produced from renewable energy.

The storage capacity is a crucial factor when choosing a storage option. The storage capacity of depleted porous reservoirs is substantially higher than salt caverns, in the order of (TWh), which is suited for seasonal time scale. From an economic point of view, it was found that aquifers and depleted reservoirs are slightly more economical compared to salt caverns for the chosen storage sites in the USA [37, 38]. However, assessing the viability of porous reservoir sites is challenging due to their inherent multiscale hetero-

geneity and uncertainty [39]. Besides economic considerations, several scientific aspects need to be investigated to ensure the safe deployment of UHS, including thermodynamics, hydrogeology, geomechanics, microbial activity, and geochemical interactions [40–42]. This chapter specifically focuses on reviewing the geomechanical effects of rocks under cyclic loading relevant to UHS.

Gas storage sites and salt caverns have been utilized in various applications such as natural gas storage [43–46], crude oil [47], compressed air energy storage (CAES) [48–50] and in recent years for CCUS operations [1, 51, 52]. Additionally, abandoned salt caverns have been repurposed for alkali waste disposal [53, 54] and for nuclear waste disposal [55, 56]. However, the understanding of underground H_2 storage is still in its nascent stage. H_2 has been stored in very few salt caverns such as Teeside (UK) and Clemens, Moss Bluff, and Spindletop in the US [33, 57, 58]. There are also a few gas storage sites that store a percentage of H_2 such as in aquifers of Beynes (France), Lobodice (Czech Republic), and in depleted gas reservoirs of Diadema (Argentina), Sun storage (Austria) [59, 60]. Recent studies have explored the technical, techno-economical aspects and risks associated with the potential of UHS in different countries [36, 61–68]. However, further extensive multidisciplinary research is needed to enable commercial use and ensure the safety and longevity of gas storage sites.

One crucial aspect of UHS which needs to be studied is the geomechanical effects on the reservoir rock, cap rock, and its surrounding area. Since the injection and production of green energy-rich fluids into underground reservoirs depends on the demand and supply of renewable energy, the loading is cyclical in nature [41, 69]. Thus, the reservoir experiences cyclic changes in porous pressure and temperature. As a result, the in-situ effective stresses are altered accordingly, which influences the stress conditions on the reservoir rock and surrounding elements, such as caprock, faults, and wells [70–74]. For instance, a decrease or increase in fluid pressure can induce fault reactivation and seismicity (earthquakes) by perturbing the stress path [75, 76]. The pressure fluctuation during storage can also induce vertical movement of the earth's surface (uplift/subsidence), which damages the infrastructures nearby [77, 78]. The use of salt caverns for storage purposes can also result in undesired outcomes such as excessive cavern convergence (i.e. loss of storage volume) [79–81], roof collapse [82, 83], fluid leakage [84], among other events [85]. Therefore, operational limits in salt caverns must be defined with caution. Hence, it is essential to understand the deformation behavior of rocks in UHS for both depleted reservoirs and salt caverns. To address this, a multiscale framework has been developed to incorporate lab-scale physics into field-scale reservoirs, as elaborated in the following section.

1.2. MULTISCALE FRAMEWORK FOR ROCK MECHANICS

The framework employed in this study focuses on investigating the deformation mechanisms exhibited by rocks, primarily through the analysis of lab-scale experimental data. This approach allows us to explore various types of rocks under different boundary conditions. However, it is important to acknowledge the limitations of experimental studies, such as the constraints imposed by the scale of the geometry, time, and heterogeneity. Consequently, in order to examine the effects of cyclic loading over longer time scales

and in large-scale reservoir models, constitutive models are commonly developed based on experimental data. These models enable the identification of different deformation mechanisms and offer valuable insights into the long-term behavior of rocks. By integrating these constitutive models into reservoir-scale simulators, it becomes possible to accurately mimic the diverse deformation mechanisms experienced by rocks and simulate their response at the field scale. Figure 1.2 provides a schematic representation of the framework. The subsequent subsections elaborate on the components of this framework.

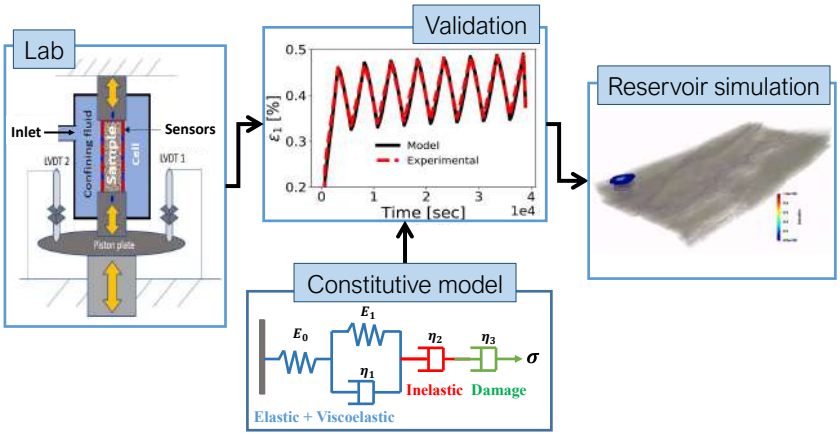

Figure 1.2: A framework employed to integrate lab-scale studies with field scale simulation. Lab scale experiments are employed to conduct cyclic loading and unloading experiments which are further used to develop constitutive models to observe their behavior in reservoir simulation. The details about the constitutive model are elaborated in Figure 1.4.

1.2.1. LAB SCALE EXPERIMENTS

Several lab-scale research studies have been conducted in previous decades to examine the strains and stresses experienced by rocks under different types of loads, including uniaxial and triaxial, as well as their cyclic variations. However, in the context of underground hydrogen storage (UHS), experimental studies are not reported in the literature specifically focusing on porous rocks with H_2 as the pore fluid. Instead, we can refer to the comprehensive review which provides a detailed analysis of cyclic loading experiments conducted on porous rocks without employing H_2 [86]. The review categorizes the experiments based on factors such as loading frequency, maximum axial stress, confinement stress, degree of saturation, anisotropy, dynamic seismic waveforms, and size of the rock sample. These factors become crucial when dealing with realistic operational stress conditions in the presence of fluctuating pore pressure. Figure 1.3 illustrates the commonly performed lab-scale experiments aimed at studying different processes involved in UHS. It is important to note that the schematic does not include rock degradation resulting from biochemical processes, as analyzing this aspect would

require multiple types of specialized equipment.

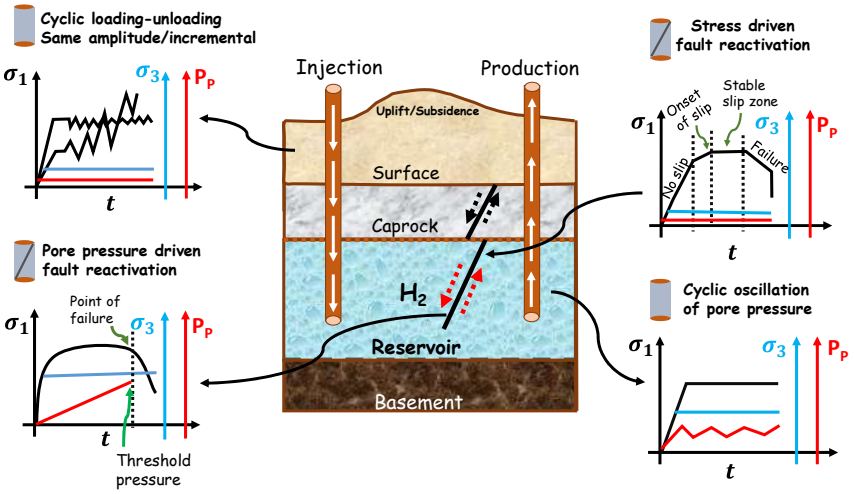

Figure 1.3: Illustration of the type of experiments being conducted in the lab scale relevant to UHS for the variation of different stresses (σ_1,σ_3) and pore pressure (P_p) with time (t).

Experimental assessment of mechanical properties of rocks in subsurface reservoirs often involves cyclic alteration of horizontal and vertical stress conditions to evaluate storage feasibility. Previous studies have reported a significant decrease in the porosity and pore connectivity of sandstones after consecutive loading cycles due to microcrack closure [87]. However, it has been shown that cyclic loading-unloading within a defined stress range has only a minor effect on permanent rock deformation [88]. Although acoustic sensors can pick up crack generation in the first few cycles, the recurrence of such events is limited unless the peak load exceeds the load applied in the previous stage due to the popularly known Kaiser effect [89]. Recently, the accumulation of plastic strain resulting from repeated low-frequency cyclic loading-unloading in the context of UHS operations has been documented [27]. Another crucial aspect to consider is the heterogeneity within rocks, which can play a critical role in crack nucleation, propagation, and the accumulation of plastic strain. The formation or growth of cracks is strongly dependent on the maximum deviatoric stress and the direction of principal stresses [90].

The caprock, which is overlying the target reservoir, is also experiencing cyclic loading and unloading because of the direct influence of the reservoir. Shale rocks, with their distinct grain structure, are expected to behave differently compared to porous sandstones. Recently, the anisotropic fatigue behavior of shale was found to be sensitive to the cyclic loading frequency and stresses because of different bedding configurations

[91]. The inherent heterogeneity of shale reservoirs, compared to sandstones, greatly influences the direction of maximum stress experienced by caprock samples, depending on the orientation of laminae or bedding planes in shales [92]. Emission of significant acoustic signals during cyclic deformation at lower stress levels, opposite to the Kaiser effect and popularly known as Felicity effect [93] can be observed in shales during cyclic loading. When considering shale as a caprock for H_2 reservoirs, it is important to assess its yield strength, ensuring it remains within the stress tolerance of reservoir stress cyclicity to prevent the formation of leakage pathways through the caprock.

The other type of experiment that is performed involves cyclic pore fluid injection, which is responsible for applying cyclic loads during the storage of energy-rich fluids in the subsurface. There have been few investigations specifically focusing on the use of H_2 as a pore fluid. However, studying the behavior and mechanics of reservoirs in relation to cyclic pore fluid injection with different fluids can provide valuable insights. An observation was made that when a significant monotonic increase in pore pressure was cyclically imposed, it had a minor effect on the mechanical properties of the rock [94]. To prevent crack generation during underground hydrogen storage (UHS) in reservoirs, it is suggested to maintain a low-frequency pore pressure oscillation and ensure a substantial difference between peak pore pressure and peak strength under in-situ stress conditions [95]. Low-frequency cyclic fluid injection maximizes pore volume utilization, reduces the risk of seismic events, and slows down the relaxation of pore fluid pressure. This approach ensures the safer operation of subsurface reservoirs by inducing permanent fatigue and minimizing energy output from future seismic events, thus enhancing long-term reservoir safety [96]. Recent numerical simulations have indicated the significant relevance of the rock's memory effect, commonly known as the Kaiser effect, in porous reservoirs, and this finding is further supported by a field-scale study involving the injection of natural gas [97, 98].

In the context of UHS, it is also essential to study fault reactivation caused by external stress and pore fluid injection to understand the possibility of fault reactivation and induced seismicity. This aspect is addressed in Section 1.3.1. The subsequent section provides an elaboration on constitutive models that have been developed based on experimental data.

1.2.2. CONSTITUTIVE MODELS

In order to gain insight into the hydro-mechanical behavior of the subsurface, it is crucial to investigate the mechanisms experienced by rocks under cyclic loading. To facilitate this, constitutive models are developed to forecast the long-term behavior of rocks. These models aid in predicting how rocks will behave under various operational conditions that cannot be replicated at the laboratory scale. Figure 1.4 provides a general depiction of how strain varies with time when a constant load is applied.

The transient region can be characterized by elastic components and time-dependent elastic strains (viscoelasticity) [99, 100]. The next region is the steady state region which can be further decomposed to time-dependent inelastic strain and time-independent inelastic strain (plasticity). Inelastic strains such as plasticity, viscoplasticity, and creep are commonly observed in underground formations. Plasticity is a permanent defor-

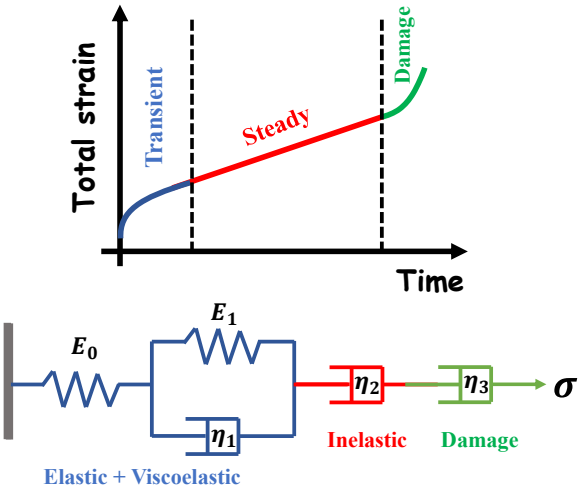

Figure 1.4: A simplistic general description of rock deformation mechanisms under a constant imposed stress σ. The parameters E_0, E_1 are Young's modulus of elastic and viscoelastic elements and η_1, η_2, η_3 are the viscosity of the elements.

mation that occurs instantaneously (time-independent) when the stress levels reach a certain yield limit (yield surface) [101–108]. Similarly, viscoplasticity also refers to a permanent deformation when the stress levels touch the yield surface. In this case, however, the rate at which stress is applied also plays an important role [109] which makes the deformation time-dependent [10, 110–112]. Another type of time-dependent inelastic deformation is known as creep deformation, in which the material constantly deforms under the application of a constant and persistent external load, irrespective of the stress levels [107, 113, 114]. Lastly, damage strain can occur which can initiate microcracks and lead to the failure of rocks [115, 116]. This particular stage must be avoided to ensure the safety of UHS technology. The subsurface consists of various types of rocks, each exhibiting distinct primary deformation mechanisms governed by different constitutive laws due to variations in grain composition.

Constitutive models relevant for subsurface energy storage in different rocks such as sandstone, shale, and carbonate rocks are presented, whereas rocksalt physics is discussed later in chapter 3. Constitutive models are relevant to underground energy storage for understanding the inelastic and frictional behavior that can be used in field scale simulation for sandstone, shale, and carbonate rocks are listed in Table 1.1.

To quantify the deformation in rocks, models based on different physics including fault slip laws, viscoelasticity, plasticity, and creep, need to be accommodated. Field-scale simulators can employ these models to compute permanent deformation, stresses in the region, and fault slips with careful calibration from lab experiments.

Table 1.1: Constitutive models of different rocks subjected to a load in the context of subsurface energy storage. The constitutive laws suitable for rocksalt are elaborated in Table 3.1.

Physics	Constitutive model	Type of rock	Characteristics
Viscoelasticity [14, 99, 117]	General Kelvin model: $\frac{\varepsilon}{\sigma} = \frac{1}{E_1} + \frac{1}{E_2}\left[1 - \exp\left(-\frac{E_2 t}{\eta_K}\right)\right]$ Fractional maxwell model: $\frac{\varepsilon}{\sigma} = \frac{1}{E_H} + \frac{1}{\eta_A^{\alpha}} \frac{t^{\alpha}}{\Gamma(1+\alpha)}$	Sandstone	Time-dependent viscosity-driven elastic behavior was shown by 18 % tight sandstone obtained from Changqing field, China [99]. Field-scale modelling shows the importance of including the viscoelastic behavior of sandstone and shows the better comparison of results with field data.
Plasticity [108, 118–121]	MCC Yield surface: $\mathscr{F}(\boldsymbol{\sigma}, \varepsilon_v^p) = q^2 + M^2 p'(p' - p_c'(\varepsilon_v^p)) = 0$ Generalized plasticity : $d\sigma = \frac{1}{H_{vp}}(n_{gL/U} \otimes n)$ General cyclic plasticity model : $f^y = (q-(p+p_c)\alpha)^2 - (p+p_c)^2(M^y)^2$	Sandstone	Permanent deformation caused due to triaxial load imposed on the sandstone is modelled using cyclic MCC [117]. Combining hyperelasticity, plastic deformation, and wetting deterioration generalized plastic model was developed [108].
Creep [107, 122]	Power law: $\dot{\varepsilon}_{cr} = Ae^{-\frac{Q}{RT}} \boldsymbol{\sigma_{vM}}^{n-1} \boldsymbol{s}\, t^{m-1}$ Linear relationship: $\varepsilon_{cr} = \frac{\sigma - \sigma_{BP}}{\eta} \Delta t$	Sandstone	Based on Norton's law and linear dependency, creep strain is derived from experimental data which is a function of time and stresses in the region.
Viscoplasticity [16, 123, 124]	Yield surface: $\mathscr{F}(\boldsymbol{\sigma}, \varepsilon_v^p) = q^2 + M^2 p'(p' - p_c'(\varepsilon_v^p)) = 0$ $\dot{\boldsymbol{\varepsilon}}^{vp} = \dot{\gamma} \frac{\partial_{\boldsymbol{\sigma}} \mathscr{F}}{\lvert\partial_{\boldsymbol{\sigma}} \mathscr{F}\rvert}$ and $\dot{\varepsilon}_v^{vp} = \dot{\gamma} \frac{\partial_{p'} \mathscr{F}}{\lvert\partial_{\boldsymbol{\sigma}} \mathscr{F}\rvert}$	Shale	Viscoplasticity in shale rocks are solved for using Duvaut Lions viscoplasticity model and Perzyna based model that could also accommodate anisotropy.
Plasticity [121, 125]	General cyclic plasticity model: $f^y = (q-(p+p_c)\alpha)^2 - (p+p_c)^2(M^y)^2$	Carbonate	Plasticity model for carbonate based marble rock when cyclic load is imposed is compared with the experiment [121]. To further accommodate hyper-elasticity and damage, Drucker-Prager based model is suggested [125]
Creep [16, 126, 127]	Yield surface: $\mathscr{F}(\boldsymbol{\sigma}, \varepsilon_v^p) = q^2 + M^2 p'(p' - p_c'(\varepsilon_v^p)) = 0$ $\dot{\boldsymbol{\varepsilon}}^{vp} = \dot{\gamma} \frac{\partial_{\boldsymbol{\sigma}} \mathscr{F}}{\lvert\partial_{\boldsymbol{\sigma}} \mathscr{F}\rvert}$ and $\dot{\varepsilon}_v^{vp} = \dot{\gamma} \frac{\partial_{p'} \mathscr{F}}{\lvert\partial_{\boldsymbol{\sigma}} \mathscr{F}\rvert}$ Power law $\frac{\varepsilon}{\sigma} = B t^n$	Carbonate	Viscoplastic formulation for carbonate rocks was able to be reproduced using Perzyna based formulation.
Fault stability models [128–131]	Byerlee law: $\tau^{max} = \lvert\mu_c + \mu_f \cdot \sigma_n\rvert$ RSF law: $\tau = \tau^* + a\sigma_n \ln\left(\frac{V}{V^*}\right) + b\sigma_n \ln\left(\frac{V^* \theta}{D_c}\right)$ CNS law: $\tau = \frac{(\tilde{\mu} + \tan\psi)\sigma_n}{1 - \tilde{\mu}\tan\psi}$	Fracture models in different rocks like carbonates	These models help in capturing the frictional behavior of faults in the reservoir to compute the fault slip and the stresses around the faults effectively.

To study the potential of fault slippage and induced seismicity in heavily faulted reservoirs, fault slip models derived from lab-scale experiments can be integrated into field simulators. For detailed information on the physics underlying these models, readers are referred to the respective references.

However, when applying constitutive models obtained from lab-scale experiments with a timescale of days or weeks to field-scale simulations spanning years or decades, it is important to exercise caution in interpreting the results. Most of these models are developed based on external loading experiments conducted on rock specimens. Therefore, it is crucial to verify the applicability of these constitutive models in scenarios involving cyclic injection and fluid production. The confidence in these constitutive models can be strengthened when they are used to predict the behavior of the reservoir over longer timescales and compared with field-scale observations. The following subsection provides elaboration on field-scale studies relevant to underground hydrocarbon storage (UHS).

1.2.3. RESERVOIR-SCALE SIMULATIONS

Table 1.2: Geomechanical studies using geodetic, analytical and experimental data

Reference	Objective	Characteristics	Summary
Vidal et al. [132] *CO_2 storage site*	An analytical study based on the solution of Eshelby is employed to evaluate the geo mechanical risk of fault reactivation in CO_2 storage in Naylor field, Otway Basin (Shale, sandstone)	Depleted natural gas field with a depth of 2025 m at pore pressure of 175 bar	Assuming strike-slip stress regimes, this work highlights the importance of Biot's coefficient and stress paths to find the maximum sustainable pore pressure increase for different inclined faults.
Verdon et al. [52] *CO_2 storage site*	Three commercial sites have been compared when CO_2 was injected for 1 megatonne/yr based on the geomechanical response monitored using geodetic methods, seismic reflection surveys and microseismic monitoring.	Sleipner (Aquifer), Weyburn (Depleted reservoir), and Salah (Depleted reservoir) in Norway, Central Canada, and Algeria.	Different monitoring methods were useful in different sites which call for site-specific characterization. Salah showed the highest uplift of up to 2 cm compared to the rest of the sites which was caused due to injection into the water leg of the reservoir.
White et al. [133] *CO_2 storage site*	Geomechanical study is conducted on leakage in Salah CO_2 storage site based on the hypothesis of reservoir only behavior, fault leakage, flow through pre-existing fractures and hydraulic fractures.	Salah reservoir (sandstone) suggested possible CO_2 migration in the lower portion of caprock (Shale, mudstone).	Using InSAR deformations, seismic velocity anomalies, well logs, and core measurements the probability of each of the hypotheses happening in the site is elaborated. This work also highlights the usage of diverse monitoring techniques.

Field-scale studies are conducted through the monitoring of geophysical data, simulation modeling of the storage site, or a combination of both approaches. A concise overview of field-scale works relevant to subsurface energy storage, based on monitoring data and well logs, is presented in Table 1.2. To obtain comprehensive real-time field

data, a combination of multiple monitoring methods tailored to the specific site is employed. Past studies on CO_2 storage sites like In Salah, Sleipner, and Weyburn have utilized analytical models and field-scale measurements such as Interferometric Synthetic Aperture Radar (InSAR) and seismic surveys [52]. For instance, the In Salah site exhibited a 2 cm uplift accompanied by numerous microseismic events due to an increase in pore pressure resulting from injection into the water leg of the reservoir [52]. Among the potential causes of observed deformations at the In Salah site, hydro-fractures induced by injection pressure were considered the most likely explanation, surpassing other possibilities such as fault leakage or reactivation of pre-existing fractures [133]. To date, no significant seismic events have been reported from any CCUS storage site [1]. The case study conducted at the In Salah site, utilizing monitoring data and field tests, emphasizes the significance of geomechanical studies in understanding the various factors that contribute to ground surface deformation.

Similar to CCUS, hydro-fractures or changes in pore pressure resulting from H_2 injection can lead to uplift, subsidence, and induced seismicity. The cyclic nature of UHS introduces fluctuations in pore pressure and temperature, potentially causing modifications in the intergranular structure and accelerating crack propagation and rock degradation compared to CCUS. Simulation studies are also valuable in comprehending and identifying potential critical zones within and around the reservoir. Field-scale simulators are instrumental in studying the variations in reservoir deformation and stress over time. There are many field scale simulators used to model geomechanics in gas storage sites, which include FLAC [134], OpenGeoSys[135], CODE-BRIGHT [136], VISAGE [137] and STARS [138]. These simulators can be coupled with fluid flow models to simulate reservoir-scale hydro-mechanics [1, 139, 140]. The choice of specific software depends on factors such as the advantages or limitations of the code, the type of geomechanical problem, and the available information. Table C.1 provides an overview of relevant geomechanical simulation studies for subsurface energy storage.

Insights obtained from geomechanical studies are highly valuable for predicting the long-term safety of UHS technology. For instance, researchers have reported that greater subsidence occurs in regions with weak faults compared to strong faults [141], and considering rock heterogeneity in simulations leads to lower subsidence and reduced CO_2 leakage risks [142, 143]. It has also been observed that higher injection rates result in earlier reactivation of highly permeable faults compared to low permeable faults [144]. Simulations also demonstrate that considering the permeability change resulting from deformations obtained from coupled flow-mechanics simulations leads to a 13% rise in the rate of CO_2 leakage [145]. Considering the higher mobility of H_2 when compared with CO_2, this shows the importance of accounting for coupled poromechanics in the context of UHS.

The risks associated with storing CO_2 and methane largely coincide with those of storing H_2, albeit with additional complexities arising from the disparities in physical and chemical properties of the stored fluid, as well as the cyclic operating conditions. Swelling of overburden clay can occur due to the change in pH caused by the H_2 injection, which results in permeability decrease and tighter storage [146]. However, due to higher diffusion, leakage risks into caprock can be higher compared to methane or CO_2 storage sites. The properties of fault friction and fracture propagation rates can vary if

there are changes in the rock properties along the fault plane due to chemical reactions. Usually, simulations assuming elasticity along with pressure boundary conditions are employed to study the propagation of fractures [1]. In the case of cyclic injection and production of H_2, incorporating inelastic deformations and considering the possibility of tensile and shear damage can become important to model the sealing capacity of the reservoir [147–149]. Caprocks such as shale are rich in organic substances [66] and microbes. The interaction of H_2 with shale caprock can result in the loss of H_2 and the production of different chemical compounds, further weakening and degrading the rocks. However, these factors are often not adequately considered in reservoir-scale simulation studies.

In recent years, there have been numerous numerical studies conducted to investigate the geo-mechanical deformation of rock salt in the context of energy storage in salt caverns [150–159]. Additionally, Multi-Scale Finite Element Method schemes (MSFEM) have been developed to address reservoir rock mechanics, considering both linear and non-linear elastic deformations [113, 160–162]. Some studies have utilized single-scale finite element models to simulate salt cavern deformation under cyclic storage loading, focusing on homogeneous 2D caverns with simplified geometries and structured grids [163, 164]. However, the application of lab-scale constitutive models for reservoir-scale analysis has been limited. One group of researchers has investigated the creep behavior of Brazilian salt rocks using a multi-mechanism deformation creep model within the ABAQUS software. Their simulations focused on axis-symmetric caverns with different elastic properties, including heterogeneities such as shale, to assess cavern tightness and integrity for energy storage [165, 166]. However, the study did not consider caverns with complex geometries or different creep mechanisms associated with heterogeneities like carnallite. Another group of studies conducted stability analyses of symmetrical caverns subjected to cyclic loading in various salt mines, considering different elastic and visco-plastic properties [167]. Recently, specific mechanical analyses of salt caverns have been conducted in Brazil [168] and China [169] to assess cavern integrity based on their dimensions and interlayer properties. However, comprehensive 3D Finite Element Method (FEM) simulation studies incorporating damage constitutive laws derived from cyclic experimental data relevant to underground hydrogen storage (UHS) are currently lacking in the literature.

Despite the significant knowledge accumulated over the years, particularly in the context of natural gas and CO_2 storage, there are still several gaps that need to be addressed to fully understand underground hydrogen storage. These gaps and research needs will be discussed further in the following section.

1.3. OTHER ASPECTS RELEVANT TO MECHANICS OF UHS

To obtain a comprehensive understanding of the geomechanical aspects related to underground hydrogen storage (UHS), there are several key areas that require further investigation. Figure 1.5 and Figure 1.6 provide visual representations of various geomechanical processes involved, highlighting potential risks associated with depleted gas fields and salt caverns. It is evident that many of these challenges overlap between depleted gas fields and salt caverns. However, it is crucial to comprehend the impact

of these geomechanical processes in order to assess their influence on the safety of UHS technology. The following subsections will delve into these processes by referencing previous literature and discussing their relevance to UHS.

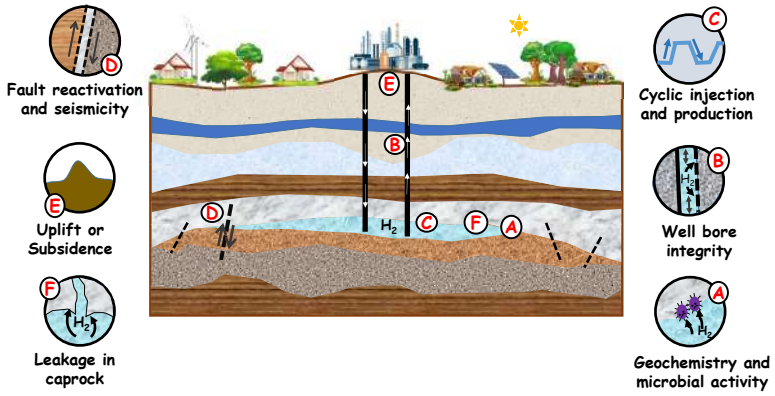

Figure 1.5: A schematic of UHS in depleted gas fields illustrating the geomechanical processes at play, highlighting potential hazards.

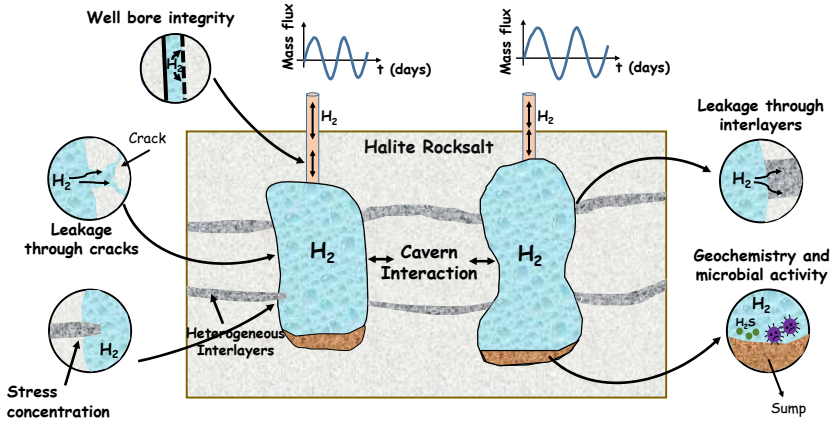

Figure 1.6: A schematic of UHS in salt caverns highlighting the geomechanical challenges and probable effects.

1.3.1. FAULT REACTIVATION AND INDUCED SEISMICITY

Insufficient knowledge about the subsurface reservoir and stress conditions, especially in faulted reservoirs, can lead to injection-induced seismicity. The worst-case scenario involves triggering an earthquake [170], which not only challenges the stability of subsurface resource storage operations but also has societal implications and raises

public concerns regarding such operations [171, 172]. Figure 1.7 illustrates the fault slip and the surrounding seismic waves caused due to H_2 injection in the subsurface.

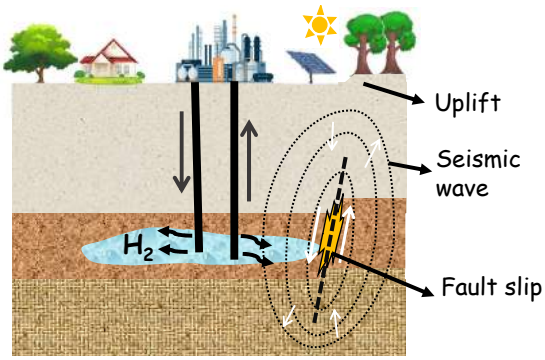

Figure 1.7: Schematic of H_2 injection-induced fault slip and the surrounding seismic waves in the subsurface. Adopted from [1, 2].

Extensive research has been conducted in this domain, addressing the issue of induced seismicity. Injection of fluids at high pressures causes a decrease in frictional strength along fault planes and a reduction in effective overburden stress within the fluid-pressurized zone. Consequently, this leads to an increase in driving shear stress and a decrease in the frictional coefficient due to lubrication [94, 173, 174]. The induced stress change can also activate remote faults depending on the injection rate and fluid diffusion rate within the reservoir. Experimental setups such as triaxial shear, direct shear, double shear, or rotary shear are typically used to study fluid-induced fault reactivation [88, 175], employing failure criteria like the Mohr-Coulomb failure criteria to analyze changes in effective normal and shear stresses along the fault plane [175].

Rocks with different permeability, when subjected to fluid injection to investigate slip, exhibit different responses in terms of change in the effective stress [176]. Depending on the injection rate and fault permeability, slips can be either seismic or aseismic [94, 177]. However, there can be a significant time lag between the injection and the occurrence of slip, influenced by local stress conditions and injection rates. It is also assumed that numerous smaller seismic events will precede a larger magnitude earthquake, however, such assumptions do not consider aseismic slips into account [178]. It is also beneficial to use strain sensors as standard monitoring strategies to accurately assess the fault plane evolution. Laboratory experiments have revealed that slow aseismic slips commonly occur both before and after seismic slips [179]. Several researchers [180–182] recommend reservoir preconditioning by injecting cooled fluid at lesser pore pressure, which reduces the possibility of larger magnitude events due to pore pressure change. Injection of cold H_2 at high pressure in faulted reservoirs can lead to a local cooling effect, however, the extent of cooling will be lower than supercritical CO_2 ($scCO_2$) injection cases [66, 183, 184].

In the case of gas production, the Groningen field in the Netherlands serves as a well-known example of induced seismicity [185]. Since the 1990s, there have been over 1000

recorded events with magnitudes greater than 1 in this field [186], and numerous studies have been conducted on this topic, encompassing numerical, analytical, and field-scale investigations. Numerical finite element simulations have shown the influence of production rate on seismic activity [187], particularly regarding the impact of fault offset in the reservoir, which leads to varied and intensified stresses on the fault caused by depletion [186]. Recent studies have also examined the effects of rupture nucleation and arrest in depleted gas fields [188]. Analytical studies have provided valuable insights into shear stress patterns resulting from injection and production in reservoirs with offset faults [189], as well as proposing advancements in fault modeling within numerical simulators to address convergence issues [190].

It is important to note the significantly lower viscosity of H_2 compared to other injected gases. For instance, at 50 °C, the dynamic viscosity of H_2 (9.4 μ Pa s) is lower than that of CO_2 (16.1 μPa s) and CH_4 (11.9 μ Pa.s) [191]. This lower viscosity contributes to the higher mobility and diffusivity of H_2, making it more prone to flow through narrower apertures. Therefore, it is crucial to revisit fault leakage experiments with a specific focus on H_2 as the pore fluid to understand the sensitivity of fault aperture to H_2 mobility.

1.3.2. IMPACT OF GEOCHEMICAL REACTIONS

The interaction between injected fluids and reservoir rocks can have long-term implications for reservoir efficiency and safety. The dissolution or precipitation of minerals along fault planes is crucial in determining slip potential and the load-bearing capacity of the faulted surface [66, 184]. Studies on the chemical interaction of the commonly injected supercritical CO_2 with host rocks have shown increased ductility and reduced cohesion in sandstones [192]. While research has been conducted on the CO_2 enriched brine interaction with sandstone and carbonate reservoirs, there is still a need for investigations into the chemical interaction of H_2 with reservoir rocks. Still, there exist a few studies contributing to this area of research. Some researchers have observed minimal changes in reservoir porosity and permeability due to the slow reaction rates between H_2 and Fe-bearing minerals [193–195]. The reactivity of H_2 with quartz or clay minerals is minimal even over geological timescales. The chemical reactivity of carbonates with H_2 is also negligible, although the extent of calcite dissolution and H_2 loss depends on the brine salinity, pH, and temperature of the reservoir [196–198]. The interaction of H_2 with formation brine can alter reservoir wettability and contribute to significant trapping of gaseous H_2, thereby reducing the relative permeability of the mobile H_2 phase [199, 200]. However, the implications of this on the mechanical properties of the rocks have yet to be documented. In carbonate reservoirs, the expansion of calcite grains during interaction with H_2 has been identified as a dominant chemical phenomenon, resulting in a reduction of the reservoir's effective porosity by up to 50

Clay minerals, which are often abundant in certain sandstones and low-permeability claystone, can also serve as hosts for H_2. While there are no significant irreversible chemical reactions between clay minerals and H_2, the swelling of clays due to sorption can lead to stress changes in the reservoir [66], as has been extensively studied for CO_2 injection in sandstone, shale, and coal reservoirs [201–203]. Volumetric sorption experiments of H_2 on clay-rich Callovo-Oxfordian rocks have shown an uptake of up to 0.1

wt% H_2 within a pressure range of 0-90 bar. However, as water and H_2 compete for adsorption sites in clay minerals, the uptake of H_2 will be significantly lower in brine-saturated reservoirs [204]. Although similar experiments and numerical modeling of H_2 sorption kinetics on natural and synthetic clays have been conducted [205, 206], the effect of sorption on the mechanical properties of clay minerals is yet to be explored. In summary, while irreversible chemical reactions may not be the dominant factor affecting the mechanical properties of rocks in subsurface UHS, further research is needed to investigate grain-scale swelling and sorption dynamics and their impact on reservoir-scale stress configurations.

1.3.3. IMPACT OF HETEROGENEITY

Reservoir heterogeneity originates from variations in grain size distribution, depositional conditions, and reaction kinetics during diagenesis. The spatial extent of heterogeneity, compositional difference, and the grain-scale response of heterogeneous layers under elevated stress conditions govern the efficiency of the reservoir for gas storage operations. Heterogeneities in sedimentary reservoir rocks originate from their depositional condition as well as the diagenesis pathway during consolidation. Disparate distribution of porosity or spatial difference in pore sizes can result in differences in mechanical responses. Similarly, cementation during diagenesis can enhance the mechanical stability of the host rock but causes a drastic reduction in pore spaces [207]. Fluid-inclusion structures and the formation of fault gouges in the reservoir can also result in local heterogeneity. Numerical simulations also found that the presence of soft heterogeneous particles in sandstone can decrease the crack initiation stress, damage stress, and static modulus values [208]. Grain-scale heterogeneity in sandstones can also govern the stress concentration points of crack initiation and crack propagation direction. Sandstones having higher porosity and larger pore sizes are more prone to fail at lower stresses compared to sandstones with lower porosity. Indeed, pores act as local weak zones, which govern the origination of cracks, and it is observed from related research reporting significant enhancement of permeability and porosity due to load cycling in high porosity sandstones [209]. Geometry, distribution, type, and orientation of heterogeneous microstructures also determine the crack propagation path and their development [210, 211].

Fine-grained reservoir rocks are preferred for gas storage operations due to their smaller pore spaces and higher pore volume. They also show higher peak strength due to diffused stress distribution compared to coarse-grained sandstones [212], which leads to the suitability of pore fluid injection at higher pressure. On one hand, heterogeneity of reservoir rocks can lead to complex strength behavior and partial fault reactivation, whereas heterogeneity of caprocks like shale can play an opposite critical role in the successful containment of gas within the reservoir. Hence more experimental and numerical studies on the effect of heterogeneity for both reservoir and caprock need to be performed for potential H_2 reservoirs and special attention should be given to the interaction of pervasive heterogeneities (e.g. bedding planes) and its orientation with the principal stress components.

Salt caverns exhibit some degree of heterogeneity, although it is not as pronounced

as in porous formations. The presence of non-salt interlayers in bedded formations introduces a strong heterogeneity that should be considered to study the geomechanical behavior of the salt cavern. However, from a purely mechanical perspective, the effect of heterogeneity for H_2 operations should not differ from the storage of other gases. Nevertheless, one should keep in mind that while non-salt interlayers with permeability higher than the surrounding salt rock would not compromise containment of other gases (e.g. natural gas, air, CO_2), they could potentially represent leaking pathways for H_2 due to its low viscosity and small molecular radius [213, 214].

Although salt rock is regarded as inert when in contact with H_2 [215], the possibility of H_2 percolation is still a concern as it would represent the failure of containment and could potentially alter the mechanical behavior of the surrounding salt rock. Because H_2 atom size is in the order of 100 pm, permeation by diffusion through salt rock lattice could not occur [216]. Nevertheless, the concern still holds as H_2 is known to cause embrittlement in metals due to the percolation of H_2 protons through the metal lattice. However, as pointed out in [216], the production of H_2 protons through ionization is not possible in the presence of halite, so this should also not be a problem.

H_2 percolation only happens when there are open cracks on the cavern walls which can result in tertiary accelerated creep leading to failure. If H_2 percolation occurs through open cracks, there could be mechanical impacts, such as additional pore pressure that modifies the effective stress on the salt rock structure [217]. Pore pressure affects the peak strength and permeability of rock salts [218]. Water content also promotes the healing ability of salt rocks (or re-crystallization) [219], so lower water content in cavern surroundings can suppress healing where it is most needed. Failure to recover micro-cracks can aggravate H_2 percolation, potentially creating a vicious cycle. The effects of water desiccation in salt rocks due to H_2 percolation have not been reported in the literature, making it difficult to predict the extent of these effects and their impact on salt cavern operations.

The presence of non-salt interlayers in bedded formations introduces a strong heterogeneity that should be considered to study the geomechanical behavior of the salt cavern. However, from a purely mechanical perspective, the effect of heterogeneity for H_2 operations should not differ from the storage of other gases. Nevertheless, one should keep in mind that while non-salt interlayers with permeability higher than the surrounding salt rock would not compromise containment of other gases (e.g. natural gas, air, CO_2), they could potentially represent leaking pathways for H_2 due to its low viscosity and small molecular radius [213, 214].

1.3.4. IMPACT OF MICROBIAL ACTIVITY

The microbial community in subsurface hydrocarbon reservoirs is well-established, but there is significant diversity within these communities, with specific groups responsive to hydrocarbons different from those interacting with H_2 [220, 221]. H_2 serves as an ideal electron donor for microbial metabolism due to its simplicity [222]. While the activity of the microbial community under reservoir conditions in the presence of H_2 is not extensively documented, lab-scale experiments have shown their metabolic sensitivity to temperature, pressure, and pH conditions [66]. Microbes consume H_2 and produce

contaminant gases such as CH_4, H_2S, and organic acids. They can also form biofilms, which can alter reservoir wettability and reduce accessible pore spaces after repeated cycles of H_2 injection and production [220]. Although there is evidence of biofilms creating flow barriers in H_2 reservoirs, few studies have investigated their impact on rock mechanical properties. However, it is expected that microbial-induced wettability alteration of the reservoir [223–225] can influence the interaction of H_2 and formation brine with pre-existing fault planes, leading to mechanical instability. Fe-reducing microbes can replace Fe from minerals in the presence of H_2, potentially impacting the mechanical stability of the reservoir depending on the abundance of Fe-bearing minerals [226]. The consumption of H_2 by microbes can also reduce reservoir pressure [226] and contribute to creeping subsidence due to increased effective stress. While the presence of biofilms might intuitively increase the mechanical stability of the reservoir, scientific evidence supporting or refuting this hypothesis is currently lacking. Given the attention given to biofilms and their influence on H_2 flow properties, it is important to study their role in altering reservoir mechanical properties.

Salt rock is known to be inert concerning H_2, so no undesired reactions should be expected in this regard [227]. Following the debrining phase, a residual brine quantity lingers within the cavern's sump. This residual brine can evaporate and potentially mix with H_2, necessitating surface treatment for H_2 dehydration. Furthermore, sulfate-reducing bacteria (SRB) can generate H_2S in the presence of sulfate (primary electron acceptor) and H_2 (electron donor). Sulfate is typically present in anhydrite layers on cavern walls or within the sump [228]. Consequently, for H_2S prevention, salt formations with highly pure halite are preferable. Essentially, bedded salt formations are more susceptible to H_2S production compared to caverns constructed within dome salts. Furthermore, findings indicate that microbial activity can be limited by factors such as low temperature, low pressure [229], and high salinity [230]. Analogous to water vapor, H_2S production compromises H_2 purity, necessitating its removal at surface facilities. Speculation has arisen about whether the presence of H_2S might diminish the self-healing capacity of salt rock [231] or other mechanical properties. Nonetheless, salt caverns have been employed for H_2 storage over extended periods, and no related issues have been reported thus far.

1.3.5. WELLBORE INTEGRITY

Wells ensures safe injection and production of H_2 into depleted reservoirs or salt caverns. Damage in wells is known to lead to the contamination of the water table [232]. It is crucial to maintain the integrity of wells and borehole infrastructure over several decades during the planning and operation phases of cyclic injection and production. Extensive research has been conducted on the integrity of wellbore infrastructure to prevent leakage during hydrocarbon production [233]. However, a lack of available monitoring data for active and abandoned wells and insufficient public data for comparing the well failure mechanisms hinders a comprehensive understanding of the system. Ensuring the safety of wells is paramount for various subsurface applications such as UGS, CCUS, geothermal energy, and lastly UHS. Although these storage technologies involve different fluids and operating conditions, the main causes of wellbore integrity loss re-

main the same. These causes include time-dependent leakage through fluid flow, solute transport, chemical reactions, mechanical stresses, annulus quality, and integrity, casing and seal deterioration, and improper abandonment operations [234].

In the context of geothermal energy, potential sources of well barrier and integrity failure include mechanical damage during well development, corrosion resulting from increased chloride concentration in drilling fluids [235, 236], thermal stresses caused by the cyclic injection of cold pore fluid into a hot reservoir [237], metal fatigue, and expansion of trapped fluids [234, 238, 239]. The high reservoir temperature and low injection fluid temperature cause differential thermal stress between the casing and cement which can reduce the shear bond strength resulting in leakage pathways [234, 237]. Thermal stresses could be avoided with proper cementing, slow preheating of the well before production, and good casing design [240, 241]. To tackle the issue of expansion of trapped fluids, a tieback liner was suggested in the casing to casing annulus [238]. A detailed review of different cement failure mechanisms in geothermal wells can be found here [241].

These sources have the potential to overlap with the UHS because of the cyclic loading nature and temperature difference between injected H_2 and the reservoir. In the context of CCUS, to avoid leakages, well design, construction, operation, evaluation, and abandonment are critical measures to be taken into account [242]. The utilization of abandoned wells for CCUS is not widely considered due to the potential creation of leakage paths caused by the degradation of well infrastructure materials over time [1, 243]. Materials used in well construction such as cement or polymers are chosen based on their resistance to corrosion from CO_2. The wells also undergo thermal stresses due to the injection of supercritical CO_2 in the subsurface [244]. The cyclic injection can cause fracture growth which results in the debonding between the cement and formation [245, 246].

Salt precipitation and scale formation have been found to have an insignificant impact on CO_2 storage [247]. Formation of ice-like crystalline compounds caused by trapping CO_2 in cages created by H_2-bonded molecules posed significant hazards like rapid pressurization and loss of injectivity [247, 248]. The role of contaminants (depends on the concentration) in the stream of CO_2 can change the rate of dissolution and precipitation rates which can react with cement and further degrade it [246]. There are a few studies that have reported casing corrosion caused by CO_2which depends on the temperature, pressure, salt concentration, pH, flow rate, and partial pressure of the injected CO_2 [249–251]. Carbonation product ($Ca(OH_2)$)can also be released when the cement reacts with CO_2 which could decrease the permeability, and porosity and further reduce the strength of the cement [252–254]. The introduction of CO_2 during injection can lead to a cooling effect, which in turn reduces the radial, axial, and tangential stresses within the composite system [169, 255, 256].

Underground gas storage offers similar technology (cyclic) as H_2 subsurface energy storage. Cyclic mechanical and thermal loading is imposed which can result in interface debonding and cracking, weakening of cement sheath and tubing connections [257], channels of mud at the contact surface, and layering in deviated wells weakens the cement integrity [258]. Sand production is another critical effect caused by changes in pore pressure and stresses, leading to erosion inside the wellbore and wellhead [259, 260]. The

effects observed in gas storage can also occur in underground hydrogen storage due to cyclic loading. Leakage of H_2 can occur through various pathways when stored underground, as depicted in Figure 1.8. These pathways include cement, casing, packer, and around cement plug-ins in the abandoned wells [4].

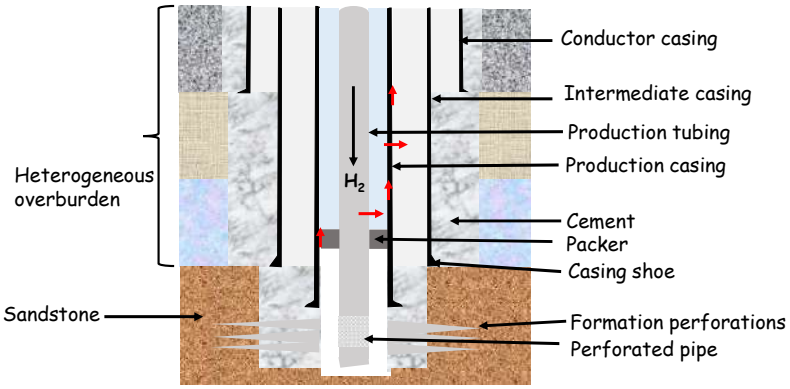

Figure 1.8: Simplistic illustration of a typical well indicating the possible H_2 leakage pathways (red arrows) through the tubing, through inside and outside of the casing, and around the packer. Adopted from [1, 3–6]. Additional pathways in the sheared well-bore and cement plug-in in the case of an abandoned well are not shown here.

The primary concerns regarding H_2 in wells pertain to its molecule size, chemical reactivity, operational cyclicity, and compatibility with materials and equipment. Due to its small size and high diffusivity, hydrogen is more prone to leakage compared to natural gas, presenting challenges for designing effective well barriers. Its high reactivity can lead to chemical interactions with rocks and reservoir fluids, potentially resulting in Microbially Induced Corrosion (MIC) of well components. Frequent injection and extraction of hydrogen cause pressure and temperature cycling, which can fatigue well components and the reservoir near the well. Ensuring compatibility with hydrogen and H_2S exposure may necessitate the use of new materials and solutions to ensure long-term operational efficiency.

However, there is limited documentation on the impact of cyclic H_2 flow in wells. H_2 can react with sulfurous minerals in the subsurface, resulting in the formation of a highly corrosive weak acid that can corrode the well infrastructure [146]. H_2 blistering and H_2 induced cracking can also take place in steel alloys, depending on the concentration of injected H_2 and operating conditions [4]. The cement bond between the rocks and casing needs to be stronger in comparison to traditional underground gas storage (UGS) sites, as the leakage effects could be more pronounced due to the small size of H_2. Rapid gas decompression of elastomers in sealing assemblies and degradation of elastomers from sulfide-reducing bacteria are potential issues in underground hydrogen storage (UHS) [4, 261]. Recent CT-scan experiments have revealed that H_2 bubbles

can become trapped in the cement, leading to a decrease in cement strength through the formation of small fractures within the cement [262]. Microbial reactions with H_2 can contribute to H_2 loss within the wellbore through metabolic activities. Moreover, the formation of biofilms that block the wellbore at the areas of contact between brine and H_2 can result in a loss of injectivity.

Further research should be conducted to investigate the impact of cyclic H_2 on various grades of cement. This research could lead to the development of new materials that can be added to cement to enhance the strength of well infrastructure, thereby reducing the risk of H_2 corrosion and long-term leakage. It may also be necessary to employ more advanced monitoring techniques to identify H_2 leakage pathways and assess well integrity. By carefully selecting the appropriate materials for well components such as casing, tubing, and cement through thorough laboratory research, significant cost savings can be achieved while ensuring the safety of H_2 storage. To gain a deeper understanding of wellbore integrity, it is beneficial to integrate laboratory experiments, modeling studies, and field-scale data from wells.

1.4. RESEARCH OBJECTIVES

Based on the challenges and the scientific needs introduced in the previous sections, this thesis has three main objectives. They are

- Identify research gaps relevant to UHS from the perspective of geomechanics.
- Investigate and implement the constitutive models for different types of deformation undergone by different rocks and benchmark it with the literature.
- Perform geo-mechanical simulations with fine-scale and multiscale methods to understand the impact of inelastic deformation in fieldscale reservoirs.

1.5. THESIS OUTLINE

The information in this thesis was gathered throughout the course of the four-year Ph.D. program and includes findings from papers that have been published in journals, conference proceedings, and lastly from a research internship. Chapter 1 provides an overview of the relevant geomechanical concepts and research related to subsurface energy storage in depleted reservoirs and salt caverns, with a specific focus on hydrogen (H_2) storage. It sets the stage for the thesis by summarizing the existing state of research in this field. Chapter 2 presents the simulation of porous rocks undergoing creep deformation using fine-scale methods employing finite element formulation and algebraic multiscale methods. Chapter 3 discusses the effect of complex shapes, heterogeneity, and other factors on salt caverns, which are commonly used for subsurface energy storage. It provides insights into the geomechanical behavior of salt caverns and their implications for subsurface energy storage operations. Chapter 4 elaborates on the understanding of the behavior of sandstone and attempts to model the cyclic behavior of sandstone by comparing the same with experimental data. It further expands on the FEM

formulation with upscaling methods for inelastic behavior, providing a comprehensive understanding of the mechanical response of rocks in subsurface energy storage applications. Chapter 5 presents the simulations of poro-inelastic behavior using the finite element method (FEM) for mechanics coupled with the finite volume method (FVM) for flow, along with upscaled algebraic multiscale techniques. It describes the numerical simulations and their results for studying the behavior of subsurface rocks under poro-inelastic conditions. Chapter 6 presents the work carried out in improving the coarsening methods for algebraic multiscale techniques using unsupervised machine learning for subsurface flow simulations. It discusses the application of machine learning techniques to enhance the efficiency and accuracy of subsurface flow simulations. Chapter 7 concludes the entire work, summarizing the key findings and contributions of the thesis. It also provides research recommendations based on the extensive literature review, suggesting potential future research directions in the field of UHS.

2

SIMULATION OF INELASTIC CREEP DEFORMATION IN ROCKS

Summary: *Subsurface geological formations provide giant capacities for large-scale (TWh) storage of renewable energy, once this energy (e.g. from solar and wind power plants) is converted to green gases, e.g. hydrogen. The critical aspects of developing this technology to full-scale will involve the estimation of storage capacity, safety, and efficiency of a subsurface formation. Geological formations are often highly heterogeneous and, when utilized for cyclic energy storage, entail complex nonlinear rock deformation physics. In this work, we present a novel computational framework to study rock deformation under cyclic loading, in the presence of nonlinear time-dependent creep physics. Both classical and relaxation creep methodologies are employed to analyze the variation of the total strain in the specimen over time. An implicit time-integration scheme is employed to preserve numerical stability, due to the nonlinear process. Once the computational framework is consistently defined using the finite element method on the fine scale, a multiscale strategy is developed to represent the nonlinear deformation not only at fine but also at coarser scales. This is achieved by developing locally computed finite element basis functions at a coarse scale. The developed multiscale method also allows for iterative error reduction to any desired level, after being paired with a fine-scale smoother. Numerical test cases are studied to investigate various aspects of the developed computational workflow, from benchmarking with experiments to analyzing the impact of nonlinear deformation for a field-scale relevant environment. Results indicate the applicability of the developed multiscale method in order to employ nonlinear physics in their laboratory-based scale of relevance (i.e., fine-scale), yet perform field-relevant simulations.*

This is from Ramesh Kumar et al., JCP 2021

2.1. INTRODUCTION

Cyclic loading has been studied in mining sciences to study hydraulic fracturing, rock cutting, forecasting volcanic hazards, and designing tunnels against earthquakes (see e.g. [263–266]). Very few researchers have studied the applications of cyclic loading on oil and gas storage both numerically and experimentally [267–269]. Relevant hysteric rock and fluid constitutive governing equations can be implemented to capture the important physics in the cyclic subsurface storage technology [57, 86, 270]. However, there is a significant need for a better understanding of the complexities involved in the subsurface storage physics to implement it safely, efficiently, and reliably on a long term basis. Especially this becomes a crucially important field of study when storage cities become closer to the urban areas.
Of particular interest is to develop a scalable (i.e., multiscale) mechanical deformation modeling concept to include not only the elastic but also time-dependent nonlinear creep physics. As geological domains span large length scales, having inelastic (nonlinear) and heterogeneous properties, development of a multiscale strategy which allows to capture these fine-scale physics and parameters in the coarse-scale systems is crucial. Such a multiscale strategy would also allow for accurate quantifications of the consequences of the pore-pressure dynamics in the subsurface geological domains. This motivates the development of the current study.

In this chapter steady-state creep deformation is accommodated as elaborated in Figure 1.4. Creep deformation depends on the type of material and the type of loading involved. Examples can be found in deep resource mining [271] and radioactive nuclear waste disposal [272], in geological reservoirs such as shale rocks [16, 123] to name a few. Several constitutive laws have been introduced in the past to study creep and this still is an active field of research in the rock physics labs and geophysical field studies. Table 1.1 shows the different creep formulations employed in the past for different materials. In this work, the constitutive equation for modeling inelastic creep deformation is chosen based on the existing literature which is elaborated in section 2.3.
The present work introduces a multiscale 3D non-linear finite element method (FEM) to study the creep mechanics that are involved in the compression of rocks under normal and cyclic loading. Classical creep and relaxation creep are the two methodologies that are used to analyze and quantify creep. Both are considered in this work. The computational framework allows using both explicit and implicit time integration schemes. However, implicit time integration is employed to guarantee convergence irrespective of the size of the time steps. For field-scale applications, one has to employ the physical constitutive laws which are validated in the laboratory settings (cm-scale) only.

Applications of these experimental laws for large (several tens of meters) grid blocks, having heterogeneous elastic and nonelastic properties, are questionable. To avoid excessive upscaling of these nonlinear terms and highly heterogeneous elasticity coefficients, a multiscale procedure is also introduced. The multiscale method is built on finite elements (hence, MSFE) to obtain coarse-scale systems using locally-supported finite-element coarse-scale basis functions. The multiscale formulation of this type, i.e. local basis function-based, has been applied and developed by various researchers in the past [162, 273–280]. Researchers have employed multiscale strategy to study flow

in porous media [281–283], geo-mechanics in porous media [284–288] and other nonlinear problems [289–291]. Note that the rich domain of multiscale modeling for inelastic deformations also includes non-basis-function-based approaches, such as FE^2 for composite materials [292], FEM-DEM (Discrete Element Method) for granular materials [293] and high-porosity rocks [294]. The multiscale strategy developed in this work aims to (1) develop local coarse-scale basis functions, (2) resolve fine-scale heterogeneities in coarse system, (3) allow for iterative error reduction to the machine accuracy, (4) allow for algebraic formulation and implementation. In these aspects, it stays novel compared to the existing literature of multiscale FEM for inelastic deformation modeling. Note that in order to guarantee convergence of the iterative multiscale error reduction strategy, the developed multiscale procedure is paired with a fine-scale smoother [295, 296].

Numerical results are presented to study various aspects of the developed computational workflow, from benchmarking with experiments to analysing the impact of nonlinear deformation for a field-scale relevant environment. Results indicate the applicability of the developed multiscale method in order to employ nonlinear physics in their laboratory-based scale of relevance (i.e. fine scale), yet perform field-relevant simulation.

The chapter is structured as follows. Firstly, FEM method for simulation of linear elasticity is briefly revisited in section 2.2. Different creep mechanisms, as inelastic deformation, are introduced in section 2.3. Constitutive equations employed to model creep is presented. The algorithms employed to model creep are described in detail. Next, the algebraic MSFE procedure for the nonlinear deformation mechanism is developed to allow for field-scale analyses without relying on excessive upscaling of the nonlinear creep physics and heterogeneous material properties in section 2.4. MSFE formulation is further extended by employing iterative MSFE. Numerical results are then presented in section 2.5 starting with (i) Uniaxial compression test case for rock salt for both fine-scale and algebraic MSFE. Next, (ii) triaxial loading of coal is studied using both fine-scale and iterative multiscale strategy. Next, (iii) tri-axial cyclic loading test case is studied for sandstone using fine-scale and iterative multiscale strategy. For the above test cases, the numerical results are compared with experimental data by using fitting parameters to understand the variation of deformation over time. Next, the influence of creep on subsidence is studied in the northern Italian field [297] by assuming plain strain. Finally, in section 2.6, the conclusion is presented.

2.2. LINEAR ELASTICITY

The momentum balance for drained solid porous medium is given by

$$\nabla \cdot (\boldsymbol{\sigma}) = \boldsymbol{f}, \tag{2.1}$$

where pore pressure is constant. The stress is given by $\boldsymbol{\sigma} = \boldsymbol{C} : \boldsymbol{\varepsilon}$, in which the elasticity coefficient matrix and strain tensor are denoted by $\boldsymbol{C}$ and $\boldsymbol{\varepsilon}$, respectively. Here $\boldsymbol{f}$ is the volumetric force expressed as $[\mathrm{N/m^3}]$. The governing equation when expressed in terms of deformation reads

$$\nabla \cdot (\boldsymbol{C} : \nabla^s \cdot \boldsymbol{u}) = \boldsymbol{f}. \tag{2.2}$$

Here, $\nabla^s u = \frac{1}{2}\left(\nabla u + \nabla^T u\right)$ is the gradient symmetric of displacement vector. The elasticity tensor is expressed using Lamé parameters λ and μ, i.e.,

$$\boldsymbol{C} = \begin{bmatrix} (\lambda+2\mu) & \lambda & \lambda & 0 & 0 & 0 \\ \lambda & (\lambda+2\mu) & \lambda & 0 & 0 & 0 \\ \lambda & \lambda & (\lambda+2\mu) & 0 & 0 & 0 \\ 0 & 0 & 0 & \mu & 0 & 0 \\ 0 & 0 & 0 & 0 & \mu & 0 \\ 0 & 0 & 0 & 0 & 0 & \mu \end{bmatrix}. \tag{2.3}$$

Here $\lambda = \frac{\nu E}{(1+\nu)(1-2\nu)}$ and $\mu = \frac{E}{2(1+\nu)}$, where E is Youngs modulus and ν is Poisson's ratio. Using Voigt's notation and transpose of divergence operator, the final set of equations in 3D are

$$\frac{\partial}{\partial x}\left[(\lambda+2\mu)\frac{\partial u_x}{\partial x} + \lambda\frac{\partial u_y}{\partial y} + \lambda\frac{\partial u_z}{\partial z}\right] + \frac{\partial}{\partial y}\left(\mu\frac{\partial u_x}{\partial y} + \mu\frac{\partial u_y}{\partial x}\right) + \frac{\partial}{\partial z}\left(\mu\frac{\partial u_x}{\partial z} + \mu\frac{\partial u_z}{\partial x}\right) = f_x \tag{2.4a}$$

$$\frac{\partial}{\partial x}\left(\mu\frac{\partial u_x}{\partial y} + \mu\frac{\partial u_y}{\partial x}\right) + \frac{\partial}{\partial y}\left[\lambda\frac{\partial u_x}{\partial x} + (\lambda+2\mu)\frac{\partial u_y}{\partial y} + \lambda\frac{\partial u_z}{\partial z}\right] + \frac{\partial}{\partial z}\left(\mu\frac{\partial u_y}{\partial z} + \mu\frac{\partial u_z}{\partial y}\right) = f_y \tag{2.4b}$$

$$\frac{\partial}{\partial x}\left(\mu\frac{\partial u_x}{\partial z} + \mu\frac{\partial u_z}{\partial x}\right) + \frac{\partial}{\partial y}\left(\mu\frac{\partial u_y}{\partial z} + \mu\frac{\partial u_z}{\partial y}\right) + \frac{\partial}{\partial z}\left[\lambda\frac{\partial u_x}{\partial x} + \lambda\frac{\partial u_y}{\partial y} + (\lambda+2\mu)\frac{\partial u_z}{\partial z}\right] = f_z. \tag{2.4c}$$

2.2.1. FEM FORMULATION OF THE SYSTEM

To solve equations (2.4a)-(2.4c), finite element formulation is followed. Using minimization of weighted residual Galerkin approach, the displacement of each element is interpolated within an element using fine-scale shape functions. The displacement inside an element ($\widetilde{u_e}$) can be approximated from nodal displacements ($\hat{u}_{e,i}$) as

$$\widetilde{u_e} \approx \sum_{i=1}^{N_{nodes,e}} \boldsymbol{N}_{i,e}\hat{u}_{e,i}. \tag{2.5}$$

Here, $\hat{u}_{e,i}$ can be written as displacements (u_x, u_y, u_z) for each node i . $\boldsymbol{N}_{i,e}$ are the shape functions used to interpolate solution between the nodes [296]. The shape functions are expressed in terms of local coordinates (ξ_1, ξ_2, ξ_3) by

$$\boldsymbol{N}_{i,e} \approx \frac{1}{8}(1\pm\xi_1)(1\pm\xi_2)(1\pm\xi_3) \qquad -1 \le (\xi_1,\xi_2,\xi_3) \le 1. \tag{2.6}$$

Using the Gauss divergence theorem, the final discrete equation for an element reads

$$\int_{\Omega_e} \boldsymbol{D}_e{}^T \boldsymbol{C}\boldsymbol{D}_e\, \widetilde{u}_e\, dV = \int_{\Omega_e} \boldsymbol{N}_e{}^T \boldsymbol{f}\, dV + \int_{\Gamma_\sigma} (\boldsymbol{N}_e)^T \boldsymbol{t}\, d\boldsymbol{S}. \tag{2.7}$$

The above volume integrals are approximated using Gauss quadrature rule by transforming it from global to local coordinate system. Here, $\boldsymbol{D}_e = \boldsymbol{div}^T \boldsymbol{N}_e$, the applied stress on the boundary along the normal is $\boldsymbol{t}$ (Neumann bc) which is integrated over area Γ_σ, the volumetric force is $\boldsymbol{f}$, integrated over an elemental volume Ω_e. The operator $\boldsymbol{div}^T$ is given by

$$\boldsymbol{div}^T = \begin{bmatrix} \frac{\partial}{\partial x} & 0 & 0 \\ 0 & \frac{\partial}{\partial y} & 0 \\ 0 & 0 & \frac{\partial}{\partial z} \\ 0 & \frac{\partial}{\partial z} & \frac{\partial}{\partial y} \\ \frac{\partial}{\partial z} & 0 & \frac{\partial}{\partial x} \\ \frac{\partial}{\partial y} & \frac{\partial}{\partial x} & 0 \end{bmatrix}. \tag{2.8}$$

Equation 2.7 can be written based on the stiffness matrix ($\boldsymbol{A}_e = \int_{\Omega_e} \boldsymbol{D}_e{}^T \boldsymbol{C} \boldsymbol{D}_e$) and right hand side force vector ($\widetilde{f}_e = \int_{\Omega_e} \boldsymbol{N}_e{}^T \boldsymbol{f}\, dV + \int_{\Gamma_\sigma} (\boldsymbol{N})^T \boldsymbol{t}\, d\boldsymbol{S}$) as

$$\boldsymbol{A}_e \widetilde{u}_e = \widetilde{f}_e. \tag{2.9}$$

By assembling the stiffness matrix for each element, the global linear system is formed as

$$\boldsymbol{A}_{\text{mech}}\ \widetilde{u} = \widetilde{f}. \tag{2.10}$$

After computing elastic deformation, stresses and strains are computed using constitutive law from Equation 2.1. Next, the nonlinear elastic deformation (creep) is revisited.

2.3. CREEP FORMULATION

Creep is the tendency of solid material to deform permanently under a certain load that depends on time and temperature. The typical creep process has three phases which are primary creep (creep rate decreasing over time), secondary creep (constant creep rate), and tertiary creep (increasing creep rate until failure) as shown in Figure 1.4. In this work, tertiary creep is not modelled. When the strains are infinitesimal, the total strain $\boldsymbol{\varepsilon}_t$ can be split as

$$\boldsymbol{\varepsilon}_t = \boldsymbol{\varepsilon}_{\text{el}} + \boldsymbol{\varepsilon}_{\text{cr}} + \boldsymbol{\varepsilon}_{\text{th}}. \tag{2.11}$$

Here, $\boldsymbol{\varepsilon}_{\text{el}}$ is elastic strain, $\boldsymbol{\varepsilon}_{\text{th}}$ is thermal strain and $\boldsymbol{\varepsilon}_{cr}$ is the creep strain. In this chapter, time independent plastic strains like viscoplasticity and thermal strains are not included. The modified creep equation which involves power law and Bingham body are [9, 23]

$$\varepsilon_{\text{cr}} = X \int_t P + Y B. \tag{2.12}$$

Depending on the type of material and formulation either power law ($X = 1,\ Y = 0$) or Burgers model ($X = 0,\ Y = 1$) can be chosen. Here,

$$P = \dot{\varepsilon_{\text{cr}}} = A e^{-\frac{Q}{RT}} \boldsymbol{\sigma}_{\mathbf{vM}}{}^{n-1} \boldsymbol{s}\, t^{m-1} \tag{2.13a}$$

$$B = \varepsilon_{\text{cr}} = \boldsymbol{s}\left(\frac{1}{2G_1} + \frac{1}{2G_2}(1 - e^{\frac{-G_2 t}{\eta_1}}) + \frac{t}{2\eta_2} \right) \tag{2.13b}$$

Material constants are A, n, m in the power model and in the Burgers model the parameters G_1, G_2 are the shear modulus, η_1, η_2 is the viscosity coefficient and t is the time. Here $\boldsymbol{s}$ is deviatoric stress and σ_{vM} is von Mises stress. The Burgers model for 3D stress state is obtained as series of elements which represent Hookean body (elastic, spring), Kelvin body (damper and spring in parallel) and Newton body (dashpot/damper). So the stresses of the individual elements are given by

$$\boldsymbol{s}_H = 2G_1\varepsilon_H \tag{2.14a}$$

$$\boldsymbol{s}_K = 2G_2\varepsilon_K + 2\eta_1\dot{\varepsilon} \tag{2.14b}$$

$$\boldsymbol{s}_N = 2\eta_2\dot{\varepsilon_N}. \tag{2.14c}$$

The non-linear strains are incorporated in the governing equation by plugging Equation 2.11 in Equation 2.2,

$$\nabla \cdot (C : \varepsilon_{\text{el}}) = \nabla \cdot (C : (\varepsilon_{\text{t}} - \varepsilon_{\text{cr}})) = f. \tag{2.15}$$

The deformation is computed by

$$\nabla \cdot (C : \nabla^s u) = \nabla \cdot (C : \varepsilon_{\text{cr}}) + f. \tag{2.16}$$

Using the principal of virtual displacements, which states that the sum of external and internal work is 0 [12], the final discrete equation can be written as a modified form of Equation 2.7, i.e.,

$$\int_{\Omega_e} \boldsymbol{D}_e{}^T \boldsymbol{C} \boldsymbol{D}_e \, \widetilde{u}_e \, dV = \int_{\Omega_e} \boldsymbol{N}_e{}^T \boldsymbol{f} \, dV + \int_{\Gamma_\sigma} (\boldsymbol{N}_e)^T \boldsymbol{t} \, d\boldsymbol{S} + \int_{\Omega_e} \boldsymbol{D}^T \boldsymbol{C} \boldsymbol{\varepsilon}_{\mathbf{cr}} dV \tag{2.17}$$

Equation 2.17 can be rewritten as

$$Au = F_{\text{b}} + F_{\text{cr}}. \tag{2.18}$$

Where, F_{cr} is the fictitious creep forces and F_{b} is the body forces.

2.3.1. NUMERICAL METHODOLOGY

The creep strain $\boldsymbol{\varepsilon}_{cr}$ can be modelled using classical creep and relaxation creep methodology [7]. Classical creep is a modelling approach, when the stress is assumed to be constant and the creep strain accumulates with respect to time. If the stress is constant, the elastic strain remains constant which would mean total strain is accumulated over time. Whereas, the relaxation creep is an approach when the total strain is assumed to be constant, and as creep strain accumulates, elastic strain $\boldsymbol{\varepsilon}_{\text{el}}$ reduces over time. This would imply that the stress reduces with time. Figure 2.1 shows the schematic diagrams of classical and relaxation creep.
These numerical methodologies are similar in nature to the stress and strain controlled compression experiments on the rocks, where either stress or strain is controlled on the rock sample when the experiments are performed.

The algorithms for classical and relaxation creep are depicted in Algorithm 1 and Algorithm 2 respectively.

Algorithm 1 : Classical creep algorithm

Input material and creep parameters
Calculate $\boldsymbol{u}, \boldsymbol{\sigma}$ and $\boldsymbol{\varepsilon_{el}}$ at time = 0, i=0. Initialize $\boldsymbol{\varepsilon_{cr}^{0}} = 0$
Compute the total number of time steps $N = T_{\text{simulation}}/\Delta t$
for $i < N$ **do**
    Compute deviatoric and von Mises stress $s_{ij}, \sigma_{\text{vM}}$
    Calculate creep strain at time step i : $\boldsymbol{\varepsilon_{cr}^{i}} = X \int_t P + YB$
    Compute total strain at time step i : $\boldsymbol{\varepsilon}_t^i = \boldsymbol{\varepsilon_e} + \boldsymbol{\varepsilon_{cr}}^i$
    Set $i = i + 1$
end for
return $u, \boldsymbol{\sigma}, \boldsymbol{\varepsilon_t}, \boldsymbol{\varepsilon_{el}}, \boldsymbol{\varepsilon_{cr}}$ at last time step

Algorithm 2 : Relaxation creep algorithm

Input material and creep parameters
Calculate $\boldsymbol{u}, \boldsymbol{\sigma}$ and $\boldsymbol{\varepsilon_{el}}$ at time = 0, i=0. Initialize $\boldsymbol{\varepsilon_{cr}^{0}} = 0$ and $\boldsymbol{\varepsilon_t} = \boldsymbol{\varepsilon_{el}}$
Compute the total number of time steps $N = T_{\text{simulation}}/\Delta t$
for $i < N$ **do**
    Compute deviatoric and von Mises stress $s_{ij}, \sigma_{\text{vM}}$
    Calculate creep strain at time step i : $\boldsymbol{\varepsilon_{cr}^{i}} = X \int_t P + YB$
    Calculate elastic strain $\boldsymbol{\varepsilon}_{\text{el}}^{i} = \boldsymbol{\varepsilon_t} - \boldsymbol{\varepsilon_{cr}^{i}}$
    Calculate stress $\boldsymbol{\sigma}^{i} = C : \boldsymbol{\varepsilon}_{\text{el}}^{i}$
    Set i = i+1
end for
return $u, \boldsymbol{\sigma}, \boldsymbol{\varepsilon_t}, \boldsymbol{\varepsilon_{el}}, \boldsymbol{\varepsilon_{cr}}$ at last time step

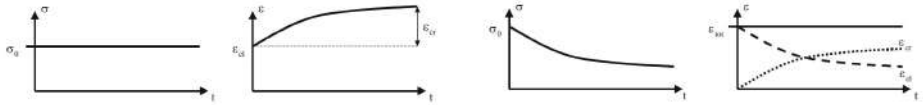

(a) **Classical creep**: constant stress. (b) **Relaxation creep**: constant strain.

Figure 2.1: Schematic diagrams of classical creep and relaxation creep methodologies [7].

Algorithm 3 : Implicit creep formulation

1: **Initialization** material and creep parameters, i = 0, $\boldsymbol{\varepsilon}_{\mathbf{cr}}^{\mathbf{0}} = 0$
2: **Compute** elastic deformation, total number of time steps (N) and set the Jacobian (J) terms
3: **for** $i < N$ **do**
4: **Set** iteration counter $\nu = 0$, creep forces $F_{\text{cr}}^{i+1} = F_{\text{cr}}^{i}$
5: **Calculate** the residual $\Re^{n+1} = \nabla \cdot (C : \varepsilon_{cr}^{n+1}) + f - \nabla \cdot (C : \nabla^s \mathbf{u}^{n+1})$.
6: **while** $||\Re^{\nu}||_2 < \epsilon_r$ and $\nu < \max(\nu)$ **do**
7: Update the residual $\Re^{\nu+1}$
8: Calculate the displacement increment $\delta\mathbf{u}^{\nu+1} = -(J^{\nu})^{-1}\Re^{\nu}$
9: Update the displacement $\mathbf{u}^{\nu+1} = \mathbf{u}^{\nu} + \delta\mathbf{u}^{\nu+1}$
10: Calculate stress ($\sigma^{\nu+1}$), strain ($\varepsilon_t^{\nu+1}$), creep strain $\boldsymbol{\varepsilon}_{\mathbf{cr}}^{\boldsymbol{\nu+1}}$ and fictitious creep forces $F_{\text{cr}}^{\nu+1}$
11: Set $\nu = \nu + 1$
12: **end while**
13: **end**
14: Set $i = i + 1$
15: **end for**
16: **end**

The developed computational framework allows to use both implicit and explicit formulation. The results shown here are obtained from implicit formulation which ensures computational stability even for higher time step sizes. The non-linear creep formulation is discretised implicitly as,

$$\varepsilon_{\text{cr}}^{i+1} = \varepsilon_{\text{cr}}^{i} + (\dot{\varepsilon}_{\text{cr}})^{i+1}\,\Delta t, \qquad \text{where, } \dot{\varepsilon}_{\text{cr}} = \text{function}(\boldsymbol{\sigma}, Q, T, t, \text{Material constants}). \tag{2.19}$$

In the classical creep formulation, the stress remains constant with respect to time. However, in relaxation the stress is dependent on time. In general, the stress term in the creep model is obtained based on the new time step ($i+1$). In this case, Newton-Raphson iterative approach is employed to solve for the displacement iteratively. The nonlinear residual reads as

$$\Re^{i+1} = \nabla \cdot (C : \varepsilon_{\text{cr}}^{i+1}) + f - \nabla \cdot (C : \nabla^s \mathbf{u}^{i+1}). \tag{2.20}$$

To find $\mathbf{u}^{i+1}$ the above equation is further linearized, i.e.,

$$\Re^{i+1} \approx \Re^{\nu+1} \approx \Re^{\nu} + \frac{\partial \Re}{\partial \mathbf{u}}\Big|^{\nu} \delta \mathbf{u}^{\nu+1}, \tag{2.21}$$

which is then solved iteratively until convergence is achieved, i.e. $\Re^{i+1} = 0$. The Jacobian $J = \frac{\partial \Re}{\partial \mathbf{u}}\Big|^{\nu}$ is computed based only on the elastic part of the residual equation. The displacement increment is computed by

$$\delta \mathbf{u}^{\nu+1} = -(J^{\nu})^{-1} \Re^{\nu}. \tag{2.22}$$

The iterations ν are repeated until the residual norm falls below the prescribed threshold, i.e., $||\Re^{\nu}||_2 < \epsilon_r$ to achieve convergence. Algorithm 3 describes the implicit formulation to model creep.

2.4. MULTISCALE FINITE ELEMENT METHOD FOR NONLINEAR DEFORMATION UNDER CYCLIC LOADING

The approximate fine scale displacement $\overline{u}^h$ is computed from coarse scale system $\overline{u}^H$ using Prolongation operator P_H^h, i.e.,

$$\overline{u}^h = P_H^h \overline{u}^H. \tag{2.23}$$

Figure 2.2 shows the computational domain. The black dots at the corners are the nodes of the coarse elements and the colored blocks are coarse elements. The prolongation operator is formed from displacement basis functions $\boldsymbol{N}^H$. The basis functions are computed by local momentum balance equations within each coarse cell as

$$\nabla \cdot (\boldsymbol{C} : \nabla^s \boldsymbol{N}_i^H) = 0 \qquad \text{in } \Omega^u \tag{2.24a}$$

$$\nabla_{||} \cdot (\boldsymbol{C} : \nabla_{||}^s \boldsymbol{N}_i^H) = 0 \qquad \text{on } \partial\Omega^u \tag{2.24b}$$

$$\boldsymbol{N}_i^H(x_j) = \delta_{ij} \qquad \forall\, j \in \{1 \ldots n_u^H\} \tag{2.24c}$$

The local conditions are solved in each coarse element Ω_i^u for basis functions $\boldsymbol{N}_i^H$ of i coarse block. Here δ_{ij} is the Kronecker delta and x_j is the position vector of coarse mesh node associated to j-th unknown. ∇^s and $\nabla_{||}^s$ denote approximate divergence and symmetric gradient operators acting in tangential direction of coarse elements boundary (local coordinate system) to solve local boundary conditions at $\partial\Omega^u$ for faces and edges, respectively.
Based on the wire basket decomposition of fine-scale system [298], a permutation matrix W is employed to rearrange all the nodes in the order of interior, faces, edges, and vertex. Based on that the fine-scale system can be written as

$$\hat{A}_h \hat{\mathbf{u}} = \hat{f}^h. \tag{2.25}$$

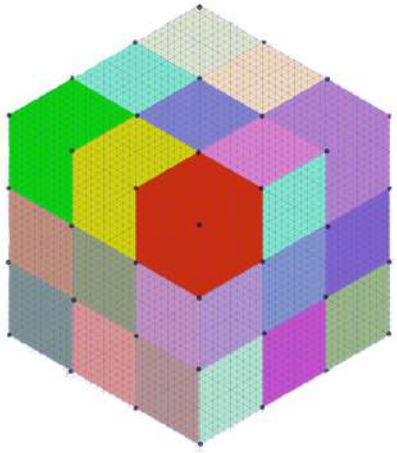

Figure 2.2: Multiscale mesh with coarse elements. The black dots at the corners are the coarse elements nodes and the colored blocks are coarse elements. The smaller cubes inside the colored elements are the fine-scale elements.

Denoting I, F, E, and V as interior, face, edge and vertex node, relative to the coarse mesh configuration, allows for re-stating the permuted system as

$$\hat{A}_h = W^T A_h W = \begin{bmatrix} \hat{A}_{II} & \hat{A}_{IF} & \hat{A}_{IE} & \hat{A}_{IV} \\ \hat{A}_{FI} & \hat{A}_{FF} & \hat{A}_{FE} & \hat{A}_{FV} \\ \hat{A}_{EI} & \hat{A}_{EF} & \hat{A}_{EE} & \hat{A}_{EV} \\ \hat{A}_{VI} & \hat{A}_{VF} & \hat{A}_{VE} & \hat{A}_{VV} \end{bmatrix}$$

and

$$\hat{u^h} = W^T \overline{u}^h = \begin{bmatrix} \hat{\mathbf{u}}_I \\ \hat{\mathbf{u}}_F \\ \hat{\mathbf{u}}_E \\ \hat{\mathbf{u}}_V \end{bmatrix}, \hat{f^h} = W^T f^h = \begin{bmatrix} \hat{\mathbf{f}}_I \\ \hat{\mathbf{f}}_F \\ \hat{\mathbf{f}}_E \\ \hat{\mathbf{f}}_V \end{bmatrix}.$$

The above matrix is reduced by performing Gaussian elimination twice which gives

$$\begin{bmatrix} \hat{A}_{II} & \hat{A}_{IF} & \hat{A}_{IE} & \hat{A}_{IV} \\ 0 & \hat{S}_{FF} & \hat{S}_{FE} & \hat{S}_{FV} \\ 0 & 0 & \hat{SS}_{EE} & \hat{SS}_{EV} \\ 0 & 0 & \hat{SS}_{VE} & \hat{SS}_{VV} \end{bmatrix} \begin{bmatrix} \hat{\mathbf{u}}_I \\ \hat{\mathbf{u}}_F \\ \hat{\mathbf{u}}_E \\ \hat{\mathbf{u}}_V \end{bmatrix} = \begin{bmatrix} I & 0 & 0 & 0 \\ -\hat{A}_{FI}\hat{A}_{II}^{-1} & I & 0 & 0 \\ -\hat{A}_{EI}\hat{A}_{II}^{-1} & -\hat{S}_{EF}\hat{S}_{FF}^{-1} & I & 0 \\ -\hat{A}_{VI}\hat{A}_{II}^{-1} & -\hat{S}_{VF}\hat{S}_{FF}^{-1} & 0 & I \end{bmatrix} \begin{bmatrix} \hat{\mathbf{f}}_I \\ \hat{\mathbf{f}}_F \\ \hat{\mathbf{f}}_E \\ \hat{\mathbf{f}}_V \end{bmatrix}. \tag{2.26}$$

Here,

$$\hat{S}_{ij} = \hat{A}_{ij} - \hat{A}_{iI}\hat{A}_{II}^{-1}\hat{A}_{Ij} \quad \forall (i,j) \in F,E,V \times F,E,V \tag{2.27}$$

$$\hat{SS}_{ij} = \hat{S}_{ij} - \hat{S}_{iF}\hat{S}_{FF}^{-1}\hat{S}_{Fj} \quad \forall (i,j) \in E,V \times E,V \tag{2.28}$$

By applying the reduced order boundary conditions it can be stated that

$$\widetilde{A}_{FF}\hat{u}_F + \widetilde{A}_{FE}\hat{u}_E + \widetilde{A}_{FV}\hat{u}_V = 0 \tag{2.29}$$

$$\widetilde{A}_{EE}\hat{u}_E + \widetilde{A}_{EV}\hat{u}_V = 0. \tag{2.30}$$

The matrices $\widetilde{A}_{FF}, \widetilde{A}_{FE}, \widetilde{A}_{FV}, \widetilde{A}_{EE}, \widetilde{A}_{EV}$ are computed by modifying the divergence and gradient operators for faces and edges respectively and solving Equation 5.12. The information from the faces is interpolated to faces, edges and vertices by reduced boundary conditions, and information from edges is interpolated to edges and vertices. This means

$$\hat{S}_{FF} \approx \widetilde{A}_{FF},\ \hat{S}_{FE} \approx \widetilde{A}_{FE},\ \hat{S}_{FV} \approx \widetilde{A}_{FV},\ \hat{SS}_{EE} \approx \widetilde{A}_{EE},\ \hat{SS}_{EV} \approx \widetilde{A}_{EV}. \tag{2.31}$$

By implementing Equation 5.12, the modified system is

$$\begin{bmatrix} \hat{A}_{II} & \hat{A}_{IF} & \hat{A}_{IE} & \hat{A}_{IV} \\ 0 & \widetilde{A}_{FF} & \widetilde{A}_{FE} & \widetilde{A}_{FV} \\ 0 & 0 & \widetilde{A}_{EE} & \widetilde{A}_{EV} \\ 0 & 0 & 0 & \hat{A}_{VV} \end{bmatrix} \begin{bmatrix} \hat{\mathbf{u}}_I \\ \hat{\mathbf{u}}_F \\ \hat{\mathbf{u}}_E \\ \hat{\mathbf{u}}_V \end{bmatrix} = \begin{bmatrix} \hat{\mathbf{f}}_I \\ \hat{\mathbf{f}}_F \\ \hat{\mathbf{f}}_E \\ \hat{\mathbf{f}}_V \end{bmatrix}. \tag{2.32}$$

Here $\hat{A}_{VV}$ is the coarse scale matrix $\hat{A}_H$. The coarse scale system is solved for $\overline{u}^H$ and all the deformations can be computed by expressing coarse scale deformation as $\overline{u}^h = P_H^h \overline{u}^H$ with

$$P_H^h = W \begin{bmatrix} -\hat{A}_{II}^{-1}(\hat{A}_{IF}\widetilde{A}_{FF}^{-1}(\widetilde{A}_{FE}\widetilde{A}_{EE}^{-1}\widetilde{A}_{EV})) - \hat{A}_{II}^{-1}\hat{A}_{IE}^{-1}(-\widetilde{A}_{EE}^{-1}\widetilde{A}_{EV}) - \hat{A}_{II}^{-1}\hat{A}_{IV} \\ \widetilde{A}_{FF}^{-1}(\widetilde{A}_{FE}\widetilde{A}_{EE}^{-1}\hat{A}_{EV}) - \widetilde{A}_{FF}^{-1}\widetilde{A}_{FV} \\ -\widetilde{A}_{EE}^{-1}\widetilde{A}_{EV} \\ I_{VV} \end{bmatrix}. \tag{2.33}$$

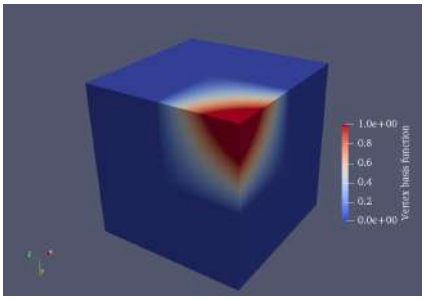

(a) Basis function at the vertex

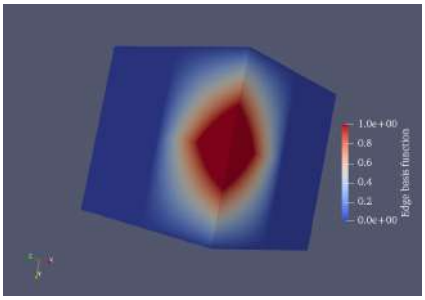

(b) Basis function at the edge node

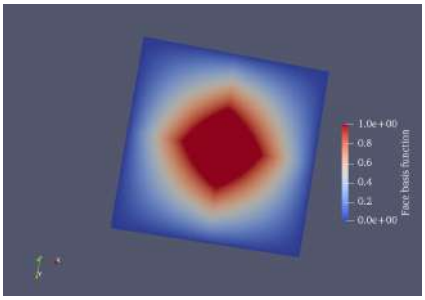

(c) Basis function at the face node

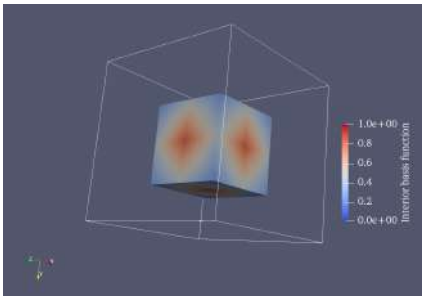

(d) Basis function at the interior, shown in the subset of $3 \times 3 \times 3$.

Figure 2.3: Examples of basis functions obtained from algebraic multiscale in uni-axial compression test case with Cr = $5 \times 5 \times 5$ along each axis and fine-scale domain of $10 \times 10 \times 10$.

The restriction operator is the transpose of prolongation matrix, i.e.,

$$R_h^H = [P_H^h]^T. \tag{2.34}$$

The coarse scale system is formulated to solve for $\overline{u}^H$

$$\hat{A}_H = R_h^H \hat{A}_h P_H^h, \qquad \hat{f}_H = R\hat{f}_h, \qquad \text{and} \qquad \hat{A}_H \overline{u}^H = \hat{f}_H. \tag{2.35}$$

Using the coarse scale deformation and employing Equation 2.23, fine scale displacements are computed.

Figure 2.3 shows the basis functions at the vertex, edge, face and interior coarse element. The coarsening ratio along each axis is given by

$$\mathrm{C}_r = \frac{\text{Number of fine elements along each axis}}{\text{Number of coarse elements along each axis}}. \tag{2.36}$$

The MSFE procedure for inelastic creep deformation is shown in Algorithm 4. The normalized average error between the fine-scale and multiscale solution is given by

$$\epsilon = \frac{||u_{\mathrm{FS}} - u_{\mathrm{MS}}||_2}{||u_{\mathrm{FS}}||_2}. \tag{2.37}$$

The solutions obtained from MS strategy employ fewer degrees of freedom which leads to the reduction of computational effort compared to finescale strategy.

Algorithm 4 : Algebraic MSFE

1: **Formulate** Permutation operator W
2: **Solve** for reduced bcs $\widetilde{A}_{FF}, \widetilde{A}_{FE}, \widetilde{A}_{FV}, \widetilde{A}_{EE}, \widetilde{A}_{EV}$
3: **Formulate** prolongation operator P_H^h
4: **Compute** restriction operator $R_h^H = (P_H^h)'$
5: **Formulate** coarse scale system $\hat{A}_H = R_h^H \hat{A}_h P_H^h$ and $f_H = R\hat{f}_h$
6: **Solve** for coarse system $\overline{u}^H$
7: **Map** it to fine scale system $\overline{u}^h = P_H^h \overline{u}^H$

2.4.1. ITERATIVE MULTISCALE SOLVER

When creep strains are included, the solutions obtained from multiscale formulation is approximate. To reduce the error to a desired tolerance, an iterative procedure is used, employing a fine scale smoother like ILU or GMRES [299, 300]. In this work, ILU(0) and GMRES is employed for few test cases to compare the higher computational efficiency and also improve MS solutions to the desired tolerance. The stopping criteria used here

Algorithm 5 : Iterative Algebraic MSFE

1: **Formulate** prolongation and restriction operators and input tolerance (tol).
2: **Iterate** until $e_r < tol$
3: **Multiscale stage 1:** $u^{\nu+\frac{1}{2}} = P_H^h (R_h^H A^h P_H^h)^{-1} R_h^H r^\nu$
4: **Compute** residual $r^{\nu+\frac{1}{2}} = ||f - A_h u^{\nu+\frac{1}{2}}||$
5: **Smoothing stage 2:** $u^{\nu+1} = (M_{sm})^{-n_s} r^{\nu+\frac{1}{2}}$

e_r is given by

$$e_r = \frac{||u_{\text{FS}} - u_{\text{MS}}||_2}{\text{Total number of nodes}}. \tag{2.38}$$

Where e_r is the average error between fine-scale and multiscale solutions. In realistic field cases, fine scale solution will not be available. In those cases, the stopping criterion can be the relative residual, i.e.,

$$\text{Stopping criteria} = = \frac{||f - A_h u||_2}{||f||_2}. \tag{2.39}$$

The procedure for iterative formulation is described in Algorithm 5. The smoothing stage (stage - 2) can be applied n_s number of times, depending on the complexity of the problem and the computational efficiency.

2.5. RESULTS

2.5.1. CONVERGENCE TEST

To check the consistency of the fine-scale 3D FEM formulation for mechanical equilibrium a synthetic test case is developed which is

$$u_x = \sin\left(\frac{\pi x}{L}\right) \tag{2.40a}$$

$$u_y = \cos\left(\frac{\pi y}{W}\right) \tag{2.40b}$$

$$u_z = \sin\left(\frac{\pi z}{H}\right) \tag{2.40c}$$

Here L, W, H are the dimensions of the rock in x, y, z directions respectively. Using the force balance, the volumetric forces are computed. Accordingly, these forces act as RHS vectors for solving the global system Equation 2.10. The boundary conditions are provided as Dirichlet boundary conditions for all the faces obtained from the analytical solutions Equation 2.40. Since the deformation along a direction are only dependent on their respective directions all the mixed derivatives term vanishes. Using Dirichlet conditions at the boundary faces with elastic moduli $E = 10^5$ and $\nu = 0.1$ as the Poisson ratio. The error is computed using,

$$\epsilon_{L2} = \sqrt{\int_\Omega (u - u^h)^2 dV} \tag{2.41}$$

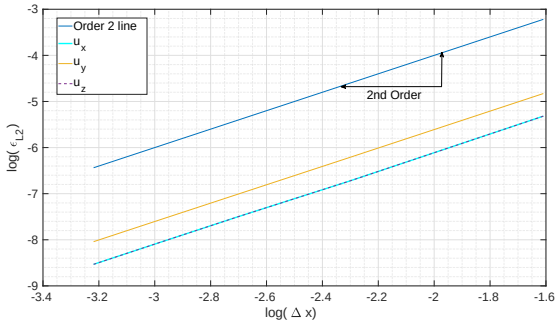

Figure 2.4: Order of convergence Energy norm which shows the norm 2 for deformations in all the directions.

The error is computed using the 2nd norm where dV is the volume of an element. Figure 2.4 shows the 2nd-order accuracy in space.

2.5.2. SYNTHETIC SHEAR TEST CASE

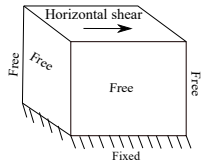

Figure 2.5: **Synthetic test case:** Schematic of the synthetic test case when a horizontal shearing load is applied on the top face. The rest of the faces have stress-free boundary conditions. The parameters used in this test case are presented in Table 2.1.

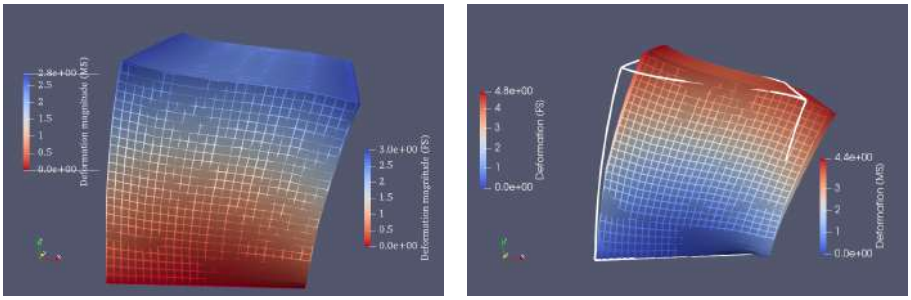

(a) (b)

Figure 2.6: **Synthetic test case:** The above snapshots show the deformed body when a force (x-direction) is applied on the top face and the bottom face is fixed. Fine-scale grid has 25 × 25 × 25 cells, and the coarsening ratio is 5 × 5 × 5. Figurre 2.6(a) shows the results at time = 0 for fine-scale (Surface) and MS (Wire-frame). Figure 2.6(b) shows the results at time = dt for fine-scale (Surface) and MS (Wire-frame) and white outline is the fine-scale result at time = 0. The parameters used in this test case are presented in Table 2.1.

In this subsection, a synthetic test case is modelled with creep to show the capabilities of the computational framework and understand the influence of creep on body deformation. Rock salt material properties are chosen for modelling this test case. Fine-scale and multiscale strategies are employed to this model. The parameters used in this test case are shown in Table 2.1. The parameters are chosen artificially, to demonstrate the deformation caused due to creep.

Table 2.1: Parameters used to model creep in synthetic test case

#	Value	#	Value	#	Value
dt	1.65 years [day]	Q	80000 [301] [J/mol]	n	4 [-]
a	5e-24 [-]	T	290 [K]	E	5 [GPa] [302]
m	0.21	ν	0.25 [-]	Traction	190 [MPa]
Cells	25 × 25 × 25	C_r	5 × 5 × 5	Dimensions	10 × 10 × 10 [m]

A horizontal shearing force is applied on the top face, the bottom face is fixed and rest of the faces are traction free. Figure 2.6(b) shows the snapshot of the deformed body at time = 0, obtained from both fine-scale and multiscale strategies. Figure 2.6(b) shows the finescale and multiscale solutions obtained after time = 1.5 years. This deformation occurs due to creep. The error between the FS and MS results as calculated from Figure 2.37 is less than 10 %. Iterative MS is not further employed in this test case. The solution obtained from MS strategy is not accurate because the reduced boundary conditions have not provided an accurate localization condition.

2.5.3. UNI-AXIAL COMPRESSION OF ROCK SALT

Uni-axial compression of rock salt is investigated in this subsection. A distributed load is imposed on the top face and all the four faces (north, east, west and south) of the domain are subjected to roller constraints. The bottom face is fixed. The schematic is shown in Figure 2.8(a). A distributed load P of 0.1-0.3 MPa is imposed for a period of 8 months. The results for P=0.2 MPa is compared with experimental results [8]. Least square fit is used on the strain rate to obtain the parameters of the creep formulation. Equation 2.13a is used here as a constitutive equation. The parameters used to model creep are presented in Table 2.2. The experiments are conducted on cylindrical specimens, however the effect of curvature is ignored in this case and only the dimensions are taken.

Table 2.2: Parameters used to model rock salt creep for uni-axial compression test case. Parameters highlighted with * are found by least-square fitting of experimental data for strain rate.

#	Value	#	Value	#	Value
dt	1 [day]	Q	80000 [301] [J/mol]	n^*	4 [-]
a*	3e-13 [-]	T	290 [K]	E	5 [GPa] [302]
m^*	0.21	ν	0.25 [-] [302]	Traction	0.1-0.3 [MPa] [8]
Cells	$30 \times 30 \times 30$	C_r	$10 \times 10 \times 10$	Dimensions	$12 \times 7 \times 7$ [cm^3]

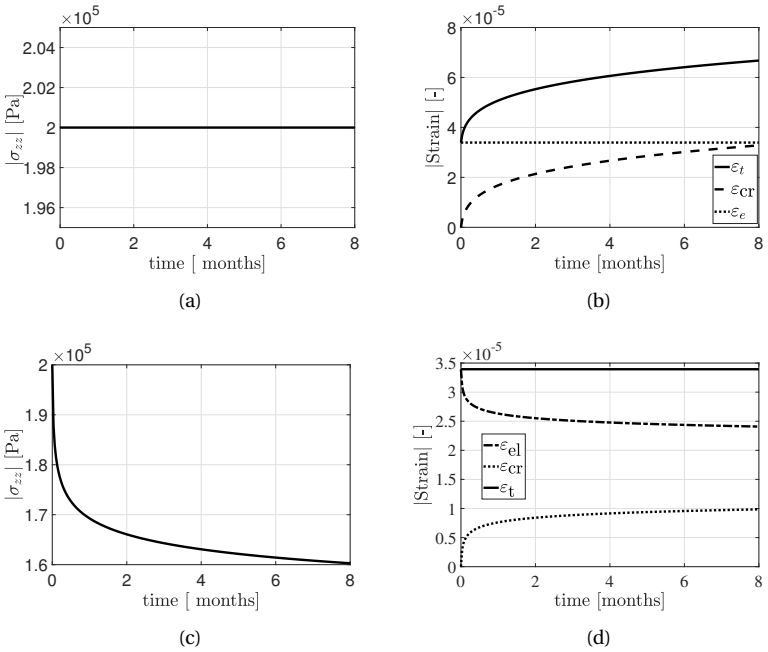

Figure 2.7: **Synthetic test case:** The above snapshots show the deformed body when a force (x-direction) is applied on the top face and the bottom face is fixed. Fine-scale grid has 25 × 25 × 25 cells, and the coarsening ratio is 5 × 5 × 5. Figure 2.6(a) shows the results at time = 0 for fine-scale (Surface) and MS (Wire-frame). Figure 2.6(b) shows the results at time = dt for fine-scale (Surface) and MS (Wire-frame) and white outline is the fine-scale result at time = 0. The parameters used in this test case are presented in Table 2.1.

Firstly, classical and relaxation creep methodology is employed to understand uni-axial compression. Figure 2.7 shows the results of both classical and relaxation creep. Figures 2.7(a) and 2.7(b) show the variation of absolute stress (σ_{zz}), absolute strains ($\varepsilon_{t,zz}$, $\varepsilon_{el,zz}$ and $\varepsilon_{cr,zz}$) with time for classical creep. Here, we can see that the stress is constant with time which means that elastic strain is constant with time. The absolute of the total strain is increasing due to increasing creep strain. Figures 2.7(c) and 2.7(d) show the variation of absolute stress (σ_{zz}), absolute strains ($\varepsilon_{t,zz}$, $\varepsilon_{el,zz}$ and $\varepsilon_{cr,zz}$) with time for relaxation creep. In this case, the total strain is constant with time, since the absolute of the creep strain is increasing the elastic strain is reducing with time. Since the elastic strain is reducing with time, the absolute stress is reducing with time. These plots depict the same methodology as shown in Figure 2.1.

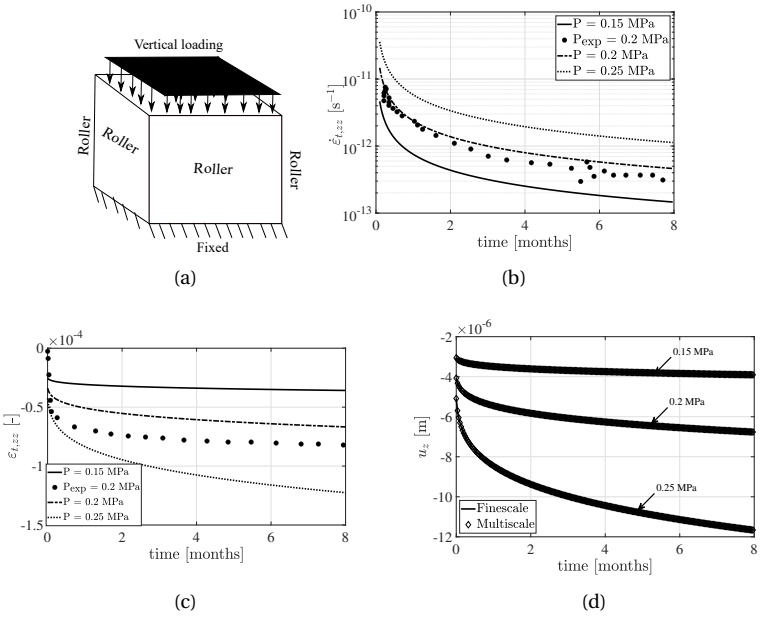

Figure 2.8: **Uni-axial compression:** The above plots show the variation of creep strain rate (Figure 2.8(b)), total strain (Figure 2.8(c)) and deformation (Figure 2.8(d)) with time for rock salt when it undergoes inelastic creep. The experimental results for vertical loading at the top of P = 0.2 MPa case [8] is compared with numerical results. The numerical results are shown for traction P = 0.15 to 0.25 MPa. Figure 2.8(d) compares the fine-scale and multiscale results for coarsening ratio of 1000. The details of the numerical model are presented in Table 2.2.

The results shown in Figure 2.8 are obtained from employing classical creep. All the results are plotted for a node that is located in the center of the top face. The variation of strain rate with time is shown in Figure 2.8(b). It can be seen that the strain rate increases when the imposed load increases. Similar observation is seen in Figure2.8(c). Least square fit is conducted on strain rate and accordingly the strain is computed. There is some difference between the experimental and numerical results for variation of strain with time Figure 2.8(c). This is because it is assumed that the properties of the rock salt are assumed to be homogeneous. However, Young's modulus and Poisson ratio vary depending on the salt composition. The presence of salt of varying compositions would affect the fitting parameters of the creep constitutive equation. Investigating the effects of the composition of rock salt on the overall behavior of the numerical model is beyond the scope of this work. Figure 2.8(d) shows the variation of deformation with time for different loading conditions shown for both fine-scale and multiscale. It can be seen that the results of fine-scale and multiscale overlap. As the imposed load increases, the elastic deformation and deformation accumulated over time due to creep increases. This is a situation in which the boundary condition imposed on local basis functions are very accurate, leading to accurate multi-scale solutions. Note that, the multiscale solution accuracy depends highly on the accuracy of the local basis functions. When the reduced

boundary condition has provided an accurate localization condition, the MS solutions are accurate.

2.5.4. TRI-AXIAL COMPRESSION

In this subsection, influence of creep on tri-axial loading is studied. Figure 2.9(a) shows the schematic of tri-axial loading where a confining stress is imposed on all the four faces (north, east, south and west), the bottom is fixed and a vertical load is imposed on the top face. Bingham body formulation is employed here, as in Equation 2.13b, to study the influence of creep on coal specimen. The parameters chosen to study this formulation are presented in Table 2.3. The experimental results [9] are compared with the numerical results. The experiment is conducted for a period of 45 minutes. The numerical results are compared for fine-scale, multiscale and iterative multiscale simulations.

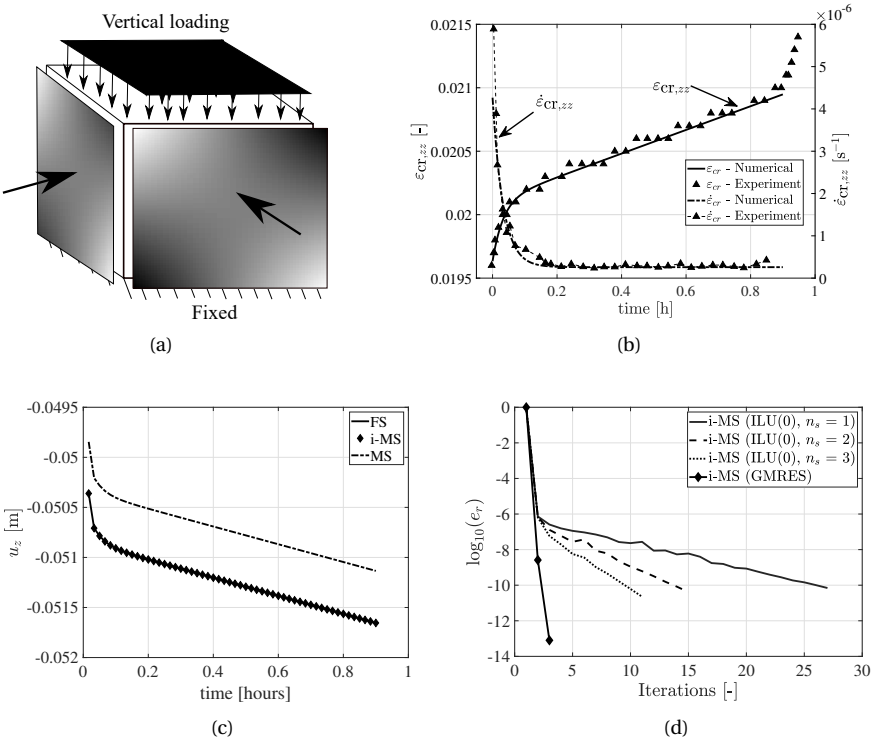

Figure 2.9: **Tri-axial compression:** The figures show the variation of strain, strain rate (Figure 2.9(b)), deformation (Figure 2.9(c)) with time for coal specimen when it undergoes creep. The experimental results [9] are compared with numerical results using parameters shown in Table 2.3. The deformation results are compared for FS, MS and iterative MS. The convergence plot obtained by using iterative MS is shown in Figure 2.9(d) for deformation (u_z). The convergence plot is shown for stage 2 of the iterative multiscale solver for different number of smoothing stages using only ILU(0) $n_s = 1,2,3$ or using only GMRES without any preconditioner.

Table 2.3: Parameters for creep formulation of coal used to simulate tri-axial compression with creep using Bingham model

#	Value	#	Value	#	Value
dt	60 [s]	s^{cr}	44.99 [MPa] [9]	Confining stress	30 [MPa] [9]
G_1	1.91 [GPa] [9]	G_2	79.01 [GPa] [9]	E	4 [GPa] [9]
η_1	2.6 [GPa h] [9]	η_2	40.18 [GPa h] [9]	ν	0.25 [-] [9]
Cells	$20 \times 20 \times 20$	C_r	$10 \times 10 \times 10$	Load	142 [MPa]

Figure 2.9(b) shows the variation of creep strain and creep strain rate with time. Here it can be seen that the experimental data fits well with the numerical data for the parameters chosen. However, the experimental data also shows the tertiary creep phase which is not captured by the numerical formulation. To model tertiary creep, a different damage constitutive formulation has to be employed that can explain the coupling of highly non-linear effects which leads to material failure. Though it is of critical importance, it is beyond the scope of this work. The variation of deformation (u_z) with time is shown in Figure 2.9(c) for a node that is located in the centre of the top face. It can be seen that the deformation increases with time for the imposed load. The primary and secondary stage of creep can also be seen in this formulation. The normalized error computed from Equation 2.37 is less than 2% for the chosen coarsening ratio.
The results of fine-scale and multiscale are slightly different. Multiscale solution is further improved by employing iterative multiscale strategy. ILU(0) and GMRES are compared for their efficiency of smoothing in i-MS strategy. Figure 2.9(d) shows the variation of error for deformation (u_z) with number of iterations to achieve convergence. The tolerance was set to 1e-10. The convergence plot is compared for ILU (0) with varying smoothing stages $n_s = 1, 2, 3$ and GMRES without any preconditioner. It can be seen that GMRES without any preconditioner converges to the solution in less than 5 iterations, at a faster rate compared to ILU (0). The deformation obtained from MS is not very different from FS. However, when the properties of rock is heterogeneous and different loading condition the convergence rate of the iterative solvers will vary.

2.5.5. TRI-AXIAL CYCLIC LOADING OF SANDSTONE

In this subsection, a cyclic load is imposed when the rock is confined by stress on all 4 sides. The experimental results [10] are compared with numerical results for sandstone. The parameters chosen for this formulation are presented in Table 2.4. Investigation of the effect of varying material properties on the fitting parameters of creep is beyond the scope of this work. The simulation is conducted for a period of 210 minutes with 4 cycles for a vertical load of 265 MPa. Equation 2.13a is used by employing classical creep in this study.

Table 2.4: Parameters for creep formulation of sandstone used to simulate tri-axial cyclic compression. Parameters highlighted with * are found by least-square fitting of experimental data for strain.

#	Value	#	Value	#	Value
dt	24 [mins]	Q	5000 [23] [cal/mol]	Confining stress	25 [MPa] [10]
n^*	1.6 [-]	Dimensions	$5 \times 5 \times 10$ [cm]	E	40 [GPa] [10]
m^*	1.005	ν	0.32 [-] [10]	a^*	1.5e-19
Cells	$30 \times 30 \times 30$	C_r	$10 \times 10 \times 10$	F	265 [MPa] [10]

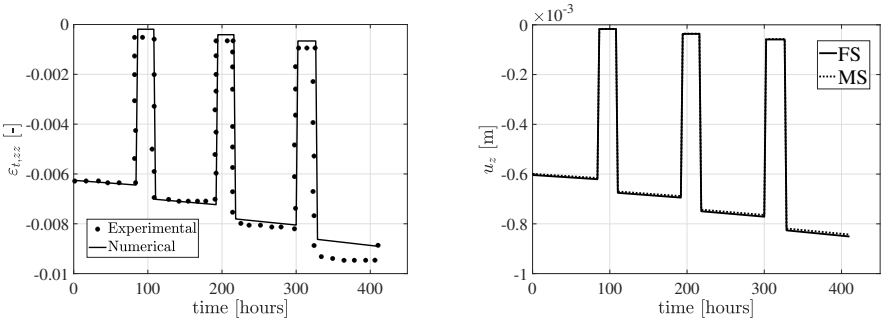

Figure 2.10: **Tri-axial cyclic loading:** Figure 2.10(a) shows the variation of total strain with time compared with the experimental results [10] for sandstone rock, and Figure 2.10(b) shows the variation of deformation (u_z) with time for both fine scale and multiscale results. The parameters used for this formulation are presented in Table 2.4.

Figure 6.6 shows the variation of total longitudinal strain and longitudinal deformation for fine-scale and multiscale strategies. 2.10(a) compares the experimental and numerical total strain data. The least square fit is employed on the experimental data only on the first cycle. The fitting parameter $m = 1.005$ is very close to 1. This would mean that the strain rate is almost not dependent on time. In addition, it can be seen that the experimental and numerical data of strain match for more than 2 cycles. The observed error between the numerical and experimental data is slightly higher in the last cycle after 300 hours. We think that this might be because due to cyclic loading, there might be opening and closing of micro-cracks or expansion of voids. To incorporate this, the fitting parameters of the creep constitutive formulation would depend on the type of loading like frequency and amplitude of loads. It is of critical importance to further investigate this effect. Due to a lack of literature, this is beyond the scope of this work.
Figure 2.10(b) compares the deformation obtained from fine-scale and multiscale strategy. The multiscale solutions are obtained using much fewer degrees of freedom. As such it clearly outperforms the fine-scale simulation strategy. The variation of the deformation of the node that is located in the center of the top face is shown here. It can be seen that the approximate solutions obtained from multiscale solutions are very close to fine-scale solutions. Hence for this test case, an iterative multiscale strategy is not further employed.

2.5.6. INFLUENCE OF CREEP ON PLAIN STRAIN SUBSIDENCE

Subsurface energy storage technology will involve cyclic injection and production of the reservoir. Due to this, subsidence and uplift of the earth's top layer might occur. To comprehend this, the influence of creep on subsidence and uplift has to be studied. In this work, the influence of non-linear deformation on land subsidence which is caused due to injection and production of the reservoir is modeled in heterogeneous media by assuming plain strain in the domain ($x-z$ plane). [297, 303] gives you the properties of the geological formation inside the domain. The domain mainly consists of clayed rock. The reservoir is modeled in the span of 10 km and for a height of 3km. The elasticity modulus is obtained from vertical uni-axial compressibility (c_M) which is given by [304], i.e.,

$$c_M = 0.01241|\sigma'_Y|^{-1.1342}. \tag{2.42}$$

Here c_M and σ'_Y are expressed in [bar^{-1}] and [bar] respectively. Here σ'_Y is the vertical effective stress. The vertical effective stress is obtained as a superposition of total vertical stress σ_Y and hydrostatic pressure p, i.e.,

$$\sigma'_Y = \sigma'_Y + p = 0.12218|y|^{1.0766} + 0.1|y|. \tag{2.43}$$

The Young's modulus can be expressed as from [304], i.e.,

$$E = \frac{(1-2\nu)(1+\nu)}{(1-\nu)c_M}. \tag{2.44}$$

The schematic of this test case is shown in Figure 2.11(a). Here, rollers are subjected to the bottom, west, and east boundary, and the north boundary is traction free. The hydrogen gas has to be stored at the right temperature and pressure for feasibility. In the natural state of the earth, lithostatic pressure would be present inside the geometrical domain. However, it is assumed that the lithostatic pressure would not cause nonlinear time-dependent deformation. A deviation from the equilibrium state, which involves injection and production of the reservoir would undergo nonlinear time-dependent deformation. Assume that the natural state of the reservoir has a pressure of $P_0 = 150$ bar without any subsidence. The effective pressure P' is given by

$$P' = P - P_0. \tag{2.45}$$

In this work, the pressure P is varied between 50 and 110 bar in the form of cyclic load as shown in Figure 2.11(b). If $P' = 0$ bar, then $P = P_0$ which means that the earth is in equilibrium and there is no subsidence. For $P = 50$ bar ($P' = -100$ bar) higher subsidence is expected compared to $P = 110$ bar ($P' = -40$ bar) because of the higher pressure drop. The temperature is chosen to be 373 K [305], with minimum microbial and bio-chemical reactions [306]. Elasticity modulus degradation due to possible reservoir rock in-elasticity is neglected. The rock material is assumed to be isotropic. Classical creep methodology is employed here.

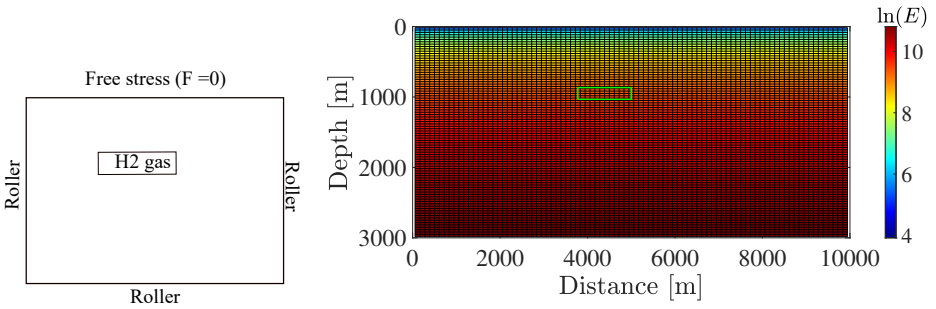

Figure 2.11: **Plain strain subsidence:** Figure 2.11(a) shows the schematic of the plain strain subsidence test case where the pressurized H_2 gas is stored in the reservoir (small box) inside the geological domain. The domain is constrained by roller boundary conditions at north, east, south, and bottom. Figure 2.11(b) depicts the distribution of Young's modulus in the x-z plane within the geological domain as described by Equation 2.44. The green box shows the location of the reservoir.

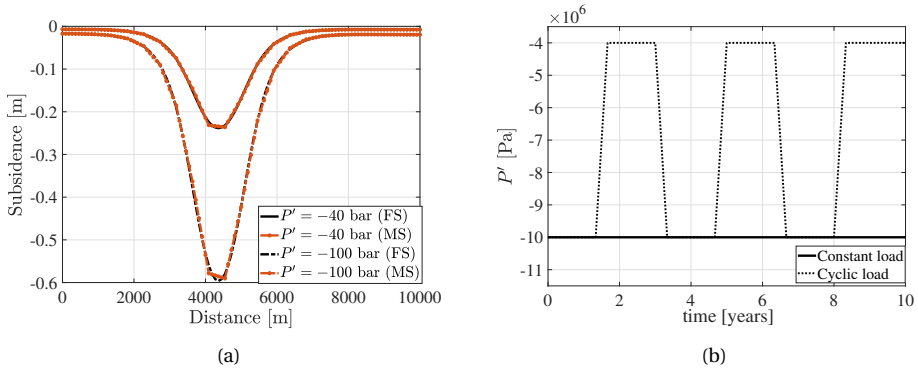

Figure 2.12: **Plain strain subsidence:** The above figures show the results for plain strain subsidence using the parameters for creep from Table 2.4. The fine-scale grid is 110×110. The multiscale solutions are shown for a coarsening ratio of 5 × 5. Figure 2.12(a) shows the subsidence plotted for fine-scale and multiscale results for P' = -40 and -100 bar at time = 0.

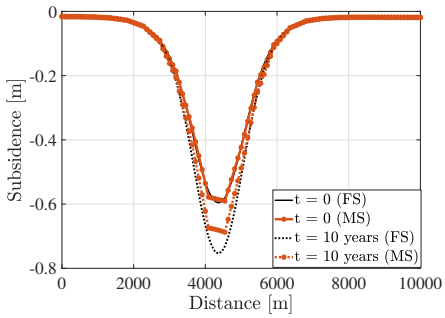

(a) **Constant load**

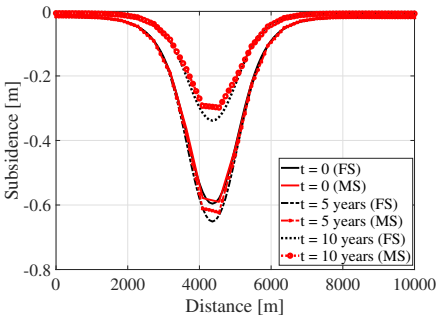

(b) **Cyclic load**

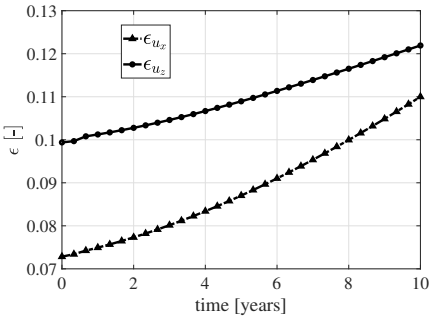

(c) **Constant load:** Variation of error.

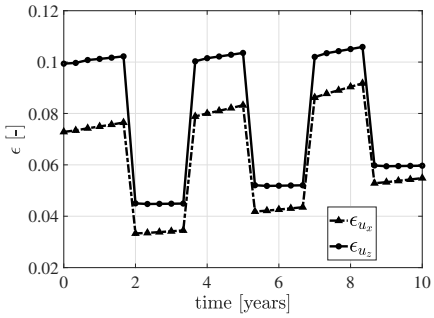

(d) **Cyclic load:** Variation of error

Figure 2.13: **Plain strain subsidence:** The above figures show the results for plain strain subsidence using the parameters for creep from Table 2.4. The fine-scale grid is 110×110. The multiscale solutions are shown for a coarsening ratio of 5 × 5. Constant pressure ($P' = -100$ bar) and cyclic pressure ($P' = -100$ to $P' = -40$ bar) is imposed inside the reservoir as shown in (Figure 2.12(b)) and the influence of creep on subsidence is shown in Figure 2.13(a) and Figure 2.13(b) respectively. The variation of the average error (Figure 2.37) between fine-scale and multi-scale solutions for u_x, u_z at each time step is shown in Figure 2.13(c) and Figure 2.13(d).

The fine-scale grid contains 110 × 110 cells, while the multiscale solver employs 22 × 22 cells, having the coarsening ratio of 5 × 5. The parameters for creep formulation are obtained from previous test case as shown in Table 2.4. The time-step (dt) size is chosen to be 4 months and the entire simulation is conducted for a period of 10 years ($30 \times dt$). The time-step size is assumed to be of similar order as Maxwell time which is given by ratio of shear viscosity to its shear modulus. The uncertainty in viscosity due to different grain sizes is not considered here. Poisson ratio is $\nu = 0.3$ and Lame's parameters are obtained from Youngs modulus in Equation 2.44.

Figure 2.13 shows the results obtained for plain strain subsidence test case when nonlinear time-dependent deformation is incorporated. Figure 2.12(a) shows the variation of subsidence inside the domain for different effective pressures $P' = -40, -100$ bar when time =0. The multiscale solutions are obtained using much fewer degrees of freedom. This reduces the computational effort and outperforms the fine-scale simulation strategy. It can be seen that the multiscale solution and fine-scale solution have similar mag-

nitude except for the smooth kink which is not obtained in the multiscale solution. This is because the number of cells occupied by the reservoir is close to the number of fine-scale elements in a coarse element. If required, an iterative MS strategy can be employed to improve the solution. Overall, the quality of the multiscale solution is good. It can be seen that the lower the effective pressure, the higher the magnitude of the subsidence due to higher pressure drop compared to the natural state. The influence of creep is studied by injection and production inside the reservoir which varies the pressures as shown in Figure 2.12(b) in the form of constant load and cyclic load for 10 years.
Figure 2.13(a) shows the subsidence inside the domain at t = 0 (without creep) and t = 10 years (with creep) at a constant load for effective pressure of $P' = -100$ bar. It can be seen that the magnitude of subsidence has increased at t=10 years compared to t = 0. Due to creep, the deformation increases which also increases the magnitude of the subsidence caused. The deviation between fine-scale and multiscale solutions has increased which is because the basis functions are constructed based on linear elasticity and the magnitude of the fictitious creep forces (F_{cr} increases with time. Figure 2.13(b) shows the variation of subsidence inside the domain when the reservoir is injected and produced cyclically. The magnitude of subsidence caused only due to creep in cyclic load will be lesser than the constant load (of higher magnitude). This is because a constant load of higher magnitude will result in higher magnitudes of stress which further results in the accumulation of higher magnitude of creep strain and deformation. It can be seen that the magnitude of error between FS and MS solutions for $P' = -40$ bar at t = 0 (as seen in Figure 2.12(a)) and at t = 10 years in cyclic loading (as seen in Figure 2.13(a)) is lower. The error between the FS and MS solutions are shown in Figure 2.13(c) and Figure 2.13(d) for constant and cyclic load respectively. The normalized error is less than 13% for constant load and 11% for cyclic load. As time increases creep strain increases which leads to an increase in the error. The error for u_x increases at a faster rate than u_z. The MS solutions can be further improved if the iterative MS strategy is used only near and around the reservoir as a block iterative MS solver. Overall the MS solutions are satisfactory, hence iterative MS strategy is not further employed in this case.

2.6. CONCLUSION

In this work, an iterative multiscale nonlinear modeling strategy was proposed which can model time-dependent nonlinear geomechanical deformation using finite element method (FEM). The developed computational framework would be of critical importance to model subsurface energy storage which involves nonlinear deformation. Constitutive formulae were chosen to model the creep strains of different rock materials from the available literature. Employing the least square fit on the experimental data, the fitting parameters of creep strain were computed. Classical creep and relaxation creep were both modelled incorporated. Due to the computational stability, an implicit time discretization strategy was followed. Multiscale finite element (MSFE) method, formulated and implemented algebraically, was then developed based on locally computed elastic basis functions. To further improve the approximate multiscale solution, 2 stage iterative strategy is developed to combine the multiscale system with a smoother at fine scale.

Several numerical experiments were conducted with synthetic and realistic material parameters, to understand the nonlinear time-dependent deformation. First, creep deformation of rock salt under uni-axial deformation is studied under both classical and relaxation creep. It was found that the fine-scale and multiscale solutions match well. Employing Bingham creep formulation, tri-axial compression of coal is studied. The difference between fine-scale multiscale solution was found to be less than 2 %. Different iterative multiscale smoothing strategies were compared to obtain fine-scale solution of desired accuracy. Since subsurface storage technology in reservoirs involves cyclic loading, as such tri-axial cyclic loading on sandstone was also studied. In agreement with the previous cases, the difference between fine-scale and multiscale solutions was less than 1%. The influence of non-linear deformation was further studied on realistic reservoirs which involved land subsidence in heterogeneous fields. Without creep, the multiscale solutions show a similar magnitude as fine-scale solutions. For the studied realistic case, the quality of multiscale solution (with no iterations) was satisfactory even when creep is incorporated.

This study allows for quantification of the inelastic time-dependent creep deformation for geoscience applications, specially those relevant to subsurface storage. It also makes it possible to represent complex nonlinear and heterogeneous systems with much fewer degrees of freedom than the fine-scale classical approaches. As such, it sheds new light in advancing the accuracy and speedup of the quantitative analyses of complex natural porous media behavior.

Future work includes poro-inelastic systems to study the influence of fluctuating pore pressure on the cyclic behavior of rock materials. It was also found in subsection 2.5.5 that as the number of cycles increases, the experimental data starts to deviate from the fitting data. This needs to be investigated further when the time scale is in years. Propagation of faults and fractures will be incorporated inside the domain to study their influence on inelastic deformation when a cyclic load is imposed.

3

GEOMECHANICAL SIMULATION OF ENERGY STORAGE IN SALT FORMATIONS

Summary: *A promising option for storing large-scale quantities of green gases (e.g., hydrogen) is in subsurface rock salt caverns. The mechanical performance of salt caverns utilized for long-term subsurface energy storage plays a significant role in long-term stability and serviceability. However, rock salt undergoes non-linear creep deformation due to long-term loading caused by subsurface storage. Salt caverns have complex geometries and the geological domain surrounding salt caverns has a vast amount of material heterogeneity. To safely store gases in caverns, a thorough analysis of the geological domain becomes crucial. To date, few studies have attempted to analyze the influence of geometrical and material heterogeneity on the state of stress in salt caverns subjected to long-term loading. In this work, we present a rigorous and systematic modeling study to quantify the impact of heterogeneity on the deformation of salt caverns and quantify the state of stress around the caverns. A 2D finite element simulator was developed to consistently account for the non-linear creep deformation. The computational scheme was benchmarked with the already existing experimental study. The impact of cyclic loading on the cavern was studied considering the maximum and minimum pressure that depends on lithostatic pressure. The influence of geometric heterogeneity such as irregularly-shaped caverns and material heterogeneity, which involves different elastic and creep properties of the different materials in the geological domain, is rigorously studied and quantified. Moreover, multi-cavern simulations are conducted to investigate the influence of a cavern on the adjacent caverns. An elaborate sensitivity analysis of parameters involved with creep constitutive laws is performed to understand the influence of creep on deformation and stress evolution around the salt cavern configurations.*

This is from Ramesh Kumar 2021, Scientific reports

3.1. INTRODUCTION

Storage of green gases (eg. hydrogen) in salt caverns offers a promising large-scale energy storage option for combating intermittent supply of renewable energy, such as wind and solar energy. Caverns are artificially created by a controlled dissolution mining process within the host rock formation [307]. Caverns typically hold volumes of about 300,000-500,000 m^3, with much larger outliers in the order of million cubic meters [308]. Salt caverns provide swift deliverability of the stored energy, i.e., excellent injection and production characteristics compared with porous rocks, and have strong sealing properties on time scales relevant for gas storage [11, 309].

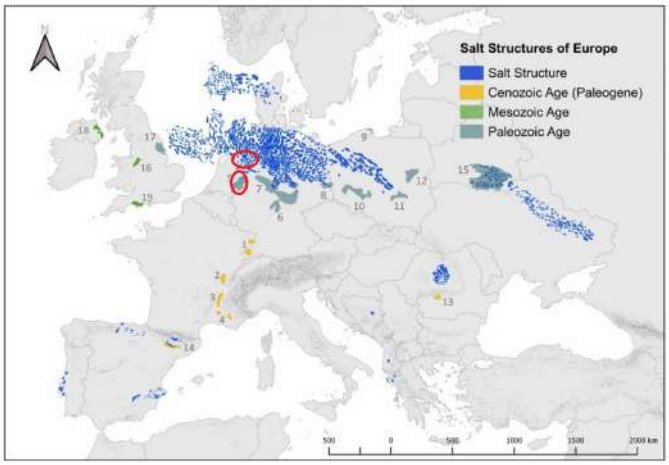

Figure 3.1: Illustration of the map of European salt deposits and salt structures as a result of suitability assessment, taken from the literature [11]. Salt deposits in the Netherlands are marked in red circles.

Salt cavern construction focuses primarily on salt diapirs or domes, formed when part of a thick bed of salt migrates vertically into denser surrounding rock strata in response to buoyancy forces over geological time scales [310, 311]. The primary depth target for salt cavern construction lies at 1,000-1,500 m, as within this depth range, the rock salt material behaves reasonably stably, and long-lived caverns can be constructed [307]. The plastic behavior of the salt defines the engineering limits at different depths, the operating pressures, and cycling characteristics, and the material characteristics of the rock salt [307]. Storage caverns usually have an elongated cylindrical shape because of their good stability, with a height from tens to a few hundred meters [11, 307]. Spherical, pear-shaped caverns and bell-shaped caverns have also been built in the past [307]. Figure Figure 3.1 shows a map of salt deposits in Europe which could be used for H2 storage [11]. For salt cavern storage, a minimum salt thickness of 200 m and the depth range of 500 m to 2000 m was chosen. In the Netherlands, the rock salt layers in the subsurface occur mainly in strata of the Permian Zechstein Group (laid down between approximately 251 and 260 million years ago) and the Triassic Röt Formation (laid down between around 238 and 244 million years ago) [312]. As seen from Figure Figure 3.1, the

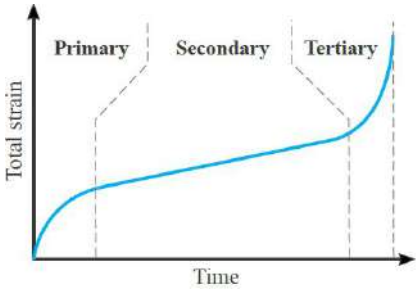

Figure 3.2: Illustration of the creep response of a material to uniaxial loading under conditions of low confinement that allow ultimate failure. Note the three stages of creep. The illustration is modified after [12].

majority of the salt deposits of the Netherlands, suitable for developing subsurface storage caverns, are located in the northern, north-eastern, and eastern parts of the country. The salt is originally accumulated in shallow, restricted salt lakes. Due to the evaporation of the seawater, salt crystals are precipitated to form today's solid rock salt layers, which in the case of the Zechstein salt in the Netherlands. The Netherlands has developed numerous domes, and pillow structures [312].

Today's Dutch salt caverns are mainly the result of salt mining operations. However, a few are being used for the storage of natural gas, industrial gases, nitrogen, and compressed air [312]. Near Zuidwending, for example, several caverns are currently being used for natural gas storage (Aardgasbuffer Zuidwending). Another example is the cavern near Heiligerlee (Stikstofbuffer Heiligerlee), which has been used for nitrogen storage since 2012 [312]. Both purpose-built caverns, and existing caverns created during solution mining operations and preserved afterward, can potentially be used to store hydrogen or other gases. But first, it is necessary to conduct reliability and stability analyses to evaluate the safety of such structures.

The primary nonlinear deformation physics of rock salts is associated with time-dependent, i.e. creep processes. Creep is a phenomenon whereby a solid material permanently deforms with time under the influence of persistent mechanical stress. Of critical importance, here, is to predict the resulting evolution of stress and deformation field over long times, to ensure the safety of the storage facility up to and into abandonment, i.e., potentially over periods of hundreds of years. As shown in Figure 3.2, after applying an external load, the material consistently goes through three stages of creep. These are often called transient (primary or reduced), steady (secondary or stationary), and tertiary (accelerated) creep stages [12]. The primary creep stage is characterized by a monotonic decrease in the rate of the creep. Secondary creep is characterized by a constant creep rate. Deformation occurring during primary and secondary creep are similar to pure elastic deformations and can be significant in the secondary phase. The tertiary creep phase, seen when mean stresses are low enough to allow the formation of microscopic cracks, is characterized by microcrack damage evolution, hence creep acceleration, and ultimately brittle rupture of the material [313]. Creep in salt occurs at rates that are significant on short and long engineering time scales at temperatures in the range of 20-200 Celsius [314] and stresses as low as 0.2 MPa [8, 314]. The de-

formation mechanics are governed by dislocation motion within the crystalline grains and by a range of grain boundary processes. As explained in the literature [315], two main deformation mechanisms have been investigated by employing laboratory tests and micro-structural analyses. The first is the dislocation creep mechanism, which in the steady case is characterized by a power-law dependence of creep strain rate on deviatoric stress and an Arrhenius dependence on temperature. This type of behavior is grain size insensitive and generally shows stress exponents in the range of 3.5-5.5 and activation energies around 60 kJ/mol [316–318]. When small (natural) quantities of brine are present, creep strains are over 5-10 %, and mean normal stresses are high enough to suppress micro-cracking, the process is accompanied by a growth of new crystals during deformation, which slightly enhances creep rate, but without changing the overall flow law significantly [315, 319–321]. Dislocation creep is favored towards higher stresses and temperatures through its highly nonlinear power-law stress dependence and Arrhenius temperature dependence. The second creep mechanism is solution-precipitation creep or pressure solution. It is a linear viscous creep mechanism that involves stress-driven dissolution-precipitation transfer of salt around water-bearing grain boundaries and is favored in fine-grained materials at low stresses, and temperatures [315, 322]. Various formulations used in the literature to model creep and dilatancy are presented in Table 3.1. They are the power-law, Hou/Lux, Munson and Dawson (MD), and lastly, Hoek Brown models. For further details on these constitutive models, refer to the references in the Table 3.1. Note Table 3.1 does not include models that explicitly account for pressure solution. It should be mentioned that there are many other formulations, including the Hampel/Schulze [323] one used here, and several that do explicitly account for pressure solution [24, 315, 324, 325].

Table 3.1: Constitutive relations presented in the literature to express creep strain rate and creep strain for Rock salt

Model	Formulation
Power law [12, 317, 318, 320, 323, 326, 327]	$\dot{\varepsilon_{cr}} = A \exp\left(\frac{-Q}{RT}\right)\sigma^n$
Hou/Lux [328]	$\dot{\varepsilon_{cr}} = \frac{3}{2}\left[\frac{1}{\eta_k(\sigma v)}\left(1-\frac{\varepsilon^{tr}}{\max(\varepsilon^{tr})}\right)+\frac{1}{\eta m(\sigma v,T)}\right]\times s_{ij}$
MD [329, 330]	$A_1 \exp\frac{-Q_1}{RT}\left[\frac{\sigma}{\mu(1-\omega)}\right]^{n_1} + A_2 \exp\frac{-Q_2}{RT}\left[\frac{\sigma}{\mu(1-\omega)}\right]^{n_2} + \lvert H(\sigma-\sigma_0)\rvert\left(B_1 \exp\frac{-Q_1}{RT} + B_2 e^{\frac{-Q_2}{RT}}\right)\sinh\left[\frac{q\left(\frac{\sigma}{1-\omega}-\sigma_0\right)}{\mu}\right]$
Hoek Brown [9, 115, 331]	$\varepsilon_{cr} = \frac{\boldsymbol{s}-D_b\boldsymbol{s}^{cr}}{1-D_b}\left(\frac{1}{2G_1}+\frac{1}{2G_2}(1-e^{\frac{-G_2 t}{\eta_1}})+\frac{t}{2\eta_2}\right)$

The present work uses the Carter [317] constitutive model constants to describe the material behavior. The model is based on the power-law creep relationship derived by quantifying the creep processes observed in the laboratory tests on natural salt at differential stresses > 5 MPa. Laws for natural salt fitted above about 5 MPa will not contain pressure solution effects as it only becomes dominant in natural salt at lower stresses [317–319, 323]. In the past years, several numerical studies [150–159] were conducted to describe geo-mechanical rock salt deformation.

The heterogeneous composition (interlayers) of the geological domain around salt caverns will affect the deformation of salt caverns. Elastic and creep properties of these rock formations vary along with the depth of the geological domain. Interlayers in salt formations are difficult to dissolve in water and pose many challenges in the process of

designing caverns and during their operation [268, 332–334]. Caverns within bedded salt formations are not as stable as those created within salt domes [309]. The heterogeneity of the rock salt may affect the solution mining process, which in turn will also affect the shape of the constructed cavern [310]. In field scale cases, salt properties are heterogeneous due to impurities such as anhydrite or potassium/magnesium salts, shale rocks, and bischofite [19, 115, 311]. Heterogeneity in the geological domain surrounding salt caverns involves many insoluble interlayers (anhydrite, potash salts, shale, gypsum, mudstone, etc.) [332, 335, 336]. Few experimental researchers have attempted to study the impact of heterogeneity in the composition of rock salt [19, 115, 332, 337]. However, very few researchers have tried to study the impact of heterogeneity by considering elastic and creep properties of interlayers in the domain [115]. Wang et al. [268] showed the effect of heterogeneity by considering only elastic properties and by considering equivalent elastic modulus. Because of different crystal lattices and compositions, every material behaves differently under stress subjected to longer timescales. Hence, it becomes critical to incorporate creep properties of the heterogeneity. In this work, we study two approaches to study the impact of heterogeneity. The first method employs only elastic properties of heterogeneity. The second method uses different elastic properties and creep constitutive relations to model creep aptly subjected to extended periods. One more aspect that becomes critical is studying the effect of the irregularly shaped cavern on the state of stress and deformation. This work attempts to study this effect allowing us to capture real-field scenarios in the computational domain.
The computational framework employs an implicit simulation model on non-uniform fully-unstructured triangular mesh and constant strain triangular (CST) elements. The model is further expanded by incorporating Eulerian strains and considering the stored product (hydrogen) density and corresponding hydrostatic pressure. Numerical methodology is employed as described in the previous chapter subsection 2.3.1. The rest of the chapter is structured as follows. Firstly a comparison of numerical and experimental results is shown. Followed by, the influence of creep under monotonic and cyclic loading on salt caverns is discussed. Then the impact of complex, realistic cavern geometries and material heterogeneity inside the geological domain with different material properties and governing equations are elaborated. A detailed sensitivity analysis of all the parameters in the chosen constitutive laws is presented. Lastly, the impact of multi-cavern simulations on stress is studied.

3.2. BOUNDARY CONDITIONS

Table 3.2: Input parameters for simulation of base test case

Parameter	Value	Parameter	Value
Rock salt density [kg/m^3]	2200 [24]	Overburden rock density [kg/m^3]	2200
Rock salt Young's modulus [GPa]	35 [24]	Depth of the top of the salt layer [m]	500
Rock salt Poisson ratio	0.25 [24]	Cavern's radius [m]	25
Roof thickness [m]	200 [11]	Cavern's height [m]	250
Floor thickness [m]	200 [11]	Time step size, [days]	1.5
Cavern volume [1000 m^3]	670	Temperature gradient [C/km]	31.3 [338]
Creep exponent n [-]	3.5 [339]	Creep constant A [Pa^n]	8.10E-27 [339]
Creep activation energy Q [J/mol]	51600 [339]	Number of elements	1960

This chapter presents numerical results of a series of 2D test cases beginning with the benchmarking of the developed simulator, and then to quantify the impact of non-linear time-dependent creep physics. For this study, many test cases are considered: (1) linear elastic deformation under constant load, (2) consistency verification of the linear elastic model, (3) nonlinear (creep) deformation under constant load, (4) nonlinear (creep) deformation under cyclic load, (5) complex heterogeneous model with creep deformation, (6) irregular cavern shape model with and without heterogeneity, (7) real field geometrical data. The input parameters, used for the first 6 test cases, are summarized in Table 3.2. The constants chosen here are obtained from lab-scale experimental data. These constants are used as a base test case for the remaining test cases. However, these constants can vary when energy is stored in the reservoir scale. Then accordingly, these constants have to be scaled considering the sensitivity of the parameter, loading conditions, and local heterogeneities beyond the scope of this work.

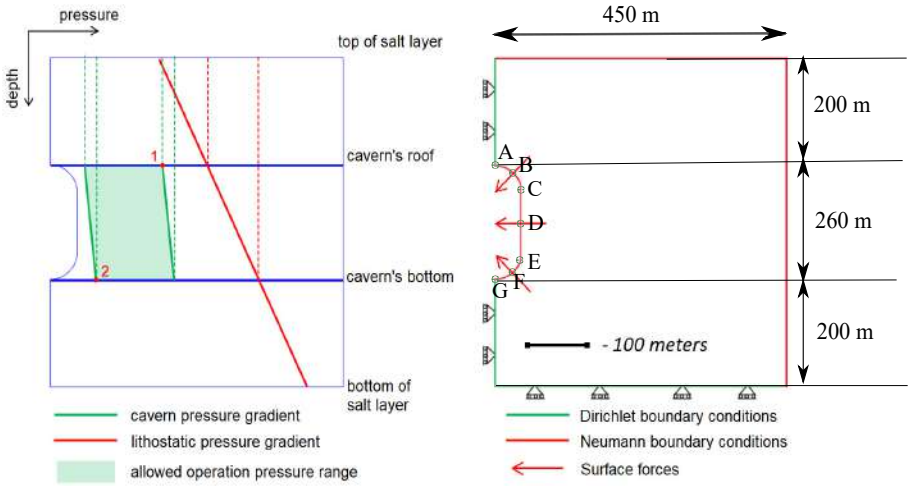

Figure 3.3: Pressure gradients and safe pressure range within the salt domain (left) and implied numerical model boundary conditions (right) for Test Cases 1-6. The dimensions of the geological domain is shown and the depth of the topmost salt layer from the ground is 600 m. Points (A,B,C,D,E,F,G) are located on the caverns wall are depicted to present the results from the numerical simulations.

To reflect real-field loading conditions, the cavern's fluid and lithostatic pressure values are set such that the fluid pressure does not exceed 24% – 80% of lithostatic pressure [11]. The minimum pressure difference between the cavern's fluid pressure and lithostatic pressure will be at the cavern's roof during the injection; and, the maximum will be at the cavern's bottom during production (see points 1 and 2 in the left Fig. 3.3). The cavern's fluid pressure, thus, is a function of the overburden rock density, rock salt density and depth of the roof and the bottom of the cavern. Roller boundary condition was imposed at the bottom and the face along the cavern. Traction free Neumann boundary conditions were imposed on the top and the far end face of the geological domain. This allows to observe any subsidence on the top face or any deformation that can cause in

the far of the geological domain.

The minimum and maximum cavern pressure and corresponding pressure difference are used to calculate the equivalent surface forces acting on the cavern's wall, as shown in Fig. 3.3 (right). The density of hydrogen is employed to compute the forces on the cavern walls. These surface forces are then converted into equivalent nodal forces, which are finally used in the numerical model as input parameters.
Triangular mesh with refinement around the caverns was used for the simulations. A mesh convergence study was also conducted. Consistency and 2nd order accuracy of deformation in the implementation for the elastic domains are confirmed.

3.3. NUMERICAL RESULTS

3.3.1. TEST CASE 1: BENCHMARKING WITH EXPERIMENTS

The computational framework which is developed here is compared with the experimental data. The numerical results were compared with the uniaxial compression experiment for a constant 20 MPa compressive load on the top face. The computational schematic and the comparison of compressive axial deformation u_z between experimental and numerical results are shown in Figure 3.4. The material parameters chosen in the creep constitutive law are shown in Table 3.2. Classical creep methodology is employed in this paper.

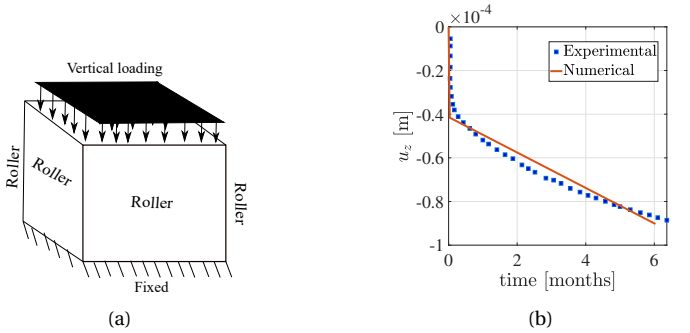

Figure 3.4: Test case 1: Figure 3.4(a) shows the schematic diagram of uniaxial compression experiment. Figure 3.4(b) shows the variation of axial displacement u_z with time for numerical and experimental data of rock salt [13].

The comparison between numerical and experimental results is satisfactory. The numerical results can be further optimised if necessary using optimization algorithms. However, in this work the chosen parameters for the creep constitutive law is obtained from the past literature [339]. Accordingly using these constants, the numerical methodology is validated and further compared with the experiments. All the further numerical experiments are conducted using the parameters from this test case as tabulated in Table 3.2.

3.3.2. TEST CASE 2: CREEP UNDER MONOTONIC LOADING

In this test case, creep under monotonic constant load with respect to time is studied for the chosen parameters as described in Table 3.2. A constant fluid pressure of 20% of lithostatic pressure with respect to time for 275 days is imposed on the caverns. The time-dependent solutions are illustrated in Fig. 3.5, which shows the displacement evolution over time and von Mises stress distribution across the domain. A higher magnitude of displacement is observed around the cavern near larger curvatures at the end of 275 days. This is due to the reason of high-stress accumulation near the curvature causing higher creep deformation. Due to the applied loading, the cavern volume shrinks.

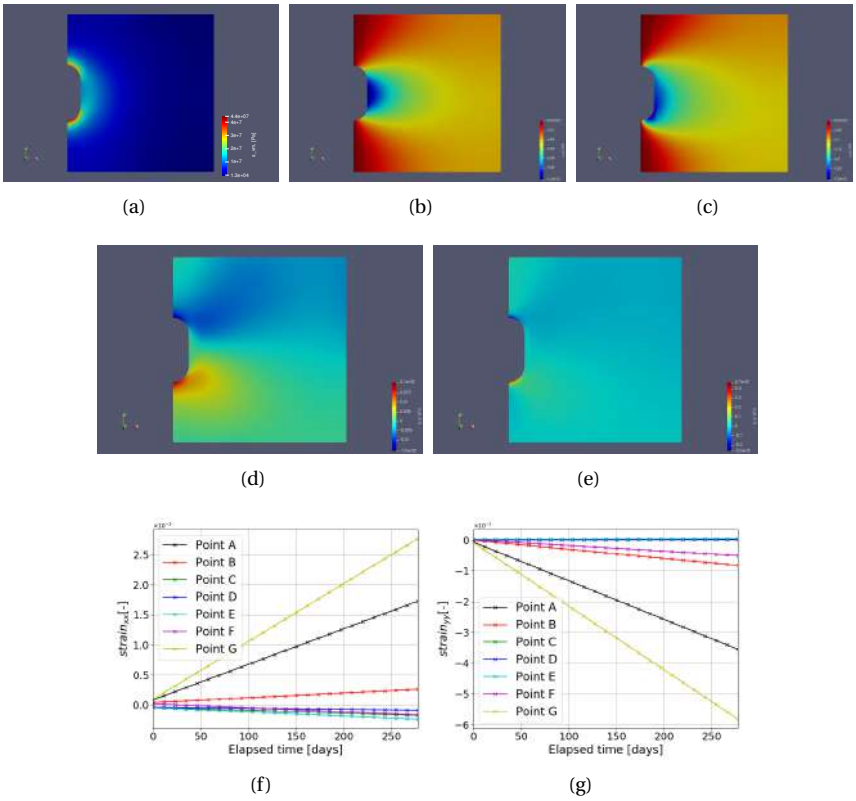

Figure 3.5: **Test Case 2:** Fig. 3.5(a) shows the Von Mises stress distribution. Fig. 3.5(b) shows the horizontal displacement (u_x) at initial time step and Fig. 3.5(c) shows the same after 275 days. Similarly Fig. 3.5(d) and Fig. 3.5(e) show the vertical deformation at initial and final time step respectively. Figure 3.5(f) and Figure 3.5(g) show the variation of strains ($\varepsilon_{xx}, \varepsilon_{yy}$) respectively with time near the cavern at the points as shown in Figure 3.3.

Figure 3.5 also demonstrates the evolution of strain $\varepsilon_{xx}, \varepsilon_{yy}$ and stress σ_{vM} over time, under constant load. Higher rates of strains ($\varepsilon_{xx}, \varepsilon_{yy}$) are observed for points A and B near the cavern roof and floor due to a high-stress distribution caused by low surface

area. Points B and F show slightly lower strain rates. Lastly, the points close to the mid-plane of the domain (C, D, and E) have very low strain rates compared to the rest of the labeled points. This shows that if there are any cracks or heterogeneity near the curvature, there is a higher probability that it will lead to failure than near the mid-plane region. Due to the low permeability of salt caverns, they are considered of best use in storage technology.

3.3.3. TEST CASE 3: CREEP UNDER CYCLIC LOADING

When excess renewable energy is produced, it is converted to green gas and stored in the subsurface. Depending on the supply and demand of the energy, the gas will be injected and produced. This will result in the cyclic loading of salt caverns. This test case addresses the important aspect of energy storage, i.e., the deformation under cyclic loading. For this reason, the cavern's fluid pressure is assumed to be a function of time. Here, a discrete step function is used as shown in Fig. 3.6. The maximum and minimum pressure applied during cyclic loading depends on the lithostatic pressure. It varies between P_{max} = 80% and P_{min} = 20% of lithostatic pressure. Fig. 3.7 shows the variation of horizontal and vertical deformation with time for different points located around the cavern. Horizontal displacement is 0 for points A and G due to the imposed roller boundary conditions as shown in Figure 3.3. The full cycle of the cavern's loading and unloading in this simulation is evaluated for 6 days.

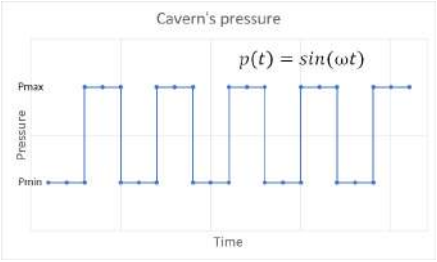

Figure 3.6: **Test Case 3**: This figure shows the step function used to impose time-dependent cyclic fluid pressure inside the cavern that varies between P_{max} = 80% and P_{min} = 20% of lithostatic pressure.

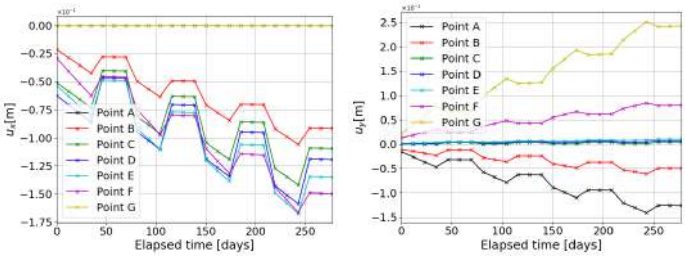

(a) (b)

Figure 3.7: **Test Case 3**: The above plots show the variation of deformation in x (u_x) and y-direction (u_y) over time for different points around the cavern as shown in Figure 3.3.

The high peak values are related to the instantaneous elastic response of the rock salt material, after which there is a short period of creep development with a linear slope representing the magnitude of the creep rate. The higher the load, the steeper the slope and the higher the creep rate. It can be seen that the creep deformation is insignificant at P_{min} compared to P_{max} (zero slope).
From Fig. 3.7(a) it can be seen that the rate of deformation for every cycle is the highest point, F. Followed by the points E, D, C, and B. This trend is observed because of incorporating the lithostatic pressure in the geological domain. So accordingly, highest depth is observed at point F, causing the highest deformation. Similarly, from Fig. 3.7(b) it can be seen that the highest magnitude of vertical deformation is observed at point G, and the next highest magnitude is observed at point A. Although these points are symmetrically placed around the cavern along the x axis mid-plane, unequal vertical deformations are observed due to the lithostatic pressure. Accordingly, the magnitude of deformation reduces from highest stress to lowest stress (in the center point D) with the least curvature. In cyclic load, the loss of volume after 275 days is less than 1.5 %.

3.3.4. TEST CASE 4: CAVERNS WITH IRREGULAR GEOMETRIES

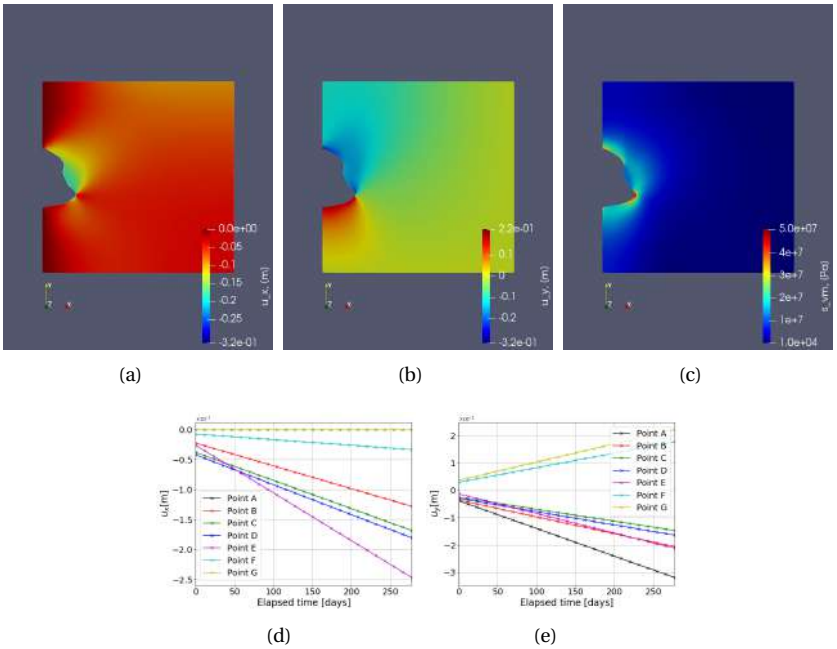

Figure 3.8: **Test Case 4:** Illustration of the horizontal displacement u_x (a), vertical displacement u_y (b), von Mises stress s_{vm} (c) for irregular cavern shape and homogeneous properties. The variation of horizontal (d) and vertical (e) deformations around caverns are also shown, for the marked points in Figure 3.9.

In this test case, irregular-shaped caverns are studied for both homogeneous and heterogeneous domains. Fig. 3.8 shows the simulation results of the model with such an irregular cavern shape. From the figures, it can be seen that the maximum displacement is higher than that of the regular cylindrical-shaped cavern. Note that a larger surface is subject to the force exerted by the pore-fluid pressure fluctuations for irregular shapes. Also, it is noted that–for the shown geometry–the displacement is lower in magnitude at the top and bottom of the cavern when compared with the cylinder-shaped cavern. Point E shows the maximum horizontal deformation in Fig. 3.8(d) at the end of 275 days and also has the highest rate of deformation. This is again due to large stresses at point E with high curvature. Fig. 3.8(e) shows the variation of vertical deformation with time. Since there is no boundary condition imposed on the vertical deformation highest magnitudes of the rate of vertical deformation is seen in Point A and Point G. The potential failure zones in the domain is point around E and the points near the floor and roof of the cavern. Due to the irregular shape of the caverns, the potential local failure zones are more important because of the high-stress zones, which might lead to micro-cracking or lead to damage. When heterogeneity is incorporated, different local properties or constitutive equations can cause different stress distributions in the geological domain leading

to different potential failure zones. This is investigated in the following sections.

3.3.5. TEST CASE 5: HETEROGENEITY OF ELASTIC MATERIAL PROPERTIES

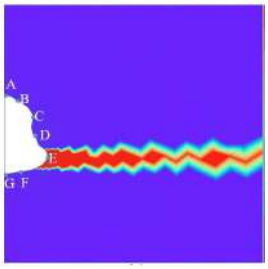

(a)

Figure 3.9: **Test Case 5:** Illustration of the heterogeneous cavern. An interlayer of 100 % impurity (red colour) near the bottom of the cavern, consisting of potash salt. The rest of the geological domain is homogeneous (i.e.,100 % pure halite).

Heterogeneity is incorporated in this work by introducing a potash interlayer within a homogeneous halite rock salt deposit, as shown in Fig. 3.9. Firstly, in this Test Case 5, we allow only elastic parameters to be heterogeneous, while plastic ones remain homogeneous. For this test case, potash Young's modulus and Poisson ratio are chosen to be 2.5 GPa and 0.35, respectively. To allow for significant deformation, these values are chosen in the lower limit of the reported values in the literature [19, 20, 340].

The deformation and von Mises stress fields are shown in Fig. 3.10. The magnitudes of deformation in the x and y directions are comparable. Moreover, it noticeable is that the introduction of the potash interlayer has impacted the stress field and the deformation. For example, point E within the interlayer (i.e., pink line in Fig. 3.10) shows higher deformation compared with the homogeneous test case. However, it shows slower creep rates for heterogeneous case, due to the lower local stress at the location of E. The maximum deformation change due to introducing the heterogeneous potash layer for this test case after 275 days is found to be approximately 9.5 % and 38 % for horizontal and vertical deformation, respectively. This is found by comparing the values of Fig. 3.8 and Fig. 3.10. Note that here, only elastic parameters are considered to be heterogeneous. These results motivate the next test case to investigate the impact of full heterogeneity in both elastic and plastic properties for the potash interlayer.

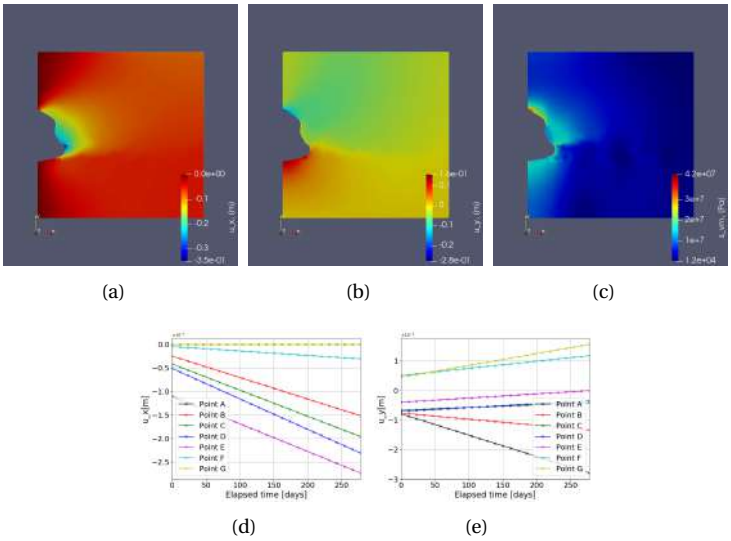

Figure 3.10: **Test Case 5:** illustration of the horizontal displacement u_x (a), vertical displacement u_y (b), von Mises stress s_{vm} (c) for irregular cavern shape model with heterogeneous properties. The variation of horizontal (d) and vertical (e) deformations over time around caverns are also shown for the marked points in Figure 3.9.

3.3.6. TEST CASE 6: HETEROGENEOUS INTERLAYERS

The second, more realistic method is employing different insoluble layers and using their elastic and creep properties. To incorporate heterogeneity in the geological domain surrounding salt caverns, interlayers considering many insoluble impurities (anhydrites, potash salts, shale, gypsum, mudstone, etc.) [332, 335, 336] are included. The detailed composition of rock salt and interlayers can vary depending on the type of region. Experimental analysis needs to be conducted to understand the structure and the lithological composition of the geological domain [332, 341]. In this work, interlayers of different materials are shown in Table 3.3 and are chosen as heterogeneity in the geological domain of halite. The table shows the constitutive parameters of creep formulations for different materials taken from the literature. Considering i) different laboratory conditions, ii) timescales for conducting experiments, ii) water content in the rock samples, iv) different loading conditions, and v) purity of the samples chosen in the literature, these creep constitutive parameters can change depending on the type of application it is being used for instance, in this case, being energy storage. This study becomes very critical given right parameters of the interlayers are chosen. The experiments were conducted for roughly about 500 hrs, and at 70° C for both carnallite and bischofite [19]. This work used these constants due to the lack of other suitable literature for energy storage applications. The creep constants are reduced by three orders of magnitude for both carnallite and bischofite because of the difference in temperature, the experiments are conducted and the current case study because of their temperature dependence from the Arrhenius formulation as shown in [301].

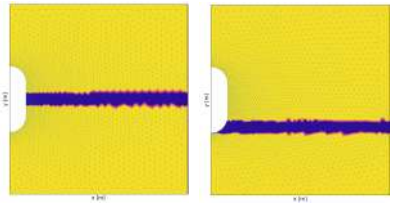

(a) (b)

Figure 3.11: **Test Case 6:** The above contours show the interlayers in the geological domain around a cylindrical cavern. Interlayers are located in the mid strip as shown in Fig. 3.11(a) and near the floor of the cavern as shown in Fig. 3.11(b). Material properties chosen for interlayers are presented in Table 3.3.

Table 3.3: **Test case 6:** Creep formulations of heterogeneity in rock salt [18–20]

Material	Formulation	Youngs modulus	Poisson ratio	n
Carnallite	2.6804e-14 $\times\sigma^5$	17 GPa	0.33	5
Bischofite	1.1e-9$\times\sigma^{4.6}$	18 GPa	0.36	4.6

Fig. 3.11 shows the interlayers in the geological domain. The width of the interlayer is 30m. The interlayers are placed in the two regions near the salt cavern. Fig. 3.11(a) shows the interlayer around the midplane of the cavern. Locally around that interlayer, the curvature is minimum. Fig. 3.11(b) shows the interlayer near the roof of the cavern with the highest curvature and more lithostatic pressure compared to the midplane. The entire simulation was conducted for 50 days. Fig. 3.12 and Fig. 3.13 show various graphs for carnallite and bischofite respectively. Von Mises stress distribution, horizontal deformation at the initial and final time step, and variation of horizontal and vertical deformation with time for points around the cavern as shown in the schematic Fig. 3.3 are shown for both the interlayer distributions. The magnitudes of von Mises stress for both carnallite and bischofite materials are the same. However compared to the homogeneous test case of cylindrical cavern Fig. 3.5(a), the minimum value of stress has reduced and the distribution is not smooth anymore. This is due to the discontinuous distribution of Young's modulus and the magnitudes of Young's modulus of interlayers is lower than halite. Due to this, the magnitudes of horizontal deformation at t=0 are similar as shown in Fig. 3.12(a), Fig. 3.12(e), Fig. 3.13(a) and Fig. 3.13(e). However, the magnitudes of these deformations are higher than the homogeneous test case as shown in Fig. 3.5(b). The deformation magnitude is higher for interlayers in the mid than the interlayer near the floor due to low stress in the central region and low curvature.

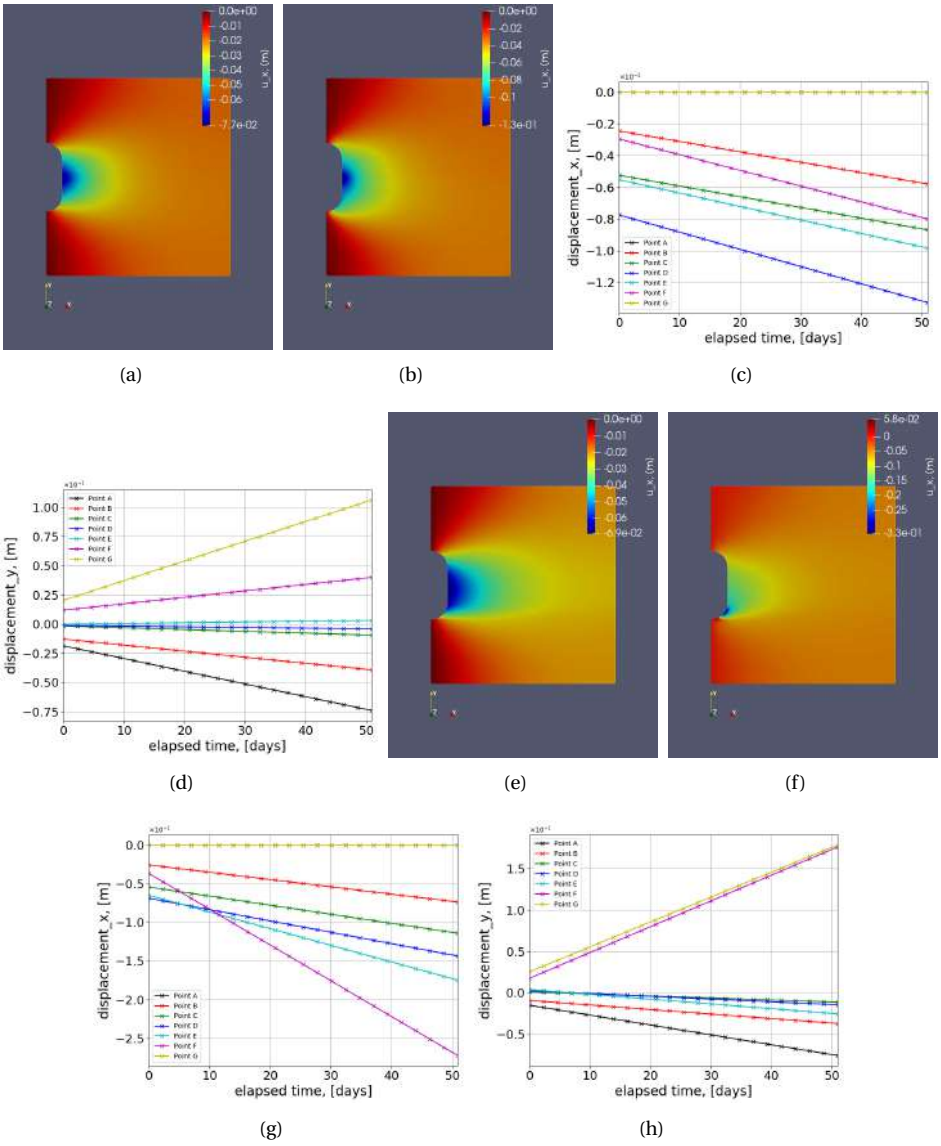

(a) (b) (c)

(d) (e) (f)

(g) (h)

Figure 3.12: **Test Case 6:** illustration of the contours for a heterogeneous domain with an interlayer of Carnallite. Figure 3.12(a) to Fig. 3.12(d) show the contours when the interlayer is in the middle of the vertical dimension. Figure 3.12(e) to Fig. 3.12(h) show the contours when the interlayer is near the floor of the cavern. Figure 3.12(a) and Fig. 3.12(b) show the horizontal deformation distribution at initial and final time steps, respectively. Figure 3.12(e) and Fig. 3.12(f) show the horizontal deformation distribution at initial and final time steps, respectively. Figure 3.12(c), Fig. 3.12(d), Fig. 3.12(g), and Fig. 3.12(h) show the variation of horizontal and vertical deformation with time for a simulation period of 50 days.

When creep is incorporated in these interlayers with separate properties, it's an ad-

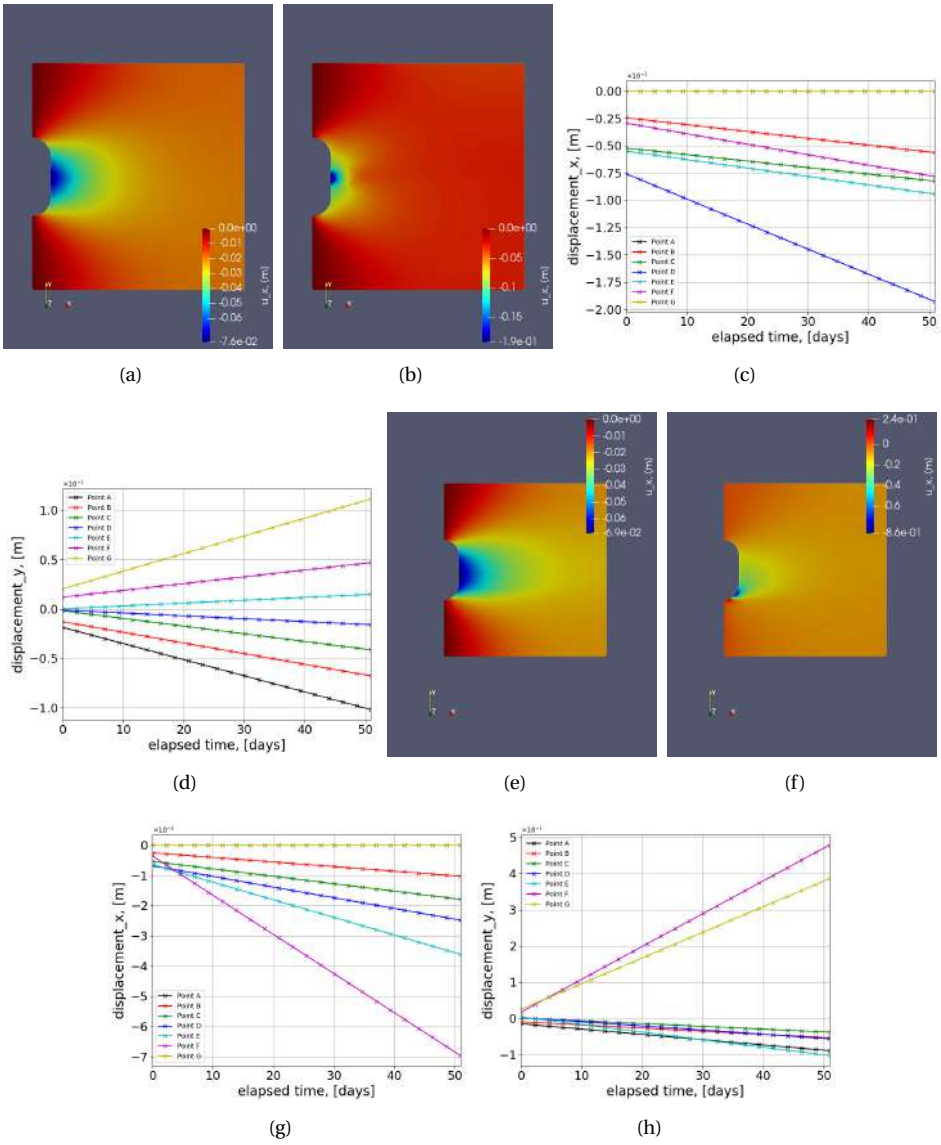

(a) (b) (c)

(d) (e) (f)

(g) (h)

Figure 3.13: **Test Case 6:** illustration of the contours for a heterogeneous domain with an interlayer of Bischofite. Figure 3.13(a) to Fig. 3.13(d) show the contours when the interlayer is in the middle of the vertical dimension. Figure 3.13(e) to Fig. 3.13(h) show the contours when the interlayer is near the floor of the cavern. Figure 3.13(a) and Fig. 3.13(b) show the horizontal deformation distribution at initial and final time-steps, respectively. Figure 3.13(e) and Fig. 3.13(f) show the horizontal deformation distribution at the initial and final time steps, respectively. Figure 3.13(c), Fig. 3.13(d), Fig. 3.13(g), and Fig. 3.13(h) show the variation of horizontal and vertical deformation with time for a simulation period of 50 days.

ditional nonlinear physics that depends on the stress distribution. Fig. 3.12(b), Fig. 3.13(b), Fig. 3.12(f), and Fig. 3.13(f) show the horizontal deformation distribution at the end of the simulation after 50 days when interlayer are incorporated comprising carnallite and bischofite respectively. Due to different stress distributions caused by lithostatic pressure and curvature, the accumulated creep deformation also varies. Fig. 3.12(b) and Fig. 3.13(b) show a similar distribution of deformation due to the same location of heterogeneity; however, the bischofite shows higher deformation magnitudes compared to carnallite. This can be because even though the creep exponent for carnallite is higher than bischofite, the creep constant of bischofite is higher than carnallite by five orders of magnitude. The sensitivity of the creep constant and creep exponent is studied in the later section. Fig. 3.12(f) and Fig. 3.13(f) show the horizontal deformation when the interlayer is located near the floor of the cavern. Qualitatively, they look similar; however, the interlayer with bischofite shows higher horizontal deformation than the carnallite test case and a homogeneous test case.
Fig. 3.12(c), Fig. 3.12(d), Fig. 3.12(g), and Fig. 3.12(h) show the variation of horizontal and vertical deformation with time at different points as shown in the schematic for carnallite interlayers. Fig. 3.13(c), Fig. 3.13(d), Fig. 3.13(g), and Fig. 3.13(h) show the variation of horizontal and vertical deformation with time at different points as shown in the schematic for bischofite interlayers. Compared to the homogeneous test case as shown in Fig. 3.5, the horizontal deformation plots for each point are more widely spread when the interlayer is in the midplane. However, when the interlayer is near the floor, Point F shows a much steeper slope than the rest of the points. This shows that given a local heterogeneity in the domain, a large amount of deformation could occur, causing the failure of the salt cavern. In the vertical deformation, the plots are magnified proportionately compared to homogeneous test cases where the magnitude is higher but the distribution looks similar when the interlayer is the midplane. When the interlayer is near the cavern floor, the magnitude of vertical deformation at point F with high curvature and heterogeneity has a higher rate of increase in deformation than a homogeneous test case. The maximum increase in percentage for horizontal and vertical deformation in the geological domain when compared to homogeneous test case (fig. 3.5) after 50 days of simulation is shown in Table 3.5.

Table 3.5: Maximum percentage increase in deformation when interlayers are incorporated when compared to homogeneous test case after 50 days

Interlayer	u_x	u_y
Midplane-carnallite	44.4%	12%
Floor-carnallite	200 %	75 %
Midplane-bischofite	111 %	20 %
Floor-bischofite	677 %	380 %

The percentages are higher for bischofite material compared to carnallite. When the interlayers are present near the cavern floor, a higher increase in deformation is observed than the mid-plane interlayer. Also, the percentage increased for both the deformations when the creep properties are incorporated to study heterogeneity is much higher than when only elastic properties are included, as shown in the previous test case. Consider-

ing the chosen creep parameters are in the realistic range, the results from this section clearly show that interlayers can fail the cavern locally around the cavern.

3.3.7. TEST CASE 7: REAL FIELD TEST CASE

Using the field data on cavern shape from echo logs of a salt cavern in Germany [308], a cross-section of the modeled cavern was generated to be used in the developed simulator. The test case simulation results are shown in Fig. 3.14. The computed displacement distribution, the simulation output, has a similar distribution to the cylinder-shaped cavern. Due to the increased lithostatic pressure, the maximum horizontal deformation is just below the midplane of the cavern. While the maximum horizontal deformation appears at the cavern roof, lower deformation values are predicted due to the Dirichlet boundary conditions along the bottom boundary. This simulation was run for two years.

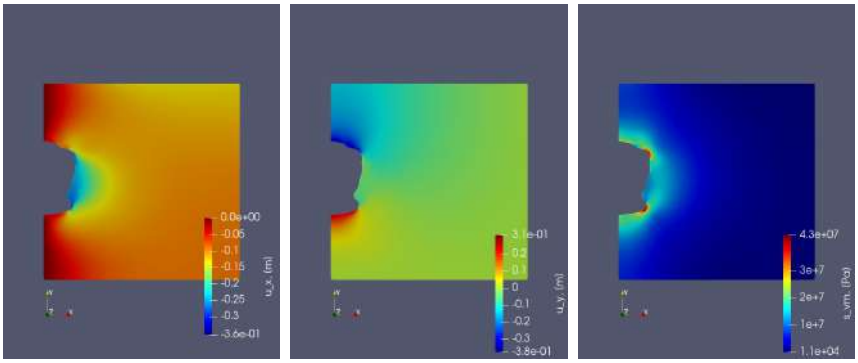

(a) (b) (c)

Figure 3.14: **Test Case 7:** The above contours show the horizontal displacement (Fig. 3.14(a)), vertical displacement (Fig. 3.14(b)) and von Mises stress (Fig. 3.14(c)) for real field cavern shape model. The simulation was run for a period of 2 years.

3.3.8. MULTI-CAVERN SIMULATIONS

Salt cavern size is limited by mechanical stability and the salt formation they are built. Storage volume can range from 10,000 m^3 to 1,880,000 m^3 [342]. To put it into perspective, the Groningen gas field in the Netherlands has a storage volume of approximately 2 billion m^3 [343]. As the need for large-scale energy storage increases, it is important to develop systems of multiple salt caverns. However, the interaction between adjacent caverns must be carefully considered.

Multi-cavern simulations are helpful when more than one cavern can be used close to each other in the geological domain for subsurface energy storage. Cavern-to-cavern distance (CTC) between the caverns is critical to understand the influence of each cavern on the other. In this study, multi-cavern simulation studies were conducted for regular and irregular-shaped caverns. CTC is the minimum cavern-to-cavern distance possible in the geological domain. CTC for a regular cylindrical-shaped cavern is shown in Figure

3.17(a). Roller boundary conditions were imposed along the caverns and traction-free boundary conditions on the top plane.
Multi-cavern simulations for regular-shaped caverns showing von Mises stress and deformation (u_y) are shown in Figure 3.15. Figure 3.16 shows the same for irregular-shaped caverns. It can be seen that as the distance between the caverns reduces, causing an increase in Von-mises stress. These simulations can be used when there is heterogeneity in the geological domain which can handle less stress. Accordingly, Drucker Prager or Von Mises failure criteria could be used to determine how critical the distance is between the caverns [344].

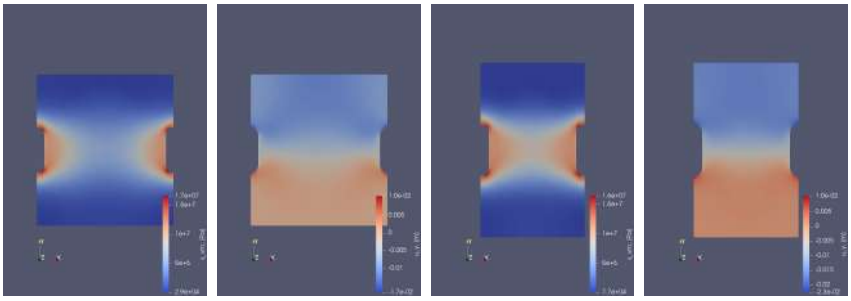

(a) (b) (c) (d)

Figure 3.15: **Multi-cavern simulation**: The above contours show the vertical displacement and von Mises stress for regular cylindrical shaped cavern after 275 days. Fig. 3.15(a) and Fig. 3.15(b) show the von Mises stress and vertical deformation for CTC = 320m respectively. Fig. 3.15(c) and Fig. 3.15(d) show the von Mises stress and vertical deformation for CTC = 200m respectively.

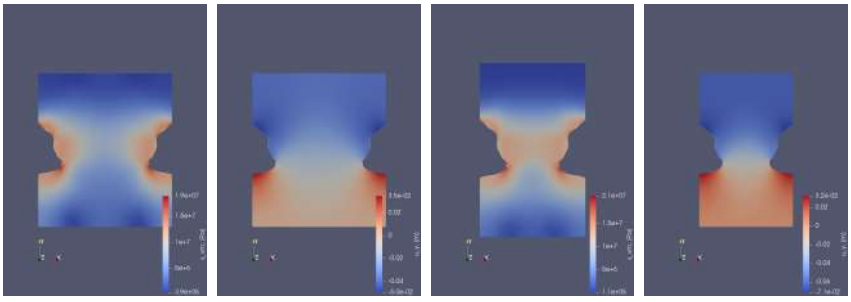

(a) (b) (c) (d)

Figure 3.16: **Multi-cavern simulation**: Illustration of the vertical displacement and von Mises stress for irregular shaped cavern after 275 days. Fig. 3.16(a) and Fig. 3.16(b) show the von Mises stress and vertical deformation for CTC = 200m respectively. Fig. 3.16(c) and Fig. 3.16(d) show the von Mises stress and vertical deformation for CTC = 140m, respectively.

Vertical deformation (u_y) is compared here since traction-free boundary conditions are applied on the top face. It can be seen that the closer the caverns it higher the vertical

deformation is observed. When the caverns have complex geometry, the magnitude of the Von- Mises stress s_{vm} and vertical deformation is higher. This could lead to subsidence [24] in the geological domain or could amplify seismicity.
Figure 3.17 shows the variation of von Mises stress along the horizontal distance in the mid-plane section for regularly shaped caverns and the minimum distance (CTC plane) for complex-shaped caverns. CTC_{mp} test case shows the variation of von Mises stress at the mid-plane section of the irregular-shaped cavern. Here from Figure 3.17(b) it can be seen that the von Mises stress distribution is more uniform similar to the Gaussian distribution. As CTC reduces, the minimum stress in the center of the homogeneous geological domain increases. Regularly-shaped caverns have minimum surface area due to their smooth surfaces. Hence, there is no higher stress observed near the cavern walls. The stress reduces slowly from peak stress closer to the cavern and drops to a minimum value near the central vertical plane of the geological domain.
From Fig. 3.17(c), it can be seen that the stress distribution at the center is more spread out, and closer to the cavern, it peaks out. This is due to the irregular shape. From the curve representing CTC_{mp}, it can be seen that the stress increases at first and then reduces again. This is because this section is not the closest distance from the adjacent cavern and not the surface with the most curvature.

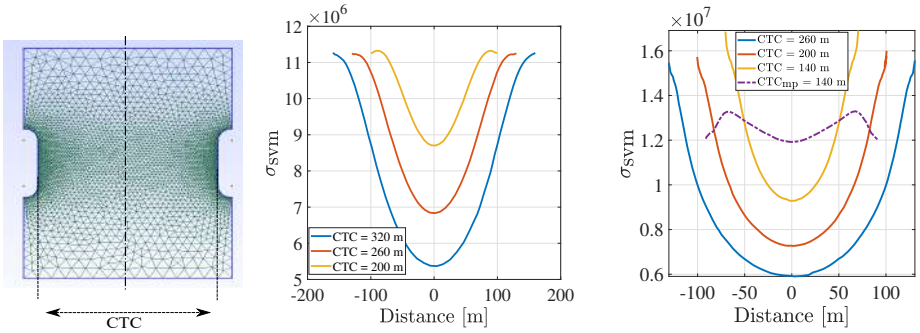

Figure 3.17: **Multi-cavern simulation**: Fig. 3.17(a) shows the example of computational mesh showing cavern to cavern distance (CTC) for regular shaped cavern. Fig. 3.17(b) shows the variation of von Mises stress with stress for regular shaped caverns at different CTC. Fig. 3.17(c) shows the variation of von Mises stress with stress for irregular shaped caverns at different CTC.

3.4. CONCLUSION

In this work, the influence of complex shapes and material heterogeneity in the geological domain on salt caverns employed for energy storage technology is studied using a 2D finite element solver. The secondary (i.e., steady-state) creep behavior is introduced in the mathematical model based on power law, and the power-law parameters were taken from the work of Carter et al. [339]. The numerical methodology and the chosen creep constitutive constants are compared with the experimental data. The developed simulator allowed for both explicit and implicit time integration schemes. After the con-

sistency check and benchmarking with the experimental data, Various conclusions can be derived from this work.
1) It is evident from the above results that creep is a slow phenomenon of insignificant magnitude compared to the elastic component for year-long operations. This justifies the present strategy of omitting the low-stress creep mechanism of pressure solution from the current analysis. However, on a scale of several years with a significant amount of heterogeneity, the effect of creep strains on the deformation and stresses can become evident, which would eventually cause the material to reach the tertiary stage leading to failure at zones of critical stress intensity. Less than five % volume changes in the cavern were observed considering cylindrical homogeneous caverns after 275 days.
2) The role of heterogeneity by considering only different elastic parameters is showed for irregular-shaped caverns. Depending on the type of impurity (potash, halite), the location of impurity in the domain, and the type of distribution imposed in the geological model, stress and deformation distributions vary.
3) When heterogeneous interlayers are incorporated in the simulation model with the right constitutive models for the composition, a much higher increase in deformation is observed locally and around the cavern than the homogeneous test case and the heterogeneous test case without considering creep properties (test case 5). In general, bischofite showed higher creep deformations compared to carnallite. When the interlayers are located near the high curvature region, that region has the highest potential to be a failure zone.
4) The influence of curvature of the caverns was studied in this work for both with and without heterogeneity. Interlayers near the high curvature showed at least five times more deformation than interlayers located near the minimum curvature. 5) A detailed sensitivity analysis of various parameters shows their influence on the deformation, which can gauge the deformation in real field test cases.
6) Multi-cavern simulations were critical to understanding the significance of CTC, the irregular shape of the caverns on the stress distributions in the geological domain.

The role of additional creep mechanisms such as pressure solution and uncertainties in dislocation creep parameters will be considered in the future, also the effects of gas (hydrogen or green methane) permeation on damage development in the cavern wall. Future work involves including thermal and (visco)plastic strains to allow for more reliable simulations and sensitivity analyses. Since the field test cases are large-scale of the order (km), efficient formulations such as multi-scale formulation would be developed to reduce the computational costs. Further research would be required to benchmark the tertiary creep model with lab and field data. Other heterogeneous interlayers such as shale rocks need to be studied considering the right creep constitutive laws and underlying physics are chosen.

4

NUMERICAL INVESTIGATION OF INELASTIC DEFORMATION

Summary: *Subsurface geological formations can be utilized to safely store large-scale (TWh) renewable energy in the form of green gases such as hydrogen. Successful implementation of this technology involves estimating feasible storage sites, including rigorous mechanical safety analyses. Geological formations are often highly heterogeneous and entail complex nonlinear inelastic rock deformation physics when utilized for cyclic energy storage. In this chapter, the behavior of sandstone rock is understood under cyclic loading. From the modeling perspectives, five types of deformation mechanisms were identified based on the governing physics: elastic, viscoelastic, compaction-based cyclic inelastic, inelastic brittle creep, and dilatation-based inelastic deformation. To model elastic, viscoelastic, and brittle creep, the Nishihara model was used. A cyclic modified cam clay model (MCC) and hardening–softening model were applied to capture plastic deformation. Next, we present a novel scalable computational framework to analyse the impact of nonlinear deformation of porous reservoirs under cyclic loading. The proposed methodology includes three different time-dependent nonlinear constitutive models to appropriately describe the behavior of sandstone, shale rock, and salt rock. These constitutive models are studied and benchmarked against both numerical and experimental results in the literature. An implicit time-integration scheme is developed to preserve the stability of the simulation. In order to ensure its scalability, the numerical strategy adopts a multiscale finite element formulation, in which coarse scale systems with locally-computed basis functions are constructed and solved. Lastly, the Bergermeer test case—an active Dutch natural gas storage field—is studied to investigate the influence of inelastic deformation on the uplift caused by cyclic injection and production of gas. The present study shows acceptable subsidence predictions in this field-scale test, once the properties of the finite element representative elementary volumes are tuned with the experimental data.*

Parts of this are published in Naderloo et al. Journal of Energy Storage 2023, Ramesh Kumar et al. Scientific Reports 2022

Subsurface storage technology is based on the injection and production of energy-rich fluids into underground reservoirs depending on the demand and supply [41, 69], resulting in cyclic loading. Thus, the reservoir experiences cyclic changes in porous pressure and temperature. As a result, the in-situ effective stresses are altered accordingly, which influences the stress conditions on the reservoir rock and surrounding elements, such as caprock, faults, and wells [70–74]. For instance, a decrease or increase in fluid pressure can induce fault reactivation and seismicity (earthquakes) by perturbing the stress path [75, 76]. The pressure fluctuation during storage can also induce subsidence, which damages the infrastructures nearby [77, 78]. Therefore, it is essential to understand about deformation behavior of sandstone reservoirs and the effect of all the different injection/depletion-related parameters, including amplitude and frequency of cycles, to reduce the risk of delaying projects and optimize the utility of the energy storage operations [345].

Several forms of constitutive models have been taken into account for various types of rocks in the literature, including rock salt [167, 346] and generalized models for brittle rocks [121]. Models such as the Maxwell model, the Kelvin-Voigt model, and the Fractional Maxwell model, attempt to consider the viscoelastic strain in rocks [99, 100]. The time-dependent plastic creep strain is modeled using a power law for rock-salt, brittle porous rocks [107, 113, 114] and also modelled using viscoplastic deformation where the plastic strain starts accumulating above a certain stress level [10, 110–112]. Lastly, in a generalized form for soil and rocks, the time-independent plastic strain has been considered [101–103, 105–108, 347]. Recently Modified Cam Clay model (MCC) [102] was employed to explain the inelastic deformation of sandstone below the brittle yield point [106]. However, there are very few attempts by researchers trying to quantify all the deformations observed in different stress regimes under cyclic loading on sandstone. Relevant constitutive models are presented in Table 1.1.

In section 4.1, the mechanical behavior of sandstone is studied using constitutive models. The deformation and acoustic emissions (AE) obtained from cyclic experiments of porous red felser sandstone are used to compare and calibrate with the constitutive models. The porosity and density of the samples are 2.1 ± 0.015 g/cm^3 and 21.14 ± 0.7 %. The details regarding the experiments can be found in [27]. In section 4.2, the governing equations employed to model sandstone using FEM formulation are elaborated. The inelastic deformations, namely creep, viscoplasticity, and plasticity, as well as the main ingredients of the MCC model, are further discussed. In section 4.3, in addition to the finite element formulation, the implementation of the combined inelastic models is described in detail. Once the discretized equations are obtained for the fine-scale grid, the multiscale (MS) strategy is employed as presented in section 2.4 to obtain the coarse grid algebraic equations. Finally, numerical experiments are carried out in section 4.4, after which the conclusions are drawn in section 4.5.

4.1. MECHANICAL BEHAVIOR OF SANDSTONE

Many experimental researchers have identified the mechanical behavior and deformation process of sandstone subjecting to conventional deviatoric testing [348–352]. This behavior is normally represented in terms of mean effective stress versus total poros-

ity reduction or deviatoric stress versus axial deformation [353, 354]. As shown in Figure 4.1, the four stages of the Red Felser sandstone deformation up to reaching maximum strength are as follows [106, 355]:

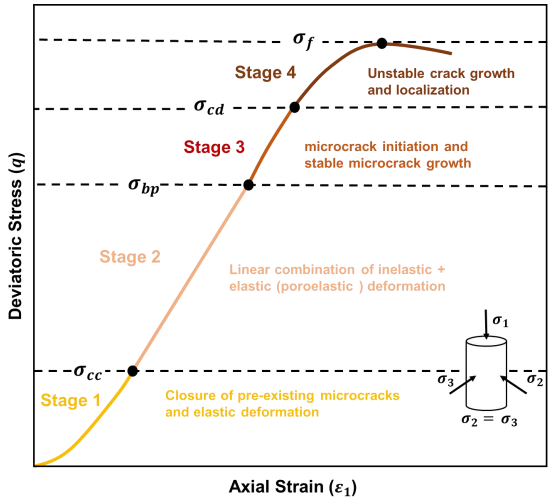

Figure 4.1: Stress-strain curve showing deformation stages of Red Felser sandstone under the condition of constant confining pressure (10 MPa). The four stages of stress levels are: the initial crack closure ($\boldsymbol{\sigma}_{cc}$), brittle yield point stress ($\boldsymbol{\sigma}_{bp}$), crack damage stress ($\boldsymbol{\sigma}_{cd}$) and maximum strength ($\boldsymbol{\sigma}_f$).

- Stage 1 (from the start to $\boldsymbol{\sigma}_{cc}$): A non-linear behavior that reflects the closure of pre-existing cracks or damage alongside poro-elastic deformation.
- Stage 2 (from $\boldsymbol{\sigma}_{cc}$ to $\boldsymbol{\sigma}_{bp}$): Near-linear behavior of sandstone which is known as purely elastic (poroelastic) deformation.
- Stage 3 (from $\boldsymbol{\sigma}_{bp}$ to $\boldsymbol{\sigma}_{cd}$): The deformation shows non-linear behavior due to the initiation of new microcracks and stable crack growth.
- Stage 4 (from $\boldsymbol{\sigma}_{cd}$ to $\boldsymbol{\sigma}_f$): The concave-down behavior in this regime is attributed to the onset of grain crushing, unstable crack growth, and shear crack localization.

Among different stages of deformation, stage 2 and the early part of stage 3 are important from an energy storage perspective. This is because all the energy storage systems should be operated below the yield point and within a safe zone to avoid failure and accumulation of inelastic deformation.

4.1.1. CONSTITUTIVE LAW FORMULATION

Based on several experiments and observed physics, different deformation mechanisms were employed, and accordingly, the total strain ($\boldsymbol{\varepsilon}^{\mathrm{t}}$) is split into elastic strain $\boldsymbol{\varepsilon}^{\mathrm{e}}$, plastic strain $\boldsymbol{\varepsilon}^{\mathrm{p}}$, visco-elastic strain $\boldsymbol{\varepsilon}^{\mathrm{ve}}$ and creep strain $\boldsymbol{\varepsilon}^{\mathrm{cr}}$ as

$$\boldsymbol{\varepsilon}^{\mathrm{t}} = \boldsymbol{\varepsilon}^{\mathrm{e}} + \boldsymbol{\varepsilon}^{\mathrm{p}} + \boldsymbol{\varepsilon}^{\mathrm{ve}} + \boldsymbol{\varepsilon}^{\mathrm{cr}}. \tag{4.1}$$

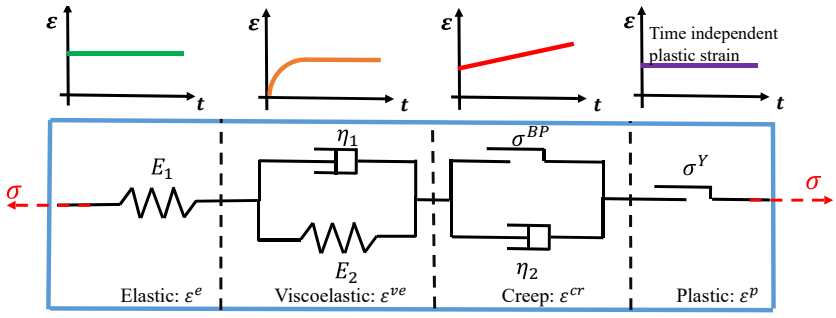

Figure 4.2: Schematic illustration of the constitutive model when a constant load is applied.

Schematic illustration of the numerical model is shown in Figure 4.2.The elastic strain based on Hooke's law is given by,

$$\boldsymbol{\varepsilon}^{\mathrm{e}} = \frac{q}{E_1}. \tag{4.2}$$

Here q is the deviatoric stress, E_1 is the elastic Young's modulus. The viscoelastic strain is the time dependent elastic strain which is given by

$$\boldsymbol{\varepsilon}^{\mathrm{ve}} = \frac{q}{E_2}\left(1 - \exp\left(\frac{-E_2}{\eta_1}t\right)\right). \tag{4.3}$$

Here E_2, η_1 are the Young's modulus and viscosity of the viscoelastic unit. The creep strain is inelastic strain which is time-dependent that is given by

$$\boldsymbol{\varepsilon}^{\mathrm{cr}} = \left(\frac{\sigma_1 - \sigma^{BP}}{\eta_2}\right)t. \tag{4.4}$$

Here σ^{BP} is the brittle yield point and η_2 is the viscosity of the brittle creep unit. Finally, the plastic strain is split into two components based on the mechanisms which are given by

$$\boldsymbol{\varepsilon}^{\mathrm{p}} = \boldsymbol{\varepsilon}^{\mathrm{p}}_{\mathrm{compaction}} + \boldsymbol{\varepsilon}^{\mathrm{p}}_{\mathrm{dilation}}. \tag{4.5}$$

To compute $\boldsymbol{\varepsilon}^{\mathrm{p}}_{\mathrm{compaction}}$ Modified Cam Clay model (MCC) [356] and for $\boldsymbol{\varepsilon}^{\mathrm{p}}_{\mathrm{dilation}}$ hardening softening model was used [101]. Finally, the total strain in the rock is given based on the brittle yield point, i.e.,

$$\boldsymbol{\varepsilon}^{\mathrm{t}} = \begin{cases} \frac{q}{E_1} + \frac{q}{E_2}(1 - \mathrm{e}^{-\frac{E_2}{\eta_1}t}) + f_1(q, \alpha_i) & \sigma_1 < \text{Brittle yield point} \\ \frac{q}{E_1} + \frac{q}{E_2}(1 - \mathrm{e}^{-\frac{E_2}{\eta_1}t}) + \frac{\sigma_1 - \sigma^{BP}}{\eta_2}t + f_2(q, \beta_i) & \sigma_1 > \text{Brittle yield point} \end{cases} \tag{4.6}$$

In the following subsections, the plasticity models are elaborated.

4.1.2. MODIFIED CAM CLAY MODEL

The MCC model uses a yield surface that determines whether rocks behave in an elastic or plastic behavior. The critical components are shown in the schematic Figure 4.3. This model has been used to account for inter-granular cracking, clay crushing, and grain sliding, which takes place below the brittle yield point [106].

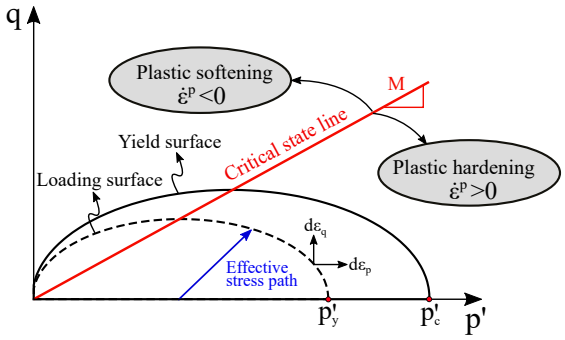

Figure 4.3: The illustration shows the schematic of the MCC model in the stress space. It indicates how the yield surface develops, depending on the effective stress path, highlighting the plastic hardening (below the CSL) and the plastic softening region (above the CSL).

In this work, the MCC model is extended to account for cyclic inelastic compaction inspired by the work done by [102]. The yield function is given by

$$f = q^2 - M^2(p(p_c - p)). \tag{4.7}$$

Here M is the slope of the critical state line, p_c is the pre-consolidation pressure, and p is the volumetric stress. The pre-consolidation pressure is expressed as

$$\frac{\delta p_c}{p_c} = \frac{\delta p_l}{p_l}. \tag{4.8}$$

Here p_l is the loading parameter derived from the yield surface envelope, which is

$$p_l = p + \frac{q}{M}^2 \left(\frac{1}{p}\right). \tag{4.9}$$

The plastic strain is computed from the consistency condition by normalizing the stresses [357, 358]. The change in void ratio is given by

$$de = -(1+e) \times \boldsymbol{\varepsilon}^{\mathrm{p}}_p. \tag{4.10}$$

The volumetric and deviatoric parts of the incremental plastic strain is given by

$$\begin{bmatrix} \Delta\boldsymbol{\varepsilon}^{\mathrm{p}}_p \\ \Delta\boldsymbol{\varepsilon}^{\mathrm{p}}_q \end{bmatrix} = \Omega \times \begin{bmatrix} M^2 - \eta & 2\eta \\ 2\eta & \frac{2\eta}{M^2 - \eta^2} \end{bmatrix} \times \begin{bmatrix} dp \\ dq \end{bmatrix}. \tag{4.11}$$

Here,

$$\Omega = \frac{\lambda_{MCC} - \kappa}{(1+e)\,p(M^2+\eta^2)} \tag{4.12}$$

in which

$$\kappa = \frac{1+e}{K} \tag{4.13}$$

and

$$K = \frac{E_{avg}}{3\,(1-2\upsilon)}. \tag{4.14}$$

Furthermore, $\eta = q/p$, $e = \phi/1-\phi$, ϕ is the porosity, and e is the void ratio. For a detailed derivation, refer to the literature [357, 358]. Also, here dp and dq are the incremental volumetric stress and deviatoric stress, respectively. To account for the cyclic part of the inelastic strains, θ is the parameter employed which accounts for the cyclic element of the MCC model Equation 4.8, which is given by

$$\frac{\delta p_c}{p_c} = \theta \frac{\delta p_l}{p_l}. \tag{4.15}$$

$$p_c^{new} = p_c^{old}\left(\frac{p_l^{max}}{p_c^{old}}\right)^{\theta} \tag{4.16}$$

So this ensures that a new pre-consolidation parameter p_c^{new} is established cycle after cycle. The evolution of the pre-consolidation parameter is ruled by equation 4.15 and equation 4.16 after integration. This p_c^{new} is lower than p_l^{max} but as the number of cycles increases p_c^{new} tends to the value of p_l^{max}. If θ is equal to 1, the model reduces to the standard MCC. This proposal is inspired by the work of [102], which dealt with the deformation of clays under cyclic loadings. So from this model, plastic strain from $\boldsymbol{\varepsilon}^{\mathrm{p}}_{\mathrm{compaction}}$ is computed.

4.1.3. HARDENING SOFTENING MODEL

The hardening-softening model is employed to model the plastic strains induced by the fracturing of the grains above the brittle yield point. The model is explained briefly here, and for a deeper understanding, the reader is referred to [101, 104]. The model for triaxial conditions ($\sigma_3 = \sigma_2$) is based on Coulomb-Mohrs yield surfaces f_1 and f_2 (equations 4.17 and 4.18), which is given by

$$f_1 = \frac{1}{2}(\sigma_3 - \sigma_1) + \frac{1}{2}(\sigma_1 + \sigma_3)\sin(\phi_f) - c \times \cos(\phi_f) = 0 \tag{4.17}$$

$$f_2 = \frac{1}{2}(\sigma_2 - \sigma_1) + \frac{1}{2}(\sigma_1 + \sigma_2)\sin(\phi_f) - c \times \cos(\phi_f) = 0. \tag{4.18}$$

Here c is the cohesion of the rock and ϕ_f is the internal friction angle. Similar surfaces are defined for the plastic potential flow, as can be seen in equations 4.19 and 4.20

$$g_1 = \frac{1}{2}(\sigma_3 - \sigma_1) + \frac{1}{2}(\sigma_1 + \sigma_3)\sin(\psi) + \text{constant} \tag{4.19}$$

$$g_2 = \frac{1}{2}(\sigma_2 - \sigma_1) + \frac{1}{2}(\sigma_1 + \sigma_2)\sin(\psi) + \text{constant}. \tag{4.20}$$

Here ψ is the dilation angle. These plastic potential functions (g_1 and g_2) are responsible for the magnitude of the plastic strain increments $\dot{\boldsymbol{\varepsilon}}^p$, as can be seen in the general plasticity rule depicted by equation 4.21 as well as in equations 4.22 and 4.23 for axial and volumetric plastic strains respectively. The rate of plastic strain is given by

$$\dot{\boldsymbol{\varepsilon}}^p = \lambda_1 \frac{\partial g_1}{\partial \boldsymbol{\sigma}} + \lambda_2 \frac{\partial g_2}{\partial \boldsymbol{\sigma}} \tag{4.21}$$

$$\dot{\varepsilon}_1^p = \frac{1}{2}(\lambda_1 + \lambda_2)(-1 + \sin(\psi)) \tag{4.22}$$

$$\dot{\varepsilon}_v^p = (\lambda_1 + \lambda_2)\sin(\psi). \tag{4.23}$$

The plastic multipliers are computed using the below expressions which are obtained from [104], given by

$$\lambda_1 = \frac{\mu_4 \left(\frac{\partial f_1}{\partial \boldsymbol{\sigma}}\right)^T \mathbb{D}\dot{\boldsymbol{\varepsilon}} - \mu_2 \left(\frac{\partial f_2}{\partial \boldsymbol{\sigma}}\right)^T \mathbb{D}\dot{\boldsymbol{\varepsilon}}}{\mu_1\mu_4 - \mu_2\mu_3} \tag{4.24}$$

$$\lambda_2 = \frac{\mu_1 \left(\frac{\partial f_2}{\partial \boldsymbol{\sigma}}\right)^T \mathbb{D}\dot{\boldsymbol{\varepsilon}} - \mu_3 \left(\frac{\partial f_1}{\partial \boldsymbol{\sigma}}\right)^T \mathbb{D}\dot{\boldsymbol{\varepsilon}}}{\mu_1\mu_4 - \mu_2\mu_3}. \tag{4.25}$$

Where μ_1,μ_2,μ_3 and μ_4 are define as:

$$\mu_1 = \left(-\frac{\partial f_1}{\partial \overline{\varepsilon}^p}\frac{\partial \overline{\varepsilon}^p}{\partial \boldsymbol{\varepsilon}^p} + \mathbb{D}\frac{\partial f_1}{\partial \boldsymbol{\sigma}}\right)^T \frac{\partial g_1}{\partial \boldsymbol{\sigma}} \tag{4.26}$$

$$\mu_2 = \left(-\frac{\partial f_1}{\partial \overline{\varepsilon}^p}\frac{\partial \overline{\varepsilon}^p}{\partial \boldsymbol{\varepsilon}^p} + \mathbb{D}\frac{\partial f_1}{\partial \boldsymbol{\sigma}}\right)^T \frac{\partial g_2}{\partial \boldsymbol{\sigma}} \tag{4.27}$$

$$\mu_3 = \left(-\frac{\partial f_2}{\partial \overline{\varepsilon}^p}\frac{\partial \overline{\varepsilon}^p}{\partial \boldsymbol{\varepsilon}^p} + \mathbb{D}\frac{\partial f_2}{\partial \boldsymbol{\sigma}}\right)^T \frac{\partial g_1}{\partial \sigma} \tag{4.28}$$

$$\mu_4 = \left(-\frac{\partial f_2}{\partial \overline{\boldsymbol{\varepsilon}}^p}\frac{\partial \overline{\varepsilon}^p}{\partial \boldsymbol{\varepsilon}^p} + \mathbb{D}\frac{\partial f_2}{\partial \boldsymbol{\sigma}}\right)^T \frac{\partial g_2}{\partial \boldsymbol{\sigma}}. \tag{4.29}$$

$\mathbb{D}$ is the elasticity matrix, and the hardening parameter $\overline{\varepsilon}^p$ is given by

$$\overline{\varepsilon}^p = \int \sqrt{\frac{2}{3}(\dot{\varepsilon}_1^p\dot{\varepsilon}_1^p + \dot{\varepsilon}_2^p\dot{\varepsilon}_2^p + \dot{\varepsilon}_3^p\dot{\varepsilon}_3^p)}\,dt. \tag{4.30}$$

Detailed explanation about this work is elaborated in [101, 104].

4.1.4. BENCHMARKING WITH CONSTITUTIVE MODELS

4.1.5. BELOW BRITTLE YIELD POINT

Firstly, the constitutive laws are calibrated with the first cycle and further they are compared with the experimental results in the remaining cycles. Experimentally it was found that the apparent inelastic strain (viscoelastic + inelastic) is directly proportional to the AE (Acoustic Emissions). Based on this observation, the number of recorded AE events for every cycle and only the estimate of inelastic strain from AE events is correlated by using a direct proportionality. Using normalized AE, the estimate of inelastic strain for each cycle is given by

$$\varepsilon_1^{Inelastic,i} = \frac{AE_i}{AE_{\text{Total}}} \times \varepsilon_{Total}^{Inelastic}. \tag{4.31}$$

Here AE_{Total} is the total number of AE events during stress cycling, AE_i is the number of AE events recorded at each cycle 'i' and $\varepsilon_{Total}^{Inelastic}$ is the total inelastic strain from the experiments. Young's modulus of the rock (elastic and viscoelastic) was initially calibrated with the first cycle of each experiment. Then, the MCC model parameters were fine-tuned using the inelastic strain from the first cycle. Using these parameters, the experimental results are compared with the analytical solutions.

Table 4.1 shows the parameters employed for the three frequencies at an amplitude of 20 MPa. Figures 4.4(a) and 4.4(c) show the variation of axial strain with time for experimental and modeling results for frequencies 0.0014 Hz and 0.0002 Hz. The modeling results showed a very good fit compared to experimental results for all the frequencies. The difference between the total inelastic strain for experimental and modeling results is also presented in the last column of Table 4.1. The highest difference between them is around 7 % for the lowest frequency.

Table 4.1: Model input parameters and difference in total inelastic strain between the model and lab measurements for tests in the 'elastic regime' (σ_{mean2} = 38 MPa) and amplitude $A1$ of 20 MPa

Test	f [Hz]	λ_{MCC}	θ	η_1 GPa s	E_{avg}	p_c	$\varepsilon^{inelastic}$ Model/Lab
$\sigma_{mean2}/F1/A1$	F1=0.014	1.50e-04	0.005	250	23.3	10	0.0314 / 0.0319
$\sigma_{mean2}/F2/A1$	F2=0.0014	1.85e-04	0.005	1900	23.3	10	0.030 / 0.031
$\sigma_{mean2}/F3/A1$	F3=0.0002	2.30e-04	0.005	13000	23.3	10	0.042 / 0.045

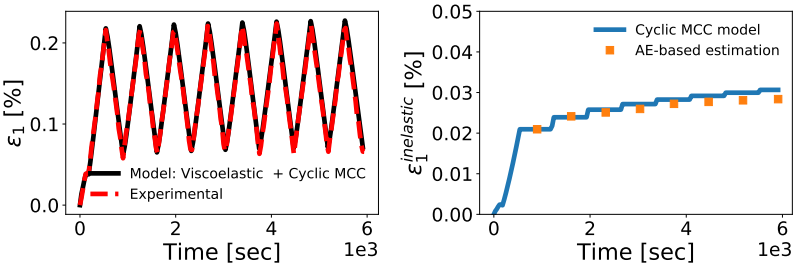

(a) Axial strain v/s time for $f = 0.0014$ Hz (b) Inelastic strain v/s time for $f = 0.0014$ Hz

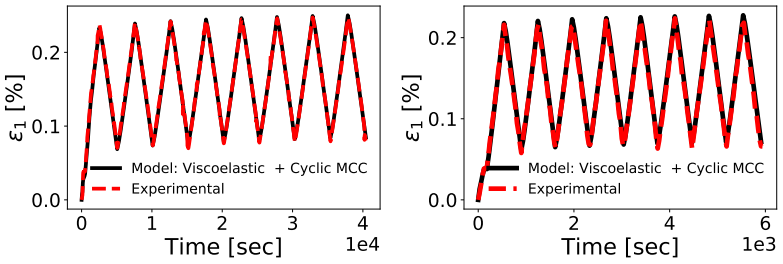

(c) Axial strain v/s time for $f = 0.0002$ Hz (d) Inelastic strain v/s time for $f = 0.0002$ Hz

Figure 4.4: **Below brittle yield point:** The above figures show the variation of axial strain with time (4.4(a), 4.4(c)). The respective inelastic strain with time is shown in (4.4(b), 4.4(d)).

Figures 4.4(b) and 4.4(d) show the variation of inelastic strain with time obtained from the MCC model, which is compared with the inelastic strain estimated using the number of events of AE (Equation 4.31) for the same frequencies. It can be seen that the MCC model is successful in capturing the inelastic strain cycle after cycle. The increase in inelastic strain for every cycle which is based on AE, follows a similar trend as the cyclic MCC model and quantitatively captures well with the experiments.

The yield surface evolution for different input loading cycles is shown in Figure 4.5. As the number of cycles increases, the yield surface slowly evolves to reach the maximum-sized final yield envelope. The plasticity model employed here with the parameters calibrated from the first cycle showed a maximum decrease in 0.2 % porosity at the end of the experiment. Though the decrease in porosity was not measured experimentally, previously few researchers have shown the decrease in porosity of sandstone under triaxial loading [106]. From the energy storage perspective, porosity reduction implies the reduction in the storage capacity of the subsurface reservoirs caused due to accumulated inelastic deformation. From the Table 4.1, it can also be seen that the parameters λ_{MCC} and viscosity η_1 are increasing with decreasing frequency. The rest of the parameters, such as θ, p_c pre-consolidation pressure, and E_{avg} are constant for all the frequencies. The viscosity of the rock increases with decreasing frequency of the applied load.

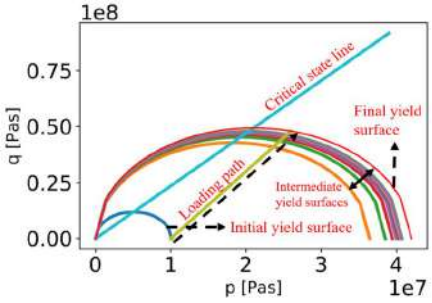

Figure 4.5: Illustration of the evolving yield envelope for every cycle of the rock using the MCC.

In the context of energy storage and upscaling the lab to energy storage conditions, viscoelastic frequency will become a key parameter when compared to rest of the material parameters used in the constitutive models. Viscoelastic frequency is a parameter directly influenced by cyclic loading frequency. It is interpreted that this viscosity could also be a function of strain rate as presented for the creep viscosity [359, 360]. Thus, as frequency decreases, the mean strain rate decreases, causing the viscosity to increase, which suggests a strain rate thinning-like behavior. To further support this, Figure 4.6 shows the viscosity variation with the loading frequency. Authors [14], model sandstone-based Bergermeer gas field storage sites with the viscoelastic model. The viscosity used by them to compare the uplift with GPS stations was around 1e8 GPa s. Using this as evidence, it can be said that depending on the frequency of cyclic loading viscosity of the viscoelastic model needs to be modified accordingly.

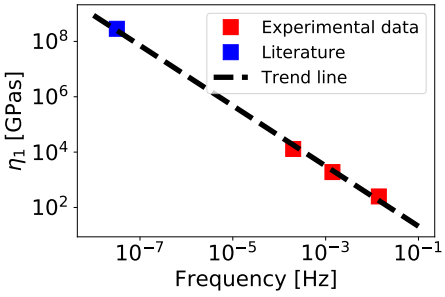

Figure 4.6: The variation of viscosity of rocks with the frequency of the cyclic loading. The field scale relevant data is from the literature [14] (Blue square).

4.1.6. ABOVE BRITTLE YIELD POINT

Here we employ the hardening softening model, and brittle creep additionally because the loading zone is above the brittle yield point. So the first step is defining the parameters of these two models, which are considered independent of the frequency of cyclic loading. For the calibration of the hardening-softening model, the range for cohesion and friction angle was established. This was done through monotonic test results

for Red Felser sandstone at different confining pressures, as shown in figure Figure 4.7. It can be seen that cohesion could range between 12MPa and 32MPa while the internal friction angle could be between 25^o and 48^o for $\sigma_3 = 10MPa$.

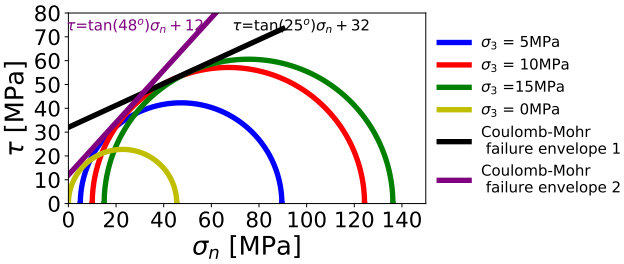

Figure 4.7: The figure shows the variation of shear stress with normal stress (failure envelop) with the equation of the Mohr-coulomb failure criteria can be seen.

The hardening softening (HS) model was further calibrated with the first loading cycle of the test case $\sigma_{mean}1/F3/A1$. This was done using the trial and error method. Next, the creep model was calibrated against the Multistage creep test. Thus, initial calibration of the viscoelastic and MCC model parameters also occurred. Figure 4.8(a) shows that it was possible to reproduce the strain of all the loading steps. The imposed axial load (σ_1) is shown in Figure 4.8(a). In this test case, the model comprises all the models (elastic, viscoelastic, creep, MCC, and HS model). Table 4.2 shows all the parameters obtained from fitting the experimental data for only the multistage creep test. The critical state line 'M' slope was taken from [106].

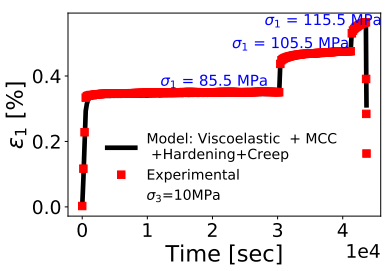

(a) Axial strain v/s time for $f = 0.0014$ Hz

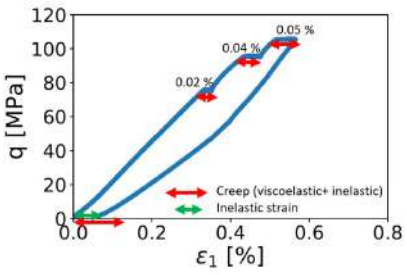

(b) Inelastic strain v/s time for $f = 0.0014$ Hz

Figure 4.8: The figure shows the variation of strain with time for the imposed stress (σ_1) as shown in the figure 4.8(a) for a multi-stage creep test. The creep strain (viscoelastic+inelastic) and the inelastic strains are highlighted in red and green arrows, respectively as shown in Figure 4.8(b).

Table 4.2: Model parameters used to reproduce experimental multistage creep test 2. These parameters will remain constant during modeling brittle cyclic tests, except for the viscosity of the visco-elastic unit, which changes depending on the frequency of the cyclic load.

Physics	Value	Value	Value	Value
Viscoelasticity	E_1 = 46 GPa	E_2 = 49 GPa	η_1 = 13e3 GPa s	ν = 0.125
MCC	M = 2.35 [106]	λ_{MCC} = 1.2e-4	p_c^0 = 10.1 MPa	ϕ = 0.2056
HS model	E_{avg} = 23.7	c = 22 MPa	$\phi_{friction}$ = 34.5	ε_f = 0.0015
Brittle creep	η_2 = 18e5 GPa s	σ^{BP} = 81 GPa s		

Figure 4.8(b) shows the variation of deviatoric stress with axial strain for the multi-stage creep test. The red and green double-headed arrows highlight the creep (visco-elastic + inelastic) strains and only inelastic strains, respectively. Using this, the visco-elastic and inelastic strain contributions could be identified, which helps calibrate the constitutive model.

Table 4.3: Model parameters: θ and visco-elastic viscosity η_1 against frequency for tests in the brittle regime. It is also mentioned the difference in total inelastic strain between the model and lab measurements. $F1 > F2 > F3$. Here σ_{mean1} = 85 MPa and $A1$ = 20 MPa.

Test	Frequency [Hz]	θ	η_1 [Gpa.s]	Eavg. [GPa]	$\varepsilon^{inelastic}$[%] Model/Lab
$\sigma_{mean1}/F1/A1$	F1=0.014	0.005	650	21.8	0.05 / 0.07
$\sigma_{mean1}/F2/A1$	F2=0.004	0.005	7800	21.8	0.058 / 0.065
$\sigma_{mean1}/F3/A1$	F3=0.0002	0.005	40000	21.8	0.0604 / 0.079

Finally, the deviatoric cyclic tests performed in the brittle regime were compared with the proposed model (equation 4.6) after the calibration as shown in Figure 4.9. Figures 4.9(a) and 4.9(c) show the variation of axial strain with time for two frequencies f = 0.0014 Hz and f = 0.0002 Hz. The inelastic strain contributions with the time of the three models are shown in Figures 4.9(b) and 4.9(d), respectively, for the same two frequencies. It can be seen that brittle creep plays an important role as the frequency decreases because there is more time for this type of deformation to become significant. In addition, cyclic plasticity was required to reproduce the experimental results of all the tests at the amplitude of 20 MPa (A1). Cyclic plasticity was more significant for high-frequency tests because of the negligible creep contribution Figure 4.9(b). The results for f = 0.014 Hz also showed a good fit for both below the yield point and above the yield point regimes.

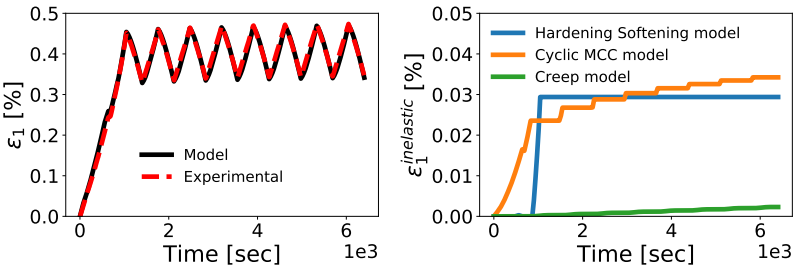

(a) Axial strain v/s time for $f = 0.0014$ Hz (b) Inelastic strain v/s time for $f = 0.0014$ Hz

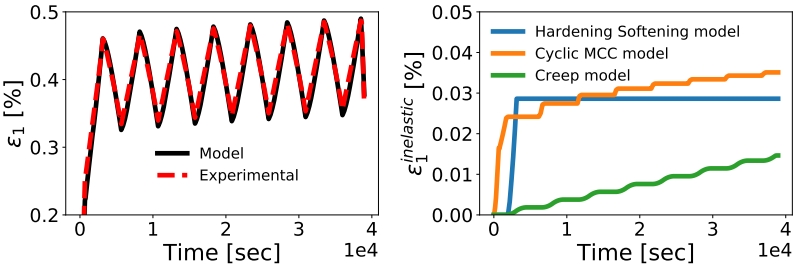

(c) Axial strain v/s time for $f = 0.0002$ Hz (d) Inelastic strain v/s time for $f = 0.0002$ Hz

Figure 4.9: **Above brittle yield point:** The variation of axial strain with time and inelastic strains with time for all the frequencies are shown. The constitutive model comprises elastic, viscoelastic, creep, MCC, and HS model.

Similar to the previous tests conducted below the brittle yield point, the viscoelastic viscosity had to be increased when the frequency of loading of cyclic tests was reduced, as shown in Table 4.3. Also, the viscosity in these test cases is consistently higher than the tests conducted in the elastic regime. The difference between the total inelastic strain for experimental and modeling results is also presented in the last column of Table 4.3. Due to the higher number of parameters involved from constitutive models, this difference is higher when compared to the previous section of below brittle yield point. No powerful optimization algorithms were employed, and lastly, the cyclicity part of dilation-based plasticity constitutive law was not accounted for. They are beyond the scope of this work.

In the subsurface energy storage perspective, considering much higher time scales with very low frequencies (max. 1e-6 Hz), creep deformation can become the most significant inelastic mechanism compared to the rest. Visco-elasticity will become critical during the injection and production of the reservoir to ensure that the strain-thinning behavior of sandstone rocks is considered.

Next, the effect of amplitude of cyclic loading for different regimes of stresses can be seen in Figure 4.10. Figures 4.10(a) and 4.10(b) show the variation of axial strain with time for mean stresses 38 MPa and 85 MPa, respectively. The parameters used in this amplitude are presented in Table 4.4.

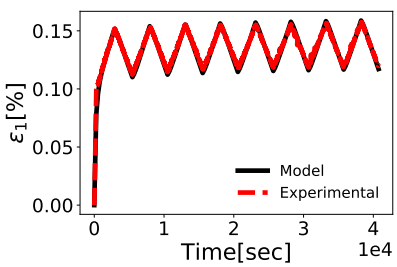

(a) σ_{mean2} = 38 MPa and A = 5.11 MPa

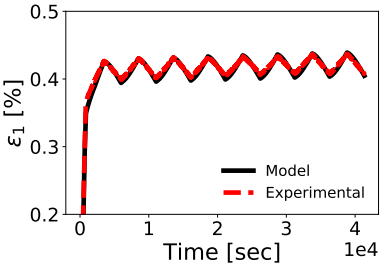

(b) σ_{mean1} = 85 MPa and A = 5.11 MPa

Figure 4.10: The variation of axial strains with time for lower amplitude A2 (A = 5.11 MPa), lowest frequency f = 0.0002 Hz and different mean stresses.

Table 4.4: Model parameters: θ and visco-elastic viscosity η_1 against frequency for tests in the brittle regime. The below parameters are for the amplitudes $A2$ = 5.11 MPa for both the means stress at the lowest frequency.

Test	Frequency [Hz]	θ	η_1 [Gpa.s]	Eavg. [GPa]
$\sigma_{mean1}/F3/A2$	F3=0.0002	0.005	13000	20.9
$\sigma_{mean2}/F3/A2$	F3=0.0002	0.005	45000	23.11

Here we see that the constitutive model fits the experimental data even for lower amplitudes. The Young's modulus (Eavg) is slightly different for mean stress 1 and 2, irrespective of amplitude and frequency. However, we did not observe any trend in the variation of Eavg depending on the stress regimes. The values of the parameters involved in constitutive models can slightly change if powerful optimization algorithms are employed. However, we expect the qualitative behavior of sandstone rock based on the above operating conditions would remain the same.

4.2. NUMERICAL MODELLING

The numerical formulation, relevant to model inelastic deformation using FEM methodology is elaborated below. The rock formations considered in this work are known to present time-dependent and time-independent inelastic deformations. Time-independent inelastic deformation basically refers to plastic deformations, which occur when the effective stress reaches a certain point. Similarly, viscoplasticity consists of irreversible deformations that develop over time, regarded that the stress levels also reach a critical value. The phenomenon known as creep also refers to a time-dependent irreversible deformation, however, it occurs for any level of stress.

In this numerical formulation, only creep is considered for the inelastic deformation of salt rock. Creep is also considered for the sandstone, in addition to plastic (time-independent) deformations. Finally, for shale rocks only viscoplastic deformations are considered. The Modified Cam-Clay (MCC) failure criteria adapted for cyclic loading

conditions is adopted for both shale rock and sandstone. For shale rock, however, the Perzyna algorithm, which adopts the concept of overstress, is employed. On the other hand, a Consistency based algorithm is used for sandstone. In what follows, the creep model, the MCC, Perzyna and Consistency algorithms are briefly presented. The associative plasticity model is employed in this work.

4.2.1. CREEP

In the presence of a constant external load, the steady-state creep is characterized by a constant strain rate, can be modeled by [23]

$$\dot{\boldsymbol{\varepsilon}}^{cr} = A \exp\left(-\frac{Q}{RT}\right) q^{n-1}\mathbf{s} \tag{4.32}$$

where Q is the activation energy, R is Boltzmann's constant and T is temperature. Finally, A and n are material constants and q is the von Misses stress, given by $q = \sqrt{\frac{2}{3}\mathbf{s}:\mathbf{s}}$, with $\mathbf{s}$ being the deviatoric stress tensor.

4.2.2. MODIFIED CAM-CLAY (MCC)

The introduction and equations employed in the MCC model are presented in subsection 4.1.2. In this subsection, briefly, the equations are presented in the tensorial format which is useful for FEM formulation. In what follows, the four ingredients mentioned at the beginning of this paragraph are presented in more detail. The elastic moduli are given by

$$K = \frac{(1+e)p'}{\kappa} \quad \text{and} \quad G = \frac{3(1-2\nu)(1+e)p'}{2(1+\nu)\kappa}, \tag{4.33}$$

with ν being the Poisson's ratio. From Eq. 4.33 it can be noticed that the elastic step in the MCC model is actually non-linear, since the elastic moduli also change with both mean stress p' and void ratio e. The yield function $\mathscr{F}$ depends on the stress level and the (visco)plastic strain, and it can be expressed as

$$\mathscr{F}(\boldsymbol{\sigma}, \varepsilon_v^p) = q^2 + M^2 p'(p' - p'_c(\varepsilon_v^p)) = 0, \tag{4.34}$$

where M is the slope of the CSL and p'_c is the hardening parameter, which is also called as the pre-consolidation pressure and it depends on the volumetric (visco)plastic strain ε_v^p. As shown in Fig. 4.3, the position of p'_c on the p' axis changes according to the yield surface $\mathscr{F}$.

HARDENING PARAMETER

The hardening parameter is characterized by the variable p'_c, which defines the position of the yield surface. Therefore, the material becomes "harder" when p'_c increases, since a higher stress level must be achieved to trigger plastic deformations. In the original approach of the MCC model, the hardening parameter increment ($\mathrm{d}p'_c$) is zero if the stress state is in the elastic regime, for instance $p'_y < p'_c$. Otherwise, if the stress state

touches the yield surface ($p'_y = p'_c$), then the hardening parameter increases proportionally to the (visco)plastic strain variation. This can be expressed as follows.

$$\frac{\mathrm{d}p'_c}{p'_c} = \begin{cases} 0 & \text{if } p'_y < p'_c, \\ \left(\dfrac{1+e}{\lambda-\kappa}\right)\mathrm{d}\varepsilon_v^p & \text{otherwise.} \end{cases} \tag{4.35}$$

where λ is the unloading/reloading index, which is obtained from isotropic plastic consolidation test [361].

The hardening rule represented by Eq. 4.35 is originally developed for monotonic loads. For cyclic loads, however, even in the elastic region, the material might reach failure sooner than predicted by the original MCC. This suggests that the yield surface actually shrinks during the process. Based on this idea, the hardening rule represented by Eq. 4.35 has been generalized for cyclic loading [362] by allowing the yield surface to shrink during unloading ($\mathrm{d}p'_y < 0$). This case can be expressed as

$$\frac{\mathrm{d}p'_c}{p'_c} = \begin{cases} 0 & \text{if } p'_y < p'_c \text{ and } \mathrm{d}p'_y \geq 0, \\ \theta\dfrac{\mathrm{d}p'_y}{p'_y} & \text{if } p'_y < p'_c \text{ and } \mathrm{d}p'_y < 0, \\ \left(\dfrac{1+e}{\lambda-\kappa}\right)\mathrm{d}\varepsilon_v^p & \text{otherwise.} \end{cases} \tag{4.36}$$

in which θ represents the fraction of shrinkage of the yield surface with respect to the "loading" surface. Notice that Eq. 4.35 is fully recovered from Eq. 4.36 when $\theta = 0$. In a recent work [117], the authors conducted cyclic triaxial experiments on sandstone rock and observed similar trend of the applicability of θ parameter in sandstone experiments.

PLASTIC FLOW RULE

Plastic strain is computed using the plastic flow rule, which is dependent on the stresses. In this work, we employ an associative flow rule, in which the plastic (or viscoplastic, in this case) strain is proportional to the gradient of the yield function with respect to stress. The incremental (visco)plastic strain tensor and the incremental volumetric (visco)plastic strain, therefore, take the following form

$$\mathrm{d}\boldsymbol{\varepsilon}^p = \gamma\frac{\partial\mathscr{F}}{\partial\boldsymbol{\sigma}} \quad \text{and} \quad \mathrm{d}\varepsilon_v^p = \gamma\frac{\partial\mathscr{F}}{\partial p'} \tag{4.37}$$

with γ denoting the plastic multiplier. The definition of this parameter depends on the numerical strategy adopted. In this work, Perzyna and Consistency based algorithms are employed for this purpose. Using the plastic flow rule, Perzyna and consistency-based algorithms are described below.

PERZYNA BASED VISCOPLASTIC ALGORITHM

In this work, we follow the approach proposed in [16], in which the viscoplastic strain rate tensor and viscoplastic volumetric strain rate are respectively given by,

$$\dot{\boldsymbol{\varepsilon}}^{vp} = \dot{\gamma}\frac{\partial_{\boldsymbol{\sigma}}\mathscr{F}}{|\partial_{\boldsymbol{\sigma}}\mathscr{F}|} \quad \text{and} \quad \dot{\varepsilon}_v^{vp} = \dot{\gamma}\frac{\partial_{p'}\mathscr{F}}{|\partial_{\boldsymbol{\sigma}}\mathscr{F}|}, \tag{4.38}$$

where $\partial_{\boldsymbol{\sigma}}\mathscr{F}$ and $\partial_{p'}\mathscr{F}$ are the partial derivatives of $\mathscr{F}$ with respect to $\boldsymbol{\sigma}$ and p', respectively. Moreover, the plastic multiplier is computed as,

$$\dot{\gamma} = \frac{\langle \mathscr{F}(\boldsymbol{\sigma}, \varepsilon_v^{vp})\rangle}{\mu(\varepsilon_v^{vp})p'} \tag{4.39}$$

with $\langle\cdot\rangle$ representing the Macaulay brackets and the viscosity expressed as

$$\mu(\varepsilon_v^{vp}) = \mu_0 \exp\left(\zeta\varepsilon_v^{vp}\right) \tag{4.40}$$

in which μ_0 and ζ are the reference viscosity and a material parameter.

Defining the residues

$$\psi = \frac{\mathscr{F}}{p'} - \dot{\gamma}\mu\left(\varepsilon_v^{vp}\right), \tag{4.41}$$

$$\mathbf{r} = -\mathrm{d}\boldsymbol{\varepsilon} + \mathrm{d}\boldsymbol{\varepsilon}^{e} + \mathrm{d}\boldsymbol{\varepsilon}^{vp}, \tag{4.42}$$

where Eq. 4.41 is the residual form of Eq. 4.39 and Eq. 4.42 neglects creep and plasticity contributions, since the Perzyna algorithm is employed here only for the shale rock, where creep and time-independent plasticity are assumed to be absent. Equations 4.41 and 4.42 depend on $\boldsymbol{\sigma}$ and $\dot{\gamma}$, therefore, applying Newton's method and solving for the increments $\mathrm{d}\boldsymbol{\sigma}$ and $\mathrm{d}\dot{\gamma}$ leads to

$$\mathrm{d}\dot{\gamma} = \frac{\psi - \partial_{\boldsymbol{\sigma}}\psi : \partial_{\boldsymbol{\sigma}}\mathbf{r}^{-1} : \mathbf{r}}{\partial_{\boldsymbol{\sigma}}\psi : \partial_{\boldsymbol{\sigma}}\mathbf{r}^{-1} : \partial_{\dot{\gamma}}\mathbf{r}}, \tag{4.43}$$

$$\mathrm{d}\boldsymbol{\sigma} = -\partial_{\boldsymbol{\sigma}}\mathbf{r}^{-1} : \left(\mathbf{r} + \partial_{\dot{\gamma}}\mathbf{r}\mathrm{d}\dot{\gamma}\right). \tag{4.44}$$

The reader is referred to [16] for the detailed formulation, including the explicit expressions for $\partial_{\boldsymbol{\sigma}}\psi$, $\partial_{\dot{\gamma}}\psi$, $\partial_{\boldsymbol{\sigma}}\mathbf{r}$ and $\partial_{\dot{\gamma}}\mathbf{r}$. Therefore, for each time step, internal iterations are required by updating stress and plastic multiplier as $\dot{\gamma}^{k+1} = \dot{\gamma}^{k} + \mathrm{d}\dot{\gamma}$ and $\boldsymbol{\sigma}^{k+1} = \boldsymbol{\sigma}^{k} + \mathrm{d}\boldsymbol{\sigma}$.

CONSISTENCY BASED PLASTIC ALGORITHM

For the sandstone, plasticity is incorporated through the consistency algorithm in conjunction with the MCC model, with the hardening parameter also computed by Eq. 4.36. Plastic deformation occurs when the yield function value is equal to 0. The return mapping algorithm using consistency condition has been used by several researchers [363–366]. We adopt the approach suggested by Liu et al. [366] in which anisotropy is ignored. Here, the plastic multiplier is computed by assuming the consistency condition, given by

$$\mathrm{d}\mathscr{F} = \frac{\partial\mathscr{F}}{\partial\boldsymbol{\sigma}} : \mathrm{d}\boldsymbol{\sigma} + \frac{\partial\mathscr{F}}{\partial p'_c}\mathrm{d}p'_c = 0. \tag{4.45}$$

The increment of stress, $\mathrm{d}\boldsymbol{\sigma}$, is proportional to the elastic strain. Since sandstone is considered in this work to undergo elastic, creep and plastic deformations, the increment of stress can be expressed as

$$\mathrm{d}\boldsymbol{\sigma} = \mathbb{C} : \left(\mathrm{d}\boldsymbol{\varepsilon} - \mathrm{d}\boldsymbol{\varepsilon}^{cr} - \mathrm{d}\boldsymbol{\varepsilon}^{p}\right) \tag{4.46}$$

with $\mathrm{d}\boldsymbol{\varepsilon}$ being the increment of total deformation. The increment of plastic deformation can be obtained from the plastic flow rule (Eq. 4.37). Additionally, Eq. 4.36 for the case of $p'_y \geq p'_c$ can be solved for the increment $\mathrm{d}p'_c$. In this manner, Eq. 4.45 becomes

$$\frac{\partial \mathscr{F}}{\partial \boldsymbol{\sigma}} : \mathbb{C} : \left(\mathrm{d}\boldsymbol{\varepsilon} - \mathrm{d}\boldsymbol{\varepsilon}^{cr}\right) - \frac{\partial \mathscr{F}}{\partial \boldsymbol{\sigma}} : \mathbb{C} : \gamma \frac{\partial \mathscr{F}}{\partial \boldsymbol{\sigma}} + \gamma \frac{\partial \mathscr{F}}{\partial p'_c} \frac{\partial \mathscr{F}}{\partial p'} \left(\frac{1+e}{\lambda - \kappa}\right) p'_c = 0 \tag{4.47}$$

Finally, solving Eq. 4.47 for γ provides

$$\gamma = \frac{\frac{\partial \mathscr{F}}{\partial \boldsymbol{\sigma}} : \mathbb{C} : \left(\mathrm{d}\boldsymbol{\varepsilon} - \mathrm{d}\boldsymbol{\varepsilon}^{cr}\right)}{\frac{\partial \mathscr{F}}{\partial \boldsymbol{\sigma}} : \mathbb{C} : \frac{\partial \mathscr{F}}{\partial \boldsymbol{\sigma}} - \frac{\partial \mathscr{F}}{\partial p'_c} \frac{\partial \mathscr{F}}{\partial p'} \left(\frac{1+e}{\lambda - \kappa}\right) p'_c} \tag{4.48}$$

The terms on the right-hand side of Eq. 4.48 must be evaluated at the current time level. For each time step, an iterative procedure (return mapping strategy) is employed on the stress until the corrected stress and the hardening parameter satisfy the yield condition.

4.2.3. INELASTIC STRAIN COMPOSITION

As depicted in Fig. 4.11, the domain Ω is decomposed in Ω_{st}, Ω_{sd} and Ω_{sh} for salt rock, sandstone and shale rock, respectively. Considering these different domains do not overlap each other, we have that

$$\Omega = \Omega_{\mathrm{st}} \cup \Omega_{\mathrm{sd}} \cup \Omega_{\mathrm{sh}}, \quad \text{and} \tag{4.49}$$

$$\Omega_{\mathrm{st}} \cap \Omega_{\mathrm{sd}} = \Omega_{\mathrm{st}} \cap \Omega_{\mathrm{sh}} = \Omega_{\mathrm{sd}} \cap \Omega_{\mathrm{sh}} = \emptyset. \tag{4.50}$$

Considering these three materials, we propose to express the inelastic strain tensor as

$$\boldsymbol{\varepsilon}^{\mathrm{ie}} = \boldsymbol{\varepsilon}_{\mathrm{st}} + \boldsymbol{\varepsilon}_{\mathrm{sh}} + \boldsymbol{\varepsilon}_{\mathrm{sd}}, \tag{4.51}$$

in which

$$\boldsymbol{\varepsilon}_{\mathrm{m}}(\mathbf{x}) = \begin{cases} \boldsymbol{\varepsilon}_{\mathrm{m}}(\mathbf{x}) & \text{if } \mathbf{x} \in \Omega_{\mathrm{m}} \\ 0 & \text{otherwise} \end{cases} \qquad \text{for m} = \mathrm{st}, \mathrm{sd}, \mathrm{sh} \tag{4.52}$$

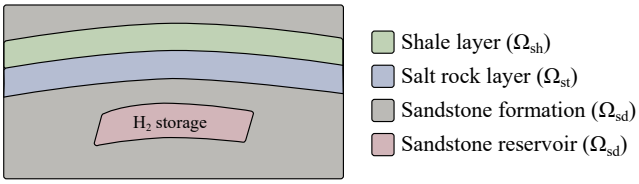

Figure 4.11: Schematic representation of the solution domain.

with the subscripts “st", “sd" and “sh" denoting salt rock, sandstone and shale rock, respectively.

As mentioned before, the inelastic deformations are considered to be only creep for rock salt, creep and plasticity for sandstone and only viscoplasticity for shale rock. Therefore, the inelastic strain tensor can be further split into

$$\boldsymbol{\varepsilon}^{\text{ie}} = \boldsymbol{\varepsilon}^{\text{cr}}_{\text{st}} + \boldsymbol{\varepsilon}^{\text{cr}}_{\text{sd}} + \boldsymbol{\varepsilon}^{\text{p}}_{\text{sd}} + \boldsymbol{\varepsilon}^{\text{vp}}_{\text{sh}}, \tag{4.53}$$

where $\boldsymbol{\varepsilon}^{\text{cr}}_{\text{st}}$ and $\boldsymbol{\varepsilon}^{\text{cr}}_{\text{sd}}$ are modeled by Eq. 5.3, and plastic and viscoplastic strains are modeled using the MCC model with cyclic hardening parameter (Eq. 4.36). Moreover, the plastic multipliers γ of $\boldsymbol{\varepsilon}^{\text{p}}_{\text{sd}}$ and $\boldsymbol{\varepsilon}^{\text{vp}}_{\text{sh}}$ are respectively obtained through the Perzyna and Consistency approaches previously discussed. We emphasize that all these inelastic strains must satisfy Eq. 4.52.

4.3. NUMERICAL FORMULATION

Consider a domain $\Omega \in \mathbb{R}^2$ bounded by a surface Γ, which is oriented by a normal vector $\mathbf{n}$ pointing outwards Ω. The boundary surface can be further split in $\Gamma = \Gamma_D \cup \Gamma_N$, where Γ_D and Γ_N denote the portions of the boundary surface in which Dirichlet and Neumann boundary conditions are applied, respectively. Moreover, we have that $\Gamma_D \cap \Gamma_N = \emptyset$. The trial and test functions are respectively defined as

$$\mathscr{U} = \{\mathbf{u} \in \mathbf{H}^1, \mathbf{u} = \overline{\mathbf{u}} \text{ on } \Gamma_D\}, \tag{4.54}$$

$$\mathscr{W} = \{\mathbf{w} \in \mathbf{H}^1, \mathbf{w} = \mathbf{0} \text{ on } \Gamma_D\} \tag{4.55}$$

where $\mathbf{H}^1$ denotes the first-order Sobolev space. In this manner, the weak form of conservation of momentum can be expressed as

$$\int_\Omega \mathbf{w}^T (\nabla \cdot \boldsymbol{\sigma} + \mathbf{f}) \mathrm{d}\Omega = 0, \quad \forall \mathbf{w} \in \mathscr{W} \tag{4.56}$$

The test function is assumed to be equal incremental solution ($\mathbf{w} = \delta\mathbf{a}, \forall \delta\mathbf{a} \in \mathscr{W}$) which satisfies the kinematic BC to minimize the residual in global domain. Using the divergence theorem,

$$\int_\Omega \delta\mathbf{a}^T (\nabla \cdot \boldsymbol{\sigma}) \mathrm{d}\Omega = -\int_\Omega \delta\boldsymbol{\varepsilon}^T \boldsymbol{\sigma}\, dV + \int_\Gamma \delta\mathbf{a}^T \mathbf{t} \mathrm{d}\Gamma \tag{4.57}$$

where the imposed traction vector is given by $\mathbf{t} = \boldsymbol{\sigma} \cdot \mathbf{n}$. Eq. 4.57 is used in Eq. 4.56 to yield,

$$\int_\Omega \delta\boldsymbol{\varepsilon}^T \boldsymbol{\sigma}\, d\Omega = \int_\Gamma \delta\mathbf{a}^T \mathbf{t}\, d\Gamma + \int_\Omega \delta\mathbf{a}^T \mathbf{f} \mathrm{d}\Omega. \tag{4.58}$$

The above equation is the incremental internal virtual work which is equal to external virtual work. In Eq. 4.58, the first and second terms on the right-hand side represent the imposed boundary traction forces and the volumetric body forces, respectively. All these

terms are evaluated at time $t+\Delta t$. In the incremental load/time-stepping scheme [367], the stress tensor can be written as

$$\boldsymbol{\sigma}^{t+\Delta t} = \boldsymbol{\sigma}^{t} + \Delta\boldsymbol{\sigma}. \tag{4.59}$$

Substituting Eq. 4.59 into Eq. 4.58,

$$\int_{\Omega} \delta\boldsymbol{\varepsilon}^{T} \Delta\boldsymbol{\sigma} \mathrm{d}\Omega = \int_{\Gamma} \delta\mathbf{a}^{T} \mathbf{t} \mathrm{d}\Gamma + \int_{\Omega} \delta\mathbf{a}^{T} \mathbf{f} \mathrm{d}\Omega - \int_{\Omega} \delta\boldsymbol{\varepsilon}^{T} \boldsymbol{\sigma}^{t} \mathrm{d}\Omega. \tag{4.60}$$

By considering Ω^{h} as a partition of Ω composed of non-overlapping quadrangles, the corresponding discrete function spaces $\mathscr{U}^{h}$ and $\mathscr{W}^{h}$ can be defined. Therefore, the displacement vector field can be approximated as

$$\delta\mathbf{a}^{T} = \delta\mathbf{u}^{T}\mathrm{N}^{T} \quad \text{and} \quad \delta\boldsymbol{\varepsilon}^{T} = \delta\mathbf{u}^{T}\mathrm{B}^{T}, \tag{4.61}$$

with N and B representing the interpolation functions and their global derivatives, respectively. Accordingly, the discretized linear momentum equation can be written as,

$$\int_{\Omega} \delta\mathbf{u}^{T}\mathrm{B}^{T} \Delta\boldsymbol{\sigma} d\Omega = \int_{\Gamma} \delta\mathbf{u}^{T}\mathrm{N}^{T}\mathbf{t} d\Gamma + \int_{\Omega} \delta\mathbf{u}^{T}\mathrm{N}^{T}\mathbf{f} d\Omega - \int_{\Omega} \delta\mathbf{u}^{T}\mathrm{B}^{T}\boldsymbol{\sigma}^{t} d\Omega \tag{4.62}$$

where $\delta\mathbf{u}^{T}$ are constants and can be readily eliminated from Eq. 4.62. The incremental stress is proportional to the increment of elastic strain, that is

$$\Delta\boldsymbol{\sigma} = \mathbb{C}\Delta\boldsymbol{\varepsilon}^{e}, \tag{4.63}$$

in which Voigt notation has been employed. However, considering infinitesimal strains, it follows that $\Delta\boldsymbol{\varepsilon} = \Delta\boldsymbol{\varepsilon}^{e} + \Delta\boldsymbol{\varepsilon}^{ie}$ and thus $\Delta\boldsymbol{\sigma} = \mathbb{C}\left(\Delta\boldsymbol{\varepsilon} - \Delta\boldsymbol{\varepsilon}^{ie}\right)$. Additionally, recalling that $\Delta\boldsymbol{\varepsilon} = \mathrm{B}\Delta\mathbf{u}$, then

$$\Delta\boldsymbol{\sigma} = \mathbb{C}\left(\mathrm{B}\Delta\mathbf{u} - \Delta\boldsymbol{\varepsilon}^{ie}\right). \tag{4.64}$$

Substituting Eq. 4.64 into Eq. 4.62,

$$\int_{\Omega} \mathrm{B}^{T}\mathbb{C}\mathrm{B}\Delta\mathbf{u} d\Omega = \int_{\Gamma} \mathrm{N}^{T}\mathbf{t} \mathrm{d}\Gamma + \int_{\Omega} \mathrm{N}^{T}\mathbf{f} \mathrm{d}\Omega - \int_{\Omega} \mathrm{B}^{T}\boldsymbol{\sigma}^{t} \mathrm{d}\Omega + \int_{\Omega} B^{T}\mathbb{C}\Delta\boldsymbol{\varepsilon}^{ie} \mathrm{d}\Omega. \tag{4.65}$$

Equation 4.65 originates a system of equations in the following form

$$\mathrm{K}\Delta\mathbf{u} = \mathbf{b}, \tag{4.66}$$

Because of the non-linearity present in $\mathbf{b}^{ie}$, due to the inelastic strains, it is convenient to define a residual vector as

$$\mathscr{R} = \mathbf{b} - \mathrm{K}\mathbf{x}, \tag{4.67}$$

where $\mathbf{x} = \Delta\mathbf{u}$. Newton's method can be applied by expanding Eq. 4.67 using Taylor series, that is,

$$\mathscr{R}^{k+1} = \mathscr{R}^{k} + \left.\frac{\partial\mathscr{R}}{\partial\mathbf{x}}\right|^{k} \Delta\mathbf{x}. \tag{4.68}$$

Enforcing the residue at the current iteration $k+1$ equal to zero, the following linearized system is repeatedly solved until convergence for each time level,

$$\mathrm{J}^{k}\Delta\mathbf{x} = -\mathscr{R}^{k}, \tag{4.69}$$

with $\mathrm{J}^{k} = \partial_{\mathbf{x}}\mathscr{R}^{k}$ representing the Jacobian matrix at iteration k.

4.3.1. IMPLEMENTATION

The implementation of the non-linear model proposed in this work is represented in the pseudocode shown in Algorithm 6 for a given load step at time level $t+\Delta t$. A load control-based algorithm is presented here. However, the displacement-controlled algorithm could also be employed. For each time step, the residual is solved for an incremental displacement. Creep, plastic, and viscoplastic strains of shale, salt, and sandstone rocks are computed in the material loop.

Algorithm 6 : Inelastic mechanical FEM

for a loading step $f^e_{t+\Delta t}$ **do** ▷ Loading loop
  Assign $\Delta\mathbf{u}^{\nu+1} \leftarrow 0$, $\Delta\mathbf{x} \leftarrow 2\epsilon$, ν is the newton iteration of time stepping loop.
  Initialize inelastic strain increment $\delta\boldsymbol{\varepsilon}^{ie} \leftarrow 0$.
  while $||\Delta\mathbf{x}||_2 > \epsilon$ OR $\nu < \max(\nu)$ **do** ▷ Assembly loop
    Assemble the Jacobian, residual $\mathscr{R} \leftarrow \mathbf{b}^e + \mathbf{b}^{ie,\nu+1} - \mathrm{K}\Delta\mathbf{u}^{\nu}$
    Solve $\mathrm{J}^{\nu}\Delta\mathbf{x} = -\mathscr{R}$
    $\Delta\mathbf{u}^{\nu+1} \leftarrow \Delta\mathbf{u}^{\nu} + \Delta\mathbf{x}$
    Compute total strain increment $\Delta\boldsymbol{\varepsilon}^{\nu+1} \leftarrow \nabla_s\Delta\mathbf{u}^{\nu+1}$
    Compute elastic strain increment $\Delta\boldsymbol{\varepsilon}^{e} \leftarrow \Delta\boldsymbol{\varepsilon}^{\nu+1} - \Delta\boldsymbol{\varepsilon}^{ie}$
    for each integration point in an element e **do** ▷ Element loop
      Compute the trial stress update $\boldsymbol{\sigma}^{trial} \leftarrow \boldsymbol{\sigma}_t + \mathbb{C}\Delta\boldsymbol{\varepsilon}^{e}$
      $(\boldsymbol{\sigma}, \Delta\boldsymbol{\varepsilon}^{cr}_{\mathrm{st}}) \leftarrow$ **ComputeSaltStrains**$(\boldsymbol{\sigma}^{trial}, \boldsymbol{\varepsilon}^{cr}_{\mathrm{st},t})$
      $(\boldsymbol{\sigma}, \Delta\boldsymbol{\varepsilon}^{vp}_{\mathrm{sh}}) \leftarrow$ **ComputeShaleStrains**$(\boldsymbol{\sigma}^{trial}, \Delta\boldsymbol{\varepsilon}, \Delta\boldsymbol{\varepsilon}^{e}, p'_c, p'_y, p'_{y,t})$
      $(\boldsymbol{\sigma}, \Delta\boldsymbol{\varepsilon}^{cr}, \Delta\boldsymbol{\varepsilon}^{p}) \leftarrow$ **ComputeSandstoneStrains**$(\boldsymbol{\sigma}^{trial}, \Delta\boldsymbol{\varepsilon}, \Delta\boldsymbol{\varepsilon}^{e}, \boldsymbol{\varepsilon}^{cr}_{t}, p'_c, p'_y, p'_{y,t})$
    end for
    $\Delta\boldsymbol{\varepsilon}^{ie} \leftarrow \Delta\boldsymbol{\varepsilon}^{cr}_{st} + \Delta\boldsymbol{\varepsilon}^{vp}_{sh} + \Delta\boldsymbol{\varepsilon}^{cr}_{sd} + \Delta\boldsymbol{\varepsilon}^{p}_{sd}$
    Set $\nu \leftarrow \nu + 1$
  end while
  Update $\boldsymbol{u}_{t+\Delta t} \leftarrow \boldsymbol{u}_t + \Delta\boldsymbol{u}^{\nu+1}$ and all the strains.
  Go to next loading step
end for

This is also extended to multiscale formulation as presented in section 2.4.

4.4. RESULTS

Several numerical experiments are conducted to benchmark our unified framework to evaluate the impact of inelastic deformation at field scale when a cyclic load is employed. The consistency of the FEM formulation was checked and the displacement field was found to be 2nd order accurate in space.

4.4.1. BENCHMARKING THE SIMULATOR

The simulator is benchmarked in the first step with the existing available data in the literature. In this test case, the material is assumed to be boston blue clay showing only plasticity without any creep and modeled using original MCC using Equation 4.35. Drained loading conditions with strain softening and undrained conditions with strain hardening are considered in this section to study the variation of von Mises stress with strain. Table 4.5 show the parameters employed in the following simulation. The effective stress paths applied can be observed in Figures 4.12(a) and 4.12(d) for drained and undrained loading conditions, respectively. As shown in these two graphics, the stress path goes from point A to B and from B to C. An increasing load is subjected to the rock similar to an over-time rise in the stresses when a fluid is continuously injected into the reservoir.

Table 4.5: Parameters employed for triaxial loading for Boston blue clay [15]

#	Value	#	Value	#	Value
κ	0.034 [-]	p'	0.25 [MPa]	ν	0.3 [-]
λ	0.17 [-]	M	1.34 [-]	e_0	1.12 [-]

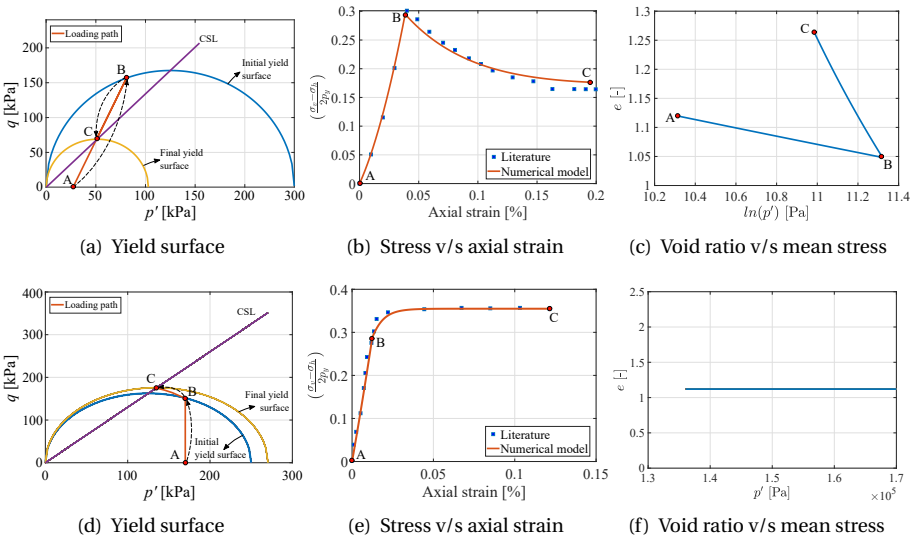

(a) Yield surface (b) Stress v/s axial strain (c) Void ratio v/s mean stress

(d) Yield surface (e) Stress v/s axial strain (f) Void ratio v/s mean stress

Figure 4.12: **Benchmarking:** Illustration of the strain softening scenario using MCC with consistency condition for drained rock (Figure 4.12(a),4.12(b),4.12(c)) and strain hardening scenario for undrained rock (Figure 4.12(d),4.12(e),4.12(f)) respectively. The simulation results are compared with [15].

The results are illustrated in Figure 4.12. Figures 4.12(a), 4.12(b) and 4.12(c) show the yield surface, variation of normalized stress with axial strain and variation of void ratio

with mean stress respectively for drained condition. Similarly Figures 4.12(d), 4.12(e) and 4.12(e) illustrate the same material, but under undrained loading conditions. In the case of drained condition (Figure 4.12(a)), the load increases from point A until it touches the initial yield surface in point B. When it returns to point C, because it is in the softening region (above the CSL), the variation in volumetric strain is negative, which makes the yield surface to shrink according to Equation 4.35. On the other hand, when undrained condition is imposed (Figure 4.12(d)), the point at which the stress state reaches the initial yield surface (point B) is below the CSL, that is, in the hardening region, where volumetric strain variation is positive. As a result, the yield envelope expands in the plasticity regime from point B to point C.

Variation of normalized stress (normalized with preconsolidation pressure) with respect to the axial strain for drained (Figure 4.12(b)) and undrained (Figure 4.12(e)) conditions are compared with the literature of numerical results [15]. The characteristic softening and hardening behaviors can be verified in these two figures, with the stress increasing after point B for Figure 4.12(e), and decreasing for Figure 4.12(b). As it can be seen from these graphics, the numerical results compare relatively well with the literature. The variation of void ratio with logarithm of volumetric stress is shown in Figure 4.12(c) and Figure 4.12(f). The change in void ratio for a drained condition is significant in the inelastic region (from point B to C) compared to the elastic region. However, the void ratio remains constant when the load is applied in an undrained fashion because only the pore pressure changes in the rock.

The parameters in Table 4.5 were employed to verify the implementation of our work. In the field scale scenario, these parameters are calibrated further based on the observed uplift by the GPS stations which is elaborated in the later section. In a field case storage scenario depending on the operating conditions and time instant the reservoir will be usually partially saturated, so porous rock might experience drained or undrained consolidation conditions. The results presented above show that the numerical scheme is able to adequately describe these two situations.

4.4.2. COMPARISON BETWEEN FINESCALE AND MULTISCALE RESULTS

In this test case, fine scale and multiscale results are compared for a homogenous rock using the same parameters as presented in Table 4.5. The respective stress paths for drained (Figure 4.13(a)) and undrained (Figure 4.13(d)) conditions are presented. In contrast to the test cases presented in the previous section, here the stress path for the drained condition promotes a hardening behavior (line B–C in Figure 4.13(a) is below CSL), while softening is obtained for the undrained stress condition (line B–C is above CSL in Figure 4.13(d)).

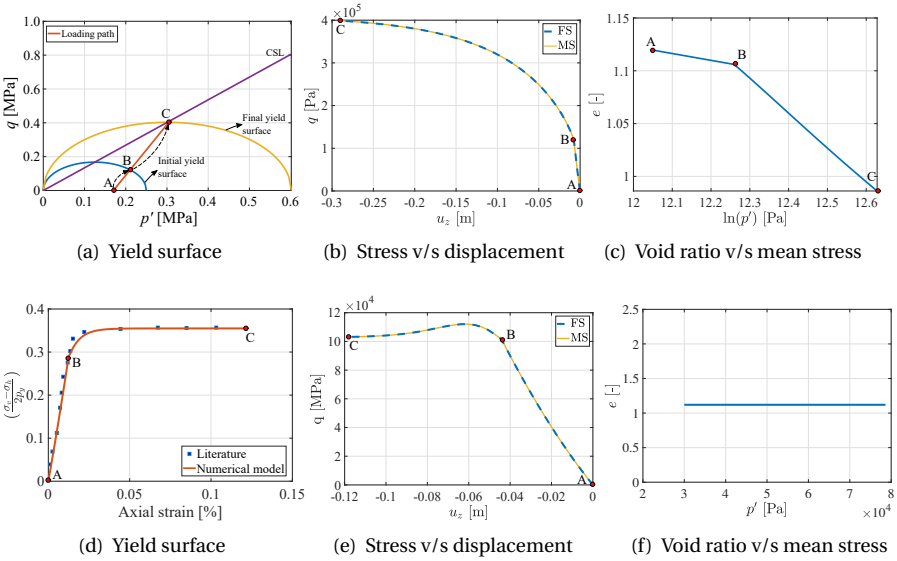

(a) Yield surface (b) Stress v/s displacement (c) Void ratio v/s mean stress

(d) Yield surface (e) Stress v/s displacement (f) Void ratio v/s mean stress

Figure 4.13: **Comparison:** Illustration of the strain hardening scenario using MCC with consistency condition for drained condition (Figure 4.13(a),4.13(b),4.13(c)) and strain softening scenario for undrained condition (Figure 4.13(d),4.13(e),4.13(f)) respectively. Here the results are compared with FS and MS simulation methods.

The results are presented in Figure 4.13. Figures 4.13(a), 4.13(b) and 4.13(c) show the yield surface, variation of normalized stress with axial strain and variation of void ratio with mean stress respectively for drained condition. Similarly Figures 4.13(d), 4.13(e) and 4.13(f) show the same for undrained condition. The variations of von Mises stress with axial displacement for finescale and multiscale are shown in Figure 4.13(b) and 4.13(e) respectively for strain hardening and strain softening test case. The difference is virtually zero because the MS strategy is able to capture all the information from reduced order boundary conditions in the homogeneous rock. The variation of void ratio with logarithm of mean stress is shown in Figure 4.13(c) and Figure 4.13(f). Similar to the previous test case, a higher change in void ratio is observed in the plastic region of the drained loading condition compared to the change in void ratio in the elastic region (that is from point B to C in Figure 4.13(c)). In addition, the volumetric strain variation is zero for undrained loading, thus resulting in no change in void ratio.

4.4.3. CYCLIC LOADING OF ROCKS

Underground energy storage will involve cyclic loading on the reservoir depending on the demand and supply of the energy (for e.g. H2). For this reason, it is important to study the effect of cyclic loading of rocks involving inelastic strains. In this test case, homogeneous sandstone and shale rock are studied to understand the effect of viscoplasticity on shale rock and the effect of creep and plasticity on sandstone rock. Considering seasonal storage of hydrogen in reservoirs, four phases of storage cycle are incorporated as elaborated in [368]. These phases include injection phase, rest phase at high pressure,

withdrawal phase and lastly rest phase at low pressure. The chosen parameters for shale rock are presented in Table 4.6 and are obtained from [16]. The rock is modelled with $20 \times 1 \times 20$ elements of dimensions $25 \times 25 \times 50$ [cm^3]. Bottom face is fixed, vertical cyclic load as shown in Figure 4.14(a) is imposed on the top face and rest of the faces have a confining stress of 40 MPa.

Table 4.6: Parameters employed in the cyclic loading for shale rock [16]

#	Value	#	Value	#	Value
κ	8.86e-3	μ_0	9.69e12 Pa s	ζ	4.33e3
λ	29.3e-3	M	1.3	p_y	43.17 [MPa]
Elements	$20 \times 1 \times 20$	e	0.089	Length	$25 \times 25 \times 50$ [cm^3]
A	$1e-17$	n	1.6	Q	5000 [mol/cal]

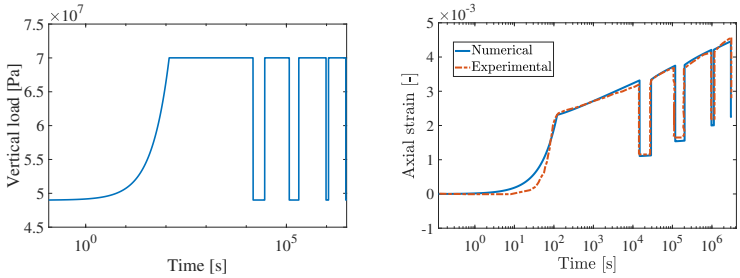

(a) Axial imposed load

(b) Strain v/s time for shale

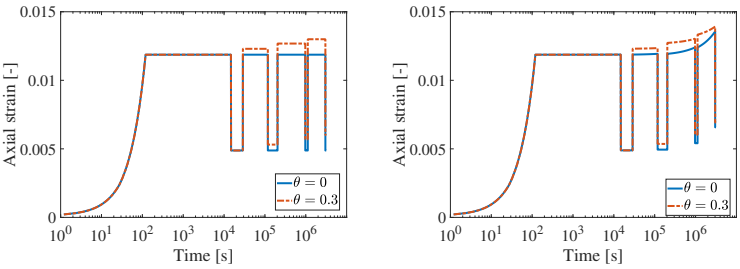

(c) Sandstone rock without creep

(d) Sandstone rock with creep

Figure 4.14: **Cyclic loading:** Illustration of the effect of the imposed cyclic load (4.14(a)) on shale rock and sandstone rock is presented here. The model parameters are chosen from the literature [16] and compared with the experimental data as shown in 4.14(b). 4.14(c) and 4.14(d) show the variation of axial strain for sandstone rock without and with creep deformation for the same imposed loading respectively.

The variation of axial strain with time for numerical and experimental results [127] is obtained here by employing Perzyna viscoplastic formulation. Viscoplastic behavior of shale rocks can be clearly observed in this test case, where the rock deforms of time at

a constant load as shown in Figure 4.14(b). As the number of cycles increases, the axial strain in the rock also increases with time. In this test case, the unloading effect of the hardening parameter as explained in Figure 4.36, is not accounted since this effect was not observed experimentally ($\theta = 0$).

Using the same load as shown in Figure 4.14(a), the effect of cyclic loading on sandstone rock is studied. The parameters used for sandstone are presented in Table 4.5. For comparison purposes, however, the pre-consolidation pressure is chosen to be p_y = 43.17 MPa which is same as the shale rock. Figure 4.14(c) shows the variation of strain with time for sandstone without incorporating creep strains. It can be seen that in Figure 4.14(c) the strain rate is 0 for constant load, since plasticity is a time-independent phenomenon. However, as θ is larger than zero, the accumulated strain increases with time for every cycle. This is due to the reloading effect, which is accommodated in the hardening parameter. When a fluid is stored in the subsurface based on the demand and supply, the higher the number of cycles for the same operating pressures, the higher will be the accumulated strain.

The interplay between creep and plasticity in sandstone was also studied. The parameters chosen for creep formulation are presented in Table 4.5. Figure 4.14(d) shows the variation of strain with time for sandstone by also considering creep strains. In this case, it can be seen that for a constant load, the strain is increasing with time due to the accumulation of creep strain. With the inclusion of creep and the reloading effect, number of cycles and the time period of the imposed load will make a significant impact on the accumulated strain.

Comparing shale rock and sandstone, it can be seen that the axial strain is higher for sandstone compared to the shale rock. This is because of the different elastic and plastic properties of the rock.

4.4.4. EFFECT OF HETEROGENEITY ON MULTISCALE

In this test case, the goal is to study the influence of heterogeneities in the mechanical response of materials. For this purpose, Perzyna's formulation is employed to observe the difference between fine-scale (FS) and multi-scale (MS) results. The strategy consists of imposing a uniform distribution for one material property at a time while the others are kept constant. The values for the heterogeneous paramenters and the corresponding ranges of variation are shown in Table 4.7. The remaining parameters (including domain dimensions) are taken from Table 4.6. The loading condition is shown in Figure 4.14(a). The domain has $20 \times 1 \times 20$ cells, with a coarsening ratio of $5 \times 1 \times 5$.

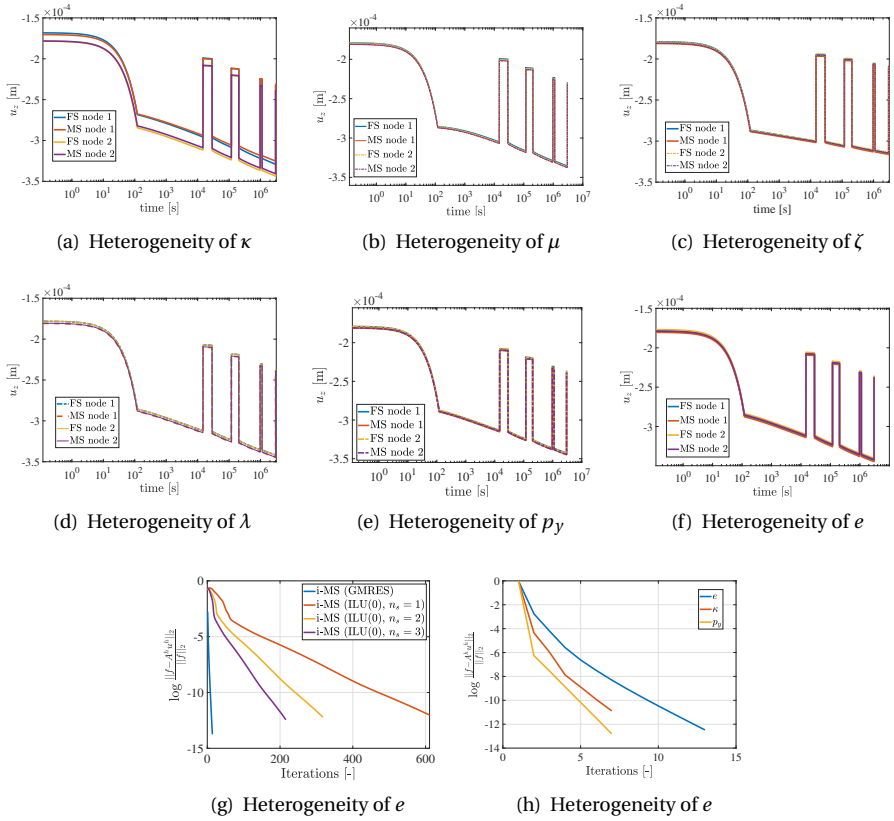

(a) Heterogeneity of κ (b) Heterogeneity of μ (c) Heterogeneity of ζ

(d) Heterogeneity of λ (e) Heterogeneity of p_y (f) Heterogeneity of e

(g) Heterogeneity of e (h) Heterogeneity of e

Figure 4.15: **Heterogeneity:** Illustration of the impact of heterogeneity in shale properties on the axial deformation. The chosen parameters and its range is shown in Table 4.7. Heterogeneity in κ, μ, ζ, λ, p_y and e is shown in the Figures 4.15(a), 4.15(b), 4.15(c), 4.15(d), 4.15(e) and 4.15(f) respectively. The convergence plot for void ratio is shown in 4.15(g) and the convergence plot for different parameters using GMRES is shown in 4.15(h).

Figure 4.15 shows the comparison of FS and MS axial displacement results for two different nodes on the top face (node 1 and node 2). Among the investigated parameters, the deformation is most sensitive to κ when heterogeneity is imposed: results obtained from two different nodes exhibit more pronounced deviations compared to the other scenarios. This occurs due to the influence of the parameter κ on the bulk modulus which causes change in the elastic deformation. Due to this significant change, a slight

Table 4.7: Different parameters chosen to study their influence of heterogeneity

#	Value	#	Value	#	Value
κ	$(5\pm3)\times10^{-3}$	λ	$(30\pm20)\times10^{-3}$	ζ	$(10\pm3)\times10^{3}$
p_y	$(40\pm10)\times10^{6}$ Pa	ϕ	0.1 ± 0.05	μ_0	$(45\pm30)\times10^{12}$ Pa s

difference of FS and MS results can be seen. Figure 4.15(b), Figure 4.15(c), Figure 4.15(d) and Figure 4.15(e) respectively show the influence heterogeneity of μ, ζ, λ and p_y on the displacement over time. The impact of heterogeneity in void ratio Figure 4.15(f) also affects the elastic part of deformation. However, the displacements at different nodes are not significant compared to Figure 4.15(a).

The results in Figure 4.15 show that the MS solution is able to satisfactorily reproduce the FS solution. To achieve higher accuracies of MS solutions, an iterative MS strategy is employed. Figure 4.15(g) shows the variation of $\log(e_r)$ with number of iterations. In iterative MS strategy [113] there are two stages. The first stage involves the multi-scale stage and the second stage involves the smoothing stage with a pre-conditioner. Depending on the required accuracy different numbers of smoothing stages n_s can be applied. In this work Incomplete LU decomposition (ILU(0)) with different number of smoothing stages and the Generalized minimal residual method (GMRES) are employed as a pre-conditioner. Figure 4.15(g) shows the convergence for each case. It can be seen that GMRES converges to the solution much faster in less than 10 iterations compared to ILU(0) as the pre-conditioner in multi-scale strategy. Figure 4.15(h) shows the convergence history for the GMRES as a smoother when heterogeneities in κ, e and p_y are considered. It can be seen that it takes fewer iterations for heterogeneity in p_y compared to the other parameters due to its influence primarily only on the inelastic deformation. MS results are quite satisfactory overall compared to the FS. In field scale situations, with high heterogeneities and lithological artifacts MS could vary from FS significantly.

4.4.5. FIELD SCALE TEST CASE

Subsurface energy storage technology will involve cyclic injection and production in the reservoir, which can lead to subsidence/uplift. Due to these time-dependent processes, it is critical to understand the influence of inelastic strains and the stress distributions around the reservoir. To study this, a synthetic test case inspired from Bergermeer gas storage site in the Netherlands is chosen. Predominantly, it is a sandstone reservoir in the Slochteren formation located in the North West of the Netherlands with faults and fractures. The seal of this reservoir is predominantly a Zechstein salt layer (ZET). The other cap-rock seal is the Zechstein platten (ZEB) formation consisting of salt such as dolomite, anhydrites, clays and shale [62, 369].Due to the heterogeneous formation, the elastic properties and their plasticity constitutive laws vary accordingly. In this work, the impact of faults and fractures are not considered in the geo-mechanical model. Although each layer is composed of different materials, for the sake of simplicity, it is assumed here a single type of material for each layer.

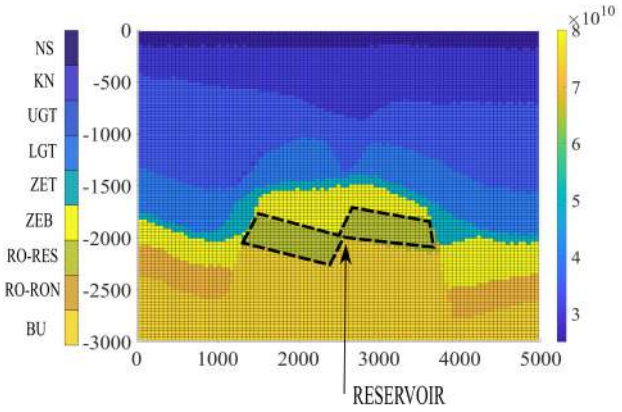

Figure 4.16: **Field scale test case:** The above shows the variation of the Youngs modulus inside the geological domain highlighting the reservoir boundary at a depth of around 2000 m. Roller boundary conditions are imposed in the left, bottom and right face and the top face has free stress boundary conditions.

A planar 2D cross-section of the reservoir is chosen [14] as presented in Figure 4.16 with varying Young's modulus along the depth. The Young's modulus and the Poisson's ratio are chosen from the literature [21, 22]. The domain has 98x1x98 cells, with the coarsening ratio of 14x1x14 for the multiscale method. The properties chosen and the type of rock assumed in each layer is presented in Table 4.8. The choice of coarsening ratio has been extensively studied for simulation of multiphase flow [298, 370] based on CPU time for 3D test cases. In our study, we have taken approximately close to the root square of the elements existing in each axis. This is in agreement with the commonly used coarsening ratios, i.e., using the coarsening ratio of 10x10x10 allows for reducing size of the mesh by 1 order of magnitude in each direction. The layers in the table are arranged along the depth in an increasing manner. Roller boundary conditions (zero normal displacement) are imposed on the left, bottom and right boundaries, whereas the top boundary is traction-free. In the earth's natural state, lithostatic pressure would be present inside the geometrical domain. However, it is assumed that the lithostatic pressure does not cause nonlinear time-dependent deformation. The deviation from the equilibrium state, therefore, is only caused by injection and production of the reservoir, which is imposed as a uniform volumetric load over the elements in the reservoir. Figure 4.16 shows the area comprising the reservoir.

Table 4.8: Lithological properties in the Bergermeer field [21, 22]

Lithology	Young's modulus [GPa]	ν [-]	Material
North Sea (NS)	25	0.25	Sandstone
Vlieland Claystone (KN)	30	0.25	Sandstone
Upper Germanic Triassic (UGT)	35	0.25	Sandstone
Lower Germanic Triassic (LGT)	40	0.25	Sandstone
Zechstein salt (ZET)	50	0.3	Rock salt
Zechstein Platten (ZEB)	80	0.25	Shale
Rotliegend Reservoir (RO-RES)	65	0.175	Sandstone
Rotliegend Non-Reservoir (RO-NON)	70	0.175	Sandstone
Carboniferous (BU)	75	0.2	Sandstone

Table 4.9: Parameters of plasticity, viscoplasticity and creep used for different rocks [15, 16, 23, 24]

Rock	Value	Value	Value	Value	Value	Value
Sandstone	$\kappa = 0.034$	$\lambda = 0.12$	$e_0 = 1.12$	$A = 1.5e-30$	$n = 1.5$	$Q = 5000$ [cal/mol]
Rocksalt	$A = 2.5e-29$	$n = 3.5$	$Q = 12325$ [cal/mol]			
Shale	$\kappa = 0.0076$	$\lambda = 8.19e-3$	$e_0 = 0.088$	$\zeta = 4.33e5$	$\mu_0 = 9.68e12$ [Pa s]	

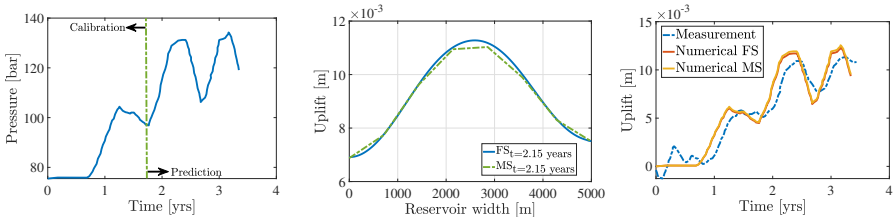

(a) Imposed pressure in the reservoir

(b) Uplift v/s Reservoir width

(c) Max Uplift v/s time

Figure 4.17: **Field scale test case:** The above illustration shows the results of uplift obtained from the reservoir model with inelasticity. 4.17(a) shows the variation of imposed pressure with time indicating the calibration and prediction phases. Figure 4.17(b) shows the uplift computed at time = 2.15 years for both FS and MS methods. The variation of uplift with time is shown in Figure 4.17(c) with the GPS measurement data [14, 17].

A number of researchers [14, 371, 372] have tried to model the Bergermeer gas field by considering faults inside the 3D domain and employing the Kelvin Voigt model to account for inelasticity. However, in this work different inelastic formulations are employed for different materials to accommodate heterogeneities more effectively. Elasticity modulus degradation due to possible reservoir rock in-elasticity is neglected. The physical properties of all materials are considered to be isotropic. The material constants which are calibrated in the previous sections for lab-scale experiments cannot be used directly in the field scale measurements due to differences in stress magnitudes on the sample, the difference in the timescales of the lab experiments with the field scale experiments, and lastly the rock samples from different field can show different microstructural properties. Hence in this work, the plasticity constants are calibrated based on the variation of the uplift with time in the period of 0 to 1.75 years. The parameters

used in the inelasticity formulation are presented in Table 4.9. These parameters are calibrated based on the uplift data from the observed GPS stations. The calibration method can be further improved using optimization processes which is beyond the scope of this work. The results are presented in Figure 4.17. The filtered uplift measurement data is obtained from GPS stations [14, 17].

Figure 4.17(a) shows the variation of the imposed pressure inside the reservoir to time. The calibration and prediction phase of the imposed pressure is separated at 1.75 years. Accordingly, based on the calibration the uplift predicted from our model is presented. Figure 4.17(b) shows the variation of uplift along the width of the reservoir at 2.15 years. The results show both fine scale and multiscale results. It can be seen that the uplift is not symmetric along the center of the reservoir, this is due to the asymmetrical position of the reservoir in the lithology. The multi-scale algorithm is able to compute the magnitude of the uplift quite satisfactorily when compared to the fine-scale solutions.

Lastly, Figure 4.17(c) shows the variation of uplift with time for the imposed pressure loading. Here it can be seen that the measurement data from 0 to 0.8 years is not predicted from the numerical algorithm. This is because of the negligible change in the imposed pressure on the reservoir during this period. The next phase is the calibration phase from 0.8 years to 1.75 years. Here it can be seen that the magnitudes of the measurement data are close to the computed uplift, however, there is a lag between the measurement data and the numerical results. This lag can be due to (i) the poroelastic behavior of the reservoir which is not captured in this work, (ii) the well pressure is assumed to be the constant pressure acting on the entire reservoir as a body force, (iii) the effect of faults and fractures in the overburden causing a delay in the uplift, and (iv) lastly viscoelastic behavior of the rocks like sandstone and primary creep in rocksalt. There are evidences presented by the researchers of this delay in the measurement and the modelling results [373]. The visco-elastic effect and the damage of rocks effect is beyond the scope of this work. However, the magnitude of the uplift is satisfactory compared to the measurement data for both fine-scale and multiscale methods. The higher the magnitude of inelasticity of the rocks around the reservoir, the larger will be the uplift shown on the surface of the earth. The main emphasis of this test case, is to emphasise on the suitability of this computational framework to accommodate inelasticity effect of the rocks and showing the applicability of multiscale strategy in the field scale involving inelasticity.

In general, nonlinear mechanics simulations, specially with a multiscale framework, are expected to be sensitive to the mesh resolution; specially for heterogeneous media. The mesh sensitivity in our studies was limited, due to 3 main reasons: (1) very small incremental time steps (thus small loading steps) were imposed on our geo-models; (2) our multiscale strategy develops locally computed basis functions, capturing heterogeneities, without applying any upscaled parameter; (3) the development of an iterative multiscale procedure which guarantees systematic error control and reduction to any desired level. Note that the performance of the iterative strategy, specially its convergence rate, does depend on the size and geometry of the basis functions. Such performance study based on CPU time is outside the scope of the current manuscript.

This work provides the first of its kind attempt to match and predict the storage dy-

namics of the subsurface storage site, using the existing recorded sparse field data. Note that not all the degrees of freedom play equal role in the fitting procedure. More precisely, the stiff layers hardly contribute to the subsidence or uplift. Thus the main fitting sensitivities would lie in the soft sandtsone layers. It can also be observed that the material parameters calibrated for the Bergermeer test case are different from those calibrated in the previous test cases for lab experiments. This can be due to two reasons. First, the rock samples taken to the laboratory might not present the same type of grain structure as the in situ lithology even though they are same type of rock. Secondly, the operating conditions (loads and time-scales) in which the rocks are subjected in the field scale is different from the lab experiments. Therefore, more experimental data involving cyclic loading of rocks for longer time-scales are required for improving reliability of the numerical results.

The initial phase of testing the field site helped us identify the suitable pressures inside the field to operate feasibly. Using the minimum and maximum pressures inside the field as a reference, the Bergermeer site could be used as a storage site for energy. Every summer when there is excess renewable energy produced from solar and wind energy, the energy can be converted to green gases and stored, and accordingly, this energy could be used in the winter when there is high energy demand. Accordingly, to simulate these conditions, a similar pressure loading is applied as shown in Figure 4.18(a). For around half a year the energy is stored in the reservoir which implies a high pressure being imposed for roughly around six months and then the fluid is produced which reduces the pressure in the system close to its natural state of the reservoir.

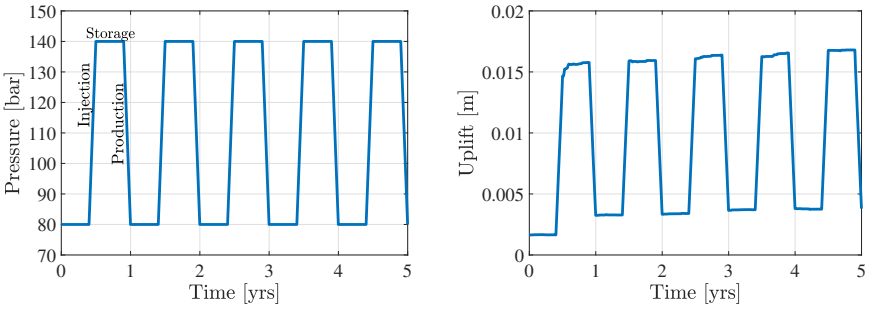

(a) Imposed pressure in the reservoir

(b) Max uplift v/s time

Figure 4.18: **Field scale test case:** The imposed pressure load is shown in 4.18(a). 4.18(b) shows the variation of the maximum uplift with time caused due to the imposed pressure.

Figure 4.18(b) shows the variation of the uplift concerning the time. Here we can see the accumulation of the uplift caused due to the inelasticity in the domain which is around 16 % (for 5 years) of the uplift caused due to the elasticity. Also, the amount of accumulated uplift in the first cycle is higher than the remaining cycles which is caused due to the plasticity of sandstone and shale that depend only on the imposed pressure. The remaining increase in the uplift with time is due to the creep deformation of the rocks in the rocks that is dependent on time. If we continue this operation for several

decades, creep deformation might be more significant compared to the rest of the inelasticity effects. In this section, the change in inelasticity parameters caused due to prolonged loading is not considered which could be possible because of the change in the grain structure of the rocks. As the subsurface energy storage technology is growing because of the world drifting toward renewable energy, these reservoir sites can be used for multiple decades to store energy causing permanent uplift on the ground surface and causing damage to the living conditions of life.

4.5. CONCLUSION

The main motivation of this work is to simulate and analyse the influence of inelasticity of porous rocks in subsurface formations relevant for cyclic energy storage. To study this, a computational framework is developed using an algebraic multiscale strategy to study the effects of plasticity, viscoplasticity and creep of different rocks found in the subsurface. Sandstone, shale and rock-salt rocks, which follow different physics and have different properties, are modelled using both fine-scale and multiscale methods using an implicit load driven time integration method. Depending on the required accuracy, a two stage iterative multiscale (MS) strategy was employed.
The simulator is benchmarked initially with the existing literature for different rocks. Comparison with the fine-scale solution, the multiscale results present acceptable accuracy with much lower computational cost. Subsurface storage technology involves cyclic loading over long periods. To study this effect, cyclic loading of shale and sandstone rocks is studied to understand the impact of inelasticity on strain with time. Lastly, a field test case is studied by including different types of rocks and their respective inelasticity physics. In this case, different lithological minerals were considered along with different elastic and plastic properties to model uplift on the surface level by using both fine-scale and multiscale methods. In this field test case, the uplift on the ground surface is compared with the computed uplift obtained from fine-scale and multiscale results.
The future scope involves accommodating visco-elasticity and further extending the formulation to poro-inelasticity to understand the effect of change in displacements on the pore pressure with time. Further, the computational framework should accommodate the modeling of faults and fractures in the field. This could be further used in modeling several porous fields realistically to understand the physics involved.

5

MULTISCALE SIMULATION OF PORO-INELASTICITY

***Abstract**: Successful transition to renewable energy supply depends on the development of cost-effective large-scale energy storage technologies. Geological formations are often highly heterogeneous over their large (km) length scales and entail complex nonlinear rock deformation physics, especially under cyclic loading. We develop a multiscale simulation strategy to address these challenges and allow for efficient, yet accurate, simulation of nonlinear inelastic deformation of rocks under cyclic loading. A coarse-scale system is constructed for the given fine-scale detailed nonlinear deformation model. The multiscale method is developed algebraically to allow for convenient uncertainty quantifications and sensitivity analyses.*

5.1. INTRODUCTION

Depleted oil and gas reservoirs, which offer large-scale storage capacities (TWh), are well characterized, and often include the already-installed facilities that can be repurposed for UGS [58], thus reducing operational costs. The vital ingredients that need to be considered in UGS include accurate and reliable storage capacity estimation and risk assessment, mainly to avoid failure due to changes in the in-situ state of stresses (subsidence, induced seismicity, fault reactivation, etc.). Underground formations are often highly heterogeneous over large (km) length scales. They also exhibit inelastic behaviors which are uncertain to a large extent. These structures also entail complex nonlinear deformations under cyclic loadings. Inelasticity can be modeled through several factors, including creep, viscoplastic and thermoplastic physics. In this work, we incorporate it through empirical creep laws, as pointed out by [166]. Notice also that the power law models, such as Carter's model [339] and Arrhenius law to account for temperature dependency, are typical for modeling creep behavior.

This work is published in IACMAG conference, 2023

To capture all the geological heterogeneities demand for field scale sizes, an algebraic multiscale strategy is developed to solve the system at a coarse scale. More precisely, this work focuses on simulating sandstone reservoirs by accounting for the inelastic deformation and solving the coupled poro-inelastic system using a hybrid Finite-Element (FE)- Finite-Volume (FV) scheme, at fine scale for mechanics and flow respectively. Built on this hybrid system, an algebraic multiscale strategy is developed based on the vast literature [162, 273–280]. This allows for solving the systems at much coarser scales to accommodate heterogeneity in the domain and nonlinear physics.

In what follows, the coupled consolidation model with creep is presented in section 5.2. section 5.3 presents the numerical formulation and section 5.4 discusses the multiscale strategy. The preliminary results are presented and followed by a conclusion.

5.2. GOVERNING EQUATIONS

The governing equations considered in this work follow Biot's consolidation theory [374]. Neglecting gravitational effects, the mass conservation equation for a fully saturated and deforming porous medium can be written as

$$b\nabla\overline{u} + \frac{1}{M_b}\dot{p} - \nabla(\lambda\cdot\nabla p) = q \tag{5.1}$$

Here, b is Biot's coefficient, M_b is Biot's modulus, q is the source term, $\overline{u}$ is the displacement, and λ is the mobility which is the ratio of rock permeability tensor k and fluid viscosity μ. Considering Terzaghi's effective stress principle, the momentum balance equation is

$$\nabla\cdot(\mathbb{C}\nabla_s\overline{u} - bp\boldsymbol{I}) = \overline{f} \tag{5.2}$$

where $\mathbb{C}$ denotes the 4th order stiffness tensor, $\boldsymbol{I}$ is the identity 2nd order tensor, ∇_s is the symmetric gradient operator, and $\overline{f}$ is the equivalent of the sum of body forces (g) and fictitious forces caused due to inelastic creep strain, that is $\overline{f} = g + \nabla\cdot(\mathbb{C}:\boldsymbol{\varepsilon}^{cr})$.

Creep is the tendency of a material to continuously deform under the application of an external load. Because this is a time-dependent phenomenon, creep is usually represented by a strain rate and it is highly dependent not just on effective stress but also on temperature T. For simplicity, this work only considers secondary (stationary) creep which is modeled by using power law formulation [339] to account for stress and temperature dependency, respectively. In this case, the creep strain rate can be expressed as

$$\dot{\boldsymbol{\varepsilon}}^{cr} = A\exp\left(-\frac{Q}{RT}\right)\sigma_{vm}^{n-1}\mathbf{s} \tag{5.3}$$

where Q is the activation energy, R is Boltzmann's constant and T is temperature. Finally, A and n are material constants and σ_{vm} is the von Mises stress, given by $q = \sqrt{\frac{2}{3}\mathbf{s}:\mathbf{s}}$, with $\mathbf{s}$ being the deviatoric stress tensor. In the next section, the numerical formulation is elaborated.

5.3. NUMERICAL FORMULATION

In this work, a hybrid FV-FE formulation is adopted for solving the model equations. Particularly, FV is employed for discretizing the mass conservation equation (Eq. 1) on a three-dimensional structured Cartesian corner-point grid, whereas a FE approach is adopted for solving the mechanical problem (Eq. 2). Although both formulations share the same computation grids, pressure, and displacements are stored at different positions, as shown in Figure 5.1. The displacements, on the other hand, are stored at the element vertices as in standard Galerkin FE formulations. A staggered grid is employed where the displacements are stored in the vertex and the pressure is stored at the cell center.

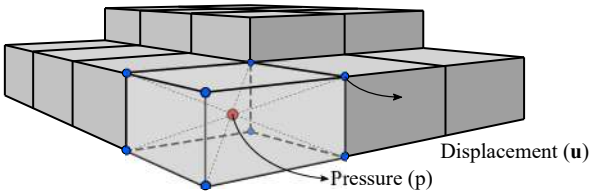

Figure 5.1: Computational grid for pressure and displacement used in FEM-FVM solver highlighting pressure in the center and displacement nodes in the corner.

After discretization with the FV-FE formulation and employing an implicit time integration (i.e., backward Euler), the resulting system of equations can be expressed as

$$K\boldsymbol{u} + L\boldsymbol{p} = \boldsymbol{f}^u \tag{5.4a}$$
$$Q\boldsymbol{u} + A\boldsymbol{p} = \boldsymbol{f}^p \tag{5.4b}$$

where matrices K, L, Q, and A represent the effective stresses, pressure gradients, volumetric strains, and the accumulation terms plus Darcy velocities, respectively. Furthermore, $\boldsymbol{f}^p$ contains pressures and volumetric strains from the previous time step, and $\boldsymbol{f}^u$ comprises the boundary conditions and the fictitious creep forces. For a given time level, the residuals of Eq. (4) for an iteration k can be expressed as

$$\boldsymbol{r}^{p,k} = \boldsymbol{f}^{p,k} - A\boldsymbol{p}^k - Q\boldsymbol{u}^k \tag{5.5a}$$
$$\boldsymbol{r}^{u,k} = \boldsymbol{f}^{u,k} - L\boldsymbol{p}^k - K\boldsymbol{u}^k \tag{5.5b}$$

Following Newton's method, the residuals at the current iteration $k+1$ are made equal to zero, which results in the following system of equations

$$\begin{bmatrix} \partial_u \boldsymbol{r}^u & \partial_p \boldsymbol{r}^u \\ \partial_u \boldsymbol{r}^p & \partial_p \boldsymbol{r}^p \end{bmatrix} \begin{bmatrix} \delta u \\ \delta p \end{bmatrix}^{k+1} = - \begin{bmatrix} r^u \\ r^p \end{bmatrix}^k \tag{5.6}$$

Finally, this linear system is solved monolithically for each timestep.

5.4. MULTISCALE FORMULATION

For geo-systems with heterogeneous coefficients which do not have separation of scales, upscaling leads to significant and uncontrollable error norms. To address this challenge, a multiscale finite element/finite volume formulation (MsFEM/FVM) in which a coarse-scale grid is superimposed to a fine-scale grid is adopted [277]. The fundamental concept behind this work is to build the system of equations in the fine-scale grid and then project and solve it onto the coarse-scale grid.

$$A_c x_c = b_c \tag{5.7}$$

Here

$$A_c = \boldsymbol{R} A_f \boldsymbol{P} \qquad\qquad b_c = \boldsymbol{R} b_f \tag{5.8}$$

This implies that $\boldsymbol{R}\,\boldsymbol{P}$ have dimensions $(4n_c \times 4n_f)$ and $(4n_f \times 4n_c)$. After solving the coarse-scale system, the fine-scale solution can be retrieved through the prolongation operator, that is

$$x_f = \boldsymbol{P} x_c \tag{5.9}$$

$$\boldsymbol{R} = \begin{bmatrix} R_u & 0 \\ 0 & R_p \end{bmatrix} \tag{5.10}$$

$$\boldsymbol{P} = \begin{bmatrix} P_u & 0 \\ 0 & P_p \end{bmatrix} \tag{5.11}$$

The prolongation and restriction operator to compute deformation (P_u, R_u) is computed as shown in section 2.4. In a similar way fashion, the prolongation and restriction operators for flow are computed by flow-only local mass balance equations which are

$$-\nabla \cdot (\lambda \cdot \nabla \boldsymbol{N}_i^H) = 0 \qquad \text{in } \Omega^p \tag{5.12a}$$

$$\nabla \cdot (\lambda : \nabla_{||} \boldsymbol{N}_i^H) = 0 \qquad \text{on } \partial\Omega^p \tag{5.12b}$$

$$\boldsymbol{N}_i^H(x_j) = \delta_{ij} \qquad \forall\, j \in \{1 \ldots n_p^H\} \tag{5.12c}$$

A detailed procedure about the multiscale basis functions for flow is elaborated in [298].

5.5. RESULTS

5.5.1. TERZAGHI TESTCASE

In this test case, we study the fluid-saturated column commonly known as the Terzaghi test case [375]. This test case is studied to benchmark the simulation strategy and has no creep deformation. The schematic is shown in Figure 5.2. A fluid-saturated column of height L is pressed with a constant load at t=0. The rest of the edges are fixed.

Drainage is allowed only on the top face and the rest of the faces have no flow boundary conditions.

Biot's modulus is 1e101 Pa, mobility is 1e-4 m2/Pa, Poisson's ratio is given by 0.2, and the load is imposed as 100 Pa with the number of cells in the grid as $15 \times 15 \times 15$.

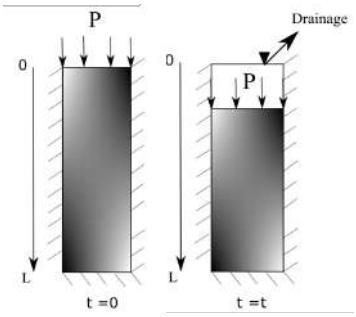

Figure 5.2: Schematic of Terzaghi test case where a saturated porous rock column is subjected to 1D compaction while fluid can flow through the top.

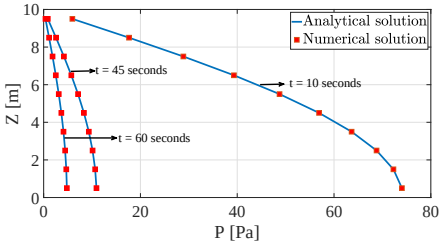

(a) Pressure history at the centre point.

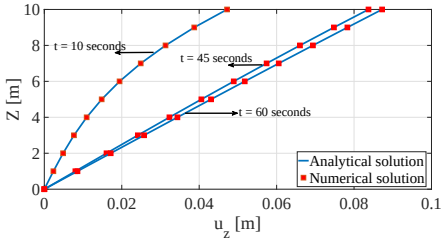

(b) Comparison between analytical and numerical for Terzaghi testcase.

Figure 5.3: Displacement in the vertical direction in uniaxial compression. Resolution of 3D FEM: $10 \times 10 \times 10$, 2D FVM: 10×10.

Figure 5.3 shows the comparison between the analytical solutions with numerical solutions. Figure 5.3(a) shows the variation of pressure history at the center point at different times. Figure 5.3(b) shows the variation of vertical displacement along the depth of the column. At initial times, the displacement is nonlinear because of the over-pressure and eventually, it becomes constant with respect to time.

5.5.2. MANDEL TESTCASE

In this section, the numerical results of the above formulation are presented. The well-known Mandel test case is studied for benchmarking linear finescale and multiscale elastic poromechanics. The schematic is shown in Figure 5.4. The problem describes an in-finitely long poroelastic slab bounded by impermeable plates with fluid. A load is

applied on the top face at t = 0, and the drainage is allowed from the east boundary. Fig. 3 shows the poroelastic Mandel test case simulation results for both fine-scale and multiscale. The parameters chosen for this test case are shown in Table 1. The analytical formulation is obtained from [375].

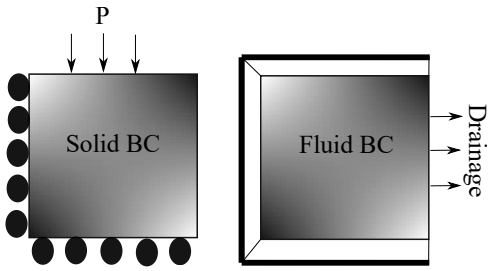

Figure 5.4: The above illustration shows the schematic of the Mandel test case. The domain is subjected to roller constraint at the south, and west, a traction-free surface in the east, and a constant load is applied on the top face. Drainage is allowed in the east face.

Table 5.1: The parameters chosen for Mandel test case for poroelastic and poro-inelastic domain

Parameter	Value	Parameter	Value	Parameter	Value
Grid	15x1x15	Poisson's ratio	0.2	M	1e100
E	1e4 Pa	n	2.5	T	300 K

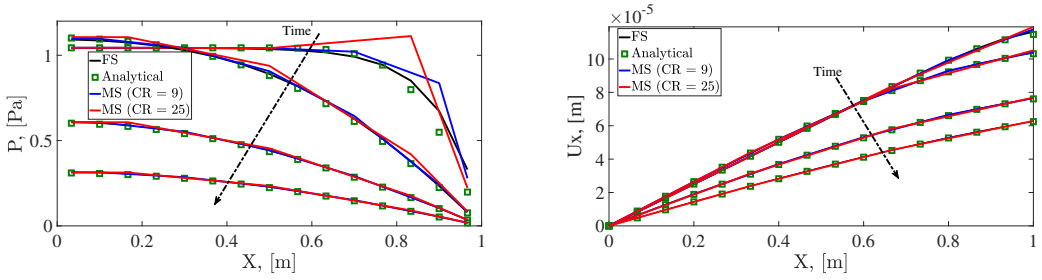

Figure 5.5: The above illustrations show the a) variation of pressure along the domain in the horizontal direction, b) variation of horizontal deformation along the domain in the horizontal direction at four-time instants [0.01, 0.1, 0.5, 0.9] x t_{end} for the 15x1x15 grid.

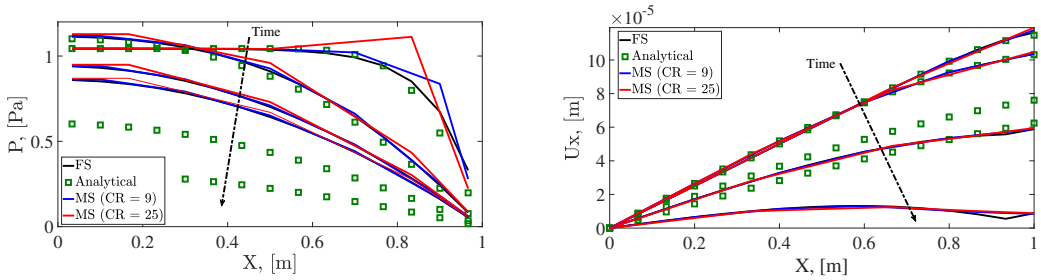

Figure 5.6: The above illustrations show the (a) variation of pressure with time, (b) variation of pressure along the domain in the horizontal direction for time instants [0.01, 0.1, 0.5, 0.9] x t_{end} for Mandel test case with creep.

The parameters chosen for the Mandel test case are shown in Table 5.1. Figure 5.5 shows the variation of pressure and displacement along the horizontal axis in the 2D domain for poroelastic Mandel test case. Two different coarsening ratios of 9 and 25 are chosen for the multiscale procedure. The overpressure at the initial timesteps is caused due to the contraction at the plate's drained edges, causing a buildup in the pore pressure. It can be seen that the multiscale solution for the coarsening ratio of 25 is not accurate compared to the finescale solution. This could be further improved by using an iterative MS strategy beyond the scope of this work [113]. It can be seen that the MS displacement are very close to the fine-scale and analytical solutions for homogeneous poroelastic rocks.

This test case is further analyzed when the rocks are considered inelastic and undergo creep deformation. The parameters chosen for the creep formulation are presented in Table 5.1. The chosen parameters are adopted in order to study the effect of creep deformation on the poromechanical system both at finescale and multiscale. Figure 5.6 shows the results of the simulation. Fig. 5.6(a) and 5.6(b) show the results of pressure and horizontal displacement along the x-axis when creep is incorporated. It can be seen that the pressure is still on the higher side as time proceeds. It can also be seen that the rock seems to shrink in the x-direction as time proceeds. This can be due to the effect of drainage close to the right edge of the surface.

5.6. CONCLUSION

Successful scaling up of this technology requires, among others, scalable simulation methods for nonlinear poromechanical systems. In this work, after developing a fully-implicit fine-scale hybrid FE-FV scheme, an algebraic multiscale strategy, consistent with the hybrid FE-FV fine-scale formulation, was developed. This allows for field-relevant test cases, in which heterogeneous geomodels are required to be solved for many possible realizations. The simulation strategy was benchmarked using the Terzaghi testcase by comparing them with the analytical solutions. The well-studied Mandel test case was investigated in more detail, especially on the applicability of the multiscale

method for coupled systems in the presence of creep.

This is just the introductory test case of the poro-inelastic formulation with algebraic multiscale. More number of test cases need to be investigated to further understand the effect of nonlinear deformation in poroelastic formulation.

6

MULTISCALE GRID COARSENING USING UNSUPERVISED MACHINE LEARNING

Summary: *Subsurface flow simulation is vital for many geoscience applications, including geoenergy extraction and gas (energy) storage. Reservoirs are often highly heterogeneous and naturally fractured. Therefore, scalable simulation strategies are crucial to enable efficient and reliable operational strategies. One of these scalable methods, which has also been recently deployed in commercial reservoir simulators, is algebraic multiscale (AMS) solvers. AMS, like all multilevel schemes, is found to be highly sensitive to the types (geometries and size) of coarse grids and local basis functions. Commercial simulators benefit from a graph-based partitioner; e.g., METIS to generate the multiscale coarse grids. METIS minimizes the amount of interfaces between coarse partitions, while keeping them of similar size which may not be the requirement to create a coarse grid. In this work, we employ a novel approach to generate the multiscale coarse grids, using unsupervised learning methods which is based on optimizing different parameter. We specifically use the Louvain algorithm and Multi-level Markov clustering. The Louvain algorithm optimizes modularity, a measure of the strength of network division while Markov clustering simulates random walks between the cells to find clusters. It is found that the AMS performance is improved when compared with the existing METIS-based partitioner on several field-scale test cases. This development has the potential to enable reservoir engineers to run ensembles of thousands of detailed models at a much faster rate.*

This chapter is currently under review in Journal of Computational Physics

6.1. INTRODUCTION

One of the main challenges in computational geosciences for flow and transport simulations is that the reservoir is highly heterogeneous and naturally fractured. This will become computationally very expensive to solve at the fine (high-resolution) scale, because of the large number of cells and non-linearities to be resolved. In addition, because of the uncertainties involved in geoscience applications, several forward simulations have to be run on many possible realisations [376]. As such, advanced simulation methods are crucial to enable safe, efficient and reliable operational strategies at field-scales. To address this, algebraic multi-scale methods [275, 276, 298, 370] were developed and evolved in the past decade to accelerate both academic and commercial reservoir simulators. Their performance, however, is highly dependent on the choice of local "basis functions", used to map between the fine- and coarser-scale systems [377]. These basis functions form partitions of unity, and are enriched once fractures are present [378].

In the recent era, machine-learning methods are being widely used in the reservoir flow modeling applications like using smart finite elements [379] or employing a physics-informed neural network to model the Buckley-Leverett problem to understand the drainage of gas into a water-filled porous medium [380]. To reduce the computational time and complexity of the system, several multiscale methods with different definitions are prevalently, such as upscaling material properties [381], algebraic multiscale methods [298] or FE2 methods for composites [382]. Few authors in recent years have used machine learning in the area of algebraic multiscale or multigrid methods [383–388]. A deep neural network was used in the geometric multigrid method, by considering every operation as a network layer [387]. Recently, a graph-based neural network (GNN) was employed to train algebraic multi-grid prolongation operator for linear systems using a single GNN [389], reinforcement learning [390] and encoder-decoder-based idea of pooling to coarsen the mesh graph [391]. A surrogate model was also developed to generate basis functions in the multiscale solver [392].

Based on the literature, most of the work is focused on employing machine learning to improve prolongation operators or optimize the AMG solvers. However, enhancing the solver performance using machine learning to find the location of the coarse grid cells in the reservoir domain was never attempted. Traditionally, commercial simulators, use the graph cut methods such as METIS package [393] to partition the fine-scaled domain into a coarse-scale system based on the connectivity of the cells. The improvement in the performance of the partitioning can be indirectly reflected in reducing the total number of Newton iterations in each timestep. The METIS package minimizes the number of edges between partitions (coarse block cells) while keeping the partitions of similar size. This is an important consideration for parallel computing; however, it might not be important for a multiscale sequentially fully implicit (SFI) solver. To tackle this, in this work, unsupervised graph-based learning algorithms are employed to cluster the fine-scale domain into a coarse-scale system. The schematic of the approach is shown in Figure 6.1.

The data, which are stored in the reservoir, are translated to a graph which captures the connectivity between the cells into the edge weights of the graph (transmissibility)

and the node weights (pore volume). Using graph clustering, communities are detected and further translated to the coarse grid. Graph clustering has been extensively used in the past to find communities based on connectivity between the nodes or edge weights and also node weights for different applications such as image segmentation[394], load balancing in parallel computing, very large scale integration systems (VLSI) [393], genetic mapping [395, 396] and social networks [397].

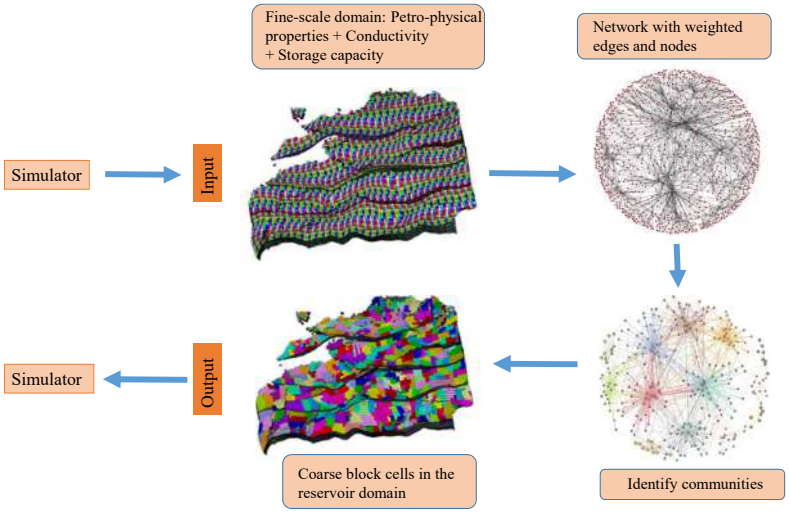

Figure 6.1: Schematic of graph clustering in reservoir simulation using algebraic multiscale methods.

Popular graph-based clustering algorithms include spectral clustering[398–400], hierarchical clustering [401], modularity-based methods [402, 403] and neural-network-based methods [404]. The spectral algorithm involves the computation of eigenvalues and vectors with approximate methods such as the Nystrom and Lanczos algorithms. The obtained eigenvectors can be sensitive to the approximation error that contributes to the poor quality of the results and does not scale well to large test cases. Neural-network-based algorithms need extensive training and testing data, which is not appropriate in this application mainly because the performance is case dependent due to high heterogeneity and insufficient data available to train the network.

In this work, the two chosen advanced algorithms to compare with METIS are the Louvain algorithm [403] and Multi-level Regularized Markov clustering (MLR-MCL) [405]. The Louvain algorithm is based on modularity optimization while the Markov clustering algorithm is iteratively employed until its stochastic matrix is converged. The Louvain algorithm, a recursive method that builds on previous work [406–410] and variants of Markov clustering algorithms based on random walk [411–413] have been previously implemented in different applications extensively. This work presents the first attempt to employ unsupervised clustering algorithms within algebraic multiscale methods to accelerate reservoir simulation. This is different from traditional surrogate models or

neural-network-based models that generally require a lot of training and testing data to obtain a generic model suitable to all simulation cases.

The chapter is structured as follows. First, the conservation of mass system to compute pressure along with the algebraic multiscale solver employed in this work is described. Then the graph-based clustering algorithms are introduced. The two algorithms, Louvain and Markov clustering, are elaborated. Several numerical experiments are further presented with increasing complexity by using the above two algorithms and comparing the solver performance with the existing METIS package. Finally, concluding remarks are presented.

6.2. GOVERNING EQUATIONS

In this work, the conservation of mass equation for single-phase incompressible flow is solved to compute fluid pressure across the reservoir. It reads as

$$-\nabla(\lambda \cdot \nabla p) = q + \nabla(\rho g \lambda \cdot \nabla h). \tag{6.1}$$

Here p is the pore pressure, λ is the positive definite mobility tensor, q is the source term, g is the gravitational acceleration, ∇h is the depth and ρ is the density of the fluid. The conservation of mass equation is solved to compute the pressure in the reservoir domain as dictated by the location of the wells.

Applying finite volume (FV) discretisation scheme and integrating the mass conservation equation over a control volume, the fine-scale FV system can be used to solve for incremental pressure (Δp). In the residual format, it can be written as

$$\boldsymbol{J}\Delta p = \boldsymbol{r} \tag{6.2}$$

To improve the computational efficiency, a multiscale system is developed as presented in next section.

6.3. MULTISCALE SOLVER

In this section, the AMS method which was extensively researched in the past, is briefly elaborated. Recently, the AMS method was also released in the commercial simulation space [414–416]. The approximate incremental fine-scale pressure p_f can be written in terms of incremental coarse-scale pressure p_c using the prolongation operator $\boldsymbol{P}$ as

$$\Delta p_f = \boldsymbol{P}\Delta p_c. \tag{6.3}$$

The prolongation operator is $\boldsymbol{P} = [N_1, N_2 ... N_H]$ where the number H is the number of coarse blocks in the domain (user defined) and p_f is the approximate fine-scale pressure solution obtained from AMS. This number and locations of the coarse grids are obtained from unsupervised learning methods in this work. The pressure increment is computed as

$$(\boldsymbol{RJP})\Delta p_c = \boldsymbol{R}r. \tag{6.4}$$

Here $\boldsymbol{R}$ is the restriction operator. The prolongation operator is computed from the finite volume Restriction matrix $\boldsymbol{R}_{FV}$ that is given by

$$\boldsymbol{R}_{FV} = \begin{cases} 1, & \text{if } x_i \in \Omega_j^b \\ 0, & \text{otherwise.} \end{cases} \tag{6.5}$$

Here Ω_j^b is the jth coarse grid. In this chapter, the multiscale finite volume prolongation matrix is computed in an iterative manner. The prolongation operator ($\boldsymbol{P}$) is computed iteratively by employing steady-state formulation which is computed from the Jacobians. Initially the prolongation operator is set as $\boldsymbol{P}^0 = \boldsymbol{R}^T$, which is further modified iteratively as

$$\boldsymbol{P}^{n+1} = \boldsymbol{P}^n - \mathscr{M}(\omega \boldsymbol{D}_b^{-1} A_b \boldsymbol{P}^n). \tag{6.6}$$

Here A_b is computed by regularizing the fluxes over the interface which is given by

$$A_b = \frac{1}{2}\Big\{\boldsymbol{J} + \boldsymbol{J}^T - \text{diag}[(\boldsymbol{J} + \boldsymbol{J}^T)\boldsymbol{1}].\Big\} \tag{6.7}$$

Here $\boldsymbol{D}_b$ is the diagonal of A_b, ω is the relaxation factor, $\mathscr{M}$ is the function which modifies the incremental pressure ensuring that the basis function is limited to the support region. Once the prolongation operator is computed, the restriction operator is defined as $\boldsymbol{R} = \boldsymbol{P}^{-1}$ similar to the finite element multiscale method. The detailed procedure can be found in [276, 416, 417].

For all the testcases, clusters were employed in the multiscale solver. Each cluster of cells forms a coarse block and will possess a corresponding basis function centered within it. The support of the basis function is the coarse block and includes a "halo" consisting of three layers of neighbouring cells surrounding it. This halo overlaps with the support areas of adjacent basis functions, resulting in off-diagonal elements within the coarse-scale system. The thicker the halo, the bigger the support and overlap, consequently increasing the density of the coarse-scale stencil. While a dense stencil might offer a more accurate portrayal of the pressure problem's global nature, it can also lead to solving a more difficult rigid coarse linear system. The computation of the basis functions follows the iterative MsRSB procedure [417]. In the next section, graph clustering algorithms employed to generate the multiscale grid is elaborated.

6.4. GRAPH CLUSTERING ALGORITHMS

Graph clustering is a technique in data analysis and machine learning that involves grouping similar nodes in a graph into clusters. A graph is a mathematical representation of a network, consisting of a set of nodes and edges connecting them. Clustering allows us to identify groups of nodes that are densely connected to each other within the graph, while being sparsely connected to nodes outside the group. In this work the Louvain algorithm and MLR-MCL have been employed and are elaborated below.

6.4.1. LOUVAIN ALGORITHM

The Louvain algorithm is based on optimizing a parameter called modularity. It is suitable for directed and weighted graphs. It is already a proven scalable algorithm, which can cluster millions of nodes within seconds. Figure 6.2 shows the schematic of the Louvain algorithm applied in multiscale methods.

Initially, the fine-scale domain is converted to a weighted and directed graph. Then, based on modularity optimization, the initial set of similar nodes are identified. Modularity is expressed as [418]

$$M = \frac{1}{2m}\sum_{i,j}[A_{ij} - \frac{t_i t_j}{2m}]\delta(v_i, v_j) \tag{6.8}$$

v_i is the community to which vertex i is assigned, $\delta(v_i, v_j) = 1$ when $v_i = v_j$ else $\delta(v_i, v_j) = 0$. Here t_i, t_j are the sum of weights of edges attached to the nodes of i and j, A_{ij} represents the weight of the edge between i and j nodes, $m = \frac{1}{2}\sum_{ij} A_{ij}$. The range of modularity is between 0 and 1. After modularity optimization, the nodes are aggregated to form a new cluster that results in a network with aggregated nodes. The pseudo-code of this algorithm can be seen in [403].

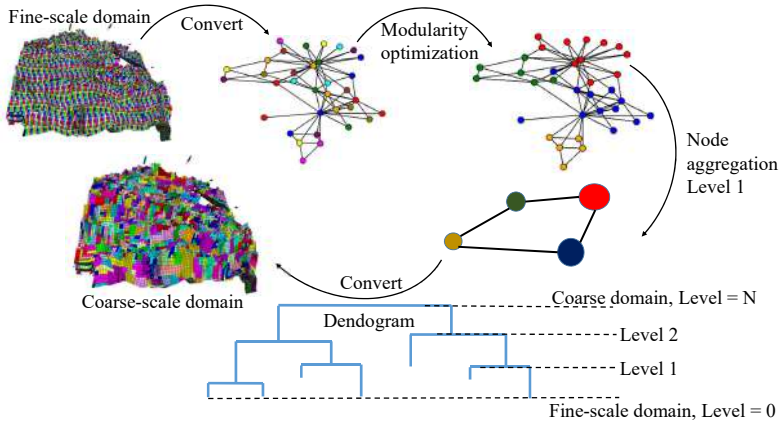

Figure 6.2: Illustration of Louvain algorithm.

The Louvain algorithm outputs the number of clusters at each level of the dendogram. There are several parameters, such as the optimization tolerance, which is the minimum increase to enter a new modularity optimization, the number of aggregations, which is the level of the dendogram at which the user is requesting. These parameters affect the number and shape of the clusters. Depending on these parameters for each level of dendogram, different numbers of clusters are output. Accordingly, the user chooses the dendogram level to obtain a certain number of clusters. Once the number of clusters are output, the cluster number and the number of cells in the respective cluster will be employed to solve the algebraic multiscale system. In this work, the Louvain algorithm

package deployed in the scikit network was employed [403, 419, 420]. The default values of parameters in these packages were reasonable to get a good estimate of the number of clusters. The edge and node weights employed for this algorithm are transmissibility and porosity, respectively. To accommodate the effect of transmissibility and porosity equally, all the weights are normalized.

6.4.2. MLR-MCL ALGORITHM

MLR-MCL is the other method that was employed in this study, which uses expansion and inflation operators. The method performs deterministic random walks through the network graph using the two operators by converting one set to another to identify the nodes in the same cluster. In this work, an extension of Markov clustering which is Regularized multi-level Markov clustering as employed by [405] is used. The schematic can be seen in Figure 6.3. The graph-based representation of the fine-scale domain is coarsened using edge-matching techniques, then the coarsest graph is obtained. By employing Markov clustering on the coarse graphs, aggregated clustered graphs are identified. Further, depending on the user conditions, the number of clusters are obtained. This is further translated to the coarse-scale domain. This algorithm is applicable to undirected and unweighted graphs.

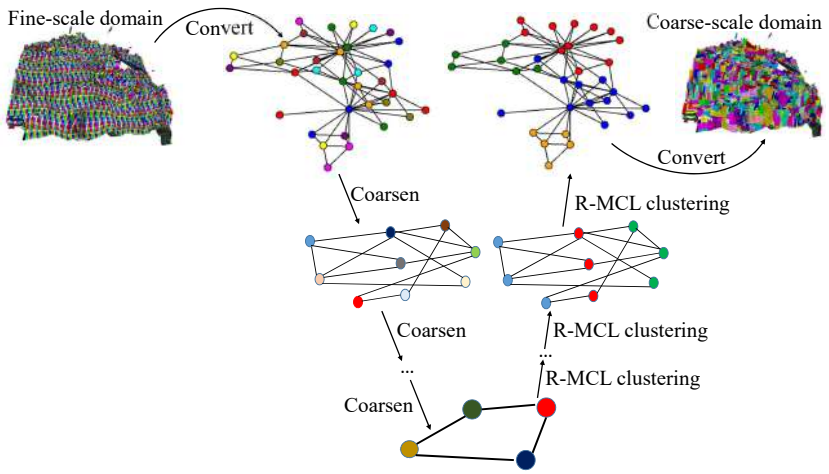

Figure 6.3: Schematic of MLR-MCL algorithm.

6.5. NUMERICAL EXPERIMENTS

In this section, METIS, MLR-MCL and Louvain algorithm are compared based on the performance of the simulator. Pressure iterations of the linear solver and the time taken to solve for the pressure solution are the two parameters chosen for comparison. In the

increasing level of complexity, the following test cases are ordered.

6.5.1. TEST CASE A

This is a small homogeneous test case that has 300 fine grid cells and 100 coarse blocks from the METIS algorithm. Louvain clustering and Markov clustering also output 100 coarse blocks with similar coarse grid structure as seen in Figure 6.4. The performance of the solver for different algorithms is shown in Table 6.1. Here the coarse blocks are grouped vertically because of more dominant connections compared to the horizontal ones. In the vertical (z) direction, there are 3 cells, while in the horizontal (x and y) directions, there are 10x10 cells each. The various colors within the grid indicate distinct coarse cells that have been clustered in the z direction. This implies that each coarse block cell consists of 3 finer cells. Upon visual inspection, it's evident that the quantity of coarse block cells is consistent across all three algorithms, and they are also arranged in the same manner, aligning with the z-direction. The computational performance and the time shown by all the algorithms are similar.

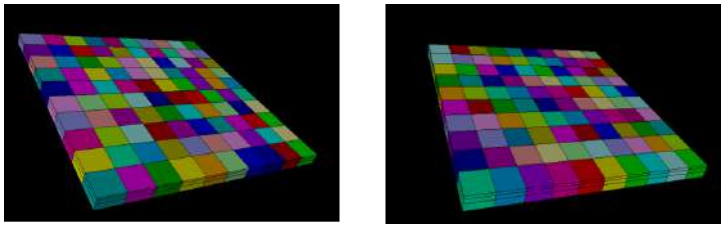

Figure 6.4: Coarse grid obtained from METIS (left) and MLR-MCL (right) simulation for this test case.

Table 6.1: Comparison of solver performance for different algorithms with number of fine cells = 300 cells. Nc is the number of coarse cells.

Algorithm	Linear pressure iterations	Pressure solution [s]	Nc
METIS	854	0.7	100
Louvain	867	0.6	100
MLR-MCL	867	0.6	100

The computational performance and time shown by all the algorithms are similar. The effect of adding weights to METIS and Louvain algorithms did not show any improvement in the performance of the solver because of a highly simplified testcase. This testcase builds confidence in the employed algorithms because of similar computational performance compared to traditional algorithm METIS.

6.5.2. TEST CASE B

The reservoir is medium-sized, geometrically complex, and heterogeneous in nature in this test case.

Table 6.2: Comparison of solver performance for different algorithms with number of fine cells = 79423. (EW: Edge weight, NW: Node weight). Here M is modularity. Lowest linear pressure iterations and least pressure solution time is bolded.

Algorithm	Linear pressure iterations	Pressure solution [s]	Nc
METIS	**507**	35.1	4019
METIS (+EW)	531	38.7	4700
METIS (+EW + NW)	541	35.4	4200
Louvain [$M = 0.67$]	654	**32.8**	3028
Louvain (+EW) [$M = 0.965$]	786	38	3516
Louvain (+EW + NW) [$M = 0.978$]	693	34.2	3206
MLR-MCL	580	37.8	4415

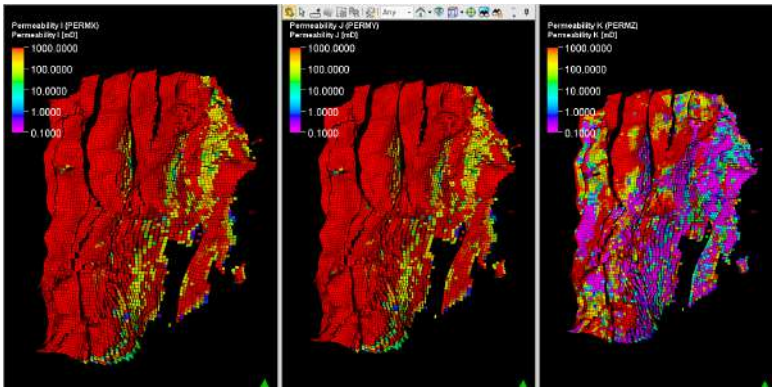

Figure 6.5: Permeability fields in x, y and z directions from left to right respectively for this testcase

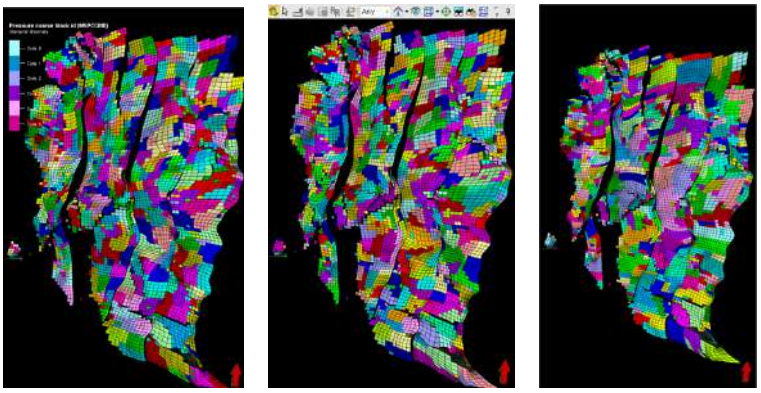

(a) METIS (b) Markov clustering (c) Louvain clustering

Figure 6.6: Coarse grids obtained from the clustering algorithms for this testcase.

The number of fine cells is 79423 and the number of coarse block cells is slightly dif-

ferent for different algorithms. The permeability fields in the x,y, and z directions are shown in Figure 6.5. The range of permeability is between 0.1 mD to 1000 mD. The coarse blocks obtained from the three algorithms are shown in Figure 6.6. The performance of the solver and the number of coarse blocks for different algorithms are shown in Table 6.2. The coarse blocks as shown in Figure 6.6 depict the grids for METIS, Markov clustering, and Louvain clustering. The coarse grids look similar for METIS and MLR-MCL; however, the coarse grids for the Louvain algorithm show nonuniform-sized coarse blocks with different numbers of fine cells. The METIS algorithm was found to have the fewest linear pressure iterations, but the Louvain algorithm was found to have the least pressure solution time. This means that the pressure solver performance was improved. The number of coarse blocks for these algorithms is slightly different, which could be causing the change in the performance of the pressure solver.

To gain a deeper insight into the distinctions within the coarse grid arrangement of these algorithms, a statistical assessment is conducted across these datasets. This comparison is visualized through violin plots, depicted in Figure 6.7.

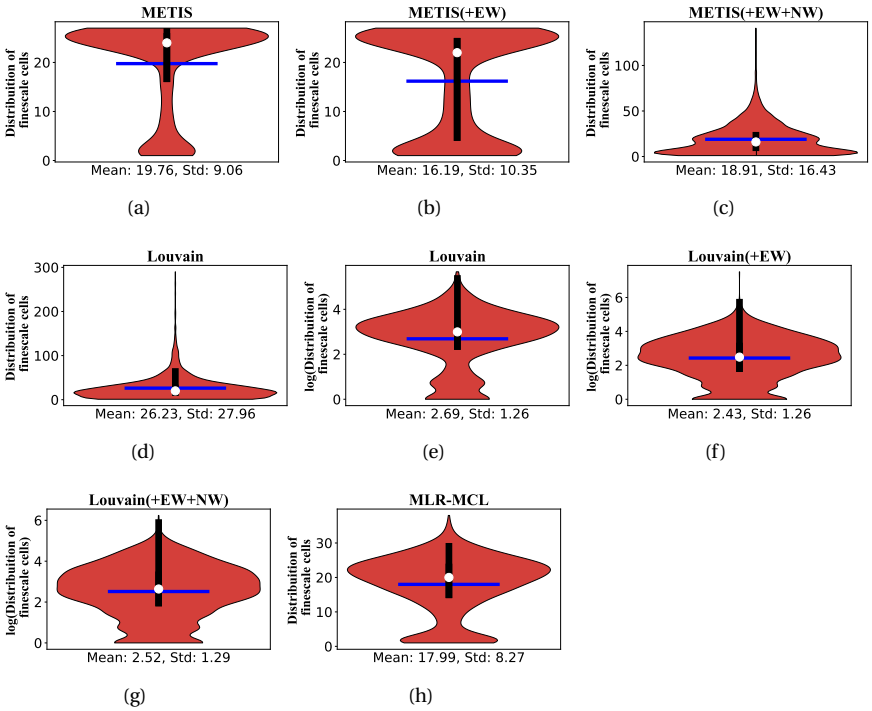

Figure 6.7: Violin plots of test case B showing the distribution of finescale cells for each of the algorithm employed. The white dot and the blue horizontal line represents the median and mean respectively. The black box represents 25 to 75 percentile of the data. Figures 6.7(e), 6.7(f) and 6.7(g) shows the distribution in log scale for Louvain algorithm.

These visualizations illustrate how the distribution of fine-scale cells varies for METIS

when considering weight inclusion, for Louvain with weight consideration, and for the MLR-MCL algorithm. Within these plots, the median is denoted by a white dot, the mean is represented by a blue line, and the interquartile range is shown by a black box. Moreover, the plots also display the mean and standard deviation values for each case. As seen in Figures 6.7(a), 6.7(b), and 6.7(c), these plots display the distribution of fine-scale cells for the METIS algorithm without any weights, with edge weights (EW), and with both edge and node weights respectively. It's evident that in the cases of METIS and METIS (+EW), the data exhibits a higher-tailed distribution on both sides, with sparser distribution in the central region. Disregarding the outliers, the median (represented by a white dot) indicates that there are roughly 20+ cells in the coarse cell region. When node weights (porosity) are included, the distribution becomes more heavily tailed, with certain outliers showing a high number of fine-scale cells in coarse cells.
Turning to the Louvain algorithm (Figure 6.7(d)), it shows a centred distribution with heavier tails, wherein numerous coarse cells have large number of fine-scale cells compared to other algorithms. To enhance the clarity of this data, a logarithmic distribution of cells is presented, wherein the distribution shows to approximate a normal distribution. This trend remains consistent across all variations of the Louvain algorithm, even when edge and node weights are included. This adherence to log-normal distribution signifies that the algorithm tends to favour large number of fine-scale cells within coarse grids. This is in line with existing literature [421] where modularity-based algorithms favor larger communities. In the case of the MLR-MCL algorithm (Figure 6.7(h)), the distribution appears to be more uniformly distributed. The mean values for METIS and MLR-MCL algorithms are similar with a small standard deviation. However for Louvain algorithm, the mean value and standard deviation values are similar showing the skewness of the data. Another interesting observation is that the standard deviation is least for MLR-MCL algorithm compared to other algorithms which means that the distribution is less spread out and uniform spaced. The data also shows a larger quartile region (data from 25 percentile to 75 percentile) for Louvain algorithm compared to METIS and the least for MLR-MCL algorithm showing the heterogeneous coarsening ratio distribution.

To assess the strength of the coupled system, we examine the matrix's connectivity bandwidth, which represents the average count of non-diagonal elements within the rows. The higher the bandwidth the stronger the coupled system. Figure 6.8 shows the variation of numbers of coarse cells with the connectivity bandwidth of the algorithms.

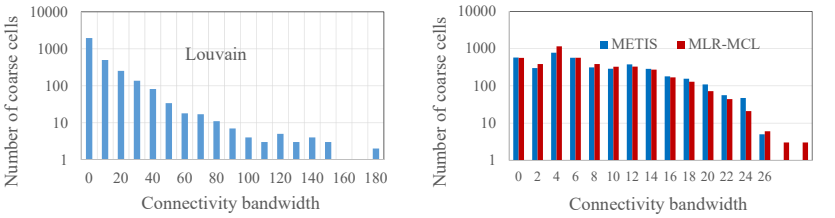

(a) Louvain algorithm

(b) METIS and MLR-MCL algorithm.

Figure 6.8: Bandwidth of the matrix obtained from the three algorithms.

6.8(a) shows higher bandwidth compared to the 6.8(b) because the output of the Louvain algorithm shows many large coarse blocks adjacent to the much smaller ones. The Louvain algorithm optimizes the number of coarse blocks based on the modularity parameter. So based on adding weights (edge and node), the ease at which the clusters could be identified is reflected in parameter modularity. When edge and node weights are accounted for, the modularity of the Louvain algorithm increases as seen in Table 6.2, which suggests that it is easier to coarsen the computational grid. However, this trend was not observed in the computational solver performance. This could be case dependent or, because the solver is highly complex, the inclusion of weights was not a dominant factor.

6.5.3. TEST CASE C

This is a medium-sized reservoir with 584220 fine cells and with heterogeneous permeability fields as shown in 6.9(a). The resulting coarse block from METIS is shown in 6.9(b). Visually it is not possible to see the difference in the coarse grids obtained from different algorithms. The performance of the solvers is shown in Table 6.3.

Table 6.3: Comparison of solver performance for different algorithms with number of fine cells = 584220. The highlighted numbers show the lowest pressure iterations and least pressure solution time.

Algorithm	Linear pressure iterations	Pressure solution [s]	Nc
METIS	10957	5835.6	11.7 k
Louvain	**8765**	5009.8	12.02 k
MLR-MCL	9317	**4828.8**	12.04 k

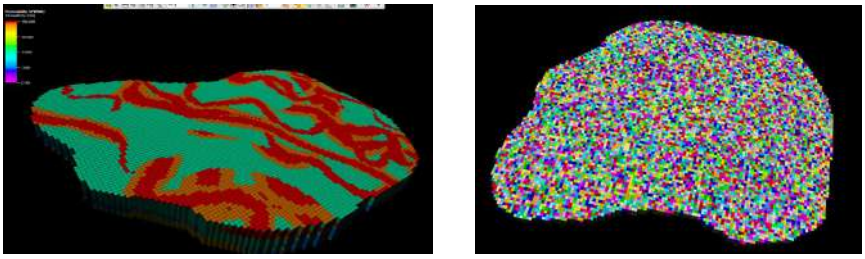

(a) Permeability (b) Coarse block.

Figure 6.9: Permeability (x direction) and coarse grid obtained from METIS.

Similar to the previous testcase, the number of linear pressure iterations are least for the Louvain algorithm. The pressure solution is also low for the MLR-MCL and Louvain algorithms compared to the traditional METIS algorithm. The number of coarse blocks is roughly the same as obtained from the algorithms. The difference in the number of coarse blocks is less than 3 %. The dissimilarities in the coarse grid structures of each of these algorithms were also studied using violin plots. Similar to the prior test case, the Louvain algorithm demonstrated a distribution with heavy tails, revealing a subset

of coarse-scale cells containing a considerable number of fine-scale cells. The MLR-MCL algorithm exhibits the lowest standard deviation, indicative of a distribution with uniformly spaced characteristics.

Figure 6.10 shows the bandwidth obtained from these algorithm. Though the connectivity bandwidth is higher for the Louvain algorithm there are few outliers which are mainly due to few large sized coarse blocks next to small sized coarse blocks.

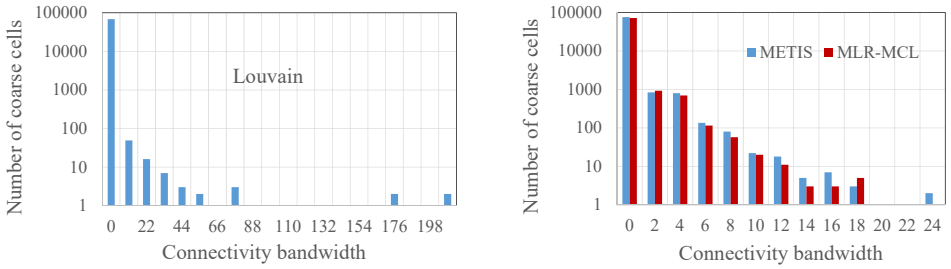

(a) Louvain algorithm

(b) METIS and MLR-MCL algorithm.

Figure 6.10: Bandwidth of the matrix obtained from the three algorithms.

6.5.4. TEST CASE D

This is another testcase with 2.36 million cells that was solved for using 32 cores in parallel using openMPI. This is the refined version of the previous reservoir testcase. The performance of the solver is shown in Table 6.4.

Table 6.4: Comparison of solver performance for different algorithms with number of fine cells = 2.36 million.

Algorithm	Pressure iterations	Pressure solution [s]	Nc	Elapsed time per iteration [s]
METIS	**10775**	1036.3	77.6 k	0.096
Louvain	12633	**964.65**	69 k	0.0763
MLR-MCL	11808	974.15	74.5 k	0.0824

Similar to the previous testcases, though the number of linear pressure iterations are lower for METIS algorithm, lower pressure solution time was observed with Louvain and MLR-MCL algorithms. The lower cost per iteration suggests that the clustering algorithms produce higher quality coarse grids than METIS.

Upon comparing the performance characteristics across all the aforementioned test cases, it becomes evident that, for simpler and smaller test cases (Testcase A and B), the performance of the Louvain or MLR-MCL algorithms is comparable to that of the traditionally employed METIS algorithm. Nevertheless, as the scale of the test cases in-

creases (Testcase C and D), the performance of the MLR-MCL and Louvain algorithms appears to hold a competitive advantage over the METIS algorithm, exhibiting a performance gain of over 8%. This upper hand observed in larger test cases is a consequence of the relatively more pronounced impact of employing a coarse scale grid. Although this percentage gain might seem modest, it holds significance in the context of commercial software aimed at solving complex problems for extensive test cases. Any enhancement in the performance of solving the coarse system, regardless of its size, is a valuable asset. It is worth acknowledging that the scalability features and the automatic determination of the coarsening ratio by these algorithms satisfy the requirements of the task at hand. Considering that this marks the inaugural effort to improve the coarse grid structure within an algebraic multiscale algorithm applied to unstructured grids using clustering algorithms, it paves the way for potential avenues of research aimed at optimizing the upscaled grid using machine learning techniques.

6.6. CONCLUSION

This chapter revolves around the novelty of implementing unsupervised learning graph based methods to generate coarse block grids in the algebraic multiscale methods for the first time. This method could also be extended to other upscaling methods such as multigrid methods. Advanced algorithms such as the Louvain and Multi-level Regularized Markov clustering algorithms were implemented into a commercial reservoir simulator to run several test cases. A few conclusions which are drawn are

- For small and simpler field test cases, conventional graph cut-based algorithms such as METIS showed similar performance as Louvain and MLR-MCL algorithms. However, the unsupervised learning algorithms had an upper edge in terms of computational time for larger and heterogeneous test cases compared to the traditional graph-cut-based METIS algorithm. Based on the violin plots (statistical analysis), it could be seen that the Louvain algorithm showed more skewed data implying that the algorithm favours bigger coarsening ratio coarse grid cells and MLR-MCl algorithm showed a more uniform distribution.
- The advantage of these algorithms is that they are highly scalable and automatically determine the number of coarse blocks, eliminating the need for users to input this information as required in the METIS algorithm-based commercial solvers. This is particularly beneficial for users who may not be familiar with upscaling.
- The impact of adding edge and node weights to the graph was evident in clustering metrics such as modularity and edge cut, showing higher modularity (easier clustering) when weights were included. However, despite this positive correlation, there was no noticeable enhancement in solver performance, possibly due to the heterogeneity of the testcases.
- In general, when dealing with large and heterogeneous test cases, these unsupervised graph-based methods demonstrate superior performance in generating a coarse grid structure compared to the conventional method known as METIS. This is evident in terms of improved computational efficiency.

7

CONCLUDING SUMMARY AND FUTURE PERSPECTIVES

7.1. CONCLUSION

UHS is a complex multidisciplinary field that requires a thorough understanding of the geological, mechanical, and geo-chemical processes involved for safe operations. In this thesis, firstly the geomechanical aspects of UHS in depleted reservoirs and salt caverns related to H_2 operations are thoroughly reviewed in chapter 1. The usage of the subsurface for storage purposes has a history of a few decades, during which a lot of experience has been accumulated, especially for natural gas storage and recently for CO_2. The practical field experience is fairly limited, especially for the loading conditions expected for the storage of green H_2 and its associated intermittent production. The history of the storage sites, relevance with previous storage knowledge, experimental studies, analytical models, and numerical simulations relevant to UHS were reviewed. Experimental studies relevant to UHS such as cyclic studies on rocks, the impact of loading signature on fault reactivation, biochemical reactions of rocks with H_2, and the effect of heterogeneity are studied. Considering the constraints of experimental studies, modeling studies in lab and field scale comprehending the gas storage sites in the past and studying their relevance to H_2 storage. Further, the well and borehole integrity was reviewed considering that the well infrastructure has different components which can behave differently with H_2 and further cause leakage from the wells. H_2 is more mobile compared to other gases, thereby having faster diffusion and being more prone to leakage. Therefore, reservoir selection criteria adopted for CO_2 or natural gases cannot be directly applied to prospective H_2 reservoirs. Optimizing the pressure fluctuation is critical for longer and safer operations. Accordingly, a "learn as you go" approach was suggested in the geomechanical perspective of H_2 storage.

Cyclic injection and production of H_2 are analogous to cyclic loading signatures on rocks that can undergo inelastic deformation under long-term cyclic loading. To study

the effect of long-term loading, initially, creep deformation of rocks was studied for porous rocks and rocksalt which accordingly is relevant for depleted gas fields and salt caverns. chapter 2 shows the importance of creep deformation in sandstone rock by employing power law as a creep constitutive model in FEM formulation. To upscale the system and improve the computational performance, algebraic multiscale methods were incorporated. Creep becomes a dominant type of permanent deformation when rocks experience cyclic loading for longer timescales (decades) which can compromise the safety of the reservoir due to high stresses in certain regions causing uplift or subsidence on the ground. Similarly, the impact of creep deformation was studied for rocksalt using 2D FEM simulations chapter 3. Since salt caverns have a smaller storage capacity compared to depleted gas fields, the effect of cyclicity can be more pronounced. Salt caverns are also known for their impermeable characteristics allowing them to be the first choices for storing any energy fluids. Steady-state creep was considered in the work to study the impact of irregular geometry, and heterogeneous interlayers with elastic and plastic properties around salt caverns. When there is excess energy produced, multiple caverns in the same region were studied. Using FEM simulations, the impact of distance between the caverns on the stresses was studied.

To further understand different types of inelastic deformations undergone by sandstone rock, cyclic experimental results were benchmarked with constitutive models as shown in chapter 4. Strain gauge measurements and acoustic emission data were employed as a reference to calibrate the constitutive models and further use them to predict. Two different regions, below the brittle point and above the brittle point were chosen to understand the effect of cyclic loading. Further, these constitutive models were employed in FEM formulation to study its behavior in a field scale test case inspired by the Bergermeer field in the Netherlands. To model this, the behavior of shale rock which is a caprock was modeled using viscoplasticity and further the rocksalt model was also integrated. Next, a poro-inelastic approach was introduced solving for both the conservation of mass and conservation of momentum simultaneously (FEM-FVM solver) in an implicit manner with creep deformation in chapter 5. To improve computational efficiency, an upscaled system with algebraic multiscale methods was employed. This would help in understanding the effect of pore-pressure injection and production. Algebraic multiscale methods have been employed in the past for different applications. In chapter 6, a first of a novel kind method was employed to integrate a graph-based unsupervised machine learning algorithm to coarsen the fine-scale grid in reservoir simulation software. Traditionally, many software uses METIS [393], however, using advanced algorithms such as Louvain and Markov clustering these algorithms gives us more insight into the connectivity of the cells and further improves the computational speed.

7.2. RESEARCH RECOMMENDATIONS

The work presented in this thesis will definitely serve as a detailed introduction to the relevance of mechanics, inelastic deformation, and upscaling techniques in reservoir simulation for UHS. As UHS is a budding topic, there are numerous research recommendations that can be provided in different scientific contexts. Considering the geo-mechanical perspective here are the detailed research recommendations:

7.2.1. DEPLETED OIL AND GAS FIELDS

- Effect of pressure and temperature of the injected H_2 on reservoir stability should be analyzed in detail through both lab-scale and field-scale trials. Area of influence and effect of the pressure and temperature fluctuations closer to the injection wellbore should be constrained and the resultant influence on stress configuration and fault reactivation should be emphasized.

- The effect of biofilm growth and chemical interaction between reservoir rocks and microbes on reservoir mechanical properties needs further investigation. More emphasis should be given to studies conducted at reservoir equivalent temperature, pressure, saturation (H_2 and brine), pH, and salinity conditions.

- Heterogeneity in reservoir rocks and especially heterogeneity in caprocks plays a critical role in governing reservoir efficiency and leakage potential. Detailed analysis of time-dependent deformation in both reservoir rocks and caprocks should be carried out at in-situ P-T conditions for developing a concrete idea of the operating window for the rate and pressure of H2 injection and production.

- There is still no consensus in terms of the validity of the Kaiser effect in H_2 reservoirs and caprocks, which will, in turn, govern the mechanism of H_2 injection as a pore fluid. More lab experiments and field-scale research should be analyzed to establish a governing relationship between seismicity and H_2 injection strategies.

- Understanding the chemical reactivity of H_2 and brine with reservoir rocks is extremely important. Contaminant gases and organic acids forming in reservoirs due to microbial influence can have higher reactivity towards reservoir rocks compared to H_2 itself. Such clarity should be developed before attempting field-scale operations.

- Usually, all the constitutive models are developed based on data obtained from tests with external loading (triaxial or uniaxial). However, loading caused by cyclic injection and production of H_2 in porous rock will give more insight into the variation of deformation which can also depend on the type of stored liquid, as it reflects better the type of loading experience by the reservoir.

- Performing progressive swelling and shrinkage cycles in lab-scale using H_2 as the fluid is imperative to enhance understanding of the behavior of rocks. The sensitivity of swelling in different clay minerals and carbonates should be studied to scope appropriate host rock for H_2. Understanding the competitive sorption of H_2 in the presence of different brine compositions should be given paramount importance.

- Coupled hydro-mechanical modeling of field scale reservoir sites with faults and fractures, solving not only for elasticity but also plasticity, under imposed cyclic injection and production of H_2, would be very important to perform sensitivity analysis of the reservoir by studying the impact of different parameters.

- Reservoir and caprock integrity tests should be performed using risk-based probabilistic methods such as Monte-Carlo simulations which can help in quantifying the effect of different input parameters and in detecting critical regions such as high-stress regions or leakage pathways.
- Effective monitoring methods need to be investigated to allow for the assessment of long-term UHS with the partially unknown characteristics of cyclic loading. The efficacy of advanced monitoring techniques such as time-lapse seismic surveys or fiber-optic sensors should be tested to ensure continuous safe storage.

7.2.2. SALT CAVERS

Although salt caverns have been used for many years for storage purposes and the understanding of the mechanics of rock salt has matured, there are still some particular unknowns when it comes to H_2 operations. Most of these issues are related to the H_2 properties and the loading conditions associated to the intermittent energy production. In what follows, we list some topics that would require further investigation. Because of its low viscosity and small molecules, H_2 can percolate through the cavern walls, especially in regions operating in the dilatancy zone. Based on this scenario, we suggest the following topics for further research:

- If H_2 percolates the cavern walls, there will be a pore pressure build-up. Consequently, it affects the effective stresses acting on the salt rock. This effect should be characterised and quantified in order to keep the stress levels under control.
- The presence of H_2 around salt grains can dry up the water-bearing grains. Although it can substantially reduce pressure solution creep, this is not expected to be important in the near wall region. However, the healing effect is important and it can be highly affected by the presence of H_2. Therefore, further research on the salt healing capacity in the presence of H_2 would be of high interest.
- It is also not clear how the presence of H_2 can affect the position of the long- and short-term boundaries of rock salt. If the area of the compressibility region is reduced, the cavern could undergo, for instance, unexpected long-term failure (tertiary creep).

The main reason for developing hydrogen storage systems is to use them as a buffer for the intermittent energy produced from renewable sources. Consequently, the cycles of injection/production for hydrogen operations are much faster than for other storage materials. These loading conditions are relatively new for salt cavern operations and need to be carefully taken into account. Some related topics for further research are listed below.

- Additional lab experiments considering cyclic loads with frequencies compatible with field operations are still of interest. Not only with respect to load levels (maximum and minimum pressure) but especially in terms of loading rates. This is important to establish the maximum injection or production rates that can be imposed inside the cavern.

- The cyclic pressurization of H_2 inside the cavern can cause temperature variations. It is not totally clear how the fatigue life of rock salt is affected by temperature, so this would also be of interest.
- As mentioned before, to meet the energy storage demand, multi-cavern systems may be developed. The effect of fast cyclic loading on multi-cavern systems is an important aspect to investigate in order to ensure safe operation.

7.2.3. WELLS

- Geochemical and microbial reactivity of H_2 can release sulfides and other reactants. This effect on the wellbore components should be studied at a laboratory scale and with numerical models implementing the kinetics of the chemical reactions because of the additional products caused by longer timescale reactions of H_2.
- Effective low-cost continuous monitoring methods to detect H_2 leakage from the wells should be researched upon, which helps in identifying the weak regions in the well infrastructure and further avoid losses.
- Develop standards for different materials and admissible flow velocities used in the wellbore infrastructure relevant for UHS based on the required mechanical and thermal properties to avoid leakage.
- Explore alternative materials and coatings for the casing of existing (legacy) wells, particularly those designated for Underground Hydrogen Storage, when installing new tubing is not feasible.
- Simulation studies on the effect of repetitive cycling of pressure and temperature on cement for longer periods will help in determining suitable mechanical and thermal properties of cement sheath along with its durability.
- Investigate the compatibility of standard equipment for measurements and monitoring in the presence of hydrogen to ensure its safe and efficient implementation.

A

ANALYTICAL SOLUTIONS OF POROELASTICITY

A.1. TERZAGHI TEST CASE

Fine scale solution can be validated with Terzaghi test case [375, 422] in 1D domain which describes the fluid saturated column of height L with constant loading applied from top. Terzaghi's principle states that when a rock is subjected to stress, it is opposed by the fluid pressure of pores in the rock. The variation of pressure and displacement due to external load can be studied using different model parameters. The analytical solution is obtained from [423]. In 3D, the problem can be solved by using solving it along the z axes.

$$p(z,t) = \frac{4}{\pi} p_0 \sum_{m=0}^{\infty} \frac{1}{2m+1} \exp\left[\frac{-(2m+1)^2\pi^2 c t}{4L^2}\right] \sin\left[\frac{(2m+1)\pi z}{2L}\right] \tag{A.1}$$

$$u(z,t) = c_M p_0 \left((L-z) - \frac{8L}{\pi^2} \sum_{m=0}^{\infty} \frac{1}{(2m+1)^2} \exp\left[\frac{-(2m+1)^2\pi^2 c t}{4L^2}\right] \cos\left[\frac{(2m+1)\pi z}{2L}\right)\right) + u_0 \tag{A.2}$$

where,

$$p_0(z) = \frac{\alpha M}{K_u + \frac{4\mu}{3}} P_L \tag{A.3}$$

$$u_0(z) = \frac{1}{K_u + \frac{4\mu}{3}} P_L (L-z) \tag{A.4}$$

Here, $M = \frac{1}{\phi\beta + (\alpha-\phi)c_{br}}$ is the Biots modulus, α si equal to 1, c_{br} is the solid grain compressibility, $K_u = \lambda + \frac{2\mu}{3} + \alpha^2 M$ is the undrained bulk modulus, $c_m = \frac{1}{\lambda+2\mu}$ the vertical uniaxial compressibility and $c = \frac{k}{\rho g(M^{-1}+\alpha^2 c_M)}$ is the consolidation coefficient expressed in [cm^2/s].

A.2. MANDEL TEST CASE

During compression of poroelastic specimen under constant boundary conditions, the pore pressure will display non-monotonic variation with consolidation time. Initial time steps, the pore pressure will increase which would be induced near the centre of the sample when it is subjected to vertical load and laterally drained. Subsequently the pressure would fall. As lateral drainage takes place, the non-uniform dissipation of induced pore pressure causes softening of the material near the edges of the sample. This would result in reduction in pore pressure.
For 3D domain in poro-elasticity, Mandel problem can be applied for 3D domain which involves a homogeneous poro-elastic slab saturated with fluid. This is bounded by boundaries which involves the following boundary conditions.
Similar model parameters as [424] is considered for easier comparison. For the modelling parameters $E = 10^4$ Pa, $\nu = 0.2$, Biots modulus $M = 10^{100}$ which would simulate the incompressible fluid and rock properties. For rock permeability of $K = 10^{-7}\ m^2$ and fluid viscosity of $\mu_f = 10^{-3}$ Pa s. The Biot's coefficient of $b = 1$ which implies strong coupling of flow mechanics system. For 3D domain the middle point of the solid si considered and the pressure distribution over fine-scale with respect to time is compared.
Fully drained is a condition under which water is able to flow into or out of a mass of soil in length of time that soil is subjected to some change in load. **Fully undrained** condition is when there is no flow of water into or out of mass of soil in length of time that soil is subjected to some change in load. Change in load causes changes in pore water pressure because water cannot move into or out in response of volume change.
The equations for analytical problem as presented in [425–427],

$$K_{dr} = \frac{E}{3(1-2\nu)} \tag{A.5}$$

$$K_{one} = K_{dr} + \frac{4}{3}\mu \tag{A.6}$$

$$c_v = \frac{\lambda_{flow} M_b K_{one}}{K_{one} + b^2 M} \tag{A.7}$$

$$t_{end} = t_c = \frac{\mathrm{L}_x^2}{C_v} \tag{A.8}$$

$$\text{Force} = \text{load} \times L_x \times L_z \tag{A.9}$$

load is the input parameter which is used to calculate forces and pressure.

$$K_{dr} = \frac{E}{3(1-2\nu)} \tag{A.10}$$

$$B = \frac{bM_b}{K_{dr} + b^2 M_b} \tag{A.11}$$

$$\nu_{\text{undrained}} = 3\nu + \frac{bB(1-2\nu)}{3-bB(1-2\nu)} \tag{A.12}$$

Analytical model equations for pressure and displacements are obtained. Initial pressure as given by

$$P = \frac{1}{3L_x} B(1+\nu_{\text{undrained}})\text{Force} \tag{A.13}$$

Initial displacements at t=0 are,

$$u_x = \frac{F\nu_{\text{undrained}}}{2\mu L_x} x \tag{A.14}$$

$$u_y = -\frac{F(1-\nu_{\text{undrained}})}{2\mu L_y} y \tag{A.15}$$

The time dependent solutions for pressure and displacements are

$$p(x,y,t) = 2p_o \sum_{m=1}^{\infty} \frac{\sin\alpha_m}{\alpha_m - \sin\alpha_m \cos\alpha_m} \times \Big(cos[\frac{\alpha_m x}{L_x}] - \cos\alpha_m\Big) exp\Big[-\frac{\alpha_m^2 c_v t}{L_x L_y}\Big] \tag{A.16}$$

$$\begin{aligned} u_x(x,y,t) = \Big[\frac{F\nu}{2\mu L_x} - \frac{F\nu}{\mu L_x} \sum_{n=1}^{\infty} \frac{\sin\alpha_m \cos\alpha_m}{\alpha_m - \sin\alpha_m \cos\alpha_m} \times exp\Big(-\frac{\alpha_m^2 c_f t}{a^2}\Big)\Big] x \\ + \frac{F}{\mu} \sum_{m=1}^{\infty} \frac{\cos\alpha_m}{\alpha_m - \sin\alpha_m \cos\alpha_m} \sin\frac{\alpha_n x}{a} \times exp\Big(\frac{-\alpha_m^2 c_v t}{a^2}\Big) \end{aligned} \tag{A.17}$$

$$u_y(x,y,t) = \Big[-\frac{F(1-\nu_{\text{undrained}})}{2\mu L_x} + \frac{F(1-\nu_u)}{\mu a} \sum_{m=1}^{\infty} \frac{\sin\alpha_m \cos\alpha_m}{\alpha_m - \sin\alpha_m \cos\alpha_m} \times exp\Big(\frac{-\alpha_m^2 c_v t}{a^2}\Big)\Big] y \tag{A.18}$$

Here $y-plane$ is $z-plane$ and c_v is the true diffusivity (generalized consolidation coefficient), α_m is the solution of the equation,

$$\tan\alpha_m = \frac{-\nu}{\nu_u - \nu} \times \alpha_m \tag{A.19}$$

is solved for range of α_m between (0,π).

B

SENSITIVITY ANALYSIS OF SALT CAVERNS

Creep is a complex phenomenon that involves various parameters that can influence the deformation and stresses over time. To quantify the impact of the critical parameters, sensitivity analysis needs to be conducted. The parameters chosen are cavern depth, creep constant, Young's modulus of halite rock, temperature, and creep exponent. Energy storage technology could involve different operating conditions and heterogeneous properties of rock salt. Due to this, the above parameters are chosen to study their influence on the time-dependent deformation. Fig. B.1(a) shows the two points (A and B) in the domain where sensitivity analysis is conducted. The influence of Young's modulus on horizontal deformation is shown in Fig. B.1(b). Change in Young's modulus changes the elastic deformation. Higher the Young's modulus, lower is the deformation. The salt cavern's far-field shows a lower slope than the node closer to the cavern because of higher stresses closer to the cavern. The sensitivity of deformation towards shear modulus is not shown here since it can be expected that the deformation is not sensitive towards it. Fig. B.1(c) shows the variation of horizontal deformation with different creep multipliers. Higher the creep multiplier, the higher the rate of change in deformation with time, leading to a higher accumulation of plastic deformation. The increase in creep constant is non-linearly increasing the deformation after a certain period.
The influence of temperature on deformation is seen in Fig. B.1(d). The higher the temperature, the higher is the accumulated creep deformation. Again, a similar trend is observed as the last plot where the temperature change is not linearly changing the change in deformation. The impact of creep exponent n is shown in Fig. B.1(e). The higher the creep exponent, the higher is the deformation. Compared to creep constant and temperature, the creep exponent is very sensitive to the accumulated deformation. For $n = 3$ and $n = 3.25$ the variation of deformation with time is almost horizontal, however for the creep exponent, $n = 3.5$, the rate of change in deformation is very high. Comparing the sensitivity plots for the creep parameters, it can be seen that the influence of creep exponent is the biggest, followed by creep constant, and lastly, it is creep temperature. Fig

B.1(f) shows the variation of horizontal deformation with time for different depths of the cavern. In the geological domain with a lot of heterogeneity and interlayers, it is important to construct the cavern in the domain with minimum cracks and heterogeneity. The depth of the cavern is a parameter that can allow this argument. The higher the depth, the higher the lithostatic pressure leading to higher creep deformation.

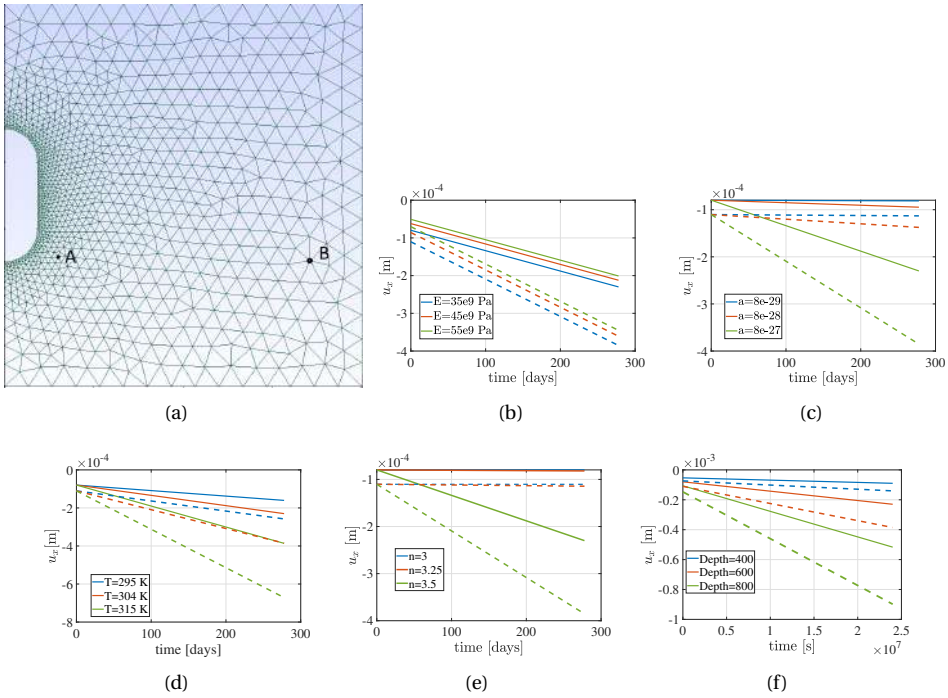

Figure B.1: The above plots show the variation of horizontal deformation at two different points A and B with time for different Young's modulus (E), creep constant (a), temperature (T), creep exponent n and depth of the cavern respectively. The dotted lines (- - -) show the variation for the node closer to the cavern (Point A) and the full lines (—) show the variation of deformation (Point B) in the far field of the cavern.

C

FIELD SCALE SUBSURFACE STORAGE STUDIES

Table C.1: Relevant field scale subsurface storage studies to understand the geomechancial impact

Reference	Objective	Characteristics	Summary
Shi et al. [428] *Eclipse 300 software*	Coupled hydromechanical simulation for CO_2 injection rates. Study potential for shear failure and activation of faults in Puchkirken formation (sandstone, shale and mudstones)	Depleted gas reservoir (Austria). Initial pressure 160 bar (depth 1.6 km).	Mohr Coulomb criteria was used assuming elastic response of the reservoir to simulate from 1963 to 2004. Tensile deformation of upto 2.1 cm was predicted for the pressure of 200 bar.
[5 ex] Vidal et al. [429] *IFP Finite volume simulator + Abaqus software*	Evaluate deformation, stresses and the potential effect on faults using one-way coupling in SMB field, France (carbonates, limestone, shale). Mohr coulomb analysis was used to determine fault slip tendency.	Depleted carbonate reservoir (SMB field). Initial pressure 145 bar, temperature 65 C (depth 1.45 km)	Assuming linear elastic response, mechanical effects of injecting CO_2 showed no effect on caprock. A decrease in shear stress was observed during injecting CO_2.
Ouellet et al. [143] *Eclipse + VISAGE software*	3D MEM model (Mechanical earth model) is built by including geologic, seismic, logging, drilling and laboratory test data to study the effect of CO_2 injection (one way coupling) in Ketzin, Germany (claystone, dolomitic mudstones, anhydrites, halite).	Saline reservoir was simulated for 477 days. Pore pressure (61.5 bar)	Zechstein salt formation as caprock had to be included in the model due to its effect on initial stress field. No effect on faults stability was observed and a minimum subsidence of 5 mm was observed.
Bergermeer field [14, 430] *DIANA software*	Geomechanical dynamic analysis which includes elastic and viscoelastic model to incorporate seismic slip to assess the safety of the project is conducted by considering seismic log data for calibration.	Production from gas storage site Bergermeer (sandstone, rock-salt). Largest subsidence was observed to be 10.5 cm.	It showed that injection of gas in Bergermeer reservoir stabilizes the intersecting faults and time dependent viscoelastic model was necessary to capture surface heave caused due to cyclic injection and production.
Rinaldi et al. [142] *TOUGH-FLAC simulator*	Studying the effects of CO_2 leakage to shallow groundwater by considering stress strain dependent permeability and its effect on leakage rates through major and minor faults.	2D simulations of two scenarios simulated in an aquifer with configurations of undetected fault and long fault.	Poor correlation was observed between the induced seismicity events and the leakage of gas stored. Heterogeneity of rocks in subsurface showed decrease in risk of CO_2 leakage within the reservoir.
Teatini et al. [431] *GEPS3D simulator*	Study the geomechanical effects of sequestering CO_2 (1 Mt/yr) in compartmentalized offshore northern Adriatic sedimentary basin using 3D FE elasto-plastic simulator.	Aquifer (2km deep) Sandstone and shale rocks.	The effect of geomechanical constraints such as maximum allowable shear failure, initial stress regime, fault slopes was found to be critical to predict failure. Small variation of cohesion or internatl friction angle can change the rate of failure of CO_2 storage site.
Konstantinovskaya et al. [144] *Tough-FLAC code*	Evaluate the potential of shear failure in pre-existing high-angle normal faults and tensile failure in caprock in St. Lawrence Lowlands, Canada using a 2D geological model.	Aquifer with sandstone, shale, limestone rocks and heavily faulted	30 years of injection with no shear or tensile failure was observed with low injection rates and maximum injection pressure. High injection rates showed that high permeable faults is reactivated earlier than low permeable faults.

Table C.1 – *Continued from previous page*

Reference	Objective	Characteristics	Summary
Zhang et al. [141] *FLAC 3D*	3D coupled flow and geomechanical study was developed using seismic, structural, experimental and structural data to assess the reservoir stability in Southern Perth Basin, Australia (Sandstone, shale, sandy clay).	Aquifer with injection rates of 3 mt/yr, simulated for 20 years at depths 2400 m.	Uplifts were found to be smaller for strong faults and with weak faults the subsidence was less than 1.85 cm for 1-5 mt/yr. No fault reactivation was observed and no upward flow discharge along the faults were observed.
Zhu et al. [139] *ToughH_2-FLAC simulator*	Coupled fluid flow and geomechanical modelling to study the effect of CO_2 injection in Shenhua, China.	Deep saline aquifer simulated for 10 years with rate of 1e5 tn/yr with multilayer injection in storage layers.	A maximum uplift of 2.22 mm was induced close to the injection well. Highest uplift was observed in first year (45 %) that depend on pressure change, injection volume and elastic properties of reservoir.
Norg Field [432]	Investigate the potential of fault reactivation and induced seismicityin Norg field, netherlands using laboratory compression experiments and numerical simulation.	Gas storage site (Sandstone, rocksalt). No seismicity observed for 17 years. at different rates	Pore pressure rise, temperature difference between injected gas and rocks and, irreversible stress paths involved with cyclic loading are investigated to have caused induced seismicity.
Bakhtiari et al. [433] *Petrel + Visage software*	Coupled hydromechanical tests were conducted with experimental data on the Sarajeh field, Iran to evaluate caprock integrity and risk of fault reactivation.	Aquifer with depth of 1775 m and 3860 bar	Maximum subsidence and uplift was found to be 16 cm and 6 cm during injection and production in the vicinity of injection wells with circular displacement fields.
Bai et al. [434]	3D hydro-mechanical simulation was employed to evaluate hydraulic and geomechanical effects during 3 annual injection-production cycles in Powder river basin, Wyoming.	Saline aquifer with depth of 2510 to 2555 m with sandstone and shale rocks	A maximum magnitude of 1.6 cm uplift was observed from simulation. Mohr coulomb criteria was used to demonstrate the safety of storage scenario.
Zeng et al. [435]	Geochemical modelling of UHS using kinetics in Majiagou carbonate formation, China to asses the risks associated with dissolution of carbonates and loss of H_2.	Carbonate natural gas reservoir with calcite, dolomite and small amounts of quartz, pyrite and feldspar	H_2 loss of 6.5 % at 0.5 years, 7.6 % after 5 years and 77.1 % over 3000 years was observed concludes that the site is suitable for short term UHS. Weakening of host rock, caprock, wellbore and formation of methane was observed from calcite dissolution.

REFERENCES

[1] J. Rutqvist, "The Geomechanics of CO2 Storage in Deep Sedimentary Formations," *Geotechnical and Geological Engineering*, vol. 30, pp. 525–551, jun 2012.

[2] J. Rutqvist, A. P. Rinaldi, F. Cappa, P. Jeanne, A. Mazzoldi, L. Urpi, Y. Guglielmi, and V. Vilarrasa, "Fault activation and induced seismicity in geological carbon storage – lessons learned from recent modeling studies," *Journal of Rock Mechanics and Geotechnical Engineering*, vol. 8, no. 6, pp. 789–804, 2016.

[3] J. D. Jansen, "Lecture notes on oilwell drilling, petroleum engineering," March 2006.

[4] E. R. Ugarte and S. Salehi, "A Review on Well Integrity Issues for Underground Hydrogen Storage," *Journal of Energy Resources Technology, Transactions of the ASME*, vol. 144, apr 2022.

[5] K. Mortezaei, A. Amirlatifi, E. Ghazanfari, and F. Vahedifard, "Potential co2 leakage from geological storage sites: advances and challenges," *Environmental Geotechnics*, vol. 8, no. 1, pp. 3–27, 2021.

[6] A. Aftab, A. Hassanpouryouzband, A. Martin, J. E. Kendrick, E. M. Thaysen, N. Heinemann, J. Utley, M. Wilkinson, R. S. Haszeldine, and K. Edlmann, "Geochemical Integrity of Wellbore Cements during Geological Hydrogen Storage," *Environmental Science and Technology Letters*, jun 2023.

[7] W. Rust, *Non-linear finite element analysis in structural mechanics*. Springer International Publishing, jan 2015.

[8] P. Bérest, H. Gharbi, B. Brouard, D. Brückner, K. DeVries, G. Hévin, G. Hofer, C. Spiers, and J. Urai, "Very Slow Creep Tests on Salt Samples," *Rock Mechanics and Rock Engineering*, vol. 52, pp. 2917–2934, sep 2019.

[9] S. Q. Yang, P. Xu, and P. G. Ranjith, "Damage model of coal under creep and triaxial compression," *International Journal of Rock Mechanics and Mining Sciences*, vol. 80, pp. 337–345, dec 2015.

[10] S. Q. Yang and B. Hu, "Creep and Long-Term Permeability of a Red Sandstone Subjected to Cyclic Loading After Thermal Treatments," *Rock Mechanics and Rock Engineering*, vol. 51, pp. 2981–3004, oct 2018.

[11] D. G. Caglayan, N. Weber, H. U. Heinrichs, J. Linßen, M. Robinius, P. A. Kukla, and D. Stolten, "Technical potential of salt caverns for hydrogen storage in Europe," *International Journal of Hydrogen Energy*, vol. 45, pp. 6793–6805, feb 2020.

[12] H. A. Konstantin Naumenko, *Modeling of Creep for Structural Analysis*. Springer-Verlag GmbH, 2007.

[13] P. Bérest, J. F. Béraud, H. Gharbi, B. Brouard, and K. DeVries, "A Very Slow Creep Test on an Avery Island Salt Sample," *Rock Mechanics and Rock Engineering 2015 48:6*, vol. 48, pp. 2591–2602, sep 2015.

[14] Fenix Consulting Delft BV, "3D Geomechanical Model for Gas Storage Bergermeer Report for TAQA Energy BV," tech. rep., Delft, 2018.

[15] Y. M. Hashash and A. J. Whittle, "Integration of the modified Cam-Clay model in non-linear finite element analysis," *Computers and Geotechnics*, vol. 14, pp. 59–83, jan 1992.

[16] E. Haghighat, F. S. Rassouli, M. D. Zoback, and R. Juanes, "A viscoplastic model of creep in shale," *GEOPHYSICS*, vol. 85, no. 3, pp. 155–166, 2020.

[17] H. V. D. Marel, "GNSS Processing Groningen – Fase 1," Tech. Rep. April, Staatstoezicht op de Mijnen (SodM) GNSS, Delft, 2015.

[18] H. Zhang, Z. Wang, Y. Zheng, P. Duan, and S. Ding, "Study on tri-axial creep experiment and constitutive relation of different rock salt," *Safety Science*, vol. 50, pp. 801–805, apr 2012.

[19] M. Nawaz, *Deformation and transport processes in salt rocks : An experimental study exploring effects of pressure and stress relaxation*. PhD thesis, Utrecht university, 2015.

[20] E. J. S. Duncan and E. Z. Lajtai, "The creep of potash salt rocks from Saskatchewan," *Geotechnical and Geological Engineering*, vol. 11, pp. 159–184, 1993.

[21] L. B. Hunfeld, J. P. T. Foeken, and B. M. M. Van Kempen, "Geomechanical parameters derived from compressional and shear sonic logs for main geothermal targets in The Netherlands," tech. rep., TNO, 2021.

[22] R. Vörös and S. Baisch, "Geomechanical Study – Small Gas Fields in the Netherlands," tech. rep., State Supervision of Mines (SodM), 2018.

[23] T. Xu, G. Zhou, M. J. Heap, S.-Q. Yang, H. Konietzky, and P. Baud, "The modeling of time-dependent deformation and fracturing of brittle rocks under varying confining and pore pressures," *Rock Mechanics and Rock Engineering*, 05 2018.

[24] G. Marketos, C. J. Spiers, and R. Govers, "Impact of rock salt creep law choice on subsidence calculations for hydrocarbon reservoirs overlain by evaporite caprocks," *Journal of Geophysical Research: Solid Earth*, vol. 121, pp. 4249–4267, jun 2016.

[25] I. Dincer, "Renewable energy and sustainable development: a crucial review," *Renewable and Sustainable Energy Reviews*, vol. 4, no. 2, pp. 157–175, 2000.

[26] M. Lehtveer, N. Mattsson, and F. Hedenus, "Using resource based slicing to capture the intermittency of variable renewables in energy system models," *Energy Strategy Reviews*, vol. 18, pp. 73–84, Dec. 2017. Publisher: Elsevier Ltd.

[27] M. Naderloo, K. Ramesh Kumar, E. Hernandez, H. Hajibeygi, and A. Barnhoorn, "Experimental and numerical investigation of sandstone deformation under cycling loading relevant for underground energy storage," *Journal of Energy Storage*, vol. 64, p. 107198, 2023.

[28] M. Shi, Y. Zhang, Y. Zhu, W. Wang, C. Wang, A. Yu, X. Pu, and J. Zhai, "A flower-like CoS2/MoS2 heteronanosheet array as an active and stable electrocatalyst toward the hydrogen evolution reaction in alkaline media," *RSC Advances*, vol. 10, pp. 8973–8981, Feb. 2020. Publisher: The Royal Society of Chemistry.

[29] J. Xu, J. Gao, W. Wang, C. Wang, and L. Wang, "Noble metal-free nico nanoparticles supported on montmorillonite/mos2 heterostructure as an efficient uv–visible light-driven photocatalyst for hydrogen evolution," *International Journal of Hydrogen Energy*, vol. 43, pp. 1375–1385, 01 2018.

[30] N. Rambhujun, M. S. Salman, T. Wang, C. Pratthana, P. Sapkota, M. Costalin, Q. Lai, and K.-F. Aguey-Zinsou, "Renewable hydrogen for the chemical industry," *MRS Energy & Sustainability*, vol. 7, p. 33, Sept. 2020.

[31] R. R. Wang, Y. Q. Zhao, A. Babich, D. Senk, and X. Y. Fan, "Hydrogen direct reduction (H-DR) in steel industry—An overview of challenges and opportunities," *Journal of Cleaner Production*, vol. 329, p. 129797, 2021.

[32] J. S. Wallace and C. A. Ward, "Hydrogen as a fuel," *International Journal of Hydrogen Energy*, vol. 8, no. 4, pp. 255–268, 1983.

[33] R. Tarkowski, "Underground hydrogen storage: Characteristics and prospects," *Renewable and Sustainable Energy Reviews*, vol. 105, pp. 86–94, May 2019. Publisher: Elsevier Ltd.

[34] S. Bauer, C. Beyer, F. Dethlefsen, P. Dietrich, R. Duttmann, M. Ebert, V. Feeser, U. Görke, R. Köber, O. Kolditz, W. Rabbel, T. Schanz, D. Schäfer, H. Würdemann, and A. Dahmke, "Impacts of the use of the geological subsurface for energy storage: An investigation concept," *Environmental Earth Sciences*, vol. 70, pp. 3935–3943, Dec. 2013.

[35] J. Andersson and S. Grönkvist, "Large-scale storage of hydrogen," *International Journal of Hydrogen Energy*, vol. 44, pp. 11901–11919, May 2019. Publisher: Elsevier Ltd.

[36] D. G. Caglayan, N. Weber, H. U. Heinrichs, J. Linßen, M. Robinius, P. A. Kukla, and D. Stolten, "Technical potential of salt caverns for hydrogen storage in Europe," *International Journal of Hydrogen Energy*, vol. 45, pp. 6793–6805, Feb. 2020. Publisher: Elsevier Ltd.

[37] A. S. Lord, P. H. Kobos, and D. J. Borns, "Geologic storage of hydrogen: Scaling up to meet city transportation demands," *International Journal of Hydrogen Energy*, vol. 39, pp. 15570–15582, Sept. 2014. Publisher: Elsevier Ltd.

[38] R. Chen, X. Jin, and H. Li, "A machine learning based solver for pressure Poisson equations," *Theoretical and Applied Mechanics Letters*, p. 100362, aug 2022.

[39] A. Kabuth, A. Dahmke, C. Beyer, L. Bilke, F. Dethlefsen, P. Dietrich, R. Duttmann, M. Ebert, V. Feeser, U. J. Görke, R. Köber, W. Rabbel, T. Schanz, D. Schäfer, H. Würdemann, and S. Bauer, "Energy storage in the geological subsurface: dimensioning, risk analysis and spatial planning: the angus+ project," *Environmental Earth Sciences*, vol. 76, pp. 1–17, 1 2017.

[40] S. Bauer, T. Pfeiffer, A. Boockmeyer, A. Dahmke, and C. Beyer, "Quantifying induced effects of subsurface renewable energy storage," *Energy Procedia*, pp. 1876–6102, 2015.

[41] N. Heinemann, J. Alcalde, J. M. Miocic, S. J. Hangx, J. Kallmeyer, C. Ostertag-Henning, A. Hassanpouryouzband, E. M. Thaysen, G. J. Strobel, C. Schmidt-Hattenberger, *et al.*, "Enabling large-scale hydrogen storage in porous media–the scientific challenges," *Energy & Environmental Science*, vol. 14, no. 2, pp. 853–864, 2021.

[42] S. R. Thiyagarajan, H. Emadi, A. Hussain, P. Patange, and M. Watson, "A comprehensive review of the mechanisms and efficiency of underground hydrogen storage," *Journal of Energy Storage*, vol. 51, July 2022. Publisher: Elsevier Ltd.

[43] F. Crotogino, S. Donadei, U. Bünger, and H. Landinger, "Large-scale hydrogen underground storage for securing future energy supplies," 01 2010.

[44] K. Basniev, R. Omelchenko, and F. Adzynova, "Underground hydrogen storage problems in russia," No. 4, p. 47 – 53, 2010. Cited by: 25.

[45] G. W. P. Council, I. Oil, G. C. Commission, *et al.*, "Underground gas storage regulatory considerations: A guide for state and federal regulatory agencies," tech. rep., Technical Report. States First Initiative, 2017.

[46] R. Tarkowski, B. Uliasz-Misiak, and P. Tarkowski, "Storage of hydrogen, natural gas, and carbon dioxide–geological and legal conditions," *International Journal of Hydrogen Energy*, vol. 46, no. 38, pp. 20010–20022, 2021.

[47] J. J. Koenig, "Preparing motor gasolines for salt cavern storage of up to 10 years," *SMRI Fall Mtg*, vol. 425, 1994.

[48] F. Crotogino, K.-U. Mohmeyer, and R. Scharf, "Huntorf caes: More than 20 years of successful operation," in *SMRI Spring meeting*, vol. 2001, 2001.

[49] S. Donadei and G.-S. Schneider, "Compressed air energy storage in underground formations," in *Storing Energy*, pp. 113–133, Elsevier, 2016.

[50] D. Evans, D. Parkes, M. Dooner, P. Williamson, J. Williams, J. Busby, W. He, J. Wang, and S. Garvey, "Salt cavern exergy storage capacity potential of uk massively bedded halites, using compressed air energy storage (caes)," *Applied Sciences*, vol. 11, no. 11, p. 4728, 2021.

[51] M. Dusseault, S. Bachu, and L. Rothenburg, "Sequestration of co2 in salt caverns," *Journal of Canadian Petroleum Technology*, vol. 43, no. 11, 2004.

[52] J. P. Verdon, J. M. Kendall, A. L. Stork, R. A. Chadwick, D. J. White, and R. C. Bissell, "Comparison of geomechanical deformation induced by megatonne-scale CO2 storage at Sleipner, Weyburn, and In Salah," *Proceedings of the National Academy of Sciences of the United States of America*, vol. 110, pp. E2762–E2771, jul 2013.

[53] J. Yang, Z. Liu, C. Yang, H. Li, Q. Lu, and X. Shi, "Mechanical and microstructural properties of alkali wastes as filling materials for abandoned salt caverns," *Waste and biomass valorization*, vol. 12, pp. 1581–1590, 2021.

[54] X. Shi, Q. Chen, H. Ma, Y. Li, T. Wang, and C. Zhang, "Geomechanical investigation for abandoned salt caverns used for solid waste disposal," *Bulletin of Engineering Geology and the Environment*, vol. 80, pp. 1205–1218, 2021.

[55] M. Dusseault and B. Davidson, "Design and management of salt solution caverns for toxic waste disposal," *Journal of Canadian Petroleum Technology*, vol. 38, no. 12, 1999.

[56] M. Langer, "Principles of geomechanical safety assessment for radioactive waste disposal in salt structures," *Engineering geology*, vol. 52, no. 3-4, pp. 257–269, 1999.

[57] L. Hashemi, M. Blunt, and H. Hajibeygi, "Pore-scale modelling and sensitivity analyses of hydrogen-brine multiphase flow in geological porous media," *Scientific Reports*, vol. 11, p. 8348, dec 2021.

[58] D. Zivar, S. Kumar, and J. Foroozesh, "Underground hydrogen storage: A comprehensive review," *International Journal of Hydrogen Energy*, Sept. 2020. Publisher: Elsevier Ltd.

[59] M. Panfilov, "4 - Underground and pipeline hydrogen storage," in *Compendium of Hydrogen Energy* (R. B. Gupta, A. Basile, and T. N. Veziroğlu, eds.), Woodhead Publishing Series in Energy, pp. 91–115, Woodhead Publishing, Jan. 2016.

[60] O. Kruck and F. Crotogino, "Benchmarking of selected storage options," *Hannover, Germany*, 2013.

[61] I. Iordache, D. Schitea, A. V. Gheorghe, and M. Iordache, "Hydrogen underground storage in Romania, potential directions of development, stakeholders and general aspects," *International Journal of Hydrogen Energy*, vol. 39, pp. 11071–11081, July 2014. Publisher: Elsevier Ltd.

[62] P. Schöpping, "Feasibility of seasonal storage of green gas in Dutch geological formations," tech. rep., Delft university of technology, 2019.

[63] Y. Qiu, S. Zhou, J. Wang, J. Chou, Y. Fang, G. Pan, and W. Gu, "Feasibility analysis of utilising underground hydrogen storage facilities in integrated energy system: Case studies in China," *Applied Energy*, vol. 269, p. 115140, July 2020. Publisher: Elsevier Ltd.

[64] A. Lemieux, A. Shkarupin, and K. Sharp, "Geologic feasibility of underground hydrogen storage in Canada," *International Journal of Hydrogen Energy*, vol. 45, pp. 32243–32259, Nov. 2020. Publisher: Elsevier Ltd.

[65] J. Scafidi, M. Wilkinson, S. M. Gilfillan, N. Heinemann, and R. S. Haszeldine, "A quantitative assessment of the hydrogen storage capacity of the UK continental shelf," *International Journal of Hydrogen Energy*, vol. 46, pp. 8629–8639, Feb. 2021. Publisher: Elsevier Ltd.

[66] N. Heinemann, M. G. Booth, R. S. Haszeldine, M. Wilkinson, J. Scafidi, and K. Edlmann, "Hydrogen storage in porous geological formations – onshore play opportunities in the midland valley (Scotland, UK)," *International Journal of Hydrogen Energy*, vol. 43, pp. 20861–20874, Nov. 2018. Publisher: Elsevier Ltd.

[67] D. Pudlo, L. Ganzer, S. Henkel, M. Kühn, A. Liebscher, M. De Lucia, M. Panfilov, P. Pilz, V. Reitenbach, D. Albrecht, H. Würdemann, and R. Gaupp, "The H2STORE project: Hydrogen underground storage - A feasible way in storing electrical power in geological media?," *Springer Series in Geomechanics and Geoengineering*, pp. 395–412, 2013.

[68] "Underground Sun Storage," tech. rep., Austria, R A G, 2020.

[69] K. Luboń and R. Tarkowski, "Numerical simulation of hydrogen injection and withdrawal to and from a deep aquifer in nw poland," *international journal of hydrogen energy*, vol. 45, no. 3, pp. 2068–2083, 2020.

[70] J. Chen, C. Du, D. Jiang, J. Fan, and Y. He, "The mechanical properties of rock salt under cyclic loading-unloading experiments," *Geomechanics and Engineering*, vol. 10, no. 3, pp. 325–334, 2016.

[71] Y. Liu, T. Ma, H. Wu, and P. Chen, "Investigation on mechanical behaviors of shale cap rock for geological energy storage by linking macroscopic to mesoscopic failures," *Journal of Energy Storage*, vol. 29, p. 101326, 2020.

[72] X. Zhang and P. Tahmasebi, "Effects of grain size on deformation in porous media," *Transport in Porous Media*, vol. 129, no. 1, pp. 321–341, 2019.

[73] P. Jeanne, Y. Zhang, and J. Rutqvist, "Influence of hysteretic stress path behavior on seal integrity during gas storage operation in a depleted reservoir," *Journal of Rock Mechanics and Geotechnical Engineering*, vol. 12, no. 4, pp. 886–899, 2020.

[74] K. Kumar, H. Honorio, and H. Hajibeygi, "Simulation of the inelastic deformation of porous reservoirs under cyclic loading relevant for underground hydrogen storage," *Scientific reports*, vol. 12, p. 21404, 2022.

[75] B. Orlic, B. Wassing, and C. Geel, "Field scale geomechanical modeling for prediction of fault stability during underground gas storage operations in a depleted gas field in the netherlands," in *47th US Rock Mechanics/Geomechanics Symposium*, OnePetro, 2013.

[76] F. Silverii, F. Maccaferri, G. Richter, B. Gonzalez Cansado, R. Wang, S. Hainzl, and T. Dahm, "Poroelastic model in a vertically sealed gas storage: a case study from cyclic injection/production in a carbonate aquifer," *Geophysical Journal International*, vol. 227, no. 2, pp. 1322–1338, 2021.

[77] P. Teatini, N. Castelletto, M. Ferronato, G. Gambolati, C. Janna, E. Cairo, D. Marzorati, D. Colombo, A. Ferretti, A. Bagliani, *et al.*, "Geomechanical response to seasonal gas storage in depleted reservoirs: A case study in the po river basin, italy," *Journal of Geophysical Research: Earth Surface*, vol. 116, no. F2, 2011.

[78] C. Janna, N. Castelletto, M. Ferronato, G. Gambolati, and P. Teatini, "A geomechanical transversely isotropic model of the po river basin using psinsar derived horizontal displacement," *International Journal of Rock Mechanics and Mining Sciences*, vol. 51, pp. 105–118, 2012.

[79] W. Dreyer, "Results of recent studies on the stability of crude oil and gas storage in salt caverns," in *Proceedings of the fourth international symposium on salt, Cleveland, USA, Northern Ohio Geological Society*, vol. 2, pp. 65–92, 1974.

[80] P. Boucly, "In situ experience and mathematical representation of the behavior of rock salt used in storage of gas," in *Proc. 1st Conf. Mech. Beh. of Salt, Pennsylvania*, pp. 453–471, 1981.

[81] P. Berest and D. N. Minh, "Deep underground storage cavities in rock salt: interpretation of in-situ data from french and foreign sites," in *Proceedings of the 1st conference on the mechanical behavior of salt, Clausthal-Zellerfeld: Trans. Tech. publications*, pp. 555–572, 1981.

[82] B. Ehgartner, J. Neal, and T. Hinkebein, "Gas releases from salt," tech. rep., Sandia National Lab.(SNL-NM), Albuquerque, NM (United States), 1998.

[83] D. E. Munson, M. A. Molecke, and R. Myers, "Interior cavern conditions and salt fall potential," tech. rep., Sandia National Lab.(SNL-NM), Albuquerque, NM (United States), 1998.

[84] W. Lolan, R. Valadie, and P. Ballou, "Remote operated vehicle (rov) design, cavern survey and gel plugging agent application to repair louisiana offshore oil port (loop) cavern 14," in *Proc. SMRI Fall Meeting, Roma*, pp. 327–345, 1998.

[85] R. Thoms and R. Gehle, "A brief history of salt cavern use," in *Proceedings of the 8th World Salt Symposium*, 2000.

[86] B. Cerfontaine and F. Collin, "Cyclic and Fatigue Behaviour of Rock Materials: Review, Interpretation and Research Perspectives," *Rock Mechanics and Rock Engineering*, vol. 51, no. 2, pp. 391–414, 2018.

[87] H. Wang, W. Xu, M. Cai, Z. Xiang, and Q. Kong, "Gas permeability and porosity evolution of a porous sandstone under repeated loading and unloading conditions," *Rock Mechanics and Rock Engineering*, vol. 50, pp. 2071–2083, 2017.

[88] X. Wang, S. Wu, H. Ge, Y. Sun, and Q. Zhang, "The complexity of the fracture network in failure rock under cyclic loading and its characteristics in acoustic emission monitoring," *Journal of Geophysics and Engineering*, vol. 15, pp. 2091–2103, jun 2018.

[89] S.-Q. Yang, Y.-H. Huang, and J.-Z. Tang, "Mechanical, acoustic, and fracture behaviors of yellow sandstone specimens under triaxial monotonic and cyclic loading," *International Journal of Rock Mechanics and Mining Sciences*, vol. 130, p. 104268, jun 2020.

[90] J. Browning, P. G. Meredith, C. Stuart, S. Harland, D. Healy, and T. M. Mitchell, "A directional crack damage memory effect in sandstone under true triaxial loading," *Geophysical Research Letters*, vol. 45, no. 14, pp. 6878–6886, 2018.

[91] C. Li, C. Gao, H. Xie, and N. Li, "Experimental investigation of anisotropic fatigue characteristics of shale under uniaxial cyclic loading," *International Journal of Rock Mechanics and Mining Sciences*, vol. 130, p. 104314, 2020.

[92] M. Wang, C. Tan, J. Meng, B. Yang, and Y. Li, "Crack classification and evolution in anisotropic shale during cyclic loading tests by acoustic emission," *Journal of Geophysics and Engineering*, vol. 14, no. 4, pp. 930–938, 2017.

[93] Q. Meng, M. Zhang, L. Han, H. Pu, and Y. Chen, "Acoustic emission characteristics of red sandstone specimens under uniaxial cyclic loading and unloading compression," *Rock Mechanics and Rock Engineering*, vol. 51, pp. 969–988, 2018.

[94] C. Noël, L. Pimienta, and M. Violay, "Time-dependent deformations of sandstone during pore fluid pressure oscillations: Implications for natural and induced seismicity," *Journal of Geophysical Research: Solid Earth*, vol. 124, pp. 801–821, jan 2019.

[95] A. Zang, J. S. Yoon, O. Stephansson, and O. Heidbach, "Fatigue hydraulic fracturing by cyclic reservoir treatment enhances permeability and reduces induced seismicity," *Geophysical Journal International*, vol. 195, pp. 1282–1287, aug 2013.

[96] A. Zang, G. Zimmermann, H. Hofmann, O. Stephansson, K.-B. Min, and K. Y. Kim, "How to reduce fluid-injection-induced seismicity," *Rock Mechanics and Rock Engineering*, vol. 52, pp. 475–493, apr 2018.

[97] J. S. Yoon, A. Zang, and O. Stephansson, "Numerical investigation on optimized stimulation of intact and naturally fractured deep geothermal reservoirs using hydro-mechanical coupled discrete particles joints model," *Geothermics*, vol. 52, pp. 165–184, oct 2014.

[98] A. G. Muntendam-Bos, G. Hoedeman, K. Polychronopoulou, D. Draganov, C. Weemstra, W. van der Zee, R. R. Bakker, and H. Roest, "An overview of induced seismicity in the netherlands," *Netherlands Journal of Geosciences*, vol. 101, p. e1, 2022.

[99] X. Ding, G. Zhang, B. Zhao, and Y. Wang, "Unexpected viscoelastic deformation of tight sandstone: Insights and predictions from the fractional Maxwell model," *Scientific Reports 2017 7:1*, vol. 7, pp. 1–11, sep 2017.

[100] J. Wang, Q. Zhang, Z. Song, S. Feng, and Y. Zhang, "Nonlinear creep model of salt rock used for displacement prediction of salt cavern gas storage," *Journal of Energy Storage*, vol. 48, p. 103951, 2022.

[101] P. A. Vermeer and R. De Borst, "Non-Associated Plasticity for Soils, Concrete and Rock," *HERON*, vol. 29, no. 3, 1984.

[102] J. P. Carter, C. P. Wroth, and J. R. J. R. Booker, "A critical state soil model for cyclic loading," in *Soil Mechanics - Transient and Cylic Loads*, pp. 219–252, John Wiley & Sons Ltd, jan 1979.

[103] M. C. Weng and H. I. Ling, "Modeling the behavior of sandstone based on generalized plasticity concept," *International Journal for Numerical and Analytical Methods in Geomechanics*, vol. 37, pp. 2154–2169, oct 2013.

[104] R. de Borst, "Integration of plasticity equations for singular yield functions," *Computers & Structures*, vol. 26, no. 5, pp. 823–829, 1987.

[105] Y. F. Dafalias, M. Asce, M. T. Manzari, and A. M. Asce, "Simple Plasticity Sand Model Accounting for Fabric Change Effects," *Journal of Engineering Mechanics*, vol. 130, pp. 622–634, jun 2004.

[106] R. Pijnenburg, B. Verberne, S. Hangx, and C. Spiers, "Inelastic deformation of the slochteren sandstone: Stress-strain relations and implications for induced seismicity in the groningen gas field," *Journal of Geophysical Research: Solid Earth*, vol. 124, no. 5, pp. 5254–5282, 2019.

[107] T. Xu, G. Zhou, M. J. Heap, S. Yang, H. Konietzky, and P. Baud, "The Modeling of Time-Dependent Deformation and Fracturing of Brittle Rocks Under Varying Confining and Pore Pressures," *Rock Mechanics and Rock Engineering*, vol. 51, pp. 3241–3263, oct 2018.

[108] M. C. Weng, "A generalized plasticity-based model for sandstone considering time-dependent behavior and wetting deterioration," *Rock Mechanics and Rock Engineering*, vol. 47, pp. 1197–1209, jul 2014.

[109] W. Sumelka and T. Łodygowski, "Viscoplasticity," *Encyclopedia of Continuum Mechanics*, pp. 1–5, 2018.

[110] L. S. Tsai, Y. M. Hsieh, M. C. Weng, T. H. Huang, and F. S. Jeng, "Time-dependent deformation behaviors of weak sandstones," *International Journal of Rock Mechanics and Mining Sciences*, vol. 45, pp. 144–154, feb 2008.

[111] X. Li and Z. Yin, "Study of creep mechanical properties and a rheological model of sandstone under disturbance loads," *Processes*, vol. 9, 8 2021.

[112] X. Wang, Q. Huang, B. Lian, N. Liu, and J. Zhang, "Modified nishihara rheological model considering the effect of thermal-mechanical coupling and its experimental verification," *Advances in Materials Science and Engineering*, vol. 2018, 2018.

[113] K. Ramesh Kumar and H. Hajibeygi, "Multiscale simulation of inelastic creep deformation for geological rocks," *Journal of Computational Physics*, vol. 440, p. 110439, sep 2021.

[114] Q. He, F. Wu, and R. Gao, "Nonlinear creep-damage constitutive model of surrounding rock in salt cavern reservoir," *Journal of Energy Storage*, vol. 55, p. 105520, 2022.

[115] L. J. Ma, X. Y. Liu, Q. Fang, H. F. Xu, H. M. Xia, E. B. Li, S. G. Yang, and W. P. Li, "A new elasto-viscoplastic damage model combined with the generalized hoek-brown failure criterion for bedded rock salt and its application," *Rock Mechanics and Rock Engineering*, vol. 46, pp. 53–66, jan 2013.

[116] D. Liang, N. Zhang, L. Xie, G. Zhao, and D. Qian, "Damage and fractal evolution trends of sandstones under constant-amplitude and tiered cyclic loading and unloading based on acoustic emission," *International Journal of Distributed Sensor Networks*, vol. 15, no. 7, p. 1550147719861020, 2019.

[117] E. Hernandez, M. Naderloo, K. R. Kumar, H. Hajibeygi, and A. Barnhoorn, "Modeling of Cyclic Deformation of Sandstones Based on Experimental Observations," *EAGE GET 2022*, vol. 2022, pp. 1–5, nov 2022.

[118] R. P. Pijnenburg, B. A. Verberne, S. J. Hangx, and C. J. Spiers, "Inelastic Deformation of the Slochteren Sandstone: Stress-Strain Relations and Implications for Induced Seismicity in the Groningen Gas Field," *Journal of Geophysical Research: Solid Earth*, vol. 124, no. 5, pp. 5254–5282, 2019.

[119] J. P. Carter, J. R. Booker, and C. P. Wroth, "A critical state soil model for cyclic loading.," *Soils under cyclic and transient loading, volume 1. Proc. international symposium, Swansea, 7-11 January, 1980*, no. May, pp. 433–434, 1980.

[120] K. R. Kumar, H. T. Honorio, and H. Hajibeygi, "Simulation of the inelastic deformation of porous reservoirs under cyclic loading relevant for underground hydrogen storage," *Scientific Reports 2022 12:1*, vol. 12, pp. 1–23, dec 2022.

[121] B. Cerfontaine, R. Charlier, F. Collin, and M. Taiebat, "Validation of a new elastoplastic constitutive model dedicated to the cyclic behaviour of brittle rock materials," *Rock Mechanics and Rock Engineering*, vol. 50, no. 10, pp. 2677–2694, 2017.

[122] X. Li and Z. Yin, "Study of Creep Mechanical Properties and a Rheological Model of Sandstone under Disturbance Loads," *Processes 2021, Vol. 9, Page 1291*, vol. 9, p. 1291, jul 2021.

[123] J. Choo, S. J. Semnani, and J. A. White, "An anisotropic viscoplasticity model for shale based on layered microstructure homogenization," *International Journal for Numerical and Analytical Methods in Geomechanics*, vol. 45, pp. 502–520, mar 2021.

[124] R. I. Borja, Q. Yin, and Y. Zhao, "Cam-Clay plasticity. Part IX: On the anisotropy, heterogeneity, and viscoplasticity of shale," *Computer Methods in Applied Mechanics and Engineering*, vol. 360, p. 112695, mar 2020.

[125] K. C. Bennett and R. I. Borja, "Hyper-elastoplastic/damage modeling of rock with application to porous limestone," *International Journal of Solids and Structures*, vol. 143, pp. 218–231, jun 2018.

[126] Y. Zhao, L. Zhang, W. Wang, W. Wan, S. Li, W. Ma, and Y. Wang, "Creep Behavior of Intact and Cracked Limestone Under Multi-Level Loading and Unloading Cycles," *Rock Mechanics and Rock Engineering*, vol. 50, pp. 1409–1424, jun 2017.

[127] F. S. Rassouli and M. D. Zoback, "Comparison of Short-Term and Long-Term Creep Experiments in Shales and Carbonates from Unconventional Gas Reservoirs," *Rock Mechanics and Rock Engineering*, vol. 51, pp. 1995–2014, jul 2018.

[128] M. Nejati, A. Paluszny, and R. W. Zimmerman, "A finite element framework for modeling internal frictional contact in three-dimensional fractured media using unstructured tetrahedral meshes," *Computer Methods in Applied Mechanics and Engineering*, vol. 306, pp. 123–150, 2016.

[129] J. D. Byerlee and M. Wyss, eds., *Friction of Rocks*, pp. 615–626. Basel: Birkhäuser Basel, 1978.

[130] A. Ruina, "Slip instability and state variable friction laws," *Journal of Geophysical Research: Solid Earth*, vol. 88, no. B12, pp. 10359–10370, 1983.

[131] J. Chen, A. R. Niemeijer, and C. J. Spiers, "Microphysically derived expressions for rate-and-state friction parameters, a, b, and dc," *Journal of Geophysical Research: Solid Earth*, vol. 122, no. 12, pp. 9627–9657, 2017.

[132] S. Vidal-Gilbert, E. Tenthorey, D. Dewhurst, J. Ennis-King, P. Van Ruth, and R. Hillis, "Geomechanical analysis of the Naylor Field, Otway Basin, Australia: Implications for CO2 injection and storage," *International Journal of Greenhouse Gas Control*, vol. 4, pp. 827–839, sep 2010.

[133] J. A. White, L. Chiaramonte, S. Ezzedine, W. Foxall, Y. Hao, A. Ramirez, and W. McNab, "Geomechanical behavior of the reservoir and caprock system at the in Salah CO2 storage project," *Proceedings of the National Academy of Sciences of the United States of America*, vol. 111, pp. 8747–8752, jun 2014.

[134] Itasca Consulting Group, "FLAC2D | US Minneapolis Inc.."

[135] L. Bilke, T. Fischer, D. Naumov, C. Lehmann, W. Wang, R. Lu, B. Meng, K. Rink, N. Grunwald, J. Buchwald, C. Silbermann, R. Habel, L. Günther, M. Mollaali, T. Meisel, J. Randow, S. Einspänner, H. Shao, K. Kurgyis, O. Kolditz, and J. Garibay, "Opengeosys," Apr. 2022.

[136] Sebastia Olivella and Jean Vaunat and Alfonso Rodriguez Dono, "CODE BRIGHT, University of Catalunya."

[137] "VISAGE Finite-Element Geomechanics Simulator."

[138] Computer Modelling Group, "CMG Software | STARS."

[139] Q. Zhu, D. Zuo, S. Zhang, Y. Zhang, Y. Wang, and L. Wang, "Simulation of geomechanical responses of reservoirs induced by CO2 multilayer injection in the Shenhua CCS project, China," *International Journal of Greenhouse Gas Control*, vol. 42, pp. 405–414, nov 2015.

[140] P. Pan, Z. Wu, X. Feng, and F. Yan, "Geomechanical modeling of CO2 geological storage: A review," *Journal of Rock Mechanics and Geotechnical Engineering*, vol. 8, pp. 936–947, dec 2016.

[141] Y. Zhang, L. Langhi, P. M. Schaubs, C. D. Piane, D. N. Dewhurst, L. Stalker, and K. Michael, "Geomechanical stability of CO2 containment at the South West Hub Western Australia: A coupled geomechanical–fluid flow modelling approach," *International Journal of Greenhouse Gas Control*, vol. 37, pp. 12–23, jun 2015.

[142] A. P. Rinaldi, J. Rutqvist, and F. Cappa, "Geomechanical effects on CO2 leakage through fault zones during large-scale underground injection," *International Journal of Greenhouse Gas Control*, vol. 20, pp. 117–131, jan 2014.

[143] A. Ouellet, T. Bérard, J. Desroches, P. Frykman, P. Welsh, J. Minton, Y. Pamukcu, S. Hurter, and C. Schmidt-Hattenberger, "Reservoir geomechanics for assessing containment in CO2 storage: A case study at Ketzin, Germany," *Energy Procedia*, vol. 4, pp. 3298–3305, jan 2011.

[144] E. Konstantinovskaya, J. Rutqvist, and M. Malo, "CO2 storage and potential fault instability in the St. Lawrence Lowlands sedimentary basin (Quebec, Canada): Insights from coupled reservoir-geomechanical modeling," *International Journal of Greenhouse Gas Control*, vol. 22, pp. 88–110, mar 2014.

[145] F. Cappa and J. Rutqvist, "Modeling of coupled deformation and permeability evolution during fault reactivation induced by deep underground injection of co2," *International Journal of Greenhouse Gas Control*, vol. 5, no. 2, pp. 336–346, 2011.

[146] DBI Gas- und Umwelttechnik GmbH, "The effects of hydrogen injection in natural gas networks for the Dutch underground storages," tech. rep., Commissioned by the ministry of Economic Affairs, 2017.

[147] J. Sun, H. Xu, J. Wang, L. Shi, C. Li, L. Tang, and R. Zhong, "Injection–production mechanisms and key evaluation technologies for underground gas storages rebuilt from gas reservoirs," *Natural Gas Industry B*, vol. 5, no. 6, pp. 616–622, 2018.

[148] D. ZHENG, H. XU, J. WANG, J. SUN, K. ZHAO, C. LI, L. SHI, and L. TANG, "Key evaluation techniques in the process of gas reservoir being converted into underground gas storage," *Petroleum Exploration and Development*, vol. 44, no. 5, pp. 840–849, 2017.

[149] P. Jeanne, Y. Zhang, and J. Rutqvist, "Influence of hysteretic stress path behavior on seal integrity during gas storage operation in a depleted reservoir," *Journal of Rock Mechanics and Geotechnical Engineering*, vol. 12, no. 4, pp. 886–899, 2020.

[150] Z. Chemia, H. Koyi, and H. Schmeling, "Numerical modelling of rise and fall of a dense layer in salt diapirs," *Geophysical Journal International*, vol. 172, pp. 798–816, feb 2008.

[151] Z. Chemia, H. Schmeling, and H. Koyi, "The effect of the salt viscosity on future evolution of the gorleben salt diapir, germany," *Tectonophysics*, vol. 473, pp. 446–456, aug 2009.

[152] Z. Chemia and H. Koyi, "The control of salt supply on entrainment of an anhydrite layer within a salt diapir," *Journal of Structural Geology*, vol. 30, pp. 1192–1200, sep 2008.

[153] H. Koyi, "Salt flow by aggrading and prograding overburdens," *Geological Society, London, Special Publications*, vol. 100, no. 1, pp. 243–258, 1996.

[154] H. Koyi, "The shaping of salt diapirs," *Journal of Structural Geology*, vol. 20, pp. 321–338, apr 1998.

[155] S. Li, L. Feng, P. Tang, G. Rao, and Y. Bao, "Calculation of depth to detachment and its significance in the kuqa depression: A discussion," *Petroleum Science*, vol. 6, pp. 17–20, feb 2009.

[156] S. Li, S. Abe, L. Reuning, S. Becker, J. L. Urai, and P. A. Kukla, "Numerical modelling of the displacement and deformation of embedded rock bodies during salt tectonics: A case study from the south oman salt basin," *Geological Society, London, Special Publications*, vol. 363, no. 1, pp. 503–520, 2012.

[157] A. Poliakov, Y. Podladchikov, and C. Talbot, "Initiation of salt diapirs with frictional overburdens: numerical experiments," *Tectonophysics*, vol. 228, pp. 199–210, dec 1993.

[158] D. Schultz-Ela, "Evolution of extensional fault systems linked with salt diapirism modeled with finite elements," *AAPG Bulletin*, vol. 77, 1993.

[159] P. van Keken, C. Spiers, A. van den Berg, and E. Muyzert, "The effective viscosity of rocksalt: implementation of steady-state creep laws in numerical models of salt diapirism," *Tectonophysics*, vol. 225, pp. 457–476, oct 1993.

[160] N. Castelletto, H. Hajibeygi, and H. A. Tchelepi, "Multiscale finite-element method for linear elastic geomechanics," *Journal of Computational Physics*, vol. 331, pp. 337–356, feb 2017.

[161] N. Castelletto, S. Klevtsov, H. Hajibeygi, and H. A. Tchelepi, "Multiscale two-stage solver for biot's poroelasticity equations in subsurface media," *Computational Geosciences*, vol. 23, no. 2, pp. 207–224, 2019.

[162] I. Sokolova, M. G. Bastisya, and H. Hajibeygi, "Multiscale finite volume method for finite-volume-based simulation of poroelasticity," *Journal of Computational Physics*, vol. 379, pp. 309–324, feb 2019.

[163] H. Ma, C. Yang, J. Liu, and J. Chen, "The influence of cyclic loading on deformation of rock salt," in *Rock Characterisation, Modelling and Engineering Design Methods*, pp. 63–68, CRC Press, may 2013.

[164] K. Khaledi, T. Schanz, and M. Datcheva, "Finite-element modeling of the behavior of underground caverns excavated in rock salt," in *Numerical Methods in Geotechnical Engineering - Proceedings of the 8th European Conference on Numerical Methods in Geotechnical Engineering, NUMGE 2014*, vol. 2, pp. 845–850, Taylor and Francis - Balkema, 2014.

[165] P. A. L. P. Firme, D. Roehl, and C. Romanel, "An assessment of the creep behaviour of Brazilian salt rocks using the multi-mechanism deformation model," *Acta Geotechnica 2016 11:6*, vol. 11, pp. 1445–1463, mar 2016.

[166] P. A. Firme, D. Roehl, and C. Romanel, "Salt caverns history and geomechanics towards future natural gas strategic storage in Brazil," *Journal of Natural Gas Science and Engineering*, vol. 72, p. 103006, dec 2019.

[167] K. Khaledi, E. Mahmoudi, M. Datcheva, and T. Schanz, "Stability and serviceability of underground energy storage caverns in rock salt subjected to mechanical cyclic loading," *International Journal of Rock Mechanics and Mining Sciences*, vol. 86, pp. 115–131, jul 2016.

[168] W. Dias, D. Roehl, C. Mejia, and P. Sotomayor, "Cavern integrity for underground hydrogen storage in the Brazilian pre-salt fields," *International Journal of Hydrogen Energy*, apr 2023.

[169] Y. Song, R. Song, and J. Liu, "Hydrogen tightness evaluation in bedded salt rock cavern: A case study of Jintan, China," *International Journal of Hydrogen Energy*, may 2023.

[170] K. M. Keranen, M. Weingarten, G. A. Abers, B. A. Bekins, and S. Ge, "Sharp increase in central oklahoma seismicity since 2008 induced by massive wastewater injection," *Science*, vol. 345, no. 6195, pp. 448–451, 2014.

[171] G. R. Foulger, M. P. Wilson, J. G. Gluyas, B. R. Julian, and R. J. Davies, "Global review of human-induced earthquakes," *Earth-Science Reviews*, vol. 178, pp. 438–514, mar 2018.

[172] J. B. Zhu, J. Q. Kang, D. Elsworth, H. P. Xie, Y. Ju, and J. Zhao, "Controlling induced earthquake magnitude by cycled fluid injection," *Geophysical Research Letters*, vol. 48, oct 2021.

[173] C. Noël, F. X. Passelègue, and M. Violay, "Brittle faulting of ductile rock induced by pore fluid pressure build-up," *Journal of Geophysical Research: Solid Earth*, vol. 126, mar 2021.

[174] W. Wu, D. Lu, and D. Elsworth, "Fluid injection-induced fault slip during unconventional energy development: A review," *Energy Reviews*, vol. 1, p. 100007, dec 2022.

[175] Y. Ji, H. Hofmann, K. Duan, and A. Zang, "Laboratory experiments on fault behavior towards better understanding of injection-induced seismicity in geoenergy systems," *Earth-Science Reviews*, vol. 226, p. 103916, mar 2022.

[176] E. Rutter and A. Hackston, "On the effective stress law for rock-on-rock frictional sliding, and fault slip triggered by means of fluid injection," *Philosophical Transactions of the Royal Society A: Mathematical, Physical and Engineering Sciences*, vol. 375, p. 20160001, aug 2017.

[177] Y. Ji, J. S. Yoon, A. Zang, and W. Wu, "Mitigation of injection-induced seismicity on undrained faults in granite using cyclic fluid injection: A laboratory study," *International Journal of Rock Mechanics and Mining Sciences*, vol. 146, p. 104881, oct 2021.

[178] E. Roland and J. J. McGuire, "Earthquake swarms on transform faults," *Geophysical Journal International*, vol. 178, pp. 1677–1690, sep 2009.

[179] Z. Ye and A. Ghassemi, "Heterogeneous fracture slip and aseismic-seismic transition in a triaxial injection test," *Geophysical Research Letters*, vol. 47, jul 2020.

[180] B. Fryer, M. Lebihain, and M. Violay, "Single-well pore pressure preconditioning for enhanced geothermal system stimulation," *Journal of Geophysical Research: Solid Earth*, p. e2022JB025443, 2023.

[181] C. Giorgetti and M. Violay, "The influence of loading path on fault reactivation: a laboratory perspective," *Geophysical Research Letters*, vol. 48, no. 8, p. e2020GL091466, 2021.

[182] B. Fryer, G. Siddiqi, and L. Laloui, "Injection-induced seismicity: strategies for reducing risk using high stress path reservoirs and temperature-induced stress preconditioning," *Geophysical Journal International*, vol. 220, pp. 1436–1446, oct 2019.

[183] M. Klell, "Handbook of hydrogen storage," *Storage of Hydrogen in the Pure Form*, 2010.

[184] J. Miocic, N. Heinemann, K. Edlmann, J. Scafidi, F. Molaei, and J. Alcalde, "Underground hydrogen storage: A review," *Geological Society, London, Special Publications*, vol. 528, no. 1, pp. SP528–2022, 2023.

[185] R. M. Van Eijs, F. M. Mulders, M. Nepveu, C. J. Kenter, and B. C. Scheffers, "Correlation between hydrocarbon reservoir properties and induced seismicity in the Netherlands," *Engineering Geology*, vol. 84, pp. 99–111, may 2006.

[186] L. Buijze, P. A. Van Den Bogert, B. B. Wassing, B. Orlic, and J. Ten Veen, "Fault reactivation mechanisms and dynamic rupture modelling of depletion-induced seismic events in a Rotliegend gas reservoir," *Netherlands Journal of Geosciences*, vol. 96, pp. s131–s148, dec 2017.

[187] J. D. Van Wees, P. A. Fokker, K. Van Thienen-Visser, B. B. Wassing, S. Osinga, B. Orlic, S. A. Ghouri, L. Buijze, and M. Pluymaekers, "Geomechanical models for induced seismicity in the Netherlands: inferences from simplified analytical, finite element and rupture model approaches," *Netherlands Journal of Geosciences*, vol. 96, pp. s183–s202, dec 2017.

[188] L. Buijze, P. A. van den Bogert, B. B. Wassing, and B. Orlic, "Nucleation and Arrest of Dynamic Rupture Induced by Reservoir Depletion," *Journal of Geophysical Research: Solid Earth*, vol. 124, pp. 3620–3645, apr 2019.

[189] J. D. Jansen, P. Singhal, and F. C. Vossepoel, "Insights From Closed-Form Expressions for Injection- and Production-Induced Stresses in Displaced Faults," *Journal of Geophysical Research: Solid Earth*, vol. 124, pp. 7193–7212, jul 2019.

[190] J. D. Jansen and B. Meulenbroek, "Induced aseismic slip and the onset of seismicity in displaced faults," *Netherlands Journal of Geosciences*, vol. 101, p. e13, jun 2022.

[191] E. W. Lemmon, I. H. Bell, M. L. Huber, and M. O. McLinden, "NIST Standard Reference Database 23: Reference Fluid Thermodynamic and Transport Properties-REFPROP, Version 10.0, National Institute of Standards and Technology," 2018.

[192] Q. Zhang, W. Ye, Y. Chen, X. Li, and S. Hu, "Mechanical behavior of sandstone pressurized with supercritical co2 and water under different confining pressure conditions," *International Journal of Geomechanics*, vol. 21, jul 2021.

[193] Z. Bo, L. Zeng, Y. Chen, and Q. Xie, "Geochemical reactions-induced hydrogen loss during underground hydrogen storage in sandstone reservoirs," *International Journal of Hydrogen Energy*, vol. 46, pp. 19998–20009, jun 2021.

[194] A. Hassanpouryouzband, K. Adie, T. Cowen, E. M. Thaysen, N. Heinemann, I. B. Butler, M. Wilkinson, and K. Edlmann, "Geological hydrogen storage: Geochemical reactivity of hydrogen with sandstone reservoirs," *ACS Energy Letters*, vol. 7, pp. 2203–2210, jun 2022.

[195] A. E. Yekta, M. Pichavant, and P. Audigane, "Evaluation of geochemical reactivity of hydrogen in sandstone: Application to geological storage," *Applied Geochemistry*, vol. 95, pp. 182–194, aug 2018.

[196] L. Zeng, M. Hosseini, A. Keshavarz, S. Iglauer, Y. Lu, and Q. Xie, "Hydrogen wettability in carbonate reservoirs: Implication for underground hydrogen storage from geochemical perspective," *International Journal of Hydrogen Energy*, vol. 47, no. 60, pp. 25357–25366, 2022.

[197] L. Zeng, A. Keshavarz, Q. Xie, and S. Iglauer, "Hydrogen storage in majiagou carbonate reservoir in china: Geochemical modelling on carbonate dissolution and hydrogen loss," *International Journal of Hydrogen Energy*, vol. 47, no. 59, pp. 24861–24870, 2022.

[198] M. Hosseini, J. Fahimpour, M. Ali, A. Keshavarz, and S. Iglauer, "Hydrogen wettability of carbonate formations: Implications for hydrogen geo-storage," *Journal of Colloid and Interface Science*, vol. 614, pp. 256–266, 2022.

[199] M. Boon and H. Hajibeygi, "Experimental characterization of h 2/water multiphase flow in heterogeneous sandstone rock at the core scale relevant for underground hydrogen storage (uhs)," *Scientific Reports*, vol. 12, no. 1, p. 14604, 2022.

[200] Z. Bo, M. Boon, H. Hajibeygi, and S. Hurter, "Impact of experimentally measured relative permeability hysteresis on reservoir-scale performance of underground hydrogen storage (uhs)," *International Journal of Hydrogen Energy*, 2023.

[201] J. Li, B. Li, Q. Cheng, and Z. Gao, "Characterization of anisotropic coal permeability with the effect of sorption-induced deformation and stress," *Fuel*, vol. 309, p. 122089, 2022.

[202] J. Wu, P. Huang, F. Maggi, and L. Shen, "Effect of sorption-induced deformation on methane flow in kerogen slit pores," *Fuel*, vol. 325, p. 124886, 2022.

[203] A. Yurikov, M. Lebedev, G. Y. Gor, and B. Gurevich, "Sorption-induced deformation and elastic weakening of bentheim sandstone," *Journal of Geophysical Research: Solid Earth*, vol. 123, no. 10, pp. 8589–8601, 2018.

[204] F. Bardelli, C. Mondelli, M. Didier, J. G. Vitillo, D. R. Cavicchia, J.-C. Robinet, L. Leone, and L. Charlet, "Hydrogen uptake and diffusion in callovo-oxfordian clay rock for nuclear waste disposal technology," *Applied Geochemistry*, vol. 49, pp. 168–177, 2014.

[205] M. Didier, L. Leone, J.-M. Greneche, E. Giffaut, and L. Charlet, "Adsorption of hydrogen gas and redox processes in clays," *Environmental Science & Technology*, vol. 46, no. 6, pp. 3574–3579, 2012.

[206] C. Mondelli, F. Bardelli, J. G. Vitillo, M. Didier, J. Brendle, D. R. Cavicchia, J.-C. Robinet, and L. Charlet, "Hydrogen adsorption and diffusion in synthetic na-montmorillonites at high pressures and temperature," *International Journal of Hydrogen Energy*, vol. 40, no. 6, pp. 2698–2709, 2015.

[207] R. H. Worden and S. D. Burley, *Sandstone Diagenesis: The Evolution of Sand to Stone*, pp. 1–44. John Wiley & Sons, Ltd, 2003.

[208] F. Wang, Z. Jie, H. Liu, D. Yin, W. Zhu, J. Zhou, and Y. Zou, "Numerical study on sandstone strength and failure characteristics with heterogeneous structure," *Bulletin of Engineering Geology and the Environment*, vol. 82, dec 2022.

[209] Y. Zhao, H. Zhou, J. Zhong, and D. Liu, "Study on the relation between damage and permeability of sandstone at depth under cyclic loading," *International Journal of Coal Science & Technology*, vol. 6, pp. 479–492, 2019.

[210] B. Liu, Y. Ma, G. Zhang, and W. Xu, "Acoustic emission investigation of hydraulic and mechanical characteristics of muddy sandstone experienced one freeze-thaw cycle," *Cold Regions Science and Technology*, vol. 151, pp. 335–344, jul 2018.

[211] W. Shuai, X. Ying, Z. Yanbo, Y. Xulong, L. Peng, and L. Xiangxin, "Effects of sandstone mineral composition heterogeneity on crack initiation and propagation through a microscopic analysis technique," *International Journal of Rock Mechanics and Mining Sciences*, vol. 162, p. 105307, feb 2023.

[212] P. L. P. Wasantha, P. G. Ranjith, J. Zhao, S. S. Shao, and G. Permata, "Strain rate effect on the mechanical behaviour of sandstones with different grain sizes," *Rock Mechanics and Rock Engineering*, vol. 48, pp. 1883–1895, dec 2014.

[213] R. Tarkowski, "Underground hydrogen storage: Characteristics and prospects," *Renewable and Sustainable Energy Reviews*, vol. 105, pp. 86–94, 2019.

[214] L. Lankof and R. Tarkowski, "Assessment of the potential for underground hydrogen storage in bedded salt formation," *International journal of hydrogen energy*, vol. 45, no. 38, pp. 19479–19492, 2020.

[215] F. Crotogino, S. Donadei, U. Bünger, and H. Landinger, "Large-scale hydrogen underground storage for securing future energy supplies," in *18th World hydrogen energy conference*, vol. 78, pp. 37–45, 2010.

[216] M. AbuAisha and J. Billiotte, "A discussion on hydrogen migration in rock salt for tight underground storage with an insight into a laboratory setup," *Journal of Energy Storage*, vol. 38, p. 102589, 2021.

[217] K. Khaledi, "Constitutive modeling of rock salt with application to energy storage caverns," 2018.

[218] P. Fokker, C. Kenter, and H. Rogaar, "The effect of fluid pressures on the mechanical stability of (rock) salt," in *Proc. 7th symp. on salt, Elsevier Sci. Pub*, 1993.

[219] J. Ter Heege, J. De Bresser, and C. Spiers, "Rheological behaviour of synthetic rocksalt: the interplay between water, dynamic recrystallization and deformation mechanisms," *Journal of Structural Geology*, vol. 27, no. 6, pp. 948–963, 2005.

[220] N. Dopffel, S. Jansen, and J. Gerritse, "Microbial side effects of underground hydrogen storage–knowledge gaps, risks and opportunities for successful implementation," *International Journal of Hydrogen Energy*, vol. 46, no. 12, pp. 8594–8606, 2021.

[221] S. P. Gregory, M. J. Barnett, L. P. Field, and A. E. Milodowski, "Subsurface microbial hydrogen cycling: Natural occurrence and implications for industry," *Microorganisms*, vol. 7, no. 2, p. 53, 2019.

[222] K.-U. Hinrichs, J. M. Hayes, W. Bach, A. J. Spivack, L. R. Hmelo, N. G. Holm, C. G. Johnson, and S. P. Sylva, "Biological formation of ethane and propane in the deep marine subsurface," *Proceedings of the National Academy of Sciences*, vol. 103, no. 40, pp. 14684–14689, 2006.

[223] M. Panfilov, I. Panfilova, A. Toleukhanov, and A. Kaltayev, "Bio-reactive two-phase transport and population dynamics in underground storage of hydrogen: Natural self-organisation," in *ECMOR 2012-13th European Conference on the Mathematics of Oil Recovery*, 2012.

[224] M. Ali, N. K. Jha, A. Al-Yaseri, Y. Zhang, S. Iglauer, and M. Sarmadivaleh, "Hydrogen wettability of quartz substrates exposed to organic acids; implications for hydrogen geo-storage in sandstone reservoirs," *Journal of Petroleum Science and Engineering*, vol. 207, p. 109081, 2021.

[225] A. Ebigbo, F. Golfier, and M. Quintard, "A coupled, pore-scale model for methanogenic microbial activity in underground hydrogen storage," *Advances in water resources*, vol. 61, pp. 74–85, 2013.

[226] E. M. Thaysen, S. McMahon, G. J. Strobel, I. B. Butler, B. T. Ngwenya, N. Heinemann, M. Wilkinson, A. Hassanpouryouzband, C. I. McDermott, and K. Edlmann, "Estimating microbial growth and hydrogen consumption in hydrogen storage in porous media," *Renewable and Sustainable Energy Reviews*, vol. 151, p. 111481, 2021.

[227] A. Ozarslan, "Large-scale hydrogen energy storage in salt caverns," *International journal of hydrogen energy*, vol. 37, no. 19, pp. 14265–14277, 2012.

[228] S. Bordenave, I. Chatterjee, and G. Voordouw, "Microbial community structure and microbial activities related to co2 storage capacities of a salt cavern," *International Biodeterioration & Biodegradation*, vol. 81, pp. 82–87, 2013.

[229] M. P. Laban, "Hydrogen storage in salt caverns: Chemical modelling and analysis of large-scale hydrogen storage in underground salt caverns.," Master's thesis, TU Delft Mechanical, Maritime and Materials Engineering, 2020.

[230] D. Zivar, S. Kumar, and J. Foroozesh, "Underground hydrogen storage: A comprehensive review," *International journal of hydrogen energy*, vol. 46, no. 45, pp. 23436–23462, 2021.

[231] A. Aftab, A. Hassanpouryouzband, Q. Xie, L. L. Machuca, and M. Sarmadivaleh, "Toward a fundamental understanding of geological hydrogen storage," *Industrial & Engineering Chemistry Research*, vol. 61, no. 9, pp. 3233–3253, 2022.

[232] R. B. Jackson, A. Vengosh, T. H. Darrah, N. R. Warner, A. Down, R. J. Poreda, S. G. Osborn, K. Zhao, and J. D. Karr, "Increased stray gas abundance in a subset of drinking water wells near Marcellus shale gas extraction," *Proceedings of the National Academy of Sciences of the United States of America*, vol. 110, pp. 11250–11255, jul 2013.

[233] R. J. Davies, S. Almond, R. S. Ward, R. B. Jackson, C. Adams, F. Worrall, L. G. Herringshaw, J. G. Gluyas, and M. A. Whitehead, "Oil and gas wells and their integrity: Implications for shale and unconventional resource exploitation," *Marine and Petroleum Geology*, vol. 56, pp. 239–254, sep 2014.

[234] R. Kiran, C. Teodoriu, Y. Dadmohammadi, R. Nygaard, D. Wood, M. Mokhtari, and S. Salehi, "Identification and evaluation of well integrity and causes of failure of well integrity barriers (A review)," *Journal of Natural Gas Science and Engineering*, vol. 45, pp. 511–526, sep 2017.

[235] H. S. Klapper and J. Stevens, "Challenges for Metallic Materials Facing HTHP Geothermal Drilling," in *CORROSION 2013, Orlando, Florida, March 2013*, OnePetro, mar 2013.

[236] A. Shadravan, J. Schubert, M. Amani, and C. Teodoriu, "HPHT Cement Sheath Integrity Evaluation Method for Unconventional Wells," *Society of Petroleum Engineers - SPE International Conference on Health, Safety and Environment 2014: The Journey Continues*, vol. 1, pp. 73–81, mar 2014.

[237] E. Therond, A. P. Bois, K. Whaley, and R. Murillo, "Large Scale Testing and Modelling for Cement Zonal Isolation of Water Injection Wells," *Proceedings - SPE Annual Technical Conference and Exhibition*, vol. 2016-January, sep 2016.

[238] J. N. A. Southon, "Geothermal well design, construction and failures," pp. 24–29, World Gethermal congress, 2005.

[239] L. Santos, A. Dahi Taleghani, and D. Elsworth, "Repurposing abandoned wells for geothermal energy: Current status and future prospects," *Renewable Energy*, vol. 194, pp. 1288–1302, 2022.

[240] E. Chiotis and G. Vrellis, "Analysis of casing failures of deep geothermal wells in greece," *Geothermics*, vol. 24, pp. 695–705, 10 1995.

[241] P. Allahvirdizadeh, "A review on geothermal wells: Well integrity issues," *Journal of Cleaner Production*, vol. 275, p. 124009, dec 2020.

[242] L. Smith, M. A. Billingham, C. H. Lee, and D. Milanovic, "Establishing and maintaining the integrity of wells used for sequestration of CO2," *Energy Procedia*, vol. 4, pp. 5154–5161, 2011.

[243] K. Mortezaei, A. Amirlatifi, E. Ghazanfari, and F. Vahedifard, "Potential CO 2 leakage from geological storage sites : advances and challenges," *Environmental geotechnics*, no. February, 2021.

[244] M. J. Thiercelin, B. Dargaud, J. F. Baret, and W. J. Rodriquez, "Cement Design Based on Cement Mechanical Response," *SPE Drilling and Completion*, vol. 13, pp. 266–273, dec 1998.

[245] R. Nygaard, S. Salehi, B. Weideman, and R. Lavoie, "Effect of Dynamic Loading on Wellbore Leakage for the Wabamun Area CO2-Sequestration Project," *Journal of Canadian Petroleum Technology*, vol. 53, pp. 69–82, feb 2014.

[246] S. Carroll, J. W. Carey, D. Dzombak, N. J. Huerta, L. Li, T. Richard, W. Um, S. D. Walsh, and L. Zhang, "Review: Role of chemistry, mechanics, and transport on well integrity in co2 storage environments," *International Journal of Greenhouse Gas Control*, vol. 49, pp. 149–160, 2016.

[247] J. Iyer, G. Lackey, L. Edvardsen, A. Bean, S. A. Carroll, N. Huerta, M. M. Smith, M. Torsæter, R. M. Dilmore, and P. Cerasi, "A Review of Well Integrity Based on Field Experience at Carbon Utilization and Storage Sites," *International Journal of Greenhouse Gas Control*, vol. 113, jan 2022.

[248] C. B. Bavoh, B. Lal, H. Osei, K. M. Sabil, and H. Mukhtar, "A review on the role of amino acids in gas hydrate inhibition, CO2 capture and sequestration, and natural gas storage," *Journal of Natural Gas Science and Engineering*, vol. 64, pp. 52–71, apr 2019.

[249] L. Cui, W. Kang, H. You, J. Cheng, and Z. Li, "Experimental Study on Corrosion of J55 Casing Steel and N80 Tubing Steel in High Pressure and High Temperature Solution Containing CO2 and NaCl," *Journal of Bio- and Tribo-Corrosion*, vol. 7, pp. 1–14, mar 2021.

[250] R. Elgaddafi, R. Ahmed, and S. Shah, "Corrosion of carbon steel in CO2 saturated brine at elevated temperatures," *Journal of Petroleum Science and Engineering*, vol. 196, p. 107638, jan 2021.

[251] T. Lin, Q. Zhang, Z. Lian, X. Chang, K. Zhu, and Y. Liu, "Evaluation of casing integrity defects considering wear and corrosion – Application to casing design," *Journal of Natural Gas Science and Engineering*, vol. 29, pp. 440–452, feb 2016.

[252] B. G. Kutchko, B. R. Strazisar, D. A. Dzombak, G. V. Lowry, and N. Thauiow, "Degradation of well cement by CO2 under geologic sequestration conditions," *Environmental Science and Technology*, vol. 41, pp. 4787–4792, jul 2007.

[253] O. Omosebi, H. Maheshwari, R. Ahmed, S. Shah, S. Osisanya, S. Hassani, G. DeBruijn, W. Cornell, and D. Simon, "Degradation of well cement in hpht acidic environment: Effects of co2 concentration and pressure," *Cement and Concrete Composites*, vol. 74, pp. 54–70, 2016.

[254] J. Condor and K. Asghari, "Experimental Study of Stability and Integrity of Cement in Wellbores Used for CO2 Storage," *Energy Procedia*, vol. 1, pp. 3633–3640, feb 2009.

[255] M. Bai, J. Sun, K. Song, K. M. Reinicke, and C. Teodoriu, "Evaluation of mechanical well integrity during CO2 underground storage," *Environmental Earth Sciences*, vol. 73, pp. 6815–6825, jun 2015.

[256] A.-P. Bois, A. Garnier, G. Galdiolo, and J.-B. Laudet, "Use of a Mechanistic Model To Forecast Cement-Sheath Integrity," *SPE Drilling and Completion*, vol. 27, pp. 303–314, 05 2012.

[257] L. Zhao, Y. Yan, P. Wang, and X. Yan, "A risk analysis model for underground gas storage well integrity failure," *Journal of Loss Prevention in the Process Industries*, vol. 62, p. 103951, nov 2019.

[258] M. Bai, A. Shen, L. Meng, J. Zhu, and K. Song, "Well completion issues for underground gas storage in oil and gas reservoirs in China," *Journal of Petroleum Science and Engineering*, vol. 171, pp. 584–591, dec 2018.

[259] X. Song, C. Peng, G. Li, and K. Wen, "A Probabilistic Model to Evaluate the Operation Reliability of the Underground System in Underground Gas Storage Transformed from Depleted Gas Reservoir," International Petroleum Technology Conference, Bangkok, Thailand, November 2016, nov 2016.

[260] C. Hu, F. Agostini, F. Skoczylas, L. Jeannin, and L. Potier, "Poromechanical Properties of a Sandstone Under Different Stress States," *Rock Mechanics and Rock Engineering*, vol. 51, pp. 3699–3717, dec 2018.

[261] V. Reitenbach, D. Albrecht, and L. Ganzer, "Einfluss von Wasserstoff auf Untertagegasspeicher - Literaturstudie - DGMK e.V.," tech. rep., 2014.

[262] A. Hussain, H. Al-hadrami, H. Emadi, F. Altawati, S. R. Thiyagarajan, and M. Watson, "Experimental Investigation of Wellbore Integrity of Depleted Oil and Gas Reservoirs for Underground Hydrogen Storage," in *Offshore Technology Conference held in Houston*, 2022.

[263] M. Ghamgosar, N. Erarslan, and D. J. Williams, "Experimental Investigation of Fracture Process Zone in Rocks Damaged Under Cyclic Loadings," *Experimental Mechanics*, vol. 57, pp. 97–113, jan 2017.

[264] Y. M. Hashash, J. J. Hook, B. Schmidt, and J. I-Chiang Yao, "Seismic design and analysis of underground structures," *Tunnelling and Underground Space Technology*, vol. 16, pp. 247–293, oct 2001.

[265] A. Zang, J. S. Yoon, O. Stephansson, and O. Heidbach, "Fatigue hydraulic fracturing by cyclic reservoir treatment enhances permeability and reduces induced seismicity," *Geophysical Journal International*, vol. 195, pp. 1282–1287, aug 2013.

[266] J. E. Kendrick, R. Smith, P. Sammonds, P. G. Meredith, M. Dainty, and J. S. Pallister, "The influence of thermal and cyclic stressing on the strength of rocks from Mount St. Helens, Washington," *Bulletin of Volcanology*, vol. 75, pp. 1–12, jun 2013.

[267] A. S. Voznesenskii, M. N. Krasilov, Y. O. Kutkin, M. N. Tavostin, and Y. V. Osipov, "Features of interrelations between acoustic quality factor and strength of rock salt during fatigue cyclic loadings," *International Journal of Fatigue*, vol. 97, pp. 70–78, apr 2017.

[268] Z. Wang, S. Li, L. Qiao, and Q. Zhang, "Finite element analysis of the hydro-mechanical behavior of an underground crude oil storage facility in granite subject to cyclic loading during operation," *International Journal of Rock Mechanics and Mining Sciences*, vol. 73, pp. 70–81, jan 2015.

[269] P. Cosenza, M. Ghoreychi, B. Bazargan-Sabet, and G. De Marsily, "In situ rock salt permeability measurement for long term safety assessment of storage," *International Journal of Rock Mechanics and Mining Sciences*, vol. 36, pp. 509–526, jun 1999.

[270] J. Chen and C. J. Spiers, "Rate and state frictional and healing behavior of carbonate fault gouge explained using microphysical model," *Journal of Geophysical Research: Solid Earth*, vol. 121, pp. 8642–8665, dec 2016.

[271] H. D. Yu, W. Z. Chen, Z. Gong, X. J. Tan, Y. S. Ma, X. L. Li, and X. Sillen, "Creep behavior of boom clay," *International Journal of Rock Mechanics and Mining Sciences*, vol. 76, pp. 256–264, jun 2015.

[272] S. Jia, C. Wen, and B. Wu, "A nonlinear elasto-viscoplastic model for clayed rock and its application to stability analysis of nuclear waste repository," *Energy Science & Engineering*, vol. 8, pp. 150–165, jan 2020.

[273] T. Y. Hou and X. H. Wu, "A multiscale finite element method for elliptic problems in composite materials and porous media," *Journal of Computational Physics*, vol. 134, pp. 169–189, jun 1997.

[274] P. Jenny, S. H. Lee, and H. A. Tchelepi, "Multi-scale finite-volume method for elliptic problems in subsurface flow simulation," *Journal of Computational Physics*, vol. 187, pp. 47–67, may 2003.

[275] H. Hajibeygi, G. Bonfigli, M. A. Hesse, and P. Jenny, "Iterative multiscale finite-volume method," *Journal of Computational Physics*, vol. 227, pp. 8604–8621, oct 2008.

[276] O. Moyner and K.-A. Lie, "A multiscale restriction-smoothed basis method for high contrast porous media represented on unstructured grids," *Journal of Computational Physics*, vol. 304, pp. 46–71, Jan. 2016.

[277] N. Castelletto, H. Hajibeygi, and H. A. Tchelepi, "Multiscale finite-element method for linear elastic geomechanics," *Journal of Computational Physics*, vol. 331, pp. 337–356, feb 2017.

[278] K. Ramesh Kumar and H. Hajibeygi, "Multi-scale Nonlinear Modeling of Subsurface Energy Storage: Cyclic Loading with Inelastic Creep Deformation," in *ECMOR XVII*, vol. 2020, pp. 1–13, European Association of Geoscientists & Engineers, sep 2020.

[279] Y. Efendiev, J. Galvis, and T. Y. Hou, "Generalized multiscale finite element methods (GMsFEM)," *Journal of Computational Physics*, vol. 251, pp. 116–135, oct 2013.

[280] E. Chung, Y. Efendiev, and T. Y. Hou, "Adaptive multiscale model reduction with Generalized Multiscale Finite Element Methods," *Journal of Computational Physics*, vol. 320, pp. 69–95, sep 2016.

[281] R. T. Guiraldello, R. F. Ausas, F. S. Sousa, F. Pereira, and G. C. Buscaglia, "The Multiscale Robin Coupled Method for flows in porous media," *Journal of Computational Physics*, vol. 355, pp. 1–21, feb 2018.

[282] F. F. Rocha, F. S. Sousa, R. F. Ausas, G. C. Buscaglia, and F. Pereira, "Multiscale mixed methods for two-phase flows in high-contrast porous media," *Journal of Computational Physics*, vol. 409, p. 109316, may 2020.

[283] B. Guo, Y. Mehmani, and H. A. Tchelepi, "Multiscale formulation of pore-scale compressible Darcy-Stokes flow," *Journal of Computational Physics*, vol. 397, p. 108849, nov 2019.

[284] M. Cusini, J. A. White, N. Castelletto, and R. R. Settgast, "Simulation of coupled multiphase flow and geomechanics in porous media with embedded discrete fractures," *International Journal for Numerical and Analytical Methods in Geomechanics*, vol. 45, pp. 563–584, apr 2021.

[285] D. L. Brown, P. Popov, and Y. Efendiev, "Effective equations for fluid-structure interaction with applications to poroelasticity," *Applicable Analysis*, vol. 93, no. 4, pp. 771–790, 2014.

[286] E. T. Chung, Y. Efendiev, and S. Fu, "Generalized multiscale finite element method for elasticity equations," *GEM - International Journal on Geomathematics*, vol. 5, pp. 225–254, nov 2014.

[287] Y. Mehmani, N. Castelletto, and H. A. Tchelepi, "Multiscale formulation of frictional contact mechanics at the pore scale," *Journal of Computational Physics*, vol. 430, p. 110092, apr 2021.

[288] J. A. White, N. Castelletto, S. Klevtsov, Q. M. Bui, D. Osei-Kuffuor, and H. A. Tchelepi, "A two-stage preconditioner for multiphase poromechanics in reservoir simulation," *Computer Methods in Applied Mechanics and Engineering*, vol. 357, p. 112575, dec 2019.

[289] Y. Efendiev, T. Hou, and V. Ginting, "Multiscale finite element methods for nonlinear problems and their applications," *Communication Maths*, vol. 2, pp. 553–589, dec 2004.

[290] T. Hou and Y. Efendiev, "Multiscale finite element methods for nonlinear equations," in *Surveys and Tutorials in the Applied Mathematical Sciences*, ch. 2, pp. 1–20, Springer New York, 2009.

[291] R. Borst and E. Ramm, eds., *Multiscale Methods in Computational Mechanics: Progress and Accomplishments*. Springer, Dordrecht, 2011.

[292] F. Feyel and J. L. Chaboche, "FE 2 multiscale approach for modelling the elastoviscoplastic behaviour of long fibre SiC/Ti composite materials," *Computer Methods in Applied Mechanics and Engineering*, vol. 183, pp. 309–330, mar 2000.

[293] N. Guo and J. Zhao, "A coupled FEM/DEM approach for hierarchical multiscale modelling of granular media," *International Journal for Numerical Methods in Engineering*, vol. 99, pp. 789–818, sep 2014.

[294] H. Wu, N. Guo, and J. Zhao, "Multiscale modeling and analysis of compaction bands in high-porosity sandstones," *Acta Geotechnica*, vol. 13, pp. 575–599, jun 2018.

[295] H. Hajibeygi and P. Jenny, "Multiscale finite-volume method for parabolic problems arising from compressible multiphase flow in porous media," *Journal of Computational Physics*, vol. 228, pp. 5129–5147, aug 2009.

[296] N. Castelletto, S. Klevtsov, H. Hajibeygi, and H. A. Tchelepi, "Multiscale two-stage solver for Biot's poroelasticity equations in subsurface media," *Computational Geosciences*, vol. 23, pp. 207–224, apr 2019.

[297] P. Teatini, D. Baú, and G. Gambolati, "Water-gas dynamics and coastal land subsidence over Chioggia Mare field, northern Adriatic Sea," *Hydrogeology Journal*, vol. 8, no. 5, pp. 462–479, 2000.

[298] Y. Wang, H. Hajibeygi, and H. A. Tchelepi, "Algebraic multiscale solver for flow in heterogeneous porous media," *Journal of Computational Physics*, vol. 259, pp. 284–303, feb 2014.

[299] Y. Saad and M. H. Schultz, "GMRES: A GENERALIZED MINIMAL RESIDUAL ALGORITHM FOR SOLVING NONSYMMETRIC LINEAR SYSTEMS*," Tech. Rep. 3, 1986.

[300] E. Chow and Y. Saad, "Experimental study of ILU preconditioners for indefinite matrices," *Journal of Computational and Applied Mathematics*, vol. 86, pp. 387–414, dec 1997.

[301] S. R. Taheri, A. Pak, S. Shad, B. Mehrgini, and M. Razifar, "Investigation of rock salt layer creep and its effects on casing collapse," *International Journal of Mining Science and Technology*, vol. 30, pp. 357–365, may 2020.

[302] W. Liang, C. Zhang, H. Gao, X. Yang, S. Xu, and Y. Zhao, "Experiments on mechanical properties of salt rocks under cyclic loading," *Journal of Rock Mechanics and Geotechnical Engineering*, vol. 4, no. 1, pp. 54–61, 2012.

[303] L. Dondi, A. Rizzini, and P. Rossi, "Recent Geological Evolution of the Adriatic Sea," in *Geological Evolution of the Mediterranean Basin*, pp. 195–214, Springer New York, 1985.

[304] D. Bau, M. Ferronato, G. Gambolati, and P. Teatini, "Basin-scale compressibility of the northern adriatic by the radioactive marker technique," *Géotechnique*, vol. 52, pp. 605–616, 01 2002.

[305] ILK Dresden, "Storage density of hydrogen under certain pressure and temperature conditions," tech. rep., Dresden, 2008.

[306] Netherlands Enterprise Agency, "'The effects of hydrogen injection in natural gas networks for the Dutch underground storages' ," tech. rep., Ministry of Economic Affairs, Netherlands, 2017.

[307] S. Donadei and G.-S. Schneider, "Chapter 6 - compressed air energy storage in underground formations," in *Storing Energy* (T. M. Letcher, ed.), pp. 113–133, Oxford: Elsevier, 2016.

[308] M. Laban, "Hydrogen storage in salt caverns: Chemical modelling and analysis of large-scale hydrogen storage in underground salt caverns," *http://resolver.tudelft.nl/uuid:d647e9a5-cb5c-47a4-b02f-10bc48398af4*, 2020.

[309] A. S. Lord, P. H. Kobos, and D. J. Borns, "Geologic storage of hydrogen: Scaling up to meet city transportation demands," *International Journal of Hydrogen Energy*, vol. 39, pp. 15570–15582, sep 2014.

[310] M. Jackson and C. Talbot, "External shapes, strain rates, and dynamics of salt structures," *Geological Society of America Bulletin - GEOL SOC AMER BULL*, vol. 97, 01 1986.

[311] M. Jeremic, *Rock Mechanics in Salt Mining*. CRC Press, 1994.

[312] TNO, "Salt extraction data sheets," tech. rep., Apr 2012.

[313] J. Betten, *Creep mechanics*. Springer, 2014.

[314] S. Li and J. L. Urai, "Rheology of rock salt for salt tectonics modeling," *Petroleum Science*, vol. 13, pp. 712–724, oct 2016.

[315] J. Urai and C. Spiers, "The effect of grain boundary water on deformation mechanisms and rheology of rocksalt during long-term deformation," in *The Mechanical Behavior of Salt - Understanding of THMC Processes in Salt*, pp. 149–158, CRC Press, dec 2017.

[316] P. Bérest, J. Béraud, M. Bourcier, A. Dimanov, H. Gharbi, B. Brouard, K. DeVries, and D. Tribout, "Very slow creep tests on rock samples," in *Mechanical Behaviour of Salt VII*, CRC Press, mar 2012.

[317] N. Carter, S. Horseman, J. Russell, and J. Handin, "Rheology of rocksalt," *Journal of Structural Geology*, vol. 15, no. 9-10, pp. 1257–1271, 1993.

[318] U. Hunsche and A. Hampel, "Rock salt—the mechanical properties of the host rock material for a radioactive waste repository," *Engineering geology*, vol. 52, no. 3-4, pp. 271–291, 1999.

[319] C. J. Peach, C. J. Spiers, and P. W. Trimby, "Effect of confining pressure on dilatation, recrystallization, and flow of rock salt at 150c," *Journal of Geophysical Research: Solid Earth*, vol. 106, pp. 13315–13328, jul 2001.

[320] J. H. Ter Heege, J. H. De Bresser, and C. J. Spiers, "Dynamic recrystallization of wet synthetic polycrystalline halite: Dependence of grain size distribution on flow stress, temperature and strain," *Tectonophysics*, vol. 396, pp. 35–57, feb 2005.

[321] J. H. Ter Heege, J. H. De Bresser, and C. J. Spiers, "Rheological behaviour of synthetic rocksalt: The interplay between water, dynamic recrystallization and deformation mechanisms," *Journal of Structural Geology*, vol. 27, pp. 948–963, jun 2005.

[322] C. J. Spiers, P. M. Schutjens, R. H. Brzesowsky, C. J. Peach, J. L. Liezenberg, and H. J. Zwart, "Experimental determination of constitutive parameters governing creep of rocksalt by pressure solution," *Geological Society Special Publication*, vol. 54, pp. 215–227, jan 1990.

[323] A. Hampel and O. Schulze, "The composite dilatancy model: A constitutive model for the mechanical behavior of rock salt," in *The Mechanical Behavior of Salt – Understanding of THMC Processes in Salt*, pp. 99–107, CRC Press, dec 2017.

[324] J. S. Cornet, M. Dabrowski, and D. W. Schmid, "Long term creep closure of salt cavities," *International Journal of Rock Mechanics and Mining Sciences*, vol. 103, pp. 96–106, mar 2018.

[325] J. S. Cornet and M. Dabrowski, "Nonlinear Viscoelastic Closure of Salt Cavities," *Rock Mechanics and Rock Engineering 2018 51:10*, vol. 51, pp. 3091–3109, may 2018.

[326] J. Betten, *Creep mechanics (Third Edition)*. Springer Berlin Heidelberg, 2008.

[327] C. Spiers, P. Schutjens, R. Brzesowsky, C. Peach, J. Liezenberg, and H. Zwart, "Experimental determination of constitutive parameters governing creep of rocksalt by pressure solution," *Geological Society, London, Special Publications*, vol. 54, no. 1, pp. 215–227, 1990.

[328] W. Xing, J. Zhao, U. Düsterloh, D. Brückner, Z. Hou, L. Xie, and J. Liu, "Experimental study of mechanical and hydraulic properties of bedded rock salt from the Jintan location," *Acta Geotechnica*, vol. 9, pp. 145–151, aug 2014.

[329] B. Y. Park, S. R. Sobolik, and C. G. Herrick, "Geomechanical Model Calibration Using Field Measurements for a Petroleum Reserve," *Rock Mechanics and Rock Engineering*, vol. 51, pp. 925–943, mar 2018.

[330] D. E. Munson and P. R. Dawson, "A transient creep model for salt during stress loading and unloading," *SAND82-0962. Sandia National Laboratories,Albuquerque*, 1982.

[331] L. Ma, M. Wang, N. Zhang, P. Fan, and J. Li, "A Variable-Parameter Creep Damage Model Incorporating the Effects of Loading Frequency for Rock Salt and Its Application in a Bedded Storage Cavern," *Rock Mechanics and Rock Engineering*, vol. 50, pp. 2495–2509, sep 2017.

[332] W. Liang, C. Yang, Y. Zhao, M. B. Dusseault, and J. Liu, "Experimental investigation of mechanical properties of bedded salt rock," *International Journal of Rock Mechanics and Mining Sciences*, vol. 44, pp. 400–411, apr 2007.

[333] N. Zhang, X. Shi, T. Wang, C. Yang, W. Liu, H. Ma, and J. J. Daemen, "Stability and availability evaluation of underground strategic petroleum reserve (SPR) caverns in bedded rock salt of Jintan, China," *Energy*, vol. 134, pp. 504–514, sep 2017.

[334] W. Liu, Z. Zhang, J. Chen, J. Fan, D. Jiang, D. Jjk, and Y. Li, "Physical simulation of construction and control of two butted-well horizontal cavern energy storage using large molded rock salt specimens," *Energy*, vol. 185, pp. 682–694, oct 2019.

[335] J. Liu, H. Xie, Z. Hou, C. Yang, and L. Chen, "Damage evolution of rock salt under cyclic loading in unixial tests," *Acta Geotechnica*, vol. 9, pp. 153–160, 2014.

[336] J. Li, X. Shi, C. Yang, Y. Li, T. Wang, and H. Ma, "Mathematical model of salt cavern leaching for gas storage in high-insoluble salt formations," *Scientific Reports 2017 8:1*, vol. 8, pp. 1–12, jan 2018.

[337] A. Luangthip, N. Wilalak, T. Thongprapha, and K. Fuenkajorn, "Effects of carnallite content on mechanical properties of Maha Sarakham rock salt," *Arabian Journal of Geosciences*, vol. 10, no. 149, pp. 1–14, 2017.

[338] D. Bonté, J.-D. van Wees, and J. Verweij, "Subsurface temperature of the onshore netherlands: new temperature dataset and modelling," *Netherlands Journal of Geosciences - Geologie en Mijnbouw*, vol. 91, pp. 491–515, dec 2012.

[339] N. L. Carter, S. T. Horseman, J. E. Russell, and J. Handin, "Rheology of rocksalt," *Journal of Structural Geology*, vol. 15, pp. 1257–1271, sep 1993.

[340] Xiao Xueying, Zhang Zhihong, Wang Jidong, Cheng Huaide, Zhang Quanyou, Dong RuDong, and ShengfaMa Yanfang, "Coagulating salt for potassium salt solid mine backfilling and manufacturing method thereof," jan China patent, 2011.

[341] N. Zhang, W. Liu, Y. Zhang, P. Shan, and X. Shi, "Microscopic Pore Structure of Surrounding Rock for Underground Strategic Petroleum Reserve (SPR) Caverns in Bedded Rock Salt," *Energies*, vol. 13, p. 1565, mar 2020.

[342] K.-H. Lux, "Design of salt caverns for the storage of natural gas, crude oil and compressed air: Geomechanical aspects of construction, operation and abandonment," *Geological Society, London, Special Publications*, vol. 313, no. 1, pp. 93–128, 2009.

[343] R. Groenenberg, J. Koornnef, J. Sijm, G. Janssen, G. Morales España, J. van Stralen, R. Hernandez-Serna, K. Smekens, J. Juez-Larre, C. Goncalves Machado, *et al.*, "Large-scale energy storage in salt caverns and depleted fields (lses)–project findings," 2020.

[344] W. Li, X. Miao, and C. Yang, "Failure analysis for gas storage salt cavern by thermo-mechanical modelling considering rock salt creep," *Journal of Energy Storage*, vol. 32, p. 102004, dec 2020.

[345] T. Bai and P. Tahmasebi, "Coupled hydro-mechanical analysis of seasonal underground hydrogen storage in a saline aquifer," *Journal of Energy Storage*, vol. 50, p. 104308, 2022.

[346] A. Pouya, C. Zhu, and C. Arson, "Micro–macro approach of salt viscous fatigue under cyclic loading," *Mechanics of Materials*, vol. 93, pp. 13–31, 2016.

[347] W. M. Wang, L. J. Sluys, and R. de Borst, "Viscoplasticity for instabilities due to strain softening and strain-rate softening," *International Journal for Numerical Methods in Engineering*, vol. 40, no. 20, pp. 3839–3864, 1997.

[348] M. Cai, "Practical estimates of tensile strength and hoek–brown strength parameter mi of brittle rocks," *Rock Mechanics and Rock Engineering*, vol. 43, no. 2, pp. 167–184, 2010.

[349] P. Baud, V. Vajdova, and T.-f. Wong, "Shear-enhanced compaction and strain localization: Inelastic deformation and constitutive modeling of four porous sandstones," *Journal of Geophysical Research: Solid Earth*, vol. 111, no. B12, 2006.

[350] Y. Wang, C. Li, Y. Hu, and X. Zhou, "A new method to evaluate the brittleness for brittle rock using crack initiation stress level from uniaxial stress–strain curves," *Environmental earth sciences*, vol. 76, no. 23, pp. 1–18, 2017.

[351] N. Brantut, M. Heap, P. Meredith, and P. Baud, "Time-dependent cracking and brittle creep in crustal rocks: A review," *Journal of Structural Geology*, vol. 52, pp. 17–43, 2013.

[352] E. Hoek, *Rock fracture under static stress conditions*. CSIR, 1965.

[353] J.-c. Zhang, Z.-n. Lin, B. Dong, and R.-x. Guo, "Triaxial compression testing at constant and reducing confining pressure for the mechanical characterization of a specific type of sandstone," *Rock Mechanics and Rock Engineering*, vol. 54, no. 4, pp. 1999–2012, 2021.

[354] T.-f. Wong and P. Baud, "The brittle-ductile transition in porous rock: A review," *Journal of Structural Geology*, vol. 44, pp. 25–53, 2012.

[355] C. Martin and N. Chandler, "The progressive fracture of lac du bonnet granite," in *International journal of rock mechanics and mining sciences & geomechanics abstracts*, vol. 31, pp. 643–659, Elsevier, 1994.

[356] K. H. Roscoe and J. B. Burland, "On the Generalized Stress-Strain Behavior of Wet Clays," in *Engineering plasticity* (J. Heyman and F. A. Leckie, eds.), 1968.

[357] O. Coussy, *Poromechanics*. Wiley, 2004.

[358] M. A. Nikolinakou, G. Luo, M. R. Hudec, and P. B. Flemings, "Geomechanical modeling of stresses adjacent to salt bodies: Part 2 - Poroelastoplasticity and coupled overpressures," *AAPG Bulletin*, vol. 96, pp. 65–85, jan 2012.

[359] B. van der Pluijm, *EARTH STRUCTURE:An Introduction to Structural Geology and Tectonics*. New York, NY: W. W. Norton & Company, Inc, 2 ed., 2004.

[360] R. Weijermars, *Principles of rock mechanics*. hahran, Saudi Arabia: Alboran Science Pub, 6 ed., 1997.

[361] D. Muir Wood, *Soil behaviour and critical state soil mechanics*. Cambridge [England]: Cambridge University Press, nv - 1 onl ed., 1990.

[362] J. Carter, J. Booker, and C. Wroth, "A critical state soil model for cyclic loading. soil mechanics transient and cyclic loads. constitutive relations and numerical treatment," 1982.

[363] R. I. Borja, "Cam-Clay plasticity, Part II: Implicit integration of constitutive equation based on a nonlinear elastic stress predictor," *Computer Methods in Applied Mechanics and Engineering*, vol. 88, pp. 225–240, jul 1991.

[364] J. Simo and T. Hughes, "Integration Algorithms for Plasticity and Viscoplasticity," in *Computational Inelasticity*, pp. 113–153, Springer-Verlag, may 2006.

[365] E. A. de Souza Neto, D. Peri, and D. R. J. Owen, *Computational Methods for Plasticity*. Chichester, UK: John Wiley and Sons, Ltd, oct 2008.

[366] K. Liu, S. L. Chen, and G. Z. Voyiadjis, "Integration of anisotropic modified Cam Clay model in finite element analysis: Formulation, validation, and application," *Computers and Geotechnics*, vol. 116, p. 103198, dec 2019.

[367] L. Sluijs, "Lecture notes in computational methods in nonlinear solid mechanics," December 2021.

[368] P. Gabrielli, A. Poluzzi, G. J. Kramer, C. Spiers, M. Mazzotti, and M. Gazzani, "Seasonal energy storage for zero-emissions multi-energy systems via underground hydrogen storage," *Renewable and Sustainable Energy Reviews*, vol. 121, p. 109629, Apr. 2020. Publisher: Elsevier Ltd.

[369] DBI GmbH, "The effects of hydrogen injection in natural gas networks for the Dutch underground storages," tech. rep., Ministry of Economic Affairs, Netherlands, Hague, 2017.

[370] M. Tene, M. S. Al Kobaisi, and H. Hajibeygi, "Algebraic multiscale method for flow in heterogeneous porous media with embedded discrete fractures (F-AMS)," *Journal of Computational Physics*, vol. 321, pp. 819–845, sep 2016.

[371] A. Muntendam-Bos, B. Wassing, C. Geel, M. Louh, and K. V. Thienen-Visser, "Bergermeer seismicity study," tech. rep., TNO, Nov 2008.

[372] J.-D. Van Wees, S. Osinga, K. Van Thienen-Visser, and P. A. Fokker, "Reservoir creep and induced seismicity: inferences from geomechanical modeling of gas depletion in the Groningen field," *Geophysical Journal International Geophys. J. Int*, vol. 212, pp. 1487–1497, 2018.

[373] M. Hettema, E. Papamichos, and P. Schutjens, "Subsidence Delay: Field Observations and Analysis," *Oil & Gas Science and Technology*, vol. 57, pp. 443–458, sep 2002.

[374] M. A. Biot, "General Theory of Three-Dimensional Consolidation," *Journal of Applied Physics*, vol. 12, pp. 155–164, 04 2004.

[375] H. Wang and P. University, *Theory of Linear Poroelasticity with Applications to Geomechanics and Hydrogeology*. Princeton Series in Geophysics, Princeton University Press, 2000.

[376] R. J. de Moraes, J. R. Rodrigues, H. Hajibeygi, and J. D. Jansen, "Multiscale gradient computation for flow in heterogeneous porous media," *Journal of Computational Physics*, vol. 336, pp. 644–663, 2017.

[377] H. Hajibeygi, *Iterative multiscale finite volume method for multiphase flow in porous media with complex physics*. PhD thesis, ETH Zurich, Switzerland, 2011.

[378] M. HosseiniMehr, C. Vuik, and H. Hajibeygi, "Adaptive dynamic multilevel simulation of fractured geothermal reservoirs," *Journal of Computational Physics: X*, vol. 7, p. 100061, 2020.

[379] G. Capuano, "Smart finite elements: An application of machine learning to reduced-order modeling of multi-scale problems," 2019.

[380] M. M. Almajid and M. O. Abu-Al-Saud, "Prediction of porous media fluid flow using physics informed neural networks," *Journal of Petroleum Science and Engineering*, vol. 208, p. 109205, 1 2022.

[381] M. Vassaux, K. Gopalakrishnan, R. C. Sinclair, R. A. Richardson, and P. V. Coveney, "Accelerating heterogeneous multiscale simulations of advanced materials properties with graph-based clustering," *Advanced Theory and Simulations*, vol. 4, p. 2000234, 2 2021.

[382] F. Feyel and J.-L. Chaboche, "Fe2 multiscale approach for modelling the elastoviscoplastic behaviour of long fibre sic/ti composite materials," *Computer Methods in Applied Mechanics and Engineering*, vol. 183, no. 3, pp. 309–330, 2000.

[383] S. Nikolopoulos, I. Kalogeris, V. Papadopoulos, and G. Stavroulakis, "AI-enhanced iterative solvers for accelerating the solution of large-scale parametrized systems," *arXiv*, 2022.

[384] T. Louw and S. McIntosh-Smith, "Applying Recent Machine Learning Approaches to Accelerate the Algebraic Multigrid Method for Fluid Simulations," *Communications in Computer and Information Science*, vol. 1512 CCIS, pp. 40–57, 2022.

[385] V. Fanaskov, "Neural Multigrid Architectures," *Proceedings of the International Joint Conference on Neural Networks*, vol. 2021-July, jul 2021.

[386] D. Greenfeld, M. Galun, R. Kimmel, I. Yavneh, and R. Basri, "Learning to Optimize Multigrid PDE Solvers," *36th International Conference on Machine Learning, ICML 2019*, vol. 2019-June, pp. 4305–4316, feb 2019.

[387] A. Katrutsa, T. Daulbaev, and I. Oseledets, "Deep Multigrid: learning prolongation and restriction matrices," *arXiv*, nov 2017.

[388] J. Brown, Y. He, S. Maclachlan, M. Menickelly, and S. M. Wild, "Tuning Multigrid Methods with Robust Optimization and Local Fourier Analysis," *SIAM Journal on Scientific Computing*, vol. 43, pp. 109–138, jan 2021.

[389] I. Luz, M. Galun, H. Maron, R. Basri, and I. Yavneh, "Learning Algebraic Multigrid Using Graph Neural Networks," in *ICML'20: Proceedings of the 37th International Conference on Machine Learning*, pp. 6489–6499, 2020.

[390] A. Taghibakhshi, S. MacLachlan, L. Olson, and M. West, "Optimization-Based Algebraic Multigrid Coarsening Using Reinforcement Learning," *Advances in Neural Information Processing Systems*, vol. 34, pp. 12129–12140, dec 2021.

[391] Z. Yang, Y. Dong, X. Deng, and L. Zhang, "AMGNET: multi-scale graph neural networks for flow field prediction," *Connection Science*, vol. 34, no. 1, pp. 2500–2519, 2022.

[392] S. Chan and A. H. Elsheikh, "Data-driven acceleration of multiscale methods for uncertainty quantification: application in transient multiphase flow in porous media," *GEM - International Journal on Geomathematics*, vol. 11, p. 3, Dec. 2019.

[393] G. Karypis, V. Kumar, and S. Comput, "A fast and high quality multilevel scheme for partitioning irregular graphs," *SIAM Journal on Scientific Computing*, vol. 20, 02 1970.

[394] J. Shi and J. Malik, "Normalized cuts and image segmentation," *IEEE Transactions on pattern analysis and machine intelligence,*, vol. 22, 7 2000.

[395] J. Cheema and J. Dicks, "Computational approaches and software tools for genetic linkage map estimation in plants," *Briefings in bioinformatics*, vol. 10, pp. 595–608, 2009.

[396] Uzma, F. Al-Obeidat, A. Tubaishat, B. Shah, and Z. Halim, "Gene encoder: a feature selection technique through unsupervised deep learning-based clustering for large gene expression data," *Neural Computing and Applications*, vol. 34, pp. 8309–8331, June 2022.

[397] R. Liu, S. Feng, R. Shi, and W. Guo, "Weighted graph clustering for community detection of large social networks," *Procedia Computer Science*, vol. 31, pp. 85–94, 1 2014.

[398] S. Sun, J. Zhao, and J. Zhu, "A review of Nyström methods for large-scale machine learning," *Information Fusion*, vol. 26, pp. 36–48, Nov. 2015.

[399] A. T. Barker, C. S. Lee, and P. S. Vassilevski, "Spectral upscaling for graph laplacian problems with application to reservoir simulation," *SIAM Journal on Scientific Computing*, vol. 39, pp. S323–S346, 2017.

[400] A. Choromanska, T. Jebara, H. Kim, M. Mohan, and C. Monteleoni, "Fast spectral clustering via the nyström method," *Lecture Notes in Computer Science (including subseries Lecture Notes in Artificial Intelligence and Lecture Notes in Bioinformatics)*, vol. 8139 LNAI, pp. 367–381, 2013.

[401] M. E. Newman, "Fast algorithm for detecting community structure in networks," *Physical Review E - Statistical Physics, Plasmas, Fluids, and Related Interdisciplinary Topics*, vol. 69, p. 5, 6 2004.

[402] A. Clauset, M. E. J. Newman, and C. Moore, "Finding community structure in very large networks," *Physical Review E - Statistical Physics, Plasmas, Fluids, and Related Interdisciplinary Topics*, vol. 70, p. 6, 8 2004.

[403] V. D. Blondel, J. L. Guillaume, R. Lambiotte, and E. Lefebvre, "Fast unfolding of communities in large networks," *Journal of Statistical Mechanics: Theory and Experiment*, p. P10008, 10 2008.

[404] W.-L. Chiang, X. Liu, S. S. G. Research, Y. L. G. Research, G. Research, C.-J. Hsieh, S. Si, Y. Li, and S. Bengio, "Cluster-gcn: An efficient algorithm for training deep and large graph convolutional networks," *Proceedings of the 25th ACM SIGKDD International Conference on Knowledge Discovery & Data Mining*, 2019.

[405] V. Satuluri and S. Parthasarathy, "Scalable graph clustering using stochastic flows: Applications to community discovery," *Proceedings of the ACM SIGKDD International Conference on Knowledge Discovery and Data Mining*, pp. 737–745, 2009.

[406] J. M. Pujol, V. Erramilli, and P. Rodriguez, "Divide and Conquer: Partitioning Online Social Networks," may 2009.

[407] C. Makris, D. Pettas, and G. Pispirigos, "Distributed Community Prediction for Social Graphs Based on Louvain Algorithm," *IFIP Advances in Information and Communication Technology*, vol. 559, pp. 500–511, 2019.

[408] X. Que, F. Checconi, F. Petrini, and J. A. Gunnels, "Scalable Community Detection with the Louvain Algorithm," *Proceedings - 2015 IEEE 29th International Parallel and Distributed Processing Symposium, IPDPS 2015*, pp. 28–37, jul 2015.

[409] Y. Lu, L. Deng, L. Wang, K. Li, and J. Wu, "Improving Metagenome Sequence Clustering Application Performance Using Louvain Algorithm," *Communications in Computer and Information Science*, vol. 1303, pp. 386–400, 2020.

[410] C. Mao, "Three-Dimensional Tree Visualization of Computer Image Data Based on Louvain Algorithm," *Lecture Notes on Data Engineering and Communications Technologies*, vol. 123, pp. 837–845, 2022.

[411] A. Bustamam, V. Y. Nurazmi, and D. Lestari, "Applications of Cuckoo search optimization algorithm for analyzing protein-protein interaction through Markov clustering on HIV," in *Applications of Cuckoo search optimization algorithm for analyzing protein-protein interaction through Markov clustering on HIV*, 2023.

[412] L. Gu, Y. Han, C. Wang, W. Chen, J. Jiao, and X. Yuan, "Module overlapping structure detection in PPI using an improved link similarity-based Markov clustering algorithm," *Neural Computing and Applications*, vol. 31, pp. 1481–1490, may 2019.

[413] A. Bustamam, "Fast Parallel Markov Clustering in Bioinformatics Using Massively Parallel Computing on GPU with CUDA and ELLPACK-R SparseFormat," *IEEE/ACM Transactions on computational biology and bioinformatics*, vol. 9, 2012.

[414] S. K. Khataniar, D. de Brito Dias, and R. Xu, "Aspects of Multiscale Flow Simulation with Potential to Enhance Reservoir Engineering Practice," *SPE Journal*, vol. 27, pp. 663–681, 02 2022.

[415] A. Kozlova, Z. Li, J. R. Natvig, S. Watanabe, Y. Zhou, K. Bratvedt, and S. H. Lee, "A Real-Field Multiscale Black-Oil Reservoir Simulator," *SPE Journal*, vol. 21, pp. 2049–2061, 10 2016.

[416] O. Moyner and K.-A. Lie, "A multiscale restriction smoothed basis method for compressible black oil models," *SPE Journal*, vol. 21, pp. 2079–2096, June 2016.

[417] O. Moyner and K.-A. Lie, *A Multiscale Method Based on Restriction-Smoothed Basis Functions Suitable for General Grids in High Contrast Media*, vol. Day 2 Tue, February 24, 2015 of *SPE Reservoir Simulation Conference*. Feb. 2015. _eprint: https://onepetro.org/spersc/proceedings-pdf/15RSS/2-15RSS/D021S008R002/1466006/spe-173265-ms.pdf.

[418] M. E. J. Newman, "Analysis of weighted networks," *Phys. Rev. E*, vol. 70, p. 056131, Nov 2004.

[419] M. J. Barber, "Modularity and community detection in bipartite networks," *Physical Review E*, vol. 76, dec 2007.

[420] N. Dugué and A. Perez, "Directed Louvain : maximizing modularity in directed networks," research report, Université d'Orléans, Nov. 2015.

[421] S. Fortunato and M. Barthélemy, "Resolution limit in community detection," *Proceedings of the National Academy of Sciences*, vol. 104, no. 1, pp. 36–41, 2007.

[422] K. Terzaghi, "Erdbaumechanik auf bodenphysikalischer grundlage," *F. Duticke, Vienna*, 1925.

[423] S.-J. Wang and K.-C. Hsu, "The application of the first-order second-moment method to analyze poroelastic problems in heterogeneous porous media," *Journal of Hydrology*, vol. 369, pp. 209–221, 05 2009.

[424] I. Sokolova, M. Bastisya, and H. Hajibeygi, "Multiscale finite volume method for finite-volume-based simulation of poroelasticity," *Journal of Computational Physics*, vol. 379, 12 2018.

[425] M. Ferronato, N. Castelletto, and G. Gambolati, "A fully coupled 3-d mixed finite element model of biot consolidation," *Journal of Computational Physics*, vol. 229, no. 12, pp. 4813 – 4830, 2010.

[426] Y. Abousleiman, A. H.-D. Cheng, L. Cui, E. Detournay, and J.-C. Roegiers, "Mandel's problem revisited," *Géotechnique*, vol. 46, no. 2, pp. 187–195, 1996.

[427] L. Cui, V. Kaliakin, Y. Abousleiman, and A.-D. Cheng, "Finite element formulation and application of poroelastic generalized plane strain problems," *International Journal of Rock Mechanics and Mining Sciences*, vol. 34, no. 6, pp. 953 – 962, 1997.

[428] J. Q. Shi and S. Durucan, "A coupled reservoir-geomechanical simulation study of CO2 storage in a nearly depleted natural gas reservoir," *Energy Procedia*, vol. 1, pp. 3039–3046, feb 2009.

[429] S. Vidal-Gilbert, J. F. Nauroy, and E. Brosse, "3D geomechanical modelling for CO2 geologic storage in the Dogger carbonates of the Paris Basin," *International Journal of Greenhouse Gas Control*, vol. 3, pp. 288–299, may 2009.

[430] A. G. Muntendam-Bos, B. B. Wassing, C. R. Geel, M. Louh, and K. Van Thienen-Visser, "Bergermeer Seismicity Study," Nov. 2008.

[431] P. Teatini, N. Castelletto, and G. Gambolati, "3D geomechanical modeling for CO2 geological storage in faulted formations. A case study in an offshore northern Adriatic reservoir, Italy," *International Journal of Greenhouse Gas Control*, vol. 22, pp. 63–76, mar 2014.

[432] N. A. MAATSCHAPPIJ, "Norg UGS fault reactivation study and implications for seismic threat," tech. rep., NEDERLANDSE AARDOLIE MAATSCHAPPIJ, Netherlands, 2016.

[433] M. Bakhtiari, S. Shad, D. Zivar, and N. Razaghi, "Coupled hydro-mechanical analysis of underground gas storage at Sarajeh field, Qom formation, Iran," *Journal of Natural Gas Science and Engineering*, vol. 92, p. 103996, aug 2021.

[434] T. Bai and P. Tahmasebi, "Coupled hydro-mechanical analysis of seasonal underground hydrogen storage in a saline aquifer," *Journal of Energy Storage*, vol. 50, p. 104308, jun 2022.

[435] L. Zeng, A. Keshavarz, Q. Xie, and S. Iglauer, "Hydrogen storage in majiagou carbonate reservoir in china: Geochemical modelling on carbonate dissolution and hydrogen loss," *International Journal of Hydrogen Energy*, vol. 47, no. 59, pp. 24861–24870, 2022.

ACKNOWLEDGEMENT

This is a humble attempt to thank everyone who were part of this wonderful PhD journey. I would like to express my deepest gratitude to the following individuals who have played a significant role in my academic journey:

First and foremost, I would like to thank my supervisor, **Dr.Hadi Hajibeygi**, for his unwavering support, guidance, and mentorship throughout my Ph.D. journey. Hadi's incredible work ethic, dedication, and passion for research have been truly inspiring. Your technical expertise, story-telling ability, and leadership qualities have taught me a great deal and I will carry them with me for the rest of my life. I hope that our relationship continues beyond my Ph.D. program. Special mention to **Prof.Kees Vuik** where because of the honors project I pursued with him during my MSc, I was able to meet Hadi through him.

I did not get to interact a lot with **Prof. dr. ir. Jan Dirk Jansen** However your effective yearly meetings have been a great help in streamlining my Ph.D. story-line and ensuring that I finished my Ph.D. on time. Your expertise in the field and your constructive feedback have been invaluable in shaping my research, and I am grateful for the guidance you provided throughout my Ph.D.

Dr.Chris Spiers, I am grateful for the collaboration we had and for sharing your knowledge about salt caverns. Your kindness, approach-ability, and willingness to share your expertise have made a significant impact on my research, and I appreciate the time you took to help me understand the complexities of your work.

Dr. Auke Barnhoorn, even though we worked together for a short period on a collaborative paper, your effective guidance and willingness to engage in scientific discussions have been immensely helpful. I appreciate the time and effort you took to share your knowledge and expertise with me.

Dr. Martin Leseur, thank you for collaborating on the review article and valuable feedback on such short notice. It did improve the writing and the structure of the paper.

I would like to thank the support staff of the department **Marlijn, Lydia, Rinda, Ralf, Ingrid, and Barbara** who has always greeted me endearingly whenever I have approached them with all kinds of problems with paperwork and laptop issues.

Dr. Jonathan Morris and **Dr. Matei Tene**, thank you for the internship opportunity at SLB. The experience was transformative, and it gave me a clearer sense of direction for my future career. I learned a great deal about software teams and how dynamic they can be, and I was able to explore my resume outside my comfort zone. Working closely with Matei has been a privilege, and his competence and skills as a software engineer have been inspiring.

I would like to acknowledge **Dr. Herminio** and **Dr. Debanjan**, two postdocs of TU Delft whom I have had the pleasure of collaborating with over the past two years. Working with both of you has been an enjoyable and rewarding experience, and I highly appreciate the effort that you both have put into our collaborations. Though your expertise

is different, both of you are highly capable of going deep into any problem statement and are really good at teaching.

Milad, working closely with you on a year-long project has been an enriching experience. Your expertise in the experimental aspects of the project has been invaluable, and I have learned a great deal about how to convey messages effectively through illustrations. It was a pleasure to work with **Edgar Hernandez**, a highly efficient master's student, and the project was a success because of our collaborative efforts.

Edgar, Artur, Romanos, and Nordin, thank you for choosing to work with me. Your contributions to our collaborative projects have been significant, and I have learned a great deal from your expertise and skills. Working with you has helped me build my leadership skills and has also taught me the importance of effective time management.

All the Admire members: **Dr. Herminio, Dr. Debanjan, Dr.Mousa, Leila, Fanxiang, Dr. Thejas, Dr. Yuhang, Willemijn, Sara, Johno, Dr.Artur, Dr.Maartje, Mengjie, and Ziliang**, attending group meetings and conferences with you has been a pleasure. I have learned a great deal from your diverse expertise and perspectives, and it has been an honor to build a social bond with each of you, especially in the challenging post-COVID times. When I started my Ph.D., I met Mousa, Leila, and Fanxiang around at the same time and I am glad that we have shared our journey together and fought tough times during COVID and happy for Mousa for defending effortlessly and securing a job.

Sian, Willemijn, Kiarash, Mohsen, Mohsan, Yuan, Gabriel, Xiaoming, Chris, Laura, Michiel, Xiacong, Artur, Herminio, and Jenny, thank you for sharing the office space with me and for being a part of the lunch group. Your company, wonderful stories from different cultures, and kindness have made my PhD journey much more enjoyable and fulfilling. I will always remember Sian's homemade cakes, Willemijn's contagious kindness, Gabriel's energy, Kiarash's ability to interact with anyone, Artur's ChatGPT stories, Mohsan's late evening IPL/cricket discussions, Mohsen's passion for films, Chris's easy and laid back marathons, Yuan's driving license exam episodes, Jenny's California stories and certainly many more.

Then it comes to the PSOR gang where I used to chill with **Entela, Shihao, Kiarash, Mohsen, Milad, Eddy, Hamed, Elahe, Aydin**. It's always fun to relax at the department pub after a long week and with your company, I was more relaxed than ever :).

Arvind, Shihao, Anand, Milad, Jimmy, Sandeep and Mohsen, thank you for being my gym buddies and always motivating me to push my boundaries. Our discussions on different gym techniques and protein intake have helped me grow mentally and physically strong. Gym has been my stress buster throughout my Ph.D. journey, and I am grateful to have had you by my side at some point in time.

I would like to thank my Kannadiga crew **Anoosh, Arvind, Karthik, Arya, Alok, Chetan, Manav, Thejas, Shrinidhi, and Akshar** for being my friends for the past five years. Moving away from my home country and finding friends from the same city has been a blessing. Our bond allowed us to share anything and everything. The long night discussions ranging from investment ideas to stupid funny memes, and escape trips to faraway countries disconnecting from every responsibility will definitely be part of my life.

Next comes the people who boarded the same boat called a PhD at the same time as me who pursued MSc at TUD. **Anand, Udhav, Arjun, Shravan, Dhanashree, Alok, Vishrut, Mihir, Kunal, and Vetri** thank you for being part of my journey. It's always good

to chat with someone and share our stories, you get different perspectives on life which might as well make it to appreciate on's own life better.

Then comes my other group of beloved friends where initially we used to meet up in Delft RH during our MSc and then we diverged in different paths because of jobs. **Sam, Anurag, Badri, Varun, Sushant, Anoosh, Arvind, Arya, Shashish, Deepika and Sharab**, thanks for organizing meetups and parties in different parts of the Netherlands from Enschede to Rijswik. I think over time it has always been relaxing to spend the entire weekend with you guys in a relaxed manner, playing FIFA, Mafia, board games, dining at fancy restaurants, playing pool, and of course, attending Sam-rag's wedding in Mumbai.

Then the beloved Rotterdam crew **Shriramji, Dhanshree, and Advait** thank you for hosting several movie/game nights, and Indian festivals at your places. We became regular customers of Bombay Corner and Nisarga over time. I hope to reach your place at the scheduled time for once :p.

I have always stayed with flatmates outside India. This allows me to meet new people from different backgrounds. Thanks to all my flatmates especially my current flatmates and really good friends **Nilay, Neel, and Savneek**. After a long day of work, it's always good to steam off by talking about what's going on in life on a regular basis along with enjoying a nice meal with watching TV.

I was fortunate to have pursued my bachelor's (Btech) in a prestigious institute called NITK, Surathkal. I am happy to have made many good friends such as from **the Common Wing, a Kannada mech gang, and VVS friends** who are currently across the globe following their passion and dream.

Then comes my **extended close family** of cousins, aunts, uncles, and especially grandparents. Because of COVID, I used to spend more than 1 month of time in India. During this time, it was ensured that I eat all kinds of foods (street to fancy) and never failed to organize family outings on long weekends. I think these instances have made our relationship stronger and I will try my best to ensure it stays this way in the long run.

Last but not least are thanking my own family who are residing in Germany my lovely brother **Varun (anna) and sister-in-law Smruthi (athige)**. Often there are lonely periods during a PhD when you question everything whats going on around you, to stay sane I used to often visit my brother. I have known you from 27 years and you have been the kindest and sweetest brother. And athige I have known you from 5 years but it feels like I have known you from my birth as well :). Thank you for hosting me several times, taking me to different countries and pampering me like a 5 year old. Ofcourse I enjoyed it.

Lastly and most importantly my parents, **Ramesh Kumar (papa) and Vanishree (amma)**. I usually don't express much to you however, the innumerable sacrifices which you guys have done and the amount of hard work you have done in your childhood and adulthood is resulting in my Ph.D. Thank you for everything which has shaped me to an able individual, even though we are on different continents my day doesn't end well when I don't hear your voice at least once :).

Once again, I would like to express my gratitude to all of the above individuals for their contributions to my Ph.D. journey. I could not have achieved this milestone without your support and encouragement.

CURRICULUM VITÆ

Kishan RAMESH KUMAR

02-01-1996 Born in Bengaluru, India.

EDUCATION

2013-2017	B.Tech (Bachelors), Mechanical Engineering National Institute of technology, Surathkal (NITK) Karnataka, India
2017-2019	MSc in Energy, flow and process technology Delft university of technology
Dec/19 - 2023	PhD. Energy transition theme, CiTG faculty Delft university of technology *Thesis:* Multiscale modelling of hydrogen storage in the sub-surface *Promotor:* Dr. H. Hajibeygi *Promotor:* Prof. dr. J. D. Jansen

INTERNSHIPS AND WORK EXPERIENCE

July-Oct 2022	Internship at **SLB**, HPC Numerics team, Abingdon, UK (Remote) **Title:** Coarsening of algebraic multiscale grid using unsupervised graph based machine learning
Jan-Oct 2019	MSc thesis, **ETH, Zurich Switzerland** **Title:** Indirect estimation of mean vorticity from polarized emission of nanoparticles in turbulent duct flows
Aug-Dec 2018	Internship, **Imperial college, London** **Title:** Studying the temperature profile of freezing of droplets using Particle Laser Induced Fluorescence
Jan-July 2018	Honors project under Prof. dr. Kees Vuik, **TU, Delft, Netherlands** **Title:** A comparison of POD and Ritz vectors for Deflated ICCG
Aug/16-Aug/17	B.Tech project, **Indian Institute of Science, Bangalore, India** **Title:** Induction heating of eutectic non-magnetic alloys - Computational and Experimental study
May-July 2016	Internship, **University of Illinois Urbana Champaign, USA** **Title:** Frosting and Defrosting of Heat Exchangers under Surface modifications Particle Laser Induced Fluorescence
May-July 2015	Internship, **Indian Institute of technology, Bombay, India** **Title:** Modelling of local formulation of shock unsteadiness k-ϵ model in turbulence

List of Publications

Journals

7. **K. Ramesh Kumar, H. Hajibeygi**, *Multiscale poroinelastic simulation of reservoirs*, Under preparation.

6. **K. Ramesh Kumar, M. Tene** , *Coarsening of algebraic multiscale grid using unsupervised graph based learning*, Under review .

5. **K. Ramesh Kumar, H.T. Honorio, D. Chandra, M. Leseur, H. Hajibeygi**, *Comprehensive review of geomechanics of underground hydrogen storage in depleted reservoirs and salt caverns*, Journal of Energy Storage, 73, Part B, 108912.

4. **M. Naderloo**[1], **K. Ramesh Kumar**[1], **E. Hernandez, H. Hajibeygi, A. Barnhoorn**, *Experimental and numerical investigation of the sandstone deformation under cycling loading relevant for underground energy storage*, Journal of Energy Storage, 64, 2352-152X.

3. **K. Ramesh Kumar, H.T. Honorio, H. Hajibeygi**, *Simulation of the inelastic deformation of porous reservoirs under cyclic loading relevant for underground hydrogen storage*, Scientific reports, 12:21404 (2022) .

2. **K. Ramesh Kumar, A. Makhmutov, C.J. Spiers, H. Hajibeygi**, *Geomechanical simulation of energy storage in salt formations*, Scientific Reports 11:1, 11(1) (2021).

1. **K. Ramesh Kumar, H. Hajibeygi**, *Multiscale simulation of inelastic creep deformation for geological rocks*, Journal of Computational Physics, **440**, 110439, (2021).

Conferences

10. **K. Ramesh Kumar, M. Tene, H. Hajibeygi**, *Coarsening of algebraic multiscale grid using unsupervised graph based learning*, SIAM Geosciences, 2023, Norway .

9. **M. Naderloo, E. Hernandez, K. Ramesh Kumar, H. Hajibeygi, A. Barnhoorn**, *Effect of stress cycling on the deformation and AE characteristics of reservoir rock from the perspective of energy storage: An experimental study*, EGU, 2023, Austria.

8. **M. Naderloo, E. Hernandez, K. Ramesh Kumar, H. Hajibeygi, A. Barnhoorn**, *Experimental study on effect of cyclic loading on deformation and AE characteristics of sandstone: Relevant for energy storage*, Interpore 2023, Edinburgh, Scotland.

7. **K. Ramesh Kumar, H.T Honorio, H. Hajibeygi**, *Simulation of the inelastic deformation of porous reservoirs under cyclic loading relevant for underground hydrogen storage*, Interpore (2023).

1: Equal contribution

6. **K. Ramesh Kumar, H. T Ḣonorio, H. Hajibeygi**, *Fully-coupled multiscale poro-mechanical simulation relevant for subsurface energy storage*, 16th International Conference of International Association for Computer Methods and Advances in Geomechanics, Italy, (2022).

5. **E. Hernandez, M. Naderloo, K. Ramesh Kumar, H. Hajibeygi, A. Barnhoorn**, *Modeling of Cyclic Deformation of Sandstones Based on Experimental Observations*, 3rd EAGE, Geoscience and Engineering in Energy Transition conference,, Hague (2022).

4. **K. Ramesh Kumar, H. Hajibeygi**, *Multiscale modeling of nonlinear viscoplastic deformation of geological rocks for subsurface energy storage*, 2nd EAGE, Geoscience and Engineering in Energy Transition conference, France (2021).

3. **K. Ramesh Kumar, H. Hajibeygi**, *Multi-scale Nonlinear Modeling of Subsurface Energy Storage: Cyclic Loading with Inelastic Creep Deformation*, ECMOR XVII, Sep 2020, Volume 2020, p.1 - 13.

2. **K. Ramesh Kumar, H. Hajibeygi**, *Influence of pressure solution and evaporate heterogeneity on the geo-mechanical behavior of salt caverns*, The Mechanical Behavior of Salt X: PROCEEDINGS OF THE 10TH CONFERENCE ON THE MECHANICAL BEHAVIOR OF SALT (SALTMECH X), UTRECHT, THE NETHERLANDS, 06-08 JULY (2022).

1. **K. Ramesh Kumar, H. Hajibeygi**, *Multi-scale Nonlinear Modeling of Subsurface Energy Storage: Cyclic Loading with Inelastic Creep Deformation*, Interpore conference, China (2020).